The Dissertation Committee for Julia Schneider certifies that this is the approved version of the following dissertation:

COMPRESSION AND PERMEABILITY BEHAVIOR OF NATURAL MUDSTONES

Committee:

Peter B. Flemings, Supervisor

David Mohrig

Meinhard B. Cardenas

Ruarri J. Day-Stirrat

John T. Germaine

COMPRESSION AND PERMEABILITY BEHAVIOR OF NATURAL MUDSTONES

by

Julia Schneider B.S.; M.S.

Dissertation

Presented to the Faculty of the Graduate School of

The University of Texas at Austin

in Partial Fulfillment

of the Requirements

for the Degree of

Doctor of Philosophy

The University of Texas at Austin

December 2011

Dedication

I dedicate my dissertation to my parents for their exceptional love and support. They accepted and supported my decision to move more than 8000 km away for more than five years to fulfill my dream of pursuing a PhD in geosciences.

Acknowledgements

I would like to extend very special thanks to my fiancé Bobby who believed in me and supported me all along, who genuinely shared my happiness in good times, cheered me up in hard times and was just there for me at all times and especially during the last couple of months. More special thanks go to my family, particularly my parents, and friends, both in Germany and the USA, for their love and support throughout the process of completing my Ph.D.

I have gained and benefited from a dissertation committee with broad expertise in the geosciences, from geotechnical engineering to morphodynamics and hydrological systems. I would like to express my highest gratitude to my supervisor Peter Flemings who taught me how to be a good researcher. I thank Peter for believing in me (and my English skills) from the first time we met on a drilling vessel in the Gulf of Mexico, and giving me the opportunity and funding to pursue a Ph.D. in the USA. I would have not gotten where I am now without Peter's persistent push, enthusiasm, and support. I am also extremely grateful to Dr. John Germaine for letting me visit his Geotechnical Engineering lab at the Massachusetts Institute of Technology for seven months, teaching me all basics of geotechnical engineering, and for his continuous invaluable advice on experimental matters throughout my PhD. I thank Ruarri Day-Stirrat, who has always been available for discussions and performed the fabric analyses on my samples. I have learned a lot from Ruarri's expertise in clay mineralogy and clay fabric. I thank David Mohrig and Bayani Cardenas for their interest in my research and their support along the way. Discussions with them helped me to understand how my research fits into the larger picture.

I thank the UT members of the GeoFluids research group. Tessa Green with her positive attitude and organized way of doing things provided great assistance during my last year, especially during the transition time between lab managers. I am especially grateful to the lab managers Peter Polito and Mark Andrews for their extensive mechanical, technical, and logistical help. I thank Heather Nelson from Penn State, who is a consultant for the GeoFluids group, for her technical assistance with logging and seismic software during my time at Penn State and later at UT. I would also like to thank Robert Reed from the Bureau of Economic Geology, who spent hours of preparing my samples for scanning electron microscopy and taking the scanning electron microscope images. Special thanks also go to Judy Sansom, Mark Wiederspahn, Kevin Johnson, and the remaining UTIG staff who helped me with accounting and technical issues.

I thank my fellow graduate students from The University of Texas at Austin; in particular Derek Sawyer, who guided, helped, and supported me throughout my PhD, and Yao You, who greatly helped me with his brilliant mathematical knowledge. I would also like to extend special thanks to Philip Guerrero, who did everything in his power to make my life as an international student easier. Without his help I would have not mastered all bureaucratic challenges.

Finally, I would like to thank the following for financial support: The University of Texas at Austin Institute of Geophysics Ewing/Worzel fellowships, Schlanger Ocean Drilling Fellowship from Ocean Leadership, Hess Fellowship, and Chevron Excellence Awards.

COMPRESSION AND PERMEABILITY BEHAVIOR OF NATURAL MUDSTONES

Julia Schneider, Ph.D.

The University of Texas at Austin, 2011

Supervisor: Peter B. Flemings

Mudstones compose nearly 70% of the volume of sedimentary basins, yet they are among the least studied of sedimentary rocks. Their low permeability and high compressibility contribute to overpressure around the world. Despite their fundamental importance in geologic processes and as seals for anthropogenic-related storage, a systematic, process-based understanding of the interactions between porosity, compressibility, permeability, and pore-size distribution in mudstones remains elusive.

I use sediment mixtures composed of varying proportions of natural mudstone such as Boston Blue Clay or Nankai mudstone and silt-sized silica to study the effect of composition on permeability and compressibility during burial. First, to recreate natural conditions yet remove variability and soil disturbance, I resediment all mixtures in the laboratory to a total stress of 100 kPa. Second, in order to describe the systematic variation in permeability and compressibility with clay fraction, I uniaxially consolidate the resedimented samples to an effective stress equivalent to about 2 km of burial under hydrostatic conditions. Scanning electron microscope images provide insights on microstructure.

My experiments illuminate the controls on mudstone permeability and compressibility. At a given porosity, vertical permeability increases by an order of magnitude for clay contents ranging from 59% to 34% by mass whereas compressibility reduces by half at a given vertical effective stress. I show that the pore structure can be described by a dual-porosity system, where one rock fraction is dominated by silt where large pores are present and the majority of flow occurs and the other fraction is dominated by clay where limited flow occurs. I use this concept to develop a coupled compressibility-permeability model in order to predict porosity, permeability, compressibility, and coefficient of consolidation. These results have fundamental implications for a range of problems in mudstones. They can be applied to carbon sequestration, hydrocarbon trapping, basin modeling, overpressure distribution and geometry as well as morphology of thrust belts, and an understanding of gas-shale behavior.

Table of Contents

List of Tables

List of Figures

Chapter 1: Introduction

Mudstones are fine-grained sedimentary rocks composed of silt and clay, commonly between 25% and 75% of clay or silt. They are found in deep sea environments as well as on continental margins and comprise about 70% of the volume of sedimentary basins around the world (e.g. Dewhurst et al., 1998). Mudstones are not well understood yet because of large variations in their mechanical and transport behavior unlike sandstone that have long been the subject to research. The high compressibility and low permeability of mudstones contribute to overpressure around the world (Broichhausen et al., 2005). Overpressure drives fluid flow in the subsurface, which impacts solute mass transport and heat transfer. Overpressure can cause slope instabilities such as submarine landslides that in turn can cause tsunamis, which can be fatal to highly populated coastal areas.

Offshore oil platforms can be destroyed if overpressure is encountered while drilling through the subsurface and drillers do not act. This can cause extensive damage to marine and wildlife habitats as well as fishing and tourism industries. Due to their low permeability mudstones are often used as barriers for CO_2 sequestration or waste deposal. They can also store large amounts of natural gas. Recent techniques have been developed to extract the natural gas economically (Zoback et al., 2010).

Mudstones consolidate as the effective stress, which is the difference between total stress and pore fluid pressure, increases. This means that the pore fluid starts to drain and porosity decreases. The change in porosity with effective stress is described as the compression behavior. As compression occurs the pores become smaller and consequently the permeability reduces. The rate at which permeability decreases with decreasing porosity depends on grain size distribution and mineralogy. Mudstones

composed of enough silt grains to form silt bridges can develop multi-porosity systems. A multi-porosity material can be described by more than a single characteristic porosity; one porosity that reflects the porosity of silt clusters and one that reflects the porosity of clay clusters. The interaction between both characteristic pore sizes at different time scales causes the solute and flow transport through multi-porosity systems to be significantly different from transport behavior through a material with a single characteristic porosity.

The porosity reduction with increasing effective stress, which is also referred to as compression trend, varies largely for mudstones as function of grain size distribution and mineralogy. Mondol et al. (2007) showed a series of compression trends for various mudstones from around the world. The evolution of porosity with effective stress is mostly described by exponential or power law functions, which are empirical, for example Athy (1930). A commonly used method to describe compression behavior now is an approach developed in the field of soil mechanics based on Terzaghi's (1925) principle of effective stress, which suggests that mechanical compression of soils and sediments is driven only by effective stress on the sediment's solid matrix (Smith, 1971).

Due to the low permeability of mudstones, *in-situ* permeability measurements are rare because long time periods are required in order to reach steady state. Therefore, various methods and models have been developed to measure permeability in the laboratory or infer it from logging data using empirical models. First, permeability has been measured in the laboratory on core samples from natural mudstones using falling-head permeameters, constant-head permeameters (Lambe and Whitman, 1979), consolidation tests (Terzaghi and Peck, 1948) or transient pulse decay (e.g. Yang and Aplin, 2007). Second, permeability is predicted from empirical relationships between permeability and porosity built from laboratory measurements (Tavenas et al., 1983;

Yang and Aplin, 2010), or from theoretical models such as Hagen-Poiseuille (e.g. Yang and Aplin, 1998), Kozeny-Carman (e.g. Revil and Cathles, 1999; Chapuis and Aubertin, 2003), or dual-component models (e.g. Koltermann and Gorelick, 1995; Revil and Cathles, 1999). Third, laboratory-prepared samples are used to analyze the effect on permeability by changing only one parameter such as grain size (Wagg and Konrad, 1990; Mondol et al., 2008a; Mondol et al., 2008b; Shafiee, 2008; Bandini and Sathiskumar, 2009).

The goal of this dissertation is to gain insights into the influence of grain size distribution and mineralogy on deformation and fluid transport behavior of mudstones. Ultimately, I wish to understand the microscale processes that control permeability and compressibility. I synthesize different approaches by looking at (1) a regional mudstone overpressure prediction to study implications of hydrogeological mudstone behavior, (2) intact cores to derive geomechanical behavior and *in-situ* stress states and permeability, (3) laboratory-prepared samples to understand systematic variations in geomechanical behavior as a function of clay fraction, and (4) microscopy imaging to study microscale processes that drive observed deformation and transport behaviors. Based on these approaches I developed a one dimensional mudstone compression and permeability model.

In Chapter 2, I use logging data, a single *in-situ* pressure measurement, bulk density data, and preconsolidation stresses derived from consolidation experiments to interpret overpressure within mudstones at two sites in the Brazos-Trinity Basin IV, on the continental slope of the Northern Gulf of Mexico.

The key result of Chapter 2 is that overpressures are 70% and 80% of the hydrostatic vertical effective stress at both sites. These high overpressures in the

mudstones within a few hundred meters of the seafloor were caused by rapid deposition. Results indicate that although overpressures are greater at the location with less overburden, a large fraction of overpressure caused by the overlying basin fill was actually dissipated by pore fluids draining upward toward the sandy and relatively permeable turbidite fill.

In Chapter 3, I use uniaxial constant-rate-of-strain consolidation experiments to describe permeability - porosity relationships and to derive *in-situ* permeabilities for mudstones from the Ursa Basin in the Gulf of Mexico.

The results show a large variation in permeability – porosity relationships over more than an order of magnitude. This work emphasizes the large spread in permeability behavior of geological mudstone samples. *In-situ* permeabilities follow the same trend as the experimentally-derived permeability – porosity relationship. The harmonic mean appears to be the best indicator of upscaled vertical permeability. I calculate upward flow rates between 1.5 and 3.0 mm/yr within the mudstones of the Ursa Basin.

In Chapter 4, I avoid this large variation in composition between several intact cores, as encountered in the Ursa Basin, by making mudstones in the laboratory using a method called resedimentation. Then I use uniaxial consolidation tests on these undisturbed and homogeneous samples that are comprised of mixtures of Boston Blue Clay and silt to systematically study the effect of grain size on permeability behavior of mudstones.

Permeability increases with decreasing clay fraction at a given porosity. I describe this behavior to result from a dual-porosity system, where large pores between silt grains that act as high permeability pathways are preserved in addition to small pores within the clay matrix. I developed a dual-porosity model to describe the permeability of clay-silt mixtures with graded grain size distributions on the basis of clay content (< 2μm by

mass) and porosity. The results are an important step toward developing a process-based understanding of the mechanics of consolidation and its consequent impacts on permeability.

Chapter 5 is based on a similar approach as was used in Chapter 4; however, instead of a glacial clay I use a marine, deepwater mudstone from offshore Japan that is more directly applicable to pore pressure predictions and basin modeling than a glacial clay. I use uniaxial consolidation tests on resedimented sediment mixtures composed of varying fractions of Nankai mudstone and silt to describe the systematic variation of permeability and compressibility with clay fraction. Backscattered electron microscope images help analyze the microstructure and address the relative change in particle alignment.

The initial porosity drops and the samples become stiffer with decreasing clay content. At a given porosity, vertical permeability varies over two orders of magnitude for clay fractions between 34 and 59%. I combine the permeability model developed in Chapter 4 with a compression model and develop a coupled compressibility – permeability model that predicts how porosity, compressibility, permeability, and coefficient of consolidation change with vertical effective stress and composition.

Chapter 6 is a comparison between Boston Blue Clay and the marine Nankai mudstone in order to explain similarities and differences. I compare both mudstones in their index properties as well as their compression and permeability behavior.

The results show that clay mineralogy and specific surface area as well as the ability to form a diffusive double layer and to interact with the pore fluid have large influences on compression and permeability behavior of mudstones. Smectite-rich mudstones compress more and decrease more in permeability for a given porosity change than do smectite-poor mudstones. This study shows that it is important to consider not

only grain size distribution but also clay mineralogy as predictions of geomechanical behavior of mudstones could otherwise be off by orders of magnitude.

One of the key contributions of my dissertation is the use of resedimentation to systematically prepare samples in the laboratory of known composition and under controlled conditions. Resedimentation is an approach novel to geosciences. So far resedimentation has only been used in civil and environmental engineering, where for construction purposes the location of interest is the uppermost tens of meters below the ground. Here I apply this method developed in geotechnical engineering to a geological problem. Where geological cores are highly variable in composition and highly disturbed due to drilling, resedimentation allows me to perform very systematic studies in order to understand underlying behaviors that control deformation and transport phenomena in mudstones. This is not possible for a series of intact cores where more than one parameter can change at a time.

The second key contribution is the development of a model based on resedimentation and consolidation experiments as well as microscopy imaging to predict porosity, compressibility, permeability, and coefficient of consolidation (diffusivity) of mudstones. These parameters are difficult to determine but are key input parameters for basin models as well as models of geometry and morphology of continental margins. The model that needs to be calibrated to a regional mudstone lithology can then predict compressibility, permeability, and coefficient of consolidation downhole as a function of clay fraction. Gamma ray logs that are an indication for clay fraction may even allow real-time prediction of these key parameters that give insight into the *in-situ* pore pressure field in the subsurface.

The third key contribution of this work is the definition of three microscale mechanisms: (1) silt bridging preserves large pores, (2) stress bridges inhibit clay particle

alignment, and (3) local clay particle compression within stress bridges alters pore size distribution. These microscale mechanisms control compression and permeability behavior of mudstones and how mudstones can develop a dual-porosity structure. Dual-porosity systems have fundamentally different transient flow and solute transport behaviors, thus, they have large implications on flow and mass transport. My results have significant implications for pore pressure predictions, basin models, modeling of geometry and morphology of accretionary wedges and pore pressures in accretionary wedges, geohazard analyses, and offshore drilling and well design.

FUTURE RESEARCH

The experimental and numerical analyses that I conducted for this research contribute to the understanding of deformation, fluid flow, and pore pressures in mudstones. However, there is now the opportunity to expand this research in order to study these processes and the controls on them further and to improve current relationships. In the next paragraphs I highlight some questions that still remain open and could form potential future research projects.

The analyses conducted in this research show that the specific surface area significantly influences the compression and permeability behavior. However, the measurements performed in this research appear to have been produced by an inappropriate method, particularly for the smectite-rich sediments from the Ursa Basin and the Nankai Trough, offshore Japan. Specific surface area measurements conducted with a wet technique such as Methylene Blue, for example, should produce much higher values than presented here using the gas adsorption technique. Thus, a more drastic difference in specific surface area between BBC and Nankai mudstone should arise. If I

had the opportunity, I would re-measure the specific surface areas of at least all Ursa Basin samples and the Nankai mudstone, and perhaps also the BBC (to be consistent for comparisons).

Another future project is to test the multi-porosity model against others. Models such as Kozeny-Carman-type models, for example, might work as well as the dual-porosity model in predicting the observed permeability behavior of clay-silt mixtures. In order to find out whether a dual-porosity model is necessary to describe the compression and permeability behavior of mudstones a solute transport model needs to be conducted.

Another question that still remains open is how particle shape, and particularly the shape of the silt grains, affects the compression and permeability behavior of mudstones. A future approach would be to choose a silt-sized silica with a different particle shape, e.g. rounder than the angular grains of the US MIN U SIL 40, and ad-mix it to the Boston Blue Clay and Nankai mudstone with the same clay size fractions as performed in this research. Then a comparison of the compression and permeability results and microscopy imaging for the sediment mixtures with the new silt and the sediment mixtures with the MIN U SIL 40 would illuminate the influence of particle shape on packing structures and compression and permeability behavior presuming nothing else is changed in the procedure. The coupled compressibility-permeability model should then be applied to the new datasets in order to see the influence of the particle shape on the model parameters.

The coupled compressibility-permeability model developed in this dissertation predicts porosities, permeabilities, compressibilities, and coefficients of consolidation that are in good agreement with the measurements. However, at this point, the model can only be applied to clay fractions over which the model is constrained (34 to 59% clay-sized particles by mass). In order to proof the model's validity at clay fractions outside the range tested here, additional sediment mixtures should be prepared. Particularly

important are the end-members: pure silt and pure clay. A potential future project is to perform an uniaxial constant-rate-of strain consolidation test on the silt-sized silica used here (US MIN U SIL 40) to determine the compression and permeability behavior. Then a comparison of these new datasets with the predictions by the coupled compressibility-permeability model would show whether the model is still valid and can be applied for clay fractions that are outside the constrained range.

Similarly, the BBC and Nankai mudstone could be centrifuged to extract the size fraction smaller than 2 μm. This extracted fraction represents the pure clay end-member in the compressibility-permeability model because all particles are finer than 2 μm, which is the cutoff used in the model. An uniaxial constant-rate-of strain consolidation test would test the validity of the model on the other side of constrained clay fractions (for small clay fractions).

Another potential project goes in hand with the two previous paragraphs. By performing additional geotechnical tests on the pure end-members, the relationships between the compression model parameters and the clay fraction can be improved resulting in a more robust model. I described the relationship between parameter C and clay fraction as linear and the relationship parameter v_0 and clay fraction as quadratic. New consolidation tests on the end-members might show that these relationships do not apply to clay fractions outside the constrained range in this research.

Through the two mudstones tested here I fortuitously studied an illite-silt and a smectite-silt system. An interesting future research project would be to perform similar analyses on a natural mudstone with a high kaolinite content symbolizing a kaolinite-silt system. Then a full comparison of compression and permeability behaviors, microstructures, and model parameters between the most common clay minerals could be obtained. This could ultimately lead to a model that predicts porosity, compressibility,

permeability, and coefficient of consolidation over large effective stress ranges as a function of not only grain size but also mineralogy.

The biggest challenge still is the understanding of the relation between field and laboratory behavior. Why does the porosity in the field reduce so much more with increasing vertical effective stress than the porosity in the resedimented, laboratory-consolidated sample? Do they have different initial structures? What could be done to make the resedimentation experiment more natural? Specifically, how could an initial structure more similar to that in nature be produced in the laboratory? An idea is to produce a flocculated mud in the resedimentation experiment. One way could be to prepare a more dilute slurry than in this research and control the chemistry while mixing all components and letting water evaporate off or decanting water.

REFERENCES

Athy, L.F., 1930. Density, porosity, and compaction of sedimentary rocks. *Am. Assoc. Pet. Geol. Bull.*, 14: 1-22.

Bandini, P., and Sathiskumar, S., 2009. Effects of Silt Content and Void Ratio on the Saturated Hydraulic Conductivity and Compressibility of Sand-Silt Mixtures. *Journal of Geotechnical and Geoenvironmental Engineering*, 135(12): 1976-1980, doi:10.1061/(ASCE)GT.1943-5606.0000177.

Broichhausen, H., Littke, R., and Hantschel, T., 2005. Mudstone compaction and its influence on overpressure generation, elucidated by a 3D case study in the North Sea. *International Journal of Earth Sciences*, 94(5-6): 956-978, doi:10.1007/s00531-005-0014-1.

Chapuis, R.P., and Aubertin, M., 2003. On the use of the Kozeny-Carman equation to predict the hydraulic conductivity of soils. *Canadian Geotechnical Journal*, 40: 616-628, doi:10.1139/T03-013.

Dewhurst, D.N., Aplin, A.C., Sarda, J.P., and Yang, Y.L., 1998. Compaction-driven evolution of porosity and permeability in natural mudstones: An experimental study. *Journal of Geophysical Research*, 103(B1): 651-661, doi:10.1019/97JB02540.

Koltermann, C.E., and Gorelick, S.M., 1995. Fractional packing model for hydraulic conductivity derived from sediment mixtures. *Water Resources Research*, 31(12): 3283-3297, doi:10.1029/95WR02020.

Lambe, T.W., and Whitman, R.V., 1979. Soil Mechanics: SI Version. New York, Wiley, 553 p.

Mondol, N.H., Bjørlykke, K., Jahren, J., and Høeg, K., 2007. Experimental mechanical compaction of clay mineral aggregates - Changes in physical properties of mudstones during burial. *Marine and Petroleum Geology*, 24: 289-311, doi:10.1016/j.marpetgeo.2007.03.006.

Mondol, N.H., Bjørlykke, K., and Jahren, J., 2008a. Experimental compaction of clays: relationship between permeability and petrophysical properties in mudstones. *Petroleum Geoscience*, 14: 319-337, doi:10.1144/1354-079308-773.

Mondol, N.H., Fawad, M., Jahren, J., and Bjørlykke, K., 2008b. Synthetic mudstone compaction trends and their use in pore pressure prediction. *First Break*, 26: 43-51, doi:10.3997/1365-2397.2008018.

Revil, A., and Cathles, L.M., 1999. Permeability of shaly sands. *Water Resources Research*, 35(3): 651-662, doi:10.1029/98WR02700.

Shafiee, A., 2008. Permeability of compacted granule - clay mixtures. *Engineering Geology*, 97: 199-208, doi:10.1016/j.enggeo.2008.01.002.

Smith, J.E., 1971. The dynamics of shale compaction and evolution of pore fluid pressure. *Math. Geol.*, 3: 239-263.

Tavenas, F., Jean, P., Leblond, P., and Leroueil, S., 1983. The permeability of natural soft clays. Part 2: Permeability characteristics. *Canadian Geotechnical Journal*, 20: 645-660.

Terzaghi, K., 1925. Erdbaumechanik auf bodenphysikalischer Grundlage. Leipzig, 399 p.

Terzaghi, K., and Peck, R.B., 1948. Soil mechanics in engineering practice. New York, Wiley.

Wagg, T.B., and Konrad, J.-M., 1990, Index properties of clay-silt mixtures, 43rd Canadian Geotechnical Conference, Volume 2: Québec City, Canada, p. 705-710.

Yang, Y., and Aplin, A.C., 2010. A permeability-porosity relationship for mudstones. *Marine and Petroleum Geology*, 27: 1692-1697, doi:10.1016/j.marpetgeo.2009.07.001.

Yang, Y.L., and Aplin, A.C., 1998. Influence of lithology and compaction on the pore size distribution and modelled permeability of some mudstones from the Norwegian margin. *Marine and Petroleum Geology*, 15(2): 163-175, doi:10.1016/S0375-6742(03)00035-9.

Yang, Y.L., and Aplin, A.C., 2007. Permeability and petrophysical properties of 30 natural mudstones. *Journal of Geophysical Research*, 112(B03206), doi:10.1029/2005JB004243.

Zoback, M.D., Kitasei, S., and Copithorne, B., 2010. Addressing the environmental risks from shale gas development, Worldwatch Institute, 19 p.

Chapter 2: Overpressure and Consolidation Near the Seafloor of Brazos-Trinity Basin IV, Northwest Deepwater Gulf of Mexico[1]

ABSTRACT

Pore water overpressures (u^*) within mudstones beneath Brazos-Trinity Basin IV (deepwater Gulf of Mexico, offshore Texas) are greater than 70% of the hydrostatic vertical effective stress (σ'_{vh}) [$\lambda^* = 0.7 = (u^*/\sigma'_{vh})$]. These results are compatible with recent observations that suggest sedimentation rates in this region are rapid (6 mm/yr). I compare the petrophysical properties and pore pressures within a 120 meter-thick package of mudstone penetrated at two locations: Integrated Ocean Drilling Program (IODP) Sites U1319 and U1320. Site U1319 is at the margin of Brazos-Trinity Basin IV whereas Site U1320 lies at its center, beneath 180 meters of turbidite fill. Experimentally derived preconsolidation stresses and an *in-situ* pore pressure measurement record overpressure at Site U1319 and Site U1320 ($\lambda^* \sim 0.2$ to 0.8 and $\lambda^* \sim 0.8$, respectively). I use these data to define an average vertical effective stress gradient. Assuming that void ratio (e) is proportional to the log of vertical effective stress (σ'_v), I predict pore pressures throughout the mudstone at both sites using bulk density data. Overpressures are greater at Site U1320 due to rapid deposition of the overlying turbidites. However, a large fraction of the overpressure induced by the turbidite load applied at Site U1320 has dissipated by drainage into the overlying basin fill. High overpressures near the seafloor drive shallow fluid flow, reduce slope stability, and may explain large submarine landslides.

[1]The full content of this chapter is published in *Journal of Geophysical Research* in 2009.

2.1 INTRODUCTION

Overpressure (pore pressure in excess of hydrostatic pressure) is generated by rapid deposition of low permeability sediments. When compressible, low permeability sediments are rapidly loaded, their pore fluids cannot drain fast enough to remain at hydrostatic pressure. As a result, pore fluids support part of the overburden and overpressure develops (Gibson, 1958; Harrison and Summa, 1991). Overpressure drives fluid flow, which impacts solute mass transport and heat transfer. This impacts a range of important geological processes: the rate of upward fluid flow has a strong control on the distribution of methane hydrates near the seafloor (Xu and Ruppel, 1999) and the depth of the sulfate methane interface (Garg et al., 2008). These processes, in turn, have significant impact on microbiology.

Overpressure can also cause slope instability (Prior and Coleman, 1982; Dugan and Flemings, 2000; Flemings et al., 2008). Repeated submarine landslides on the Mississippi Fan have been driven by overpressure (Prior and Coleman, 1982). Shallow, lateral fluid flow occurs on the New Jersey continental slope (Dugan and Flemings, 2000) and on the Gulf of Mexico continental slope in the Ursa Basin (Flemings et al., 2008), where numerous slope failures have been documented (Sawyer et al., 2007).

Special caution is required when drilling through overpressured sediments. Estimates of maximum pore pressures are necessary prior to drilling to adequately adjust drilling fluid densities, design appropriate casing programs, and employ the right drilling and safety equipment for blow-out prevention (Fertl and Chilingarian, 1987).

It would be ideal to measure pore pressure directly. However direct pore pressure measurements are rare because measurements taken by probes inserted into the formation are challenging and when successful require long equilibration times (Long et al., 2007; Long et al., 2008). Therefore, other methods have been established to estimate pore

pressure. Laboratory consolidation tests are used to estimate preconsolidation stresses (Casagrande, 1936; Becker et al., 1987), the maximum past *in-situ* vertical effective stress a core has experienced. When coupled with knowledge of the vertical stress, which is the stress due to the mass of the overlying bulk sediment, pore pressures can be predicted (Saffer et al., 2000; Dugan et al., 2003; Saffer, 2003; Dugan and Germaine, 2008). In the absence of direct information, pore pressures are often predicted based on an assumed or empirically-derived relationship between porosity and vertical effective stress (Hart et al., 1995; Gordon and Flemings, 1998; Flemings et al., 2002; Flemings and Lupa, 2004) or void ratio and vertical effective stress (Terzaghi and Peck, 1948; Dugan et al., 2003; Saffer, 2003).

I use logging data and preconsolidation stresses to interpret overpressure within mudstones at two sites in the Brazos-Trinity Basin IV, on the continental slope of the Northern Gulf of Mexico, offshore Texas, USA. The results from IODP Expedition 308 allow us to study how rapid sedimentation of low permeability mudstones and the overlying turbidite fill controls mudstone overpressure in this young sedimentary basin. Brazos-Trinity Basin IV was initially targeted for drilling because low sedimentation rates and very little overpressure were expected (Ostermeier et al., 2001). However, more recent studies (e.g. Flemings et al. (2006); (2008); O'Hayer (2009)) show the basin's mudstone deposition rate was considerably higher than envisioned.

2.2 GEOLOGIC SETTING: BRAZOS-TRINITY BASIN IV

Brazos-Trinity Basin IV is located ~250 km south-southeast of Houston (Texas) on the northwestern continental slope of the Gulf of Mexico (Figure 2.1). It has an oval shape with a northeast – southwest oriented primary axis and is 16 km long and 10 km

wide (Figure 2.2) (Mallarino et al., 2006). Water depths range from 1000 m at the margin to 1480 m in the center. Brazos-Trinity Basin IV belongs to a system consisting of three minibasins (Basins I, II, IV) and a graben (Basin III) (Satterfield and Behrens, 1990; Winker, 1996; Badalini et al., 2000; Mallarino et al., 2006). These basins form the Brazos- Trinity fan, a late Pleistocene depositional system (Winker, 1996; Badalini et al., 2000). Brazos-Trinity Basin IV is connected to Basin II by two feeder channels in the northwest and northeast (Figure 2.2). A series of sandy turbidite packages interbedded with bioturbated muds filled Brazos-Trinity Basin IV through these two feeders. Both sand content and thickness of turbidite packages increase upward. Basin IV is the deepest basin in the system and does not have an outlet: therefore, is the final sedimentary sink for gravity flows (Mallarino et al., 2006). The three up-dip basins are filled, but Brazos-Trinity Basin IV is under-filled (a relief of at least 370 meters exists between the seafloor and Basin IV rim) (Badalini et al., 2000).

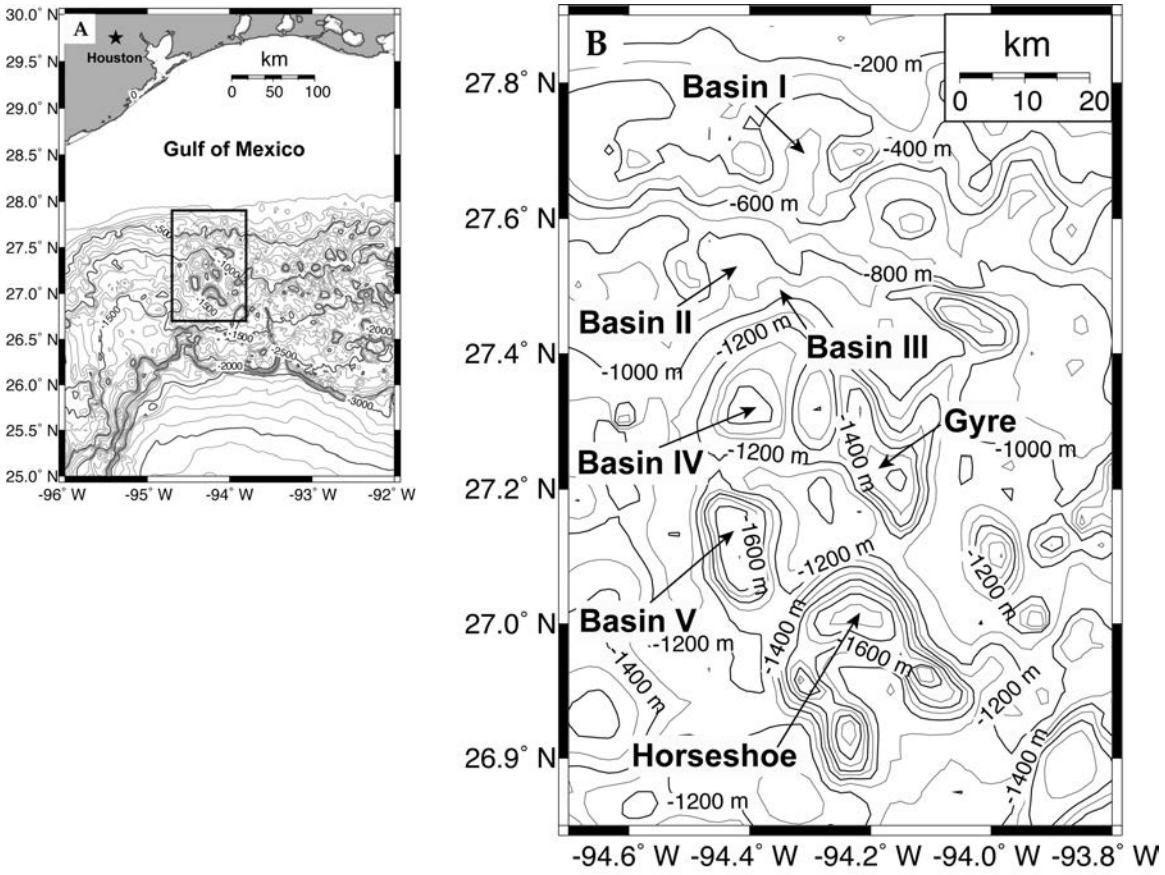

Figure 2.1: Geologic setting of Brazos-Trinity Basin IV. (a) Bathymetry map showing study area on the northwestern continental slope of the Gulf of Mexico. Contour lines are shown every 100m below sea level, annotated every 500m. (b) Bathymetry map of Brazos-Trinity Basin System, which is located about 250km south-southeast of Houston, Texas. Contour lines are shown every 100m below sea level, annotated every 200m. Data plotted is Gebco 1 minute grid.

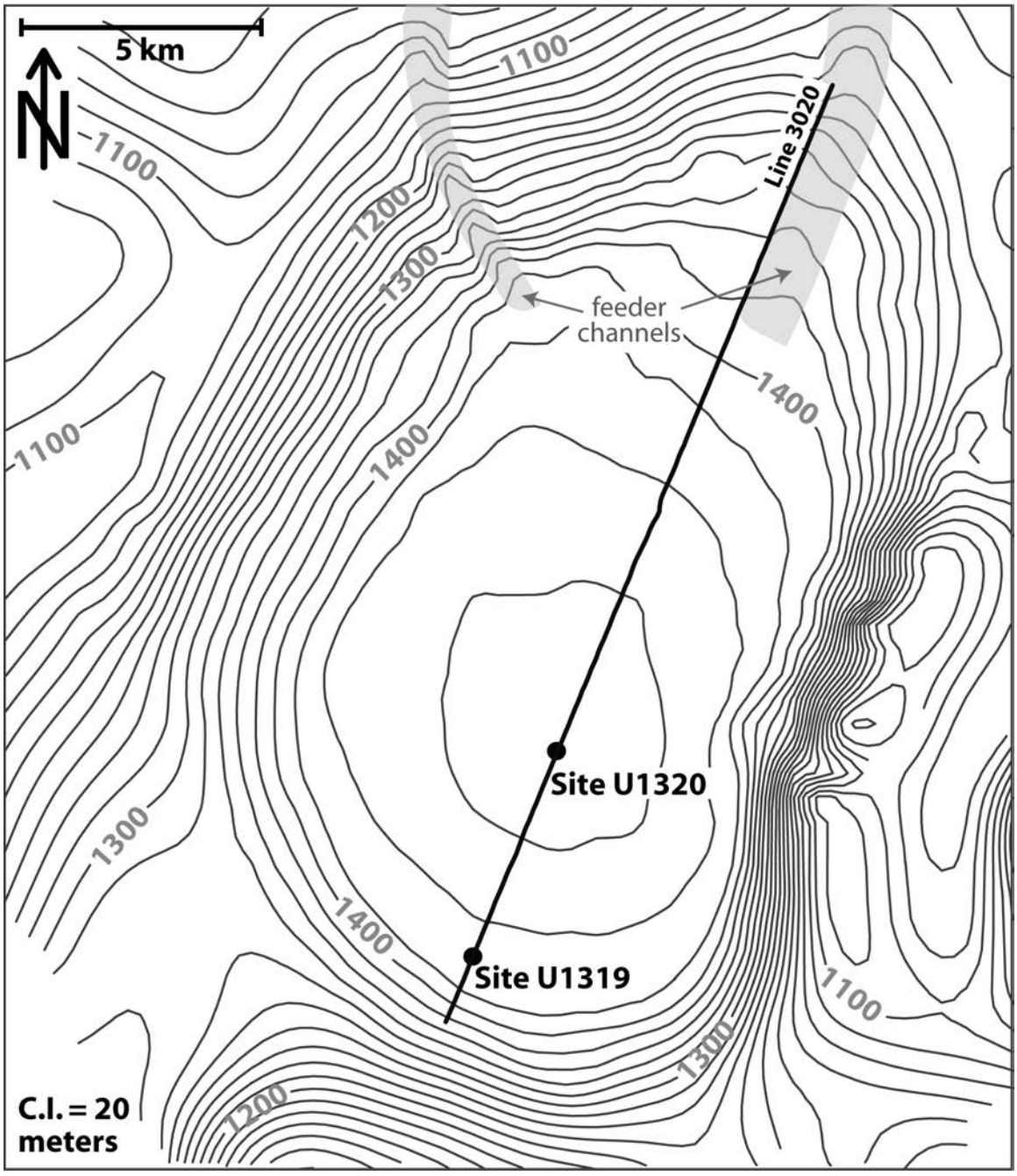

Figure 2.2: Contour map of the seafloor of Brazos-Trinity Basin IV. Depth in meters below sea level. Contour lines are shown every 20m, annotated every 100m. The two IODP Expedition 308 Sites U1319 and U1320 are indicated. Seismic dip line 3020 (bold solid line) is shown in Figure 2.3. C.I., contour interval. Data plotted is Gebco 1 minute grid.

2.3 MUDSTONE GEOLOGY

A mudstone layer that is at least 120 meters thick (the depth of our penetration) underlies the sedimentary fill of Brazos-Trinity Basin IV (Figure 2.3). Seismic data (Figure 2.3) suggest these mudstones extend considerably deeper. Mudstones are composed of greenish gray to reddish brown silty clays punctuated by dark gray to black organic-rich, locally pyritic layers (Flemings et al., 2006). Bioclastic sediments such as shell fragments and foraminifers are enriched locally within burrow fills and laminae (Flemings et al., 2006). These mudstones are on average composed of 62% clay-sized particles, 38% silt-sized particles and less than 1% sand-sized particles by mass.

In seismic data, mudstones are recorded by highly reflective, parallel and continuous reflectors (Figure 2.3). Seismic reflector R40 marks the boundary between the turbidite fill and the top of the mudstones (Flemings et al., 2006). Beneath R40, there is another distinct seismic reflector present within the mudstones (R50), which occurs at approximately 55 m below R40 (Figure 2.3).

The mudstones that underlie and surround the Brazos-Trinity basins are composed of hemipelagic sediments (Beaubouef and Friedmann, 2000). They were deposited from muddy river plumes or from distal turbidity currents spilling from adjacent intraslope basins prior to salt withdrawal, basin subsidence, and turbidite deposition (Beaubouef and Friedmann, 2000; Flemings et al., 2006). To illustrate the approximate geometry during deposition of the mudstones that underlie the turbidite fill, I flatten the seismic data on surface R50 (Figure 2.4a). I then use a vertical seismic profile, derived at Site U1320 (Flemings et al., 2006), to correlate the well logs in depth with seismic data in time. I visually correlate Site U1320 with U1319 based on a comparison of logging-while-drilling (LWD) gamma ray (GR), resistivity (RES) and porosity (n) logs from both sites

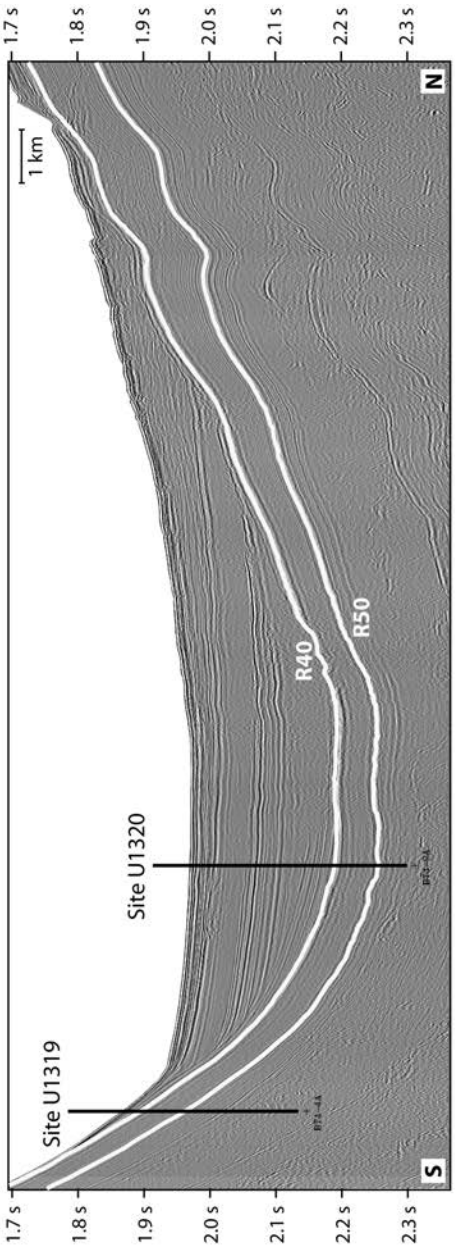

Figure 2.3: Seismic cross-section along dip line 3020 from south-southwest to north-northeast. Vertical axis is two-way traveltime (TWT) in seconds. IODP Expedition 308 Site U1319 is located at the basin margin, Site U1320 is located in the basin center. Seismic reflectors R40 and R50 are shown as white solid lines. Mudstones (beneath R40) are overlain by the turbidite basin fill. The basin fill is approximately 28m thick at Site U1319 and 180m at Site U1320. R50 is approximately 55m below R40 at both sites.

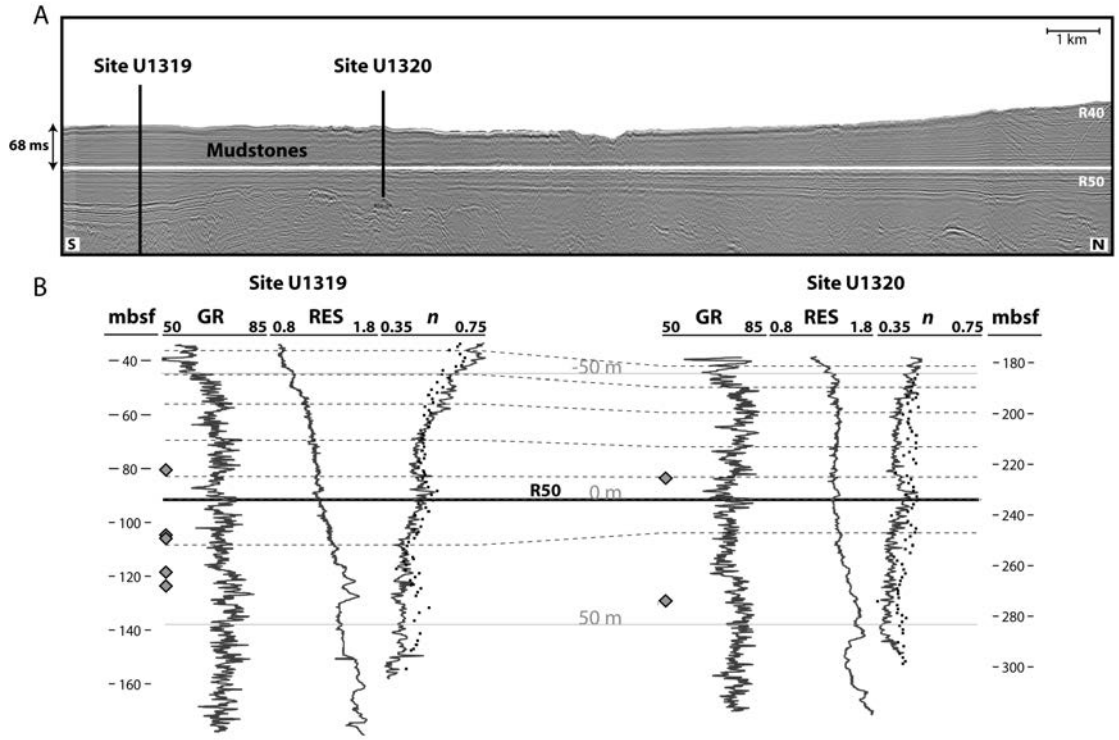

Figure 4

Figure 2.4: Seismic well log tie. (a) Seismic cross-section along dip line 3020 flattened to seismic reflector R50 (solid white line). Basin fill (above R40) is removed. Locations of IODP Expedition 308 Sites U1319 and U1320 are shown as vertical black lines. Two-way traveltime (TWT) difference between R40 and R50 at the southern end of the cross-section is about 68ms. (b) Logging-while-drilling data from (left) Site U1319 and (right) U1320 referenced to seismic reflector R50 (zero meters); mbsf, depth in meters below seafloor; GR, gamma ray (in American Petroleum Institute gamma ray units, gAPI); RES, resistivity log on logarithmic scale (in ohm m); and *n*, porosity from logging-while-drilling (solid line) and from shipboard moisture and density (MAD) measurements (squares). Logging-while-drilling (LWD) porosity is calculated from the bulk density log assuming a grain density of 2690 kg/m^3 and fluid density of 1024 kg/m^3. Dashed lines correlate individual events between both sites. Locations of uniaxial consolidation test samples are shown as diamonds. Their names, depths, and results are listed in Table 2.1.

(Figure 2.4b). Porosity (*n)* is calculated from the bulk density (ρ_b) log, assuming a grain density (ρ_g) of 2690 kg/m^3 and a fluid density (ρ_f) of 1024 kg/m^3:

$$n = \frac{\rho_g - \rho_b}{\rho_g - \rho_f}. \tag{2.1}$$

I am able to correlate individual events in the resistivity and porosity logs at the scale of a few meters between Sites U1319 and U1320 (Figure 2.4, 2.5). Beneath 128 meters below seafloor (mbsf) (42 meters beneath R50) at Site U1319 and 259.5 mbsf (25.5 meters beneath R50) at Site U1320, I am unable to confidently correlate the log and core data (Figure 2.4 and 2.5). In this zone, the seismic data are also difficult to correlate between sites.

Over the entire mudstone section, porosity is lower and resistivity is higher at Site U1320 than at Site U1319 (Figure 2.5). Greater consolidation at Site U1320 is due to the 180 meters of sediment that overlie the mudstone; only 28 meters of sediment overlie the mudstones at Site U1319. The difference in porosity and resistivity at equivalent stratigraphic horizons decreases with depth (Figure 2.5).

Within the mudstone, porosities measured with shipboard moisture and density measurements (MAD) are generally greater than porosities measured with logging data (LWD). For example, beneath 70 mbsf at Site U1319, and beneath 195 mbsf at Site U1320, MAD porosity is generally about 6% higher than LWD porosity (Figure 2.4b). I interpret that the MAD porosity is greater because the core expanded when it was brought to the surface. This is commonly observed in the Integrated Ocean Drilling Program (e.g. Shipboard Scientific Party, 2002). Below 115 mbsf at Site U1319, and between 270-290 mbsf at Site U1320, MAD porosity is as much as 12% greater than LWD porosity (Figure

2.4b). In this zone, high concentrations of methane were measured in cores and gas exsolution was observed (Flemings et al., 2006).

The MAD porosity is less than the LWD porosity in the uppermost 35 meters of the mudstone (-60 to -25 m referenced relative to horizon R50, Figure 2.4) at Site U1319. I interpret from the caliper log that borehole washout caused low apparent bulk densities in the LWD in this zone. Borehole washout decreases from the seafloor to 67 mbsf (-19 m referenced relative to horizon R50) at Site U1319. I corrected the LWD porosity for borehole washout in the following manner. I first corrected the MAD data for 6% core expansion by assuming that the *in-situ* porosity was 94% of the MAD porosity. To match these *in-situ* porosity values with the LWD data, I applied a linear correction with depth from 15% borehole washout at the seafloor to 0% borehole washout at 67 mbsf (35 meters below the top of the mudstones). The result is the dashed curve (Figure 2.5).

The mudstones beneath R40 were deposited during early interglacial Marine Isotope Stage (MIS) 5 and late glacial MIS 6 (Beaubouef and Friedmann, 2000; O'Hayer, 2008). I infer that the age of the top of the mudstone lies between 128 ka and 129 ka based on the presence of the *G. menardii* X/W1 zone boundary at 31.6 mbsf at Site U1319 (O'Hayer, 2009). This zone boundary, approximately at the MIS 5 / MIS 6 transition, is dated at 129 ka (Kennett and Huddleston, 1972). I assume a constant deposition rate of mudstone between 6 mm/yr and 9 mm/yr (O'Hayer, 2009) for the depth interval between 31.6 mbsf and the top of the mudstones at 28 mbsf. O'Hayer (2009) interpreted mudstone deposition rates between 6 mm/yr and 9 mm/yr based on the assumption that sediments penetrated by all three drilled wells are younger than approximately 150 ka. Because *G. menardii*, a foraminifera species that lives in warm tropical waters (Kennett and Huddleston, 1972), is entirely absent in sediment cores

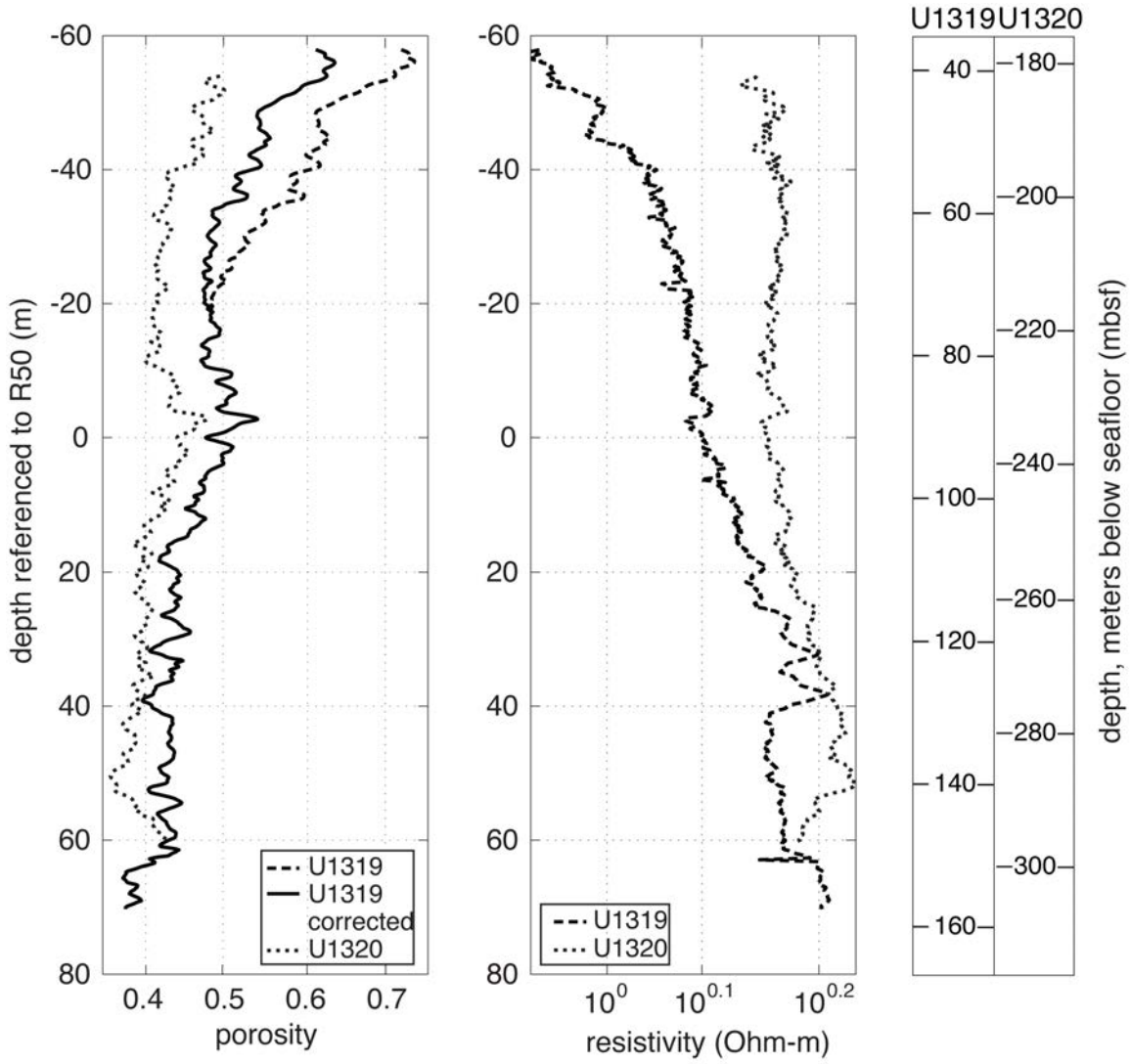

Figure 2.5: Mudstone logging-while-drilling porosity and resistivity logs at Sites U1319 (dashed lines) and U1320 (dotted lines). Porosity log at Site U1319 is corrected for borehole washout (solid line) between top of mudstone and 67 mbsf (19 m above R50). Vertical axis is depth in meters referenced to seismic reflector R50 within mudstones (see Figures 2.3 and 2.4). R50 lies at 86 mbsf at Site U1319 and 234 mbsf at Site U1320. Individual depths in meters below seafloor are shown on the right. Porosity logs are calculated from LWD bulk density log assuming a grain density of 2690 kg/m^3 and fluid density of 1024 kg/m^3. All porosity and resistivity logs are shown with a nine-point moving average.

below the X/W1 boundary (O'Hayer, 2009), the whole section below 31.6 mbsf is interpreted to belong to Zone W1 (O'Hayer, 2009). Because Zone W1 only represents the latest 21 ka of the glacial MIS 6 (Kennett and Huddleston, 1972), O'Hayer (2009) inferred an age of the deepest penetrated mudstone of younger than approximately 150 ka. These mudstones were deposited significantly more rapidly than the overlying basin fill (0.2 mm/yr to 2 mm/yr) (Flemings et al., 2006).

2.4 PRESSURE CHARACTERIZATION

2.4.1 Preconsolidation Stress

Sediments previously consolidated by burial that are then re-consolidated in laboratory experiments initially deform elastically, and subsequently deform elasto-plastically (Lambe and Whitman, 1979). The transition from elastic to elasto-plastic behavior defines the maximum past vertical effective stress that the soil has been subjected to. This is defined as the preconsolidation stress (σ'_{pc}) (Casagrande, 1936; Becker et al., 1987). If σ'_{pc} records the *in-situ* vertical effective stress (i.e. there has been no unloading of the sediments subsequent to their reaching σ'_{pc}), then *in-situ* pore pressure (u) can be determined:

$$u = \sigma_v - \sigma'_{pc}, \tag{2.2}$$

where the vertical stress (σ_v) is calculated from the integrated logging-while-drilling (LWD) bulk density (ρ_b) data that have been corrected for borehole washout.

Several methods have been established to determine preconsolidation stresses from uniaxial consolidation tests (Casagrande, 1936; Burmister, 1942, 1951; Schmertmann, 1955; Janbu et al., 1981; Becker et al., 1987). I use the work-stress method

of Becker et al. (1987) (Figure 2.6). This method uses a relationship between work per unit volume, which corresponds to the area beneath the stress-strain curve, and vertical effective stress. Based on Becker et al. (1987), I extrapolate the linear portions of the pre-yield (elastic deformation) and post-yield (elasto-plastic consolidation) behavior. The intersection of the extrapolated lines defines the preconsolidation stress (σ'_{pc}).

It is difficult to estimate the true preconsolidation stress when there is significant sample disturbance. It is commonly assumed that sample disturbance results in a lower apparent value of the preconsolidation stress (Jamiolkowski, 1985). To account for sample disturbance, I bound our best estimation for σ'_{pc} with minimum and maximum values ($\sigma'_{pc\ min}$, $\sigma'_{pc\ max}$) based on the approach of Dugan and Germaine (2008). This approach is similar but more conservative than previous approaches (Saffer et al., 2000; Santagata and Germaine, 2002).

I estimate overpressure (u^*) from hydrostatic vertical effective stress (σ'_{vh}), the difference between vertical stress and hydrostatic pressure, and define minimum and maximum bounds (u^*_{min} and u^*_{max}, respectively):

$$u^*_{min} = \sigma'_{vh} - \sigma'_{pc\,max}, \quad u^* = \sigma'_{vh} - \sigma'_{pc}, \quad u^*_{max} = \sigma'_{vh} - \sigma'_{pc\,min}. \tag{2.3}$$

I interpret preconsolidation stresses for seven sediment samples (with their minimum and maximum bounds) from uniaxial, constant rate of strain consolidation (CRSC) experiments (Table 2.1). Estimated overpressures derived from σ'_{pc} are shown as gray dots in Figure 2.7. These uniaxial consolidation experiments were run on five specimens from Site U1319 and two specimens from Site U1320 in two different laboratories (Rice University and Massachusetts Institute of Technology).

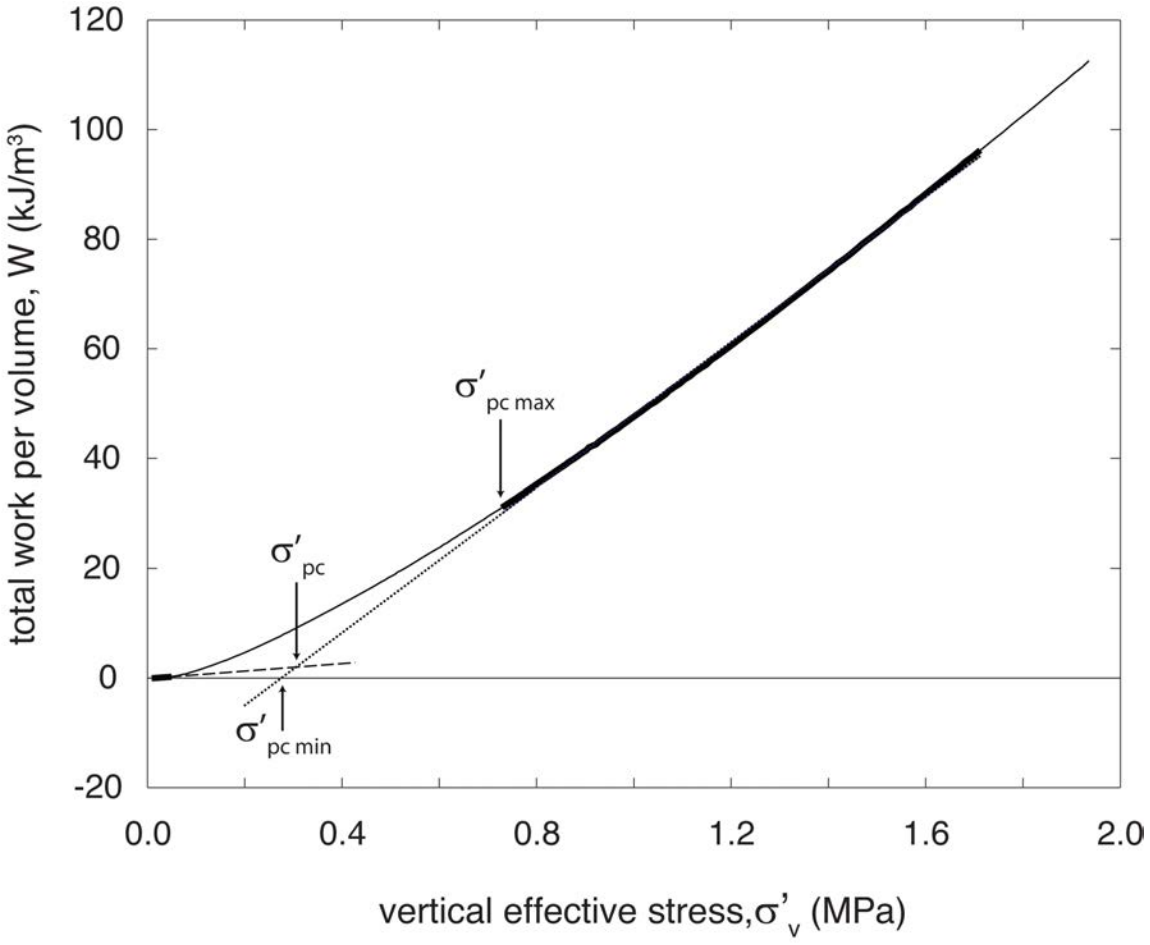

Figure 2.6: Determination of preconsolidation stress (σ'_{pc}) from a constant-rate-of-strain consolidation (CRSC) experiment based on the work stress method of Becker et al. (1987). The intersection of the extrapolated lines of the linear portions on the preyield part (dashed line) and postyield part of the curve (dotted line) defines the preconsolidation stress (σ'_{pc}); $\sigma'_{pc\ min}$ is defined as the intersection of the extrapolated line through the postyield data (dotted line) with the zero work line (horizontal line through W = 0 kJ/m3) (Santagata and Germaine, 2002; Dugan and Germaine, 2008); $\sigma'_{pc\ max}$ is defined by the beginning of the postyield data (Dugan and Germaine, 2008).

Test #	*Sample*	*Depth (mbsf)*	σ'_{vh} *(MPa)*	σ'_{pc} *(MPa)*	e_i
CRS834_mit	U1319A-9H-7WR	79.96	0.568	0.456	1.130
CRS836_mit	U1319A-12H-CCWR	106.27	0.798	0.199	0.934
CRS837_mit	U1319A-14X-4WR	118.61	0.912	0.301	0.963
CRS858_mit	U1319A-14X-4WR	123.62	0.958	0.305	0.973
CRS859_mit	U1319A-12H-CCWR	104.27	0.780	0.142	1.047
CRS023_rice	U1320A-26X-3WR	225.41	1.494	0.315	0.938
CRS024_rice	U1320A-31X-3WR	273.70	1.958	0.530	0.784

Table 2.1: Sample Summary and Consolidation Parameters[a].

[a] Numbering of sites, holes, cores, and sections follows the standard IODP procedure; depth in meters below seafloor (mbsf); σ'_{vh} is calculated using LWD bulk density data (corrected for borehole washout at Site U1319) and a fluid density of 1024 kg/m3; σ'_{pc} is determined based on work stress method after Becker et al. (1987); e_i is the initial void ratio measured on the tested specimen.

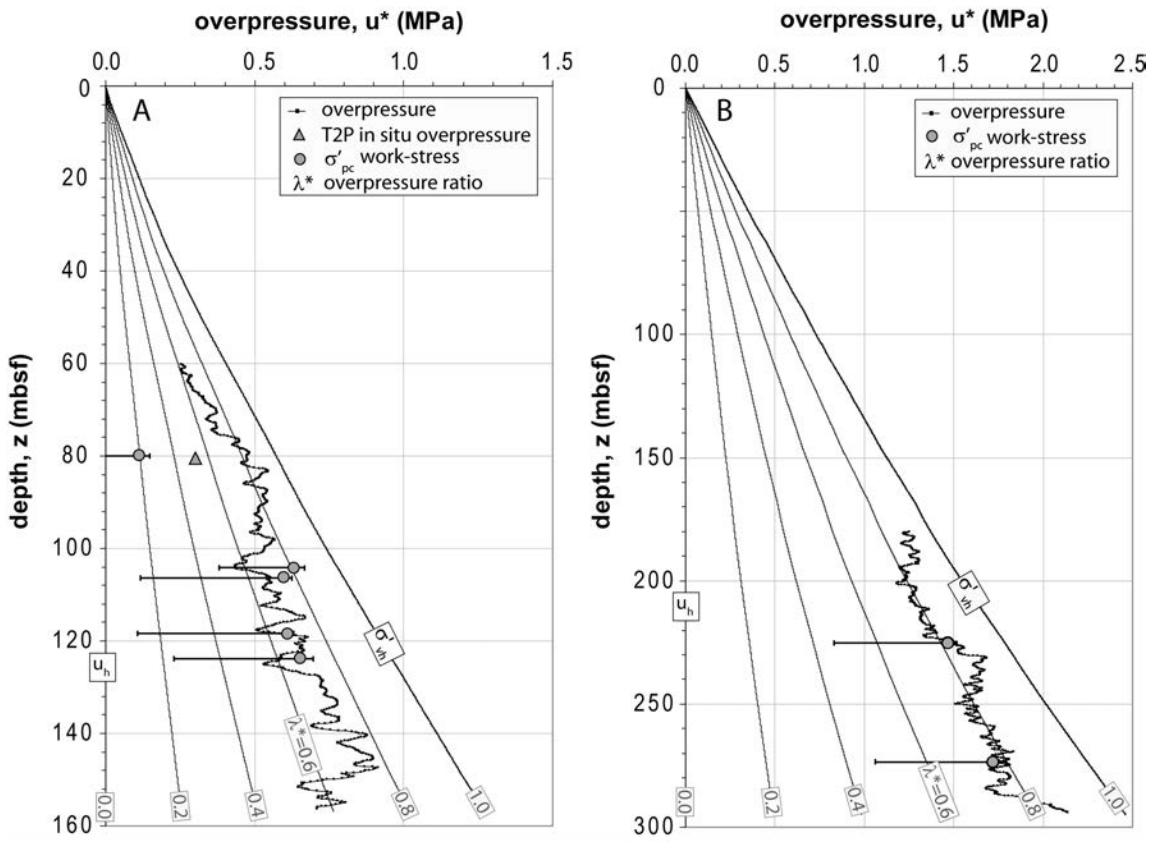

Figure 2.7: Overpressure prediction for (a) Site U1319 and (b) Site U1320. Depth is referenced to meters below seafloor (mbsf). Estimated *in-situ* overpressure from penetrometer measurement at Site U1319 is shown as triangle. Overpressure estimates from σ'_{pc} using the work stress method by Becker et al. (1987) are shown as gray dots with minimum and maximum bounds indicated by error bars. Black dotted line refers to void-ratio based overpressure prediction assuming an overpressure ratio of $\lambda^* = 0.7$ at Site U1319. Overpressures are averaged over a moving window of nine measurements (equal to 1.35 m) to minimize impact of unusual lithologies, localized cementation, or measurement errors. Thin lines labeled from 0.0 to 1.0 refer to overpressure ratios from $\lambda^* = 0.0$ to $\lambda^* = 1.0$ in 0.2 increments; u_h is hydrostatic pressure; σ'_{vh} is hydrostatic vertical effective stress.

At Site U1319, overpressures derived from preconsolidation stresses lie between 70% and 80% of the hydrostatic vertical effective stress, except the shallowest estimated overpressure which is about 20% of the hydrostatic vertical effective stress (Figure 2.7). At Site U1320, in the basin center, overpressures derived from preconsolidation stresses are predicted to be around 80% of the hydrostatic vertical effective stress (Figure 2.7).

2.4.2 Direct Pore Pressure Measurement

A single direct pore pressure measurement in the mudstones was taken at 80.5 mbsf at Site U1319 during IODP Expedition 308 (Long et al., 2008) (Figure 2.7) using a down-hole penetrometer. Long et al. (2008) used an extrapolation technique based on the inverse of the square root of time ($1/\sqrt{t}$) to determine the *in-situ* pore pressure, because the penetrometer measurement did not reach the *in-situ* pressure at the end of deployment. The overpressure at this depth reaches approximately 64% of the hydrostatic vertical effective stress. A detailed description of the pressure probe (T2P), deployment, and calibration is given by Flemings et al. (2008) and Long et al. (2007; 2008).

2.4.3 Pressure Prediction From Void Ratio

To estimate pore pressure from consolidation state, a unique relation between vertical effective stress (σ'_v) and porosity (*n)* or void ratio (*e*) must be defined. Then pore pressures (*u*) can be calculated from vertical effective stresses as described below. In some cases, the relationship between porosity and vertical effective stress is defined using an exponential relationship (Athy, 1930; Rubey and Hubbert, 1959; Hart et al., 1995; Gordon and Flemings, 1998); in others, void ratio is related to the log of vertical

effective stress (Terzaghi and Peck, 1948; Lambe and Whitman, 1979). Here, I assume that void ratio (e) is proportional to the log of vertical effective stress (σ'_v, in MPa):

$$e = e_0 - C_c \log\left(\sigma'_v\right), \tag{2.4}$$

where $$e = \frac{n}{1-n}, \tag{2.5}$$

and e_0 is the void ratio at a vertical effective stress of unity (σ'_v = 1 MPa) and C_c is the compression index describing deformation along the yield surface (i.e. primary consolidation). The constants e_0 and C_c are obtained as described below. Vertical effective stress (σ'_v) is the vertical stress (σ_v) less the pore pressure (u):

$$\sigma'_v = \sigma_v - u. \tag{2.6}$$

Vertical stress (σ_v), porosity (n), and void ratio (e) are calculated from logging-while-drilling (LWD) bulk density (ρ_b) measurements, corrected for borehole washout in the shallow section of Site U1319.

Equations (2.4) and (2.6) are combined to calculate pore pressure (u):

$$u = \sigma_v - \sigma'_v = \sigma_v - \left(10^{-\left(\frac{e-e_0}{C_c}\right)}\right). \tag{2.7}$$

I plot overpressure (u^*) versus depth beneath seafloor (mbsf) (Figure 2.7). Pore pressure (u) equals the hydrostatic pressure (u_h) when overpressure (u^*) is zero; pore pressure equals the vertical stress (σ_v) when the overpressure (u^*) equals the hydrostatic vertical effective stress (σ'_{vh}). I also use the overpressure ratio, which is the ratio of overpressure (u^*) to hydrostatic vertical effective stress (σ'_{vh}),

$$\lambda^* = (u - u_h) / (\sigma'_{vh}) \tag{2.8}$$

to characterize the relationship between pore pressure and vertical stress.

It is common to assume vertical effective stresses are known in one location (either at a reference borehole, or in the shallow section at the location of interest) (Dugan and Flemings, 2000; Saffer, 2003) and to use these data to constrain the compaction parameters (C_c and e_0). These parameters are then applied via equation (2.7) to predict pore pressures in a location where vertical effective stresses are unknown. For example, (Hart et al., 1995) assumed the known section is hydrostatically pressured. Others have used direct observations of pressure to constrain the vertical effective stress at a known location (Flemings and Lupa, 2004). Our approach is to use laboratory experiments and a direct pore pressure measurement from Site U1319 to infer the vertical effective stress and pore pressure at Site U1319. I then derive e_0 and C_c using void ratio data from Site U1319 and apply this to predict pore pressures at Site U1320.

Because I express the *in-situ* vertical effective stress state at the reference site in terms of overpressure ratio (λ^*), I modify equation (2.4) by combining equations (2.7) and (2.8):

$$e = e_0 - C_c \log(1 - \lambda^*) - C_c \log(\sigma'_{vh}). \tag{2.9}$$

Equation (2.9) illustrates how the parameters e_0 and C_c depend on the overpressure ratio at the reference site. This is important because often there is no *a priori* knowledge of the *in-situ* vertical effective stress for the reference location. For different values of λ^*, the compression index (C_c) does not change while the intercept (e_0) does.

Preconsolidation stresses and the direct pore pressure measurement suggest overpressures may reach as much as 70% of the hydrostatic vertical effective stress at the reference Site U1319 (Figure 2.7). Therefore, I assume an overpressure ratio of $\lambda^* = 0.7$ in equation 2.9. I then use void ratio data from the mudstones at Site U1319 to perform a least squares regression of e vs. log (σ'_v) (Figure 2.8) to define e_0 and $C_{c.}$ I find C_c equal to 0.54 and e_0 equal to 0.47 (Figure 2.8). I use these values to estimate pore pressures at both sites using equation (2.7).

At Site U1319, estimated overpressures vary around 70% of σ'_{vh} ($\lambda^* = 0.7$): this must be the case as $\lambda^* = 0.7$ was our starting assumption (Figure 2.7a). The variation in predicted pressure could be due to variation of the material properties of the mudstone itself. For example, stiffer material will result in a higher predicted pore pressure.

I next calculate the pore pressure at the more deeply buried Site U1320. I apply the void ratio – log of vertical effective stress relationship derived from Site U1319 (C_c = 0.54, e_0 = 0.47) to void ratios from Site U1320. Mudstone overpressures at Site U1320 reach 80% of σ'_{vh} ($\lambda^* = \sim 0.8$) (Figure 2.7b). Once again, there are significant variations in the magnitude of estimated overpressure that could be due to variations in material properties. Overpressures estimated from void ratio are in good agreement with those estimated from preconsolidation stresses at Site U1320 (Figure 2.7b).

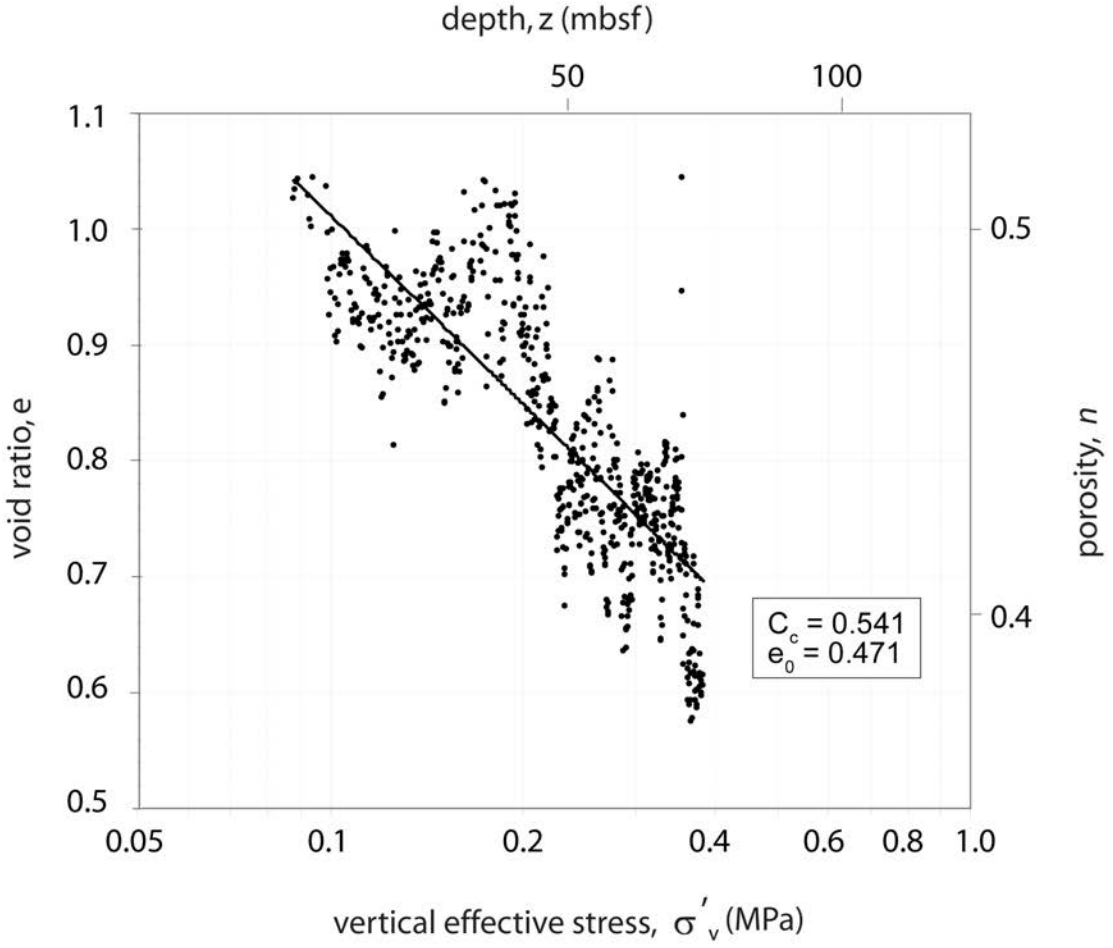

Figure 2.8: Linear relationship between void ratio and log of vertical effective stress assuming an overpressure ratio of $\lambda^* = 0.7$ at Site U1319. A least squares linear regression (equation (2.9)) provides the fitting parameters compression index ($C_c = 0.54$) and void ratio at a vertical effective stress of unity ($\sigma'_v = 1$ MPa) ($e_0 = 0.47$).

2.5 DISCUSSION

I interpret severe overpressure ($\lambda^* = 0.7$) at Site U1319 and even greater overpressure ($\lambda^* = 0.8$) at Site U1320 in the Brazos-Trinity Basin IV (Figure 2.7). Our analysis is based on the integration of uniaxial consolidation experiments, one direct pressure measurement, observations of porosity, and vertical stresses interpreted from bulk density logs. These high overpressures surprised us because pre-drilling estimates suggested very low sedimentation rates and low overpressures in this region (Ostermeier et al., 2001). As described above, subsequent studies (e.g. Flemings et al., 2006; Flemings et al., 2008; O'Hayer, 2009) have shown the sedimentation rate to lie between 6 mm/yr and 9 mm/yr. I suggest the overpressure was driven by this rapid sedimentation. The high pore pressures in the Brazos-Trinity Basin IV region fit into a range of results that have recently documented overpressures in the shallow sub-seafloor (Ostermeier et al., 2000; Orange et al., 2003; Flemings and Lupa, 2004; Dugan and Germaine, 2008; Flemings et al., 2008).

At Site U1319, there was almost no loading by the overlying turbidite fill (Figure 2.3); thus, the overpressure that is present must have been generated by the deposition and consolidation of the mudstone itself. Gibson's (1958) analytical, one-dimensional consolidation model of a clay layer which increases in thickness with time can be used to estimate the amount of overpressure for these sediments (e.g. Flemings et al., 2008). The degree of overpressure is controlled by Gibson's dissipation time factor, $T = m^2 t / C_v$, where m is the sedimentation rate, t is the time duration, and C_v is the hydraulic diffusivity. As described, the sedimentation rate (m) of mudstones in this region lies between 6 mm/yr and 9 mm/yr (O'Hayer, 2009). I use a constant hydraulic diffusivity (C_v) for the mudstones of 4.8 x 10^{-8} m^2/s, which is determined from our uniaxial constant rate of strain consolidation experiments. The duration of sedimentation (t) is unknown

because mudstones extend deeper than the base of the drilled wells. However, if I assume the base of the drilled well at Site U1319 is the base of the mudstone, then it takes either 21 ky or 14 ky to deposit 127 m of mudstone at 6 mm/yr or 9 mm/yr, respectively. I find dimensionless time factors of $T = 0.5$ and $T = 0.75$ respectively for rates of 6 mm/yr and 9 mm/yr. These time factors result in estimated overpressure ratios at the base of the mudstone of $\lambda^* = 0.19$ and $\lambda^* = 0.23$, which are significantly lower than overpressure ratios predicted from void ratio and preconsolidation stresses.

To get overpressures at the base of the drilled well at Site U1319 that are 70% of the hydrostatic vertical effective stress, mudstones must have been deposited for a longer duration than assumed above. Seismic data support this hypothesis as they show that mudstones extend considerably deeper than drilled during IODP Expedition 308 (Figure 2.3). Mudstone deposited at 6 mm/yr for 105 ky results in a dissipation factor of $T = 2.5$. This time factor results in an overpressure ratio around $\lambda^* = 0.7$ at the depth of interest (127 m below top of mudstones). Similarly, for a mudstone column deposited at 9 mm/yr for 54 ky I find $T = 2.9$. This time factor also results in an overpressure ratio of $\lambda^* = 0.7$. Thus, the pore pressures observed are reasonable if the observed sedimentation rates lasted for 54 to 105 ky.

At Site U1320, 180 meters of turbidite fill loaded the mudstone, increasing the vertical stress by 2.86 MPa. In contrast, only 28 meters of sediment was deposited on top of the mudstone at Site U1319, adding 0.45 MPa of vertical stress. This provides an opportunity to examine the effects of differential sediment loading on the same material. If the mudstones at Site U1319 had been buried to the depth and vertical stress of Site U1320 and there was no drainage of the mudstone, there would be no consolidation, and the vertical effective stresses would not change. However at Site U1320, the porosity is less than at Site U1319 (Figure 2.5, 2.9a). The degree of consolidation in the basin center

is evidence that the mudstones drained more at Site U1320 than at Site U1319; as a result the vertical effective stresses are higher at Site U1320 than at Site U1319 (Figure 2.9b, c).

In general, the difference between the vertical effective stress at Site U1319 and Site U1320 is greatest at the top of the mudstone and decreases with depth (Figure 2.9c). This trend is not perfect. As already described, the upper 35 meters of the mudstone at Site U1319 were influenced by borehole washout. The data correction or assumed value for core expansion may not be perfect, thus the vertical effective stress difference at the top of the mudstone could possibly be larger. In addition, it was not possible to correlate the deepest 25 meters at Site U1320 with Site U1319. Thus, the large increase in vertical effective stress in this zone (Figure 2.9c) may reflect that I am not comparing equivalent rocks.

I suggest the higher vertical effective stress at Site U1320 records dissipation of pressure from the mudstone into the overlying turbidite fill. Accumulation of the permeable turbidite fill induced overpressure in the mudstone; this overpressure was dissipated by pore fluids draining upward toward the much more permeable and lower-pressured turbidite basin fill. I can estimate the volume loss based on the void ratio difference at equivalent stratigraphic horizons between Site U1319 and U1320: The reduction in volume per unit volume (dV/V_i) can be written in terms of void ratio (Craig, 1974; Lambe and Whitman, 1979):

$$\frac{dV}{V_i} = \frac{de}{1+e_i}, \tag{2.10}$$

where de is the change in void ratio and e_i is the initial void ratio at Site U1319. The void ratio difference in the mudstones between Site U1319 and U1320 generally decreases with depth from 0.70 to 0.06 (porosity difference of 0.14 to 0.02, respectively). This

results in a volume loss of 27% at the top and 3.5% at the base of the mudstone. This volume loss range is similar to those found by Screaton et al. (2002) who used porosity data to estimate volume of pore fluid expelled in underthrust sediments that were rapidly loaded by the Nankai accretionary prism. They found 12% volume loss between a reference site, which is located 11 km seaward of the deformation front, and a site drilled within the protothrust zone, ~1.5 km landward of the deformation zone.

Our analysis parallels studies of accretionary wedges (Bekins et al., 1995; Saffer and Bekins, 1998; Saffer et al., 2000; Screaton et al., 2002; Saffer, 2003; Screaton and Saffer, 2005), where hemipelagic sediments seaward of the accretionary prism are subsequently underthrust beneath the accretionary prism. These examples from Barbados, Costa Rica and Nankai show that rapid loading of the accretionary prism induces upward drainage and consolidation that is greatest at the top of the underthrust sediments.

I used preconsolidation stresses derived from uniaxial consolidation experiments and a single *in-situ* pressure measurement to interpret an overpressure ratio of $\lambda^* = 0.7$ for Site U1319 (Figure 2.7). I then used these data to constrain a void ratio versus vertical effective stress relationship at Site U1319 to predict pore pressures at Site U1320 and found $\lambda^* = 0.8$. These predicted pore pressures match pore pressures derived from two preconsolidation stresses available from Site U1320 (Figure 2.7). An alternative approach would have been to assume that Site U1319 had no overpressure ($\lambda^* = 0$). In this scenario, e_0 would change from 0.47 to 0.75 and C_c would be unchanged (equation 2.9). When I use this approach, I still find significant overpressure at Site U1320 with $\lambda^* = 0.5$. A fundamental result is that regardless of what overpressure ratio is assumed at Site U1319, the overpressure ratio is greater at Site U1320.

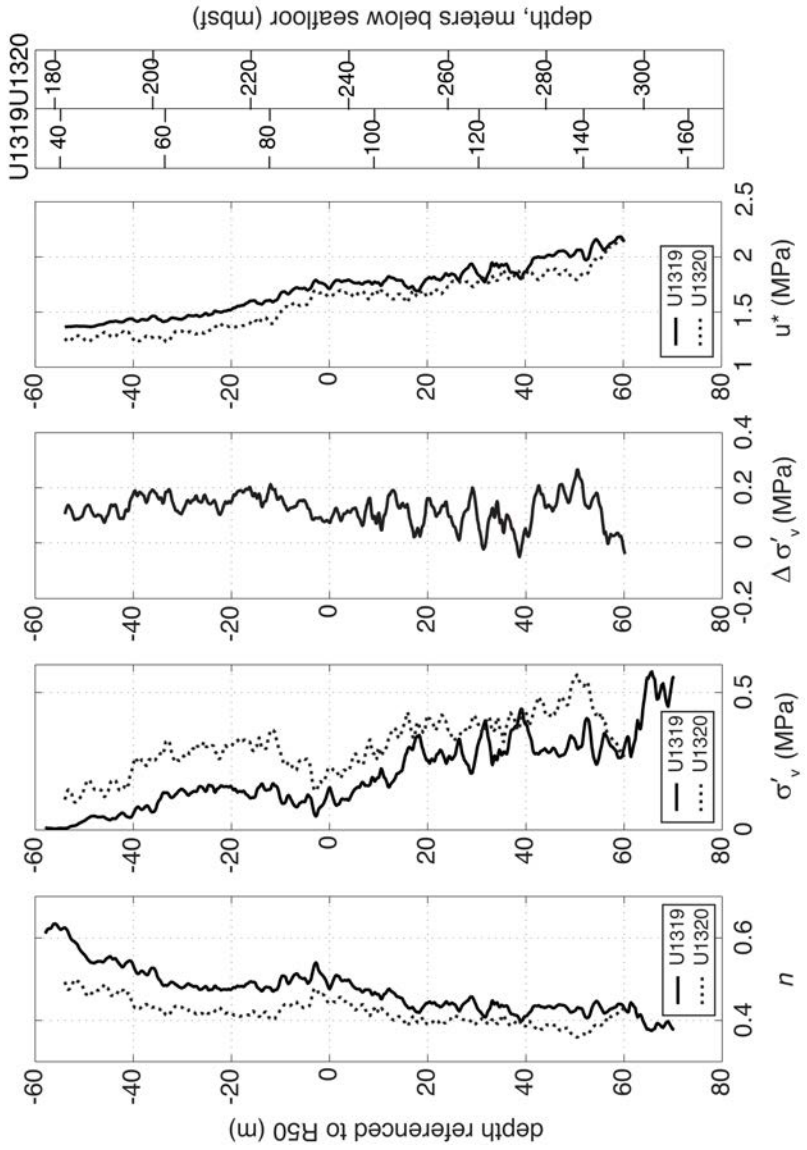

Figure 2.9: For Site U1319 (solid line) and Site U1320 (dotted line), (a) porosity calculated from logging-while-drilling bulk density, (b) estimates in vertical effective stresses assuming $\lambda^* = 0.7$ at Site U1319 (equation (2.9)), (c) difference in vertical effective stresses between both sites, and (d) predicted undrained overpressure at Site U1319 compared to predicted overpressure at Site U1320. Data are shown with a nine-point moving average. Site U1319 is corrected for borehole washout. Porosity is calculated from bulk density log assuming a grain density of 2690 kg/m3 and fluid density of 1024 kg/m^3. Vertical axes for all logs are depth in meters referenced to seismic reflector R50 within mudstones (see Figures 2.3 and 2.4). Individual depths in meters below seafloor are shown on the right.

Our field-derived value of $C_c = 0.54$ exceeds laboratory-derived values that range between 0.13 and 0.36: thus, the field value indicates a more compressible material than the laboratory-derived values. A possible explanation for this behavior is that core disturbance has caused the experimental value to be lower than the actual value (Schmertmann, 1955; Wood, 1990; Santagata and Germaine, 2002). An alternative view is that the field curve, which is developed over geologic time during sedimentation and consolidation, may record more deformation than generated during rapid geotechnical testing leading to higher compression indices than observed in the laboratory. Dugan et al. (2003) observed a similar laboratory vs. *in-situ* compression behavior at ODP Site 1073 on the US mid-Atlantic continental slope.

Our field-derived value of $e_0 = 0.47$ is less than the laboratory-derived values that range between 0.65 and 0.95. This again could result from core disturbance (projection of high values of C_c). An alternate interpretation is that there is no overpressure at Site U1319. Under these conditions, e_0 would increase to 0.75 and result in a value similar to those from laboratory experiments. However, as described above, the predicted overpressures with this approach are less than the overpressures estimated from laboratory-derived preconsolidation stresses and the single *in-situ* pressure measurement. I have not explored here the possibility that either the overpressure ratio (λ^*) or the compression index (C_c) change as a function of depth or vertical effective stress.

I have yet to resolve why the single *in-situ* pore pressure measurement at Site U1319 and the preconsolidation stress from a similar depth at this location (Table 2.1, CRS834_mit) record different overpressures. The overpressure ratio for the laboratory-derived pressure estimate is 2.5 times smaller than the overpressure ratio for the penetrometer measurement. I do not observe any significant difference in consolidation

behavior of the specimen tested in this experiment (CRS834_mit) compared to other specimens from greater depths at the same location.

2.6 CONCLUSIONS

I used a single direct pressure measurement, logging-while-drilling (LWD) bulk density data, and laboratory-derived preconsolidation stresses from IODP Expedition 308 Sites U1319 and U1320 to predict overpressures in mudstones beneath Brazos-Trinity Basin IV. I find overpressures are 70% of the hydrostatic vertical effective stress ($\lambda^* = 0.7$) at Site U1319 and 80% of the hydrostatic vertical effective stress at Site U1320 ($\lambda^* = 0.8$). These high overpressure estimates are compatible with recent estimates of sedimentation rates that lie between 6 mm/yr and 9mm/yr if the duration of mudstone sedimentation is between 105 and 54 ky, respectively. The mudstones at Site U1320 are located beneath 180 m of turbidite fill whereas those at Site U1319 are not significantly loaded: this is an excellent opportunity to study the effects of very different loading over geologic time on identical material. Our results show that although overpressures are greater at Site U1320, a large fraction of the overpressure caused by the overlying basin fill was dissipated by pore fluids draining upward toward the sandy and relatively permeable turbidite fill. High pore pressures in the Brazos-Trinity Basin IV region fit into a range of results that have recently documented overpressures in the shallow sub-seafloor.

NOMENCLATURE

Symbol	*Name*	*Unit*
c_v	hydraulic diffusivity	m^2/s
C_c	compression index	MPa^{-1}
e	void ratio	dimensionless
e_0	void ratio at σ'_v = 1 MPa	dimensionless
e_i	initial void ratio	dimensionless
de	change in void ratio	dimensionless
g	gravity acceleration	m/s^2
m	sedimentation rate	mm/yr
n	porosity	dimensionless
t	total time	yr
T	dissipation time factor	dimensionless
u	pore pressure	MPa
u_h	hydrostatic pressure	MPa
u^*	overpressure	MPa
u^*_{max}	maximum bound on overpressure	MPa
u^*_{min}	minimum bound on overpressure	MPa
V_i	initial total volume	m^3
dV	change in pore volume	m^3
z	depth in meters below seafloor	m
λ^*	overpressure ratio	dimensionless
ρ_b	bulk density	kg/m^3
ρ_f	fluid density	kg/m^3
ρ_g	grain density	kg/m^3
σ_v	vertical stress	MPa
σ'_{pc}	preconsolidation stress	MPa
$\sigma'_{pc\ max}$	maximum bound on preconsolidation stress	MPa
$\sigma'_{pc\ min}$	minimum bound on preconsolidation stress	MPa
σ'_v	vertical effective stress	MPa
$\Delta\sigma'_v$	difference in vertical effective stress	MPa
σ'_{vh}	hydrostatic vertical effective stress	MPa

ACKNOWLEDGEMENTS

I thank the crew, technicians, and scientific staff of the *Joides Resolution* for their extraordinary efforts during Expedition 308. This work was supported by the National Science Foundation (OCE#0351085 and EAR#0447235), the Petroleum Research Fund (PRF# 44476-AC8), the Penn State Geofluids Consortium (supported by 9 energy companies), and JOI-USSAC IODP Expedition 308 support to Flemings. I thank Chevron and the Institute for Geophysics at the University of Texas at Austin for their generous support of J. Schneider through the Chevron Fellowship and the Ewing/Worzel Fellowship. This research used samples and data provided by the Integrated Ocean Drilling Program (IODP). IODP is sponsored by the U.S. National Science Foundation (NSF) and participating countries. I thank Shell Exploration and Production Company for supplying the seismic data. The software packages Seisworks and Geolog from Landmark were used for this project. I appreciate the careful review of this manuscript by D. Saffer. D. Sawyer helped us with useful comments and suggestions. H. Nelson provided software assistance.

REFERENCES

Athy, L.F., 1930. Density, porosity, and compaction of sedimentary rocks. *Am. Assoc. Pet. Geol. Bull.*, 14: 1-22.

Badalini, G., Kneller, B., and Winker, C.D., 2000, Architecture and Processes in the Late Pleistocene Brazos-Trinity Turbidite System, Gulf of Mexico Continental Slope, GCSSEPM Foundation 20th Annual Research Conference, Deep-Water Reservoirs of the World.

Beaubouef, R.T., and Friedmann, S.J., 2000, High Resolution Seismic/Sequence Stratigraphic Framework for the Evolution of Pleistocene Intra Slope Basins, Western Gulf of Mexico: Depositional Models and Reservoir Analogs, GCSSEPM Foundation 20th Annual Research Conference, Deep-Water Reservoirs of the World.

Becker, D.E., Crooks, J.H.A., Been, K., and Jefferies, M.G., 1987. Work as a Criterion for Determining Insitu and Yield Stresses in Clays. *Canadian Geotechnical Journal*, 24(4): 549-564.

Bekins, B.A., McCaffrey, A.M., and Dreiss, S.J., 1995. Episodic and constant flow models for the origin of low-chloride waters in a modern accretionary complex. *Water Resources Research*, 31(12): 3205-3215.

Burmister, D.M., 1942. Laboratory investigations of soils at Flushing Meadow Park. *Transactions of the American Society of Civil Engineers*, 107: 187.

Burmister, D.M., 1951. The application of controlled test methods in consolidation testing. *Symposium on Consolidation Testing of Soils, American Society for Testing and Materials*, Special Technical Publication 126: 83.

Casagrande, A., 1936. The determination of the pre-consolidation load and its practical significance. *In* Casagrande, A., Rutledge, P.C., and Watson, J.D., eds., Proc. 1st International Conf. Soil Mech. Foun. Eng., Am. Soc. Civ. Eng., p. 60-64.

Craig, R.F., 1974. Soil Mechanics. New York, Van Nostrand Reinhold, 275 p.

Dugan, B., and Flemings, P.B., 2000. Overpressure and Fluid Flow in the New Jersey Continental Slope: Implications for Slope Failure and Cold Seeps. *Science*, 289(5477): 288-291.

Dugan, B., Flemings, P.B., Olgaard, D.L., and Gooch, M.J., 2003. Consolidation, effective stress, and fluid pressure of sediments from ODP Site 1073, US mid-Atlantic continental slope. *Earth and Planetary Science Letters*, 215: 13-26, doi:10.1016/S0012-821X(03)00425-4.

Dugan, B., and Germaine, J., 2008. Near-seafloor overpressure in the deepwater Mississippi Canyon, northern Gulf of Mexico. *Geophysical Research Letters*, 35(L02304), doi:10.1029/2007GL032275.

Fertl, W.H., and Chilingarian, G.V., 1987. Abnormal formation pressures and their detection by pulsed neutron capture logs. *Journal of Petroleum Science and Engineering*, 1: 23-38.

Flemings, P.B., Stump, B.B., Finkbeiner, T., and Zoback, M., 2002. Flow focusing in overpressured sandstones: Theory, observations, and applications. *American Journal of Science*, 302(10): 827-855, doi:10.2475/ajs.302.10.827.

Flemings, P.B., and Lupa, J.A., 2004. Pressure prediction in the Bullwinkle Basin through petrophysics and flow modeling (Green Canyon 65, Gulf of Mexico). *Marine and Petroleum Geology*, 21: 1311-1322, doi:10.1016/j.marpetgeo.2004.09.005.

Flemings, P.B., Behrmann, J.H., John, C.M., and Scientists, E., 2006. Gulf of Mexico Hydrogeology, Proc. IODP, Volume 308: College Station, TX (Integrated Ocean Drilling Program Management International, Inc.), doi:10.2204/iodp.proc.308.2006.

Flemings, P.B., Long, H., Dugan, B., Germaine, J.T., John, C., Behrmann, J.H., Sawyer, D.E., and Scientists, I.E., 2008. Pore pressure penetrometers document high overpressure near the seafloor where multiple submarine landslides have occurred on the continental slope, offshore Louisiana, Gulf of Mexico. *Earth and Planetary Science Letters*, 269: 309-325, doi:10.1016/j.epsl.2007.12.005.

Garg, S.K., Pritchett, J.W., Katoh, A., Baba, K., and Fujii, T., 2008. A mathematical model for the formation and dissociation of methane hydrates in the marine environment. *Journal of Geophysical Research-Solid Earth*, 113(B01201), doi:10.1029/2006JB004768.

Gibson, R.E., 1958. The progress of consolidation in a clay layer increasing in thickness with time. *Geotechnique*, 8: 171-182.

Gordon, D.S., and Flemings, P.B., 1998. Generation of overpressure and compaction-driven fluid flow in a Plio-Pleistocene growth-faulted basin, Eugene Island 330, offshore Louisiana. *Basin Research*, 10(2): 177-196, doi:10.1046/j.1365-2117.1998.00052.

Harrison, W.J., and Summa, L.L., 1991. Paleohydrology of the Gulf of Mexico Basin. *American Journal of Science*, 291(2): 109-176.

Hart, B.S., Flemings, P.B., and Deshpande, A., 1995. Porosity and Pressure - Role of Compaction Disequilibrium in the Development of Geopressures in a Gulf-Coast Pleistocene Basin. *Geology*, 23(1): 45-48.

Jamiolkowski, M., 1985, New developments in field and laboratory testing of soils, 11th Int. Conf. on Soil Mechanis and Foundation Engineering, Volume 1: San Francisco, p. 57-153.

Janbu, N., Tokheim, O., and Senneset, K., 1981, Consolidation test with continuous loading, 10th International Conference on Soil Mechanics and Foundation Engineering, Volume 1: Stockholm, p. 645-654.

Kennett, J.P., and Huddleston, P., 1972. Late Pleistocene paleoclimatology, foraminiferal biostratigraphy, and tephrochronology: Western Gulf of Mexico. *Quaternary Research*, 2: 38-69.

Lambe, T.W., and Whitman, R.V., 1979. Soil Mechanics: SI Version. New York, Wiley, 553 p.

Long, H., Flemings, P.B., and Germaine, J.T., 2007. Interpreting *in situ* pressure and hydraulic properties with borehole penetrometers in ocean drilling: DVTPP and Piezoprobe deployments at southern Hydrate Ridge, offshore Oregon. *Journal of Geophysical Research*, 112(B4), doi:10.1029/2005JB004165.

Long, H., Flemings, P.B., Dugan, B., Germaine, J.T., and Ferrell, D., 2008. Data report: penetrometer measurements of *in situ* temperature and pressure, IODP Expedition 308. *In* Flemings, P.B., Behrmann, J.H., John, C.M., and Scientists, t.E., eds., Proc. IODP, Volume 308: College Station, TX, Proc. IODP, Sci. Results, p. 68, doi:10.2204/iodp.proc.308.203.2008.

Long, H., Flemings, P.B., Dugan, B., Germaine, J.T., and Ferrell, D., in press., Data Report: Penetrometer measurements of *in situ* temperature and pressure on IODP Expedition 308, Proc. IODP, Sci. Results.

Mallarino, G., Beaubouef, R.T., Droxler, A.W., Abreu, V., and Labeyrie, L., 2006. Sea level influence on the nature and timing of a minibasin sedimentary fill (northwestern slope of the Gulf of Mexico). *AAPG Bulletin*, 90(7): 1089-1119, doi:10.1306/02210605058.

O'Hayer, W.W., 2008. Laurentide Ice Sheet Meltwater Influences and Millennial Scale Climate Oscillations on the Northwestern Slope of the Gulf of Mexico During Marine Isotope Stage 6 and Termination II [MS thesis]. Houston, Texas, Rice University, NNN p.

O'Hayer, W.W., 2009. Laurentide Ice Sheet Meltwater Influences and Millennial Scale Climate Oscillations on the Northwestern Slope of the Gulf of Mexico During Marine Isotope Stage 6 and Termination II [MS thesis]. Houston, Texas, Rice University, NNN p.

Orange, D.L., Saffer, D.M., Jeanjean, P., Al-Khafaji, Z., Humphrey, G., and Riley, G., 2003. Measurements and modeling of the shallow pore pressure regime at the Sigsbee Escarpment: Successful prediction of overpressure and ground-truthing with borehole measurements. *Leading Edge*, 22: 906-913.

Ostermeier, R.M., Pelletier, J.H., Winker, C.D., Nicholson, J.W., Rambow, F.H., and Cowan, K.M., 2000. Dealing with shallow-water flow in the deepwater Gulf of

Mexico. *paper presented at Offshore Technology Conference 2000*, Soc. of Petrol. Eng., Houston, TX.

Ostermeier, R.M., Pelletier, J.H., Winker, C.D., and Nicholson, J.W., 2001. Trends in shallow sediment pore pressures: Deepwater Gulf of Mexico. *paper presented at 2001 SPE/IADC Drilling Conference*, Soc. of Petrol. Eng., Amsterdam.

Prior, D.B., and Coleman, J.M., 1982. Active slides and flows in underconsolidated marine sediments on the slope of the Mississippi delta. *In* Saxov, S., and Nieuwenhuis, J.K., eds., Marine slides and other mass movements: New York, NY: Plenum Press, p. 21-49.

Rubey, W.W., and Hubbert, M.K., 1959. Overthrust belt in geosynclinal area of western Wyoming in light of fluid-pressure hypothesis, 2: Role of fluid pressure in mechanics of overthrust faulting. *GSA Bulletin*, 70(2): 167-205.

Saffer, D.M., and Bekins, B.A., 1998. Episodic fluid flow in the Nankai accretionary complex: Timescale, geochemistry, flow rates, and fluid budget. *Journal of Geophysical Research*, 103(B12): 30351-30370.

Saffer, D.M., Silver, E.A., Fisher, A.T., Tobin, H., and Moran, K., 2000. Inferred pore pressures at the Costa Rica subduction zone: implications for dewatering processes. *Earth and Planetary Science Letters*, 177(3-4): 193-207, doi:10.1016/S0012-821X(00)00048-0.

Saffer, D.M., 2003. Pore pressure development and progressive dewatering in underthrust sediments at the Costa Rican subduction margin: Comparison with northern Barbados and Nankai. *Journal of Geophysical Research*, 108(B5): 2261, doi:10.1029/2002JB001787.

Santagata, M.C., and Germaine, J.T., 2002. Sampling disturbance effects in normally consolidated clays. *J. Geotech. Geoenviron. Eng.*, 128(12): 997-1006, doi:10.1061/(ASCE)1090-0241(2002)128:12(997).

Satterfield, W.M., and Behrens, E.W., 1990. A Late Quaternary Canyon Channel System, Northwest Gulf of Mexico Continental-Slope. *Marine Geology*, 92(1-2): 51-67, doi:10.1016/0025-3227(90)90026-G.

Sawyer, D.E., Flemings, P.B., Shipp, R.C., and Winker, C.D., 2007. Seismic geomorphology, lithology, and evolution of the late Pleistocene Mars-Ursa turbidite region, Mississippi Canyon area, northern Gulf of Mexico. *AAPG Bulletin*, 91(2): 215-234, doi:10.1306/08290605190.

Schmertmann, J.M., 1955. The undisturbed consolidation of clay. *Transactions of the American Society of Civil Engineers*, 120: 1201.

Screaton, E., Saffer, D.M., Henry, P., and Hunze, S., 2002. Porosity loss within the underthrust sediments of the Nankai accretionary complex: Implications for

overpressures. *Geology*, 30(1): 19-22, doi:10.1130/0091-7613(2002)030<0019:PLWTUS>2.0.CO;2.

Screaton, E., and Saffer, D.M., 2005. Fluid expulsion and overpressure development during initial subduction at the Costa Rica convergent margin. *Earth and Planetary Science Letters*, 233(3-4): 361-374, doi:10.1016/j.epsl.2005.02.017.

Shipboard-Scientific-Party, 2002. Site 1173, Leg 196 summary: Deformation and fluid flow processes in the Nankai Trough accretionary prism: Logging-while-drilling and Advanced CORKs, Proc. Ocean Drill. Program Initial Rep., 196, Volume 196, p. 1-29, doi:10.2973/odp.proc.ir.196.101.2002.

Terzaghi, K., and Peck, R.B., 1948. Soil mechanics in engineering practice. New York, Wiley.

Winker, C.D., 1996, High-resolution seismic stratigraphy of a Late Pleistocene submarine fan ponded by salt-withdrawal mini-basins on the Gulf of Mexico continental slope, Proceedings from 1996 Offshore Technology Conference: Houston, Texas, p. 619-628, Paper OTC 8024, May 6-9, 1996.

Wood, D.M., 1990. Soil Behaviour and Critical State Soil Mechanics. Cambridge, U.K., Cambridge Univ. Press, 462 p.

Xu, W., and Ruppel, C., 1999. Predicting the occurrence, distribution, and evolution of methane gas hydrate in porous marine sediments. *J. Geophs. Res.*, 104(B3): 5081-5095.

Chapter 3: Permeability – Porosity Behavior of Shallow Mudstones in the Ursa Basin, Northern Deepwater Gulf of Mexico

ABSTRACT

Uniaxial consolidation experiments constrain vertical permeability in overpressured mudstones near the seafloor of the Ursa Basin, Northern Gulf of Mexico. I analyze silty clays and clayey silts collected within the uppermost 600 meters below seafloor at Integrated Ocean Drilling Program (IODP) Sites U1324 and U1322. A single sample of clayey silt has a vertical permeability that ranges from $7.74 \cdot 10^{-17}$ to $8.49 \cdot 10^{-19}$ m^2 as porosity declines from 0.37 to 0.19 during the experiment. Twenty-nine samples of silty clay were found to have a permeabilities of up to two orders of magnitude lower at any given porosity. I infer *in-situ* permeabilities (k_i) by extrapolating the individual log-linear relationship between permeability and porosity back to *in-situ* porosities (n_i). *In-situ* vertical permeability decreases slightly with depth. Low vertical permeabilities, accompanied by high sedimentation rates, can cause severe overpressure near the seafloor, which controls fluid flow and can reduce slope stability as observed in the Mississippi Canyon region. Thus, well-constrained permeability measurements are needed for accurate basin modeling of particularly overpressured sediments in the shallow subsurface.

3.1 INTRODUCTION

The permeability of marine sediments strongly depends on lithology and effective stress, but also on other factors such as diagenesis. It controls the nature of fluid flow through sediments and hydrothermal circulation (Spinelli et al., 2004). The permeability also controls the degree to which sediments can hydraulically isolate the oceanic

basement aquifer (Spinelli et al., 2004). This influences the basement fluid temperature, circulation patterns, and residence time (Davis and Becker, 2004; Fisher, 2004) as well as the heat flow through the seafloor (Anderson and Hobart, 1976; Sclater et al., 1976; Stein and Stein, 1994; Harris and Chapman, 2004), the nature of hydrothermal alteration of the crust (Alt and Teagle, 1999; Alt, 2004), the evolution of crustal properties (Jacobson, 1992; Grevemeyer and Bartetzko, 2004), and the ocean chemistry through the exchange of solutes (Mottl and Wheat, 1994; Bickle and Elderfield, 2004; Wheat and Mottl, 2004).

Permeability, in addition to sediment compressibility and deposition rate is a key parameter in understanding shallow subsurface overpressure generation and evolution. When compressible sediments that have a low permeability are rapidly loaded, consolidation of these sediments is reduced because pore fluids cannot drain fast enough to remain at hydrostatic pressure and overpressure develops. This was predicted by modeling studies (Gibson, 1958; Harrison and Summa, 1991) and documented in several recent studies (Dugan and Flemings, 2000; Orange et al., 2003; Dugan and Germaine, 2008; Flemings et al., 2008; Schneider et al., 2009). These high overpressures especially near the seafloor drive shallow fluid flow (Dugan and Flemings, 2000; Dugan and Germaine, 2008; Flemings et al., 2008), may reduce slope stability (Prior and Coleman, 1982; Dugan and Flemings, 2000; Flemings et al., 2008), and can result in large submarine landslides (Prior and Suhayda, 1979; Dugan and Flemings, 2000; Sawyer et al., 2007; Flemings et al., 2008). Thus, the relationship between vertical permeability and porosity is a key constitutive input to numerical basin models simulating fluid flow in sedimentary basins (Smith, 1971; Sharp and Domenico, 1976; Hermanrud, 1993; Schneider et al., 1993; Dugan and Germaine, 2008) as well as the evolution of basin slope stability (Dugan and Flemings, 2000).

There are several approaches to measure permeability in mudstones. Measuring vertical permeability in mudstones *in-situ* is difficult due to very low flow rates. Thus, *in-situ* permeability measurements are rare. But permeability is often determined in the laboratory by using either falling-head permeameters, constant-head permeameters (Lambe and Whitman, 1979), consolidation tests (Terzaghi and Peck, 1948), or transient pulse decay techniques (e.g. Yang and Aplin, 2007). Several studies evaluated permeability from more easily measured physical properties such as pore size distribution (Leonards, 1962; Scheidegger, 1974; Garcia-Bengochea et al., 1979; Pittman, 1992; Yang and Aplin, 1998, 2007) and porosity and specific surface area (see Leonards, 1962).

In this study I have the great opportunity to study sediments, for which a lot of measurements are available, within 500 meters of the seafloor in an area where known overpressure exists and sedimentation rate is known. With uniaxial consolidation testing, I determine the relationship between porosity and vertical permeability over a range of vertical effective stresses for these sediments of varying compositions. I then derive *in-situ* permeabilities for all 30 samples by extrapolating the permeability-porosity relationship back to the *in-situ* porosities. Based on measured permeabilities of the mudstones at two drill sites and given pore pressure measurements performed during the IODP Expedition 308, I estimate upward flow rates through the uppermost mudstones in the Ursa Basin. The results have implications for how sediments consolidate and what overpressure is generated.

3.2 GEOLOGIC SETTING

The Ursa Basin in the northern deepwater Gulf of Mexico is located 95 km south of the Mississippi River, offshore Louisiana (Figure 3.1). It is an active hydrologic

system as documented by shallow subsurface fluid flow (Dugan and Germaine, 2008; Flemings et al., 2008), active deformation through recent faulting (Dugan and Germaine, 2008), mud volcanoes (Ruppel et al., 2005) as well as large slope failures (Sawyer et al., 2007; Sawyer et al., 2009). Asymmetric, rapid sedimentation of low permeable sediments on top of a permeable aquifer resulted in fluids draining upward near the seafloor but also migrating laterally from regions of thicker overburden to regions of thinner overburden (Dugan and Germaine, 2008; Flemings et al., 2008).

Integrated Ocean Drilling Program (IODP) Expedition 308 drilled three sites in this area: U1324, U1323, and U1322 (Figure 3.1, 3.2). Water depths vary between 1319 m and 1055 m. Late Pleistocene deposits consist of a regional, sand-dominated package (the Blue Unit) overlain by levee-channel deposits and a thick package of mudstone (Figure 3.2). The Blue Unit is composed of interbedded sandstone and mudstone. Levee-channel deposits consist of a sand-cored channel and are flanked by mud-prone levee deposits. As documented in three-dimensional seismic data and by the IODP drill sites, these levee deposits thin from the west to the east reducing its thickness from ~600 m near Site U1324 to ~230 m at Site U1322 (Figure 3.2) (Flemings et al., 2006). These levee-channel deposits are buried by hemipelagic mud.

The two Sites U1324 and U1322 are hydrologically connected at depth below 600 mbsf by the regional aquifer Blue Unit (Dugan and Flemings, 2000; Dugan and Germaine, 2008; Flemings et al., 2008). Flemings et al. (2008) measured direct pore fluid pressures in the shallow mudstones and showed that the low permeable sediments near the seafloor are highly overpressured (~70% of the hydrostatic effective stress).

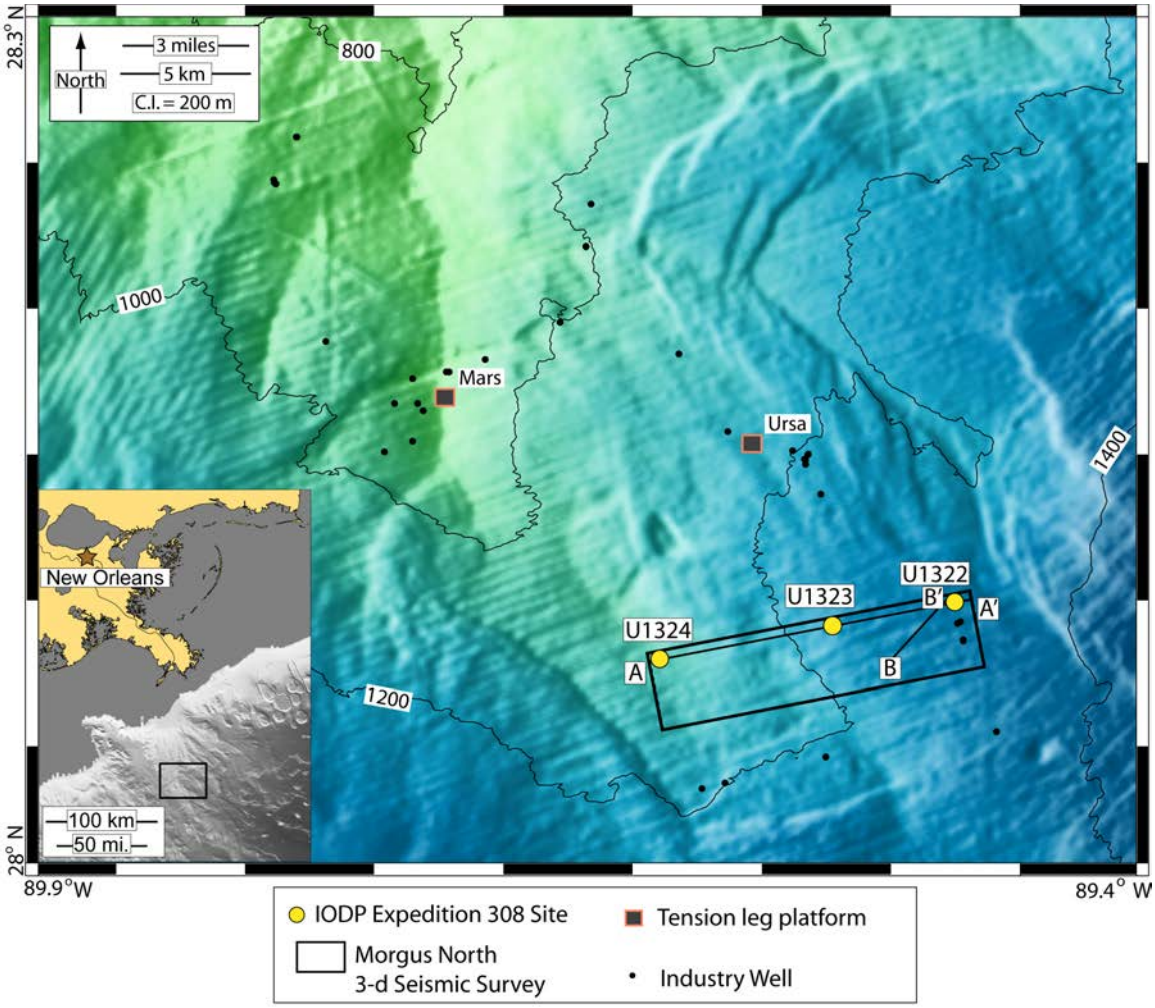

Figure 3.1: The Ursa Region is located 210 km SE of New Orleans, Louisiana, USA (inset map). The IODP drilling transect is located in 1000 – 1300 meters of water. IODP sites (circles), three-dimensional seismic survey (black rectangle), Ursa and Mars tensionleg platforms (squares), and top-hole position industry wells (black dots) are shown (Sawyer et al., 2009).

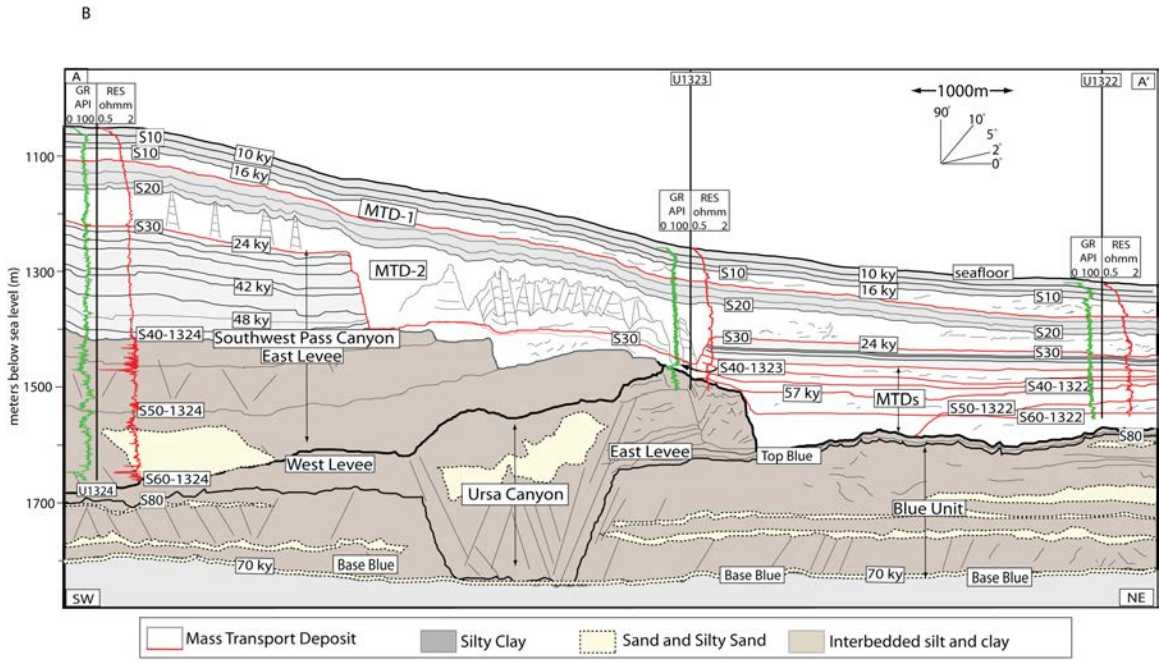

Figure 3.2: Interpreted well-log cross-section A-A' illustrating main depositional units and lithology at Ursa. Mass transport deposits (MTDs) occur primarily within the thick silty clay levee deposits (Sawyer et al., 2009).

3.3 Experimental Analyses

3.3.1 Sample descriptions

I used 30 whole core samples from mudstones that were drilled during IODP Expedition 308 at Sites U1324 and U1322. Nine samples were collected from Site U1322 between 27 and 210 msbf and 21 samples from Site U1324 between 32 and 578 mbsf. The samples were sealed with wax, end caps, and electrical tape and then immediately refrigerated until use to keep the original water content. Sawyer et al. (2008) performed grain size analyses on mudstone samples from the same drill sites and described two characteristic lithologies within the mudstones above the Blue Unit in the Ursa Basin: silty clays and clayey silts, hereafter called Ursa Mud and Ursa Silt, respectively. The Ursa Mud is composed of approximately 60% (+/-10%) clay-sized particles, 40% silt-sized particles and less than 1% sand-sized particles by mass (Table 3.1) (Sawyer et al., 2008). The composition of Ursa Silt is approximately 32% clay-sized particles, 67% silt-sized particles, and 1% sand-sized particles by mass (Sawyer et al., 2008). Figure 3.3 shows the grain size distributions of the tested samples in this study (Sawyer et al., 2008). Based on quantitative X-Ray mineralogy, illite and smectite appear to be the dominant minerals in the Ursa Mud samples (Long et al., 2008). Together they comprise 37%–60% of the bulk rock weight (Long et al., 2008).

CRS #[a]	*Lithology*	*Hole-Core-Section*	*Depth*[b] *(mbsf)*	*% Sand* [c]	*% Silt* [c]	*% Clay* [c]
CRS 21	Ursa Mud	U1322D-3H-3WR	103.44	0.07	48.21	51.72
CRS 796	Ursa Mud	U1322D-2H-2WR				
CRS 798	Ursa Mud	U1322D-2H-2WR				
CRS 808	Ursa Mud	U1322B-15H-1WR	125.80	0.00	29.60	70.40
CRS 810	Ursa Mud	U1322B-18H-6WR	157.30	0.70	33.70	65.60
CRS 815	Ursa Mud	U1322B-4H-3WR				
CRS 824	Ursa Mud	U1322B-25H-6WR				
CRS 825	Ursa Mud	U1322B-21H-3WR				
CRS 826	Ursa Mud	U1322D-1H-2WR				
CRS 01	Ursa Mud	U1324C-6H-3WR	304.02	0.11	37.09	62.80
CRS 02	Ursa Mud	U1324C-6H-3WR	303.94	0.03	36.37	63.60
CRS 04	Ursa Mud	U1324C-1H-1WR	51.14	0.04	42.59	57.37
CRS 05	Ursa Mud	U1324B-13H-7WR	117.40	0.03	40.07	59.90
CRS 06	Ursa Mud	U1324B-70X-6WR	578.13	0.03	38.17	61.80
CRS 07	Ursa Mud	U1324B-60X-2WR	476.86	0.02	41.33	58.65
CRS 08	Ursa Silt	U1324C-7H-1WR	405.81	1.54	66.73	31.73
CRS 13	Ursa Mud	U1324B-4H-7WR	32.14	0.7	34.20	65.10
CRS 14	Ursa Mud	U1324B-4H-7WR	32.10	0.00	44.70	55.30
CRS 15	Ursa Mud	U1324B-7H-7WR	60.62	0.00	50.40	49.60
CRS 19	Ursa Mud	U1324B-31H-3WR	261.02	0.02	43.34	56.64
CRS 20	Ursa Mud	U1324B-21H-3WR	183.14	0.01	35.84	64.15
CRS 797	Ursa Mud	U1324C-1H-1WR				
CRS 799	Ursa Mud	U1324C-1H-1WR	51.10	0.00	31.90	68.10
CRS 800	Ursa Mud	U1324B-4H-7WR	31.86	0.00	44.50	55.50
CRS 801	Ursa Mud	U1324B-16H-5WR	141.24	0.00	42.00	58.00
CRS 802	Ursa Mud	U1324B-7H-7WR	60.31	0.00	39.00	61.00
CRS 803	Ursa Mud	U1324B-15H-5WR	134.20	0.30	37.70	62.00
CRS 807	Ursa Mud	U1324C-2H-4WR	104.50	0.00	49.20	50.80
CRS 812	Ursa Mud	U1324B-23H-5WR	199.80	0.12	40.79	59.09
CRS 813	Ursa Mud	U1324B-10H-7WR	88.80	0.00	39.70	60.30

Table 3.1: Permeability properties.

[a] CRS #: constant-rate-of-strain (CRS) consolidation test number
[b] Depth: depth of the center of the whole core sample in mbsf
[c] %Sand, %Silt, %Clay: grain size distributions measured by Sawyer et al. (2008)

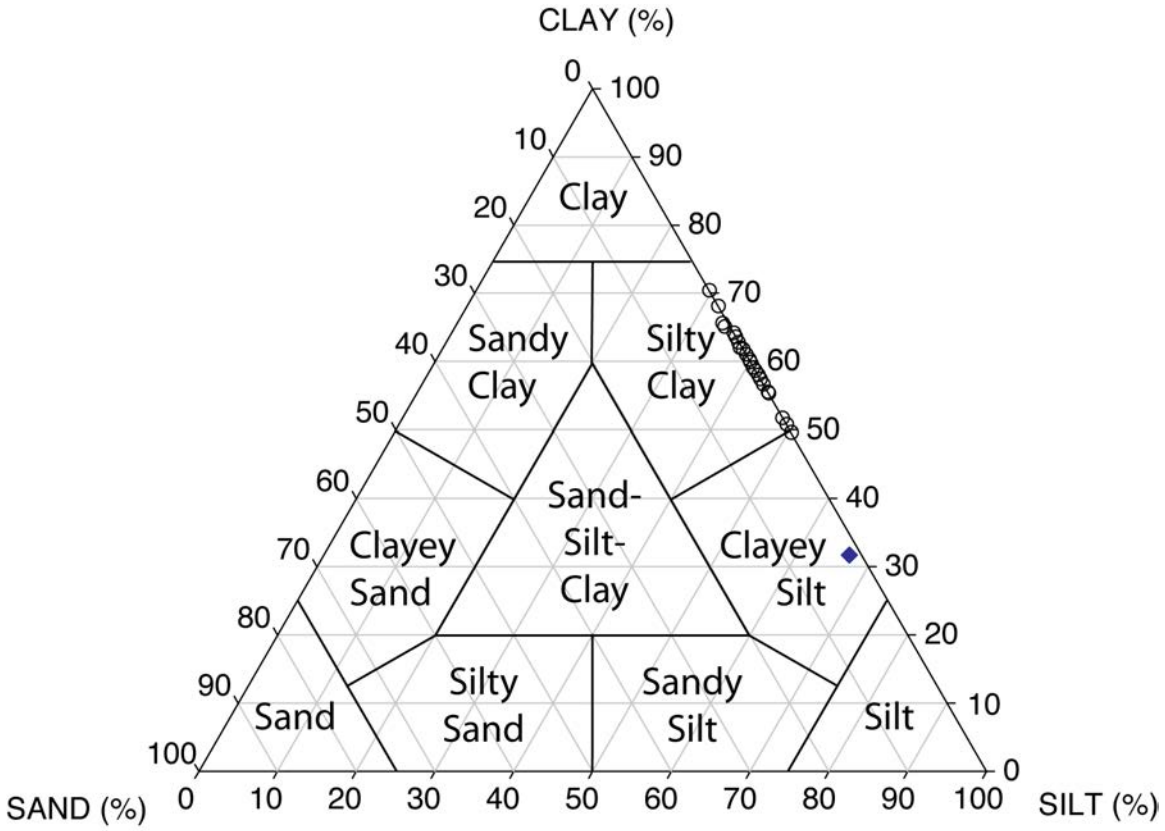

Figure 3.3: Grain size distributions of all 30 whole cores including one Ursa Silt (blue diamond) and 29 Ursa Mud (black circles) samples from both Sites U1324 and U1322 (Table 3.1) (modified after Sawyer et al. (2008)).

3.3.2 Uniaxial consolidation experiments

Uniaxial, constant-rate-of-strain (CRS) consolidation experiments are used to derive geotechnical properties such as compression behavior, preconsolidation stress, and permeability (Dugan et al., 2003). CRS experiments were performed on the 30 whole core samples collected from Sites U1324 and U1322. These tests were run in three different laboratories (The Pennsylvania State University, Rice University, and the Massachusetts Institute of Technology). Fixed-diameter rings were used in the test setup to maintain uniaxial strain. Axial load, specimen height, and pore fluid pressure at the top and base of the specimen are monitored throughout the test. I assume linear soil behavior, i.e. coefficient of volume compressibility is constant. Then the hydraulic conductivity can be directly calculated as described in Equation 3.1 (ASTM International, 2006; Tan et al., 2006; Long et al., 2008).

$$K = \frac{d\varepsilon/dt \, H_0 H \gamma_w}{2\Delta u}, \tag{3.1}$$

where K is hydraulic conductivity, $d\varepsilon/dt$ is strain rate, H_0 is initial specimen height, H is specimen height, γ_w is unit weight of water, and Δu is excess pore pressure. Vertical permeability (k) is related to hydraulic conductivity (K) by:

$$k = \frac{K \cdot \mu_w}{\rho_w \cdot g}, \tag{3.2}$$

where ρ_w and μ_w are fluid properties such as density and viscosity, respectively, and g is acceleration due to gravity.

3.3.3 Experimentally-derived porosity – permeability relationship

I plot vertical permeability of all 30 sediment samples estimated from the steady state portion of CRS experiments against porosity. This relationship is only true over the data range that corresponds to the virgin consolidation part, when steady state conditions are reached (as shown exemplary in Figure 3.4). All experiments show a distinct linear relationship between the log of vertical permeability and porosity (Figure 3.5). Table 3.2 lists permeability properties for all 30 Ursa samples. Vertical permeabilities of the Ursa Mud range over an order of magnitude at a given porosity. The single Ursa Silt sample has a permeability – porosity relationship that is about one order of magnitude larger than the highest vertical permeability estimated in the Ursa Mud at a given porosity.

I characterize the permeability – porosity behavior of all 30 samples using a least squares regression of the form:

$$\log(k) = \gamma * n + \log(k_0), \tag{3.3}$$

where γ is the permeability index and $\log(k_0)$ the y-intercept at a porosity of zero. Permeabilities in m^2 can then be described by equation 3.4.

$$k = 10^{(\gamma n + \log(k_0))}. \tag{3.4}$$

The vertical permeability – porosity relationship for the Ursa Silt can be approximated by linear regression:

$$\log(k) = 8.60 * n - 19.63. \tag{3.5}$$

The slopes of all permeability – porosity (γ) relationships do not vary significantly, however, the y-intercepts (k_0) do (Figure 3.6). Due to very similar

mineralogy in all samples, vertical permeability decreases with porosity similarly for all samples. Only the varying grain size distribution causes the difference in k_0.

Due to the large number of Ursa Mud samples and variation in vertical permeability over more than an order of magnitude at a given porosity, a single Ursa Mud permeability – porosity relationship cannot easily be defined. I used two possible models for characterizing the Ursa Mud permeability behavior. First, I assume a horizontal layering. The horizontal layering can be described by the arithmetic mean, the sum of permeabilities divided by the number of data points. An alternative model is to assume a vertical layering, which can be described by the harmonic mean. The harmonic mean numerically is the number of data points divided by the sum of the inverse of permeabilities.

In the calculation of the arithmetic mean, all data points are lined up in series. Therefore, it describes flow parallel to bedding resulting in an average value on the higher side of the spectrum. On the other hand, the harmonic mean is calculated by theoretically stacking all data points on top of each other. Therefore, it describes flow perpendicular to bedding resulting in an average value on the lower end of the spectrum. This means lower permeabilities are weighted more than higher permeabilities.

An upscaled vertical permeability – porosity relationship for the Ursa Mud can be approximated averaging all γ and k_0 of the 29 samples using the arithmetic and harmonic mean, respectively:

$$\log (k) = 9.18 * n - 21.19 \quad (3.6)$$

$$\log (k) = 9.01 * n - 22.16 \quad (3.7)$$

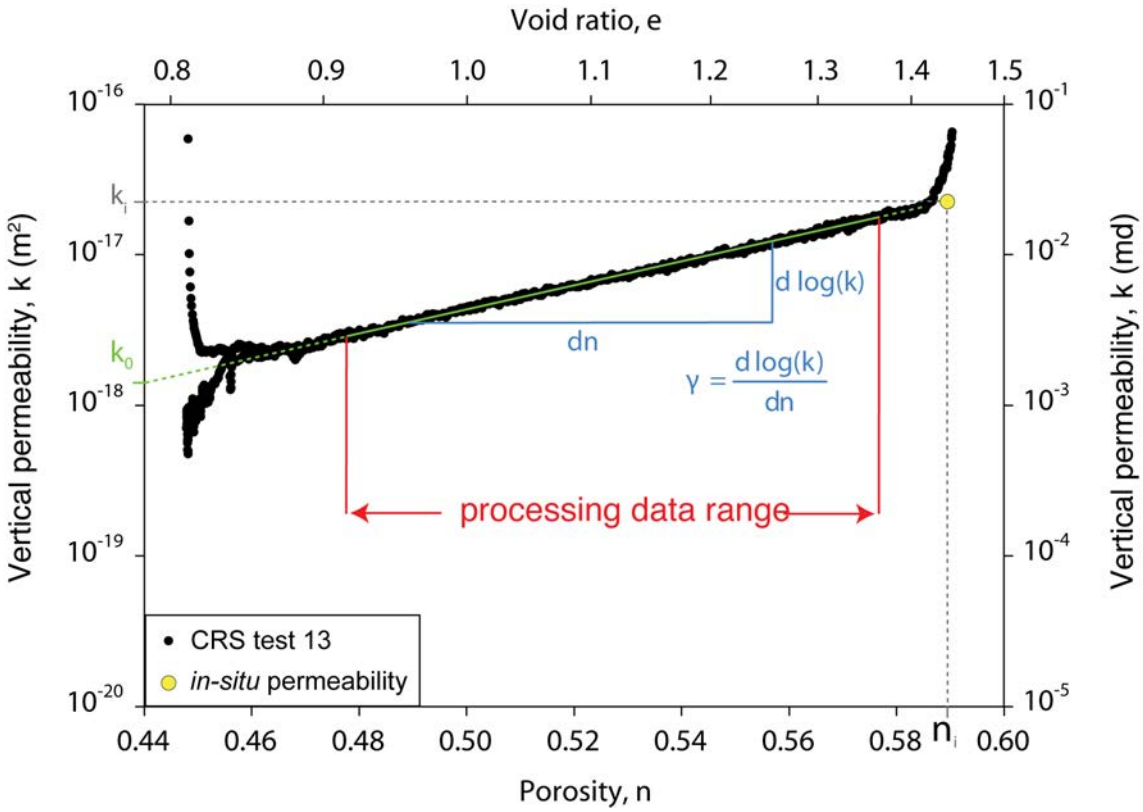

Figure 3.4: Example permeability – porosity data set (CRS 13) derived from uniaxial constant-rate-of-strain consolidation experiments. Slope and intercept of the log-linear relationship is determined over steady-state phase of test indicated by 'processing data range'. *In-situ* permeability is calculated by extrapolating log-linear relationship between permeability and porosity back to *in-situ* porosity. The *in-situ* porosity is derived from logging-while-drilling bulk density log.

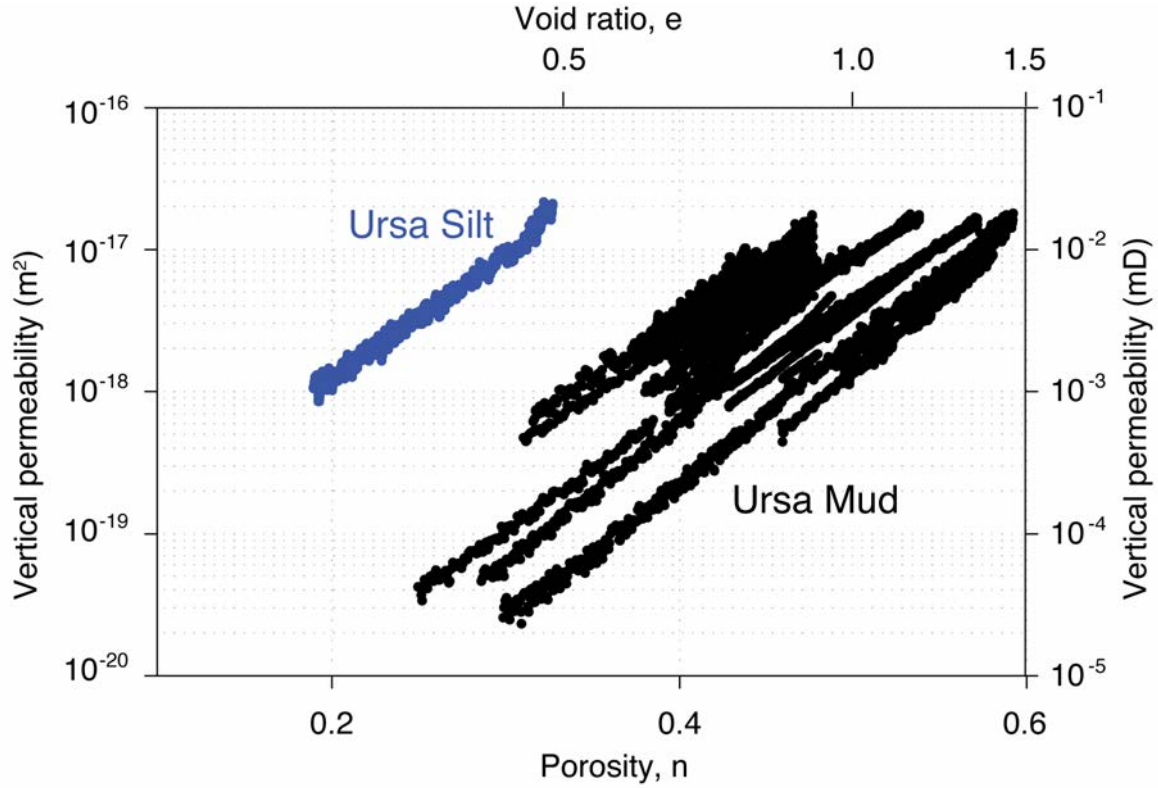

Figure 3.5: Permeability results of all 30 mudstone samples from Ursa Basin (IODP Sites U1322 and U1324). Single sample of Ursa Silt (blue) and 29 samples of Ursa Mud (black) are shown. Permeability properties of all log-linear relationships between permeability and porosity are listed in Table 3.2.

CRS #[a]	*Litho-logy*	*MTD*[b]	*Hole-Core-Section*	*Depth*[c] *(mbsf)*	ρ_b[d] *(kg/ m^3)*	n_i[e]	γ[f]	*log* (k_0)[g] *(m^2)*	k_i[h] *(m^2)*
CRS 21	Ursa Mud	X	U1322D-3H-3WR	103.44	1880	0.50	10.95	-21.90	3.87E-17
CRS 796	Ursa Mud		U1322D-2H-2WR	72.00	1800	0.55	8.34	-21.74	6.74E-18
CRS 798	Ursa Mud		U1322D-2H-2WR	72.00	1800	0.55	9.78	-21.99	2.33E-17
CRS 808	Ursa Mud		U1322B-15H-1WR	125.80	1850	0.52	7.67	-20.80	1.51E-17
CRS 810	Ursa Mud	X	U1322B-18H-6WR	157.30	1910	0.48	11.05	-22.27	1.19E-17
CRS 815	Ursa Mud		U1322B-4H-3WR	27.17	1620	0.65	10.04	-22.74	6.50E-17
CRS 824	Ursa Mud	X	U1322B-25H-6WR	209.81	1920	0.48	10.07	-22.27	3.48E-18
CRS 825	Ursa Mud	X	U1322B-21H-3WR	177.54	1920	0.48	10.74	-21.77	2.30E-17
CRS 826	Ursa Mud	X	U1322D-1H-2WR	41.55	1700	0.61	9.20	-22.05	3.36E-17
CRS 01	Ursa Mud		U1324C-6H-3WR	304.02	1900	0.49	9.00	-21.05	2.27E-17
CRS 02	Ursa Mud		U1324C-6H-3WR	303.94	1940	0.47	7.28	-20.59	6.37E-18
CRS 04	Ursa Mud	X	U1324C-1H-1WR	51.14	1700	0.61	9.36	-22.40	1.87E-17
CRS 05	Ursa Mud	X	U1324B-13H-7WR	117.40	1840	0.52	8.59	-21.31	1.57E-17
CRS 06	Ursa Mud		U1324B-70X-6WR	578.13	2080	0.38	8.72	-21.59	5.81E-19
CRS 07	Ursa Mud	X	U1324B-60X-2WR	476.86	2000	0.43	10.08	-22.24	1.28E-18
CRS 08	Ursa Silt		U1324C-7H-1WR	405.81	1830	0.53	8.60	-19.63	8.52E-16
CRS 13	Ursa Mud		U1324B-4H-7WR	32.14	1650	0.64	7.84	-21.28	5.01E-17
CRS 14	Ursa Mud		U1324B-4H-7WR	32.10	1650	0.64	7.29	-20.70	8.52E-17
CRS 15	Ursa Mud		U1324B-7H-7WR	60.62	1710	0.60	8.16	-20.95	8.87E-17
CRS 19	Ursa Mud	X	U1324B-31H-3WR	261.02	1960	0.45	9.32	-21.18	1.14E-17
CRS 20	Ursa Mud		U1324B-21H-3WR	183.14	1920	0.48	9.81	-21.65	1.09E-17
CRS 797	Ursa Mud	X	U1324C-1H-1WR	51.10	1700	0.61	9.64	-22.66	1.52E-17
CRS 799	Ursa Mud	X	U1324C-1H-1WR	51.10	1700	0.61	10.38	-23.05	1.74E-17
CRS 800	Ursa Mud		U1324B-4H-7WR	31.86	1630	0.65	7.53	-20.83	1.10E-16
CRS 801	Ursa Mud	X	U1324B-16H-5WR	141.24	1940	0.47	7.49	-20.50	9.81E-18
CRS 802	Ursa Mud		U1324B-7H-7WR	60.31	1720	0.59	8.36	-21.55	2.63E-17
CRS 803	Ursa Mud	X	U1324B-15H-5WR	134.20	1900	0.49	7.76	-20.64	1.44E-17
CRS 807	Ursa Mud	X	U1324C-2H-4WR	104.50	1830	0.53	10.00	-22.03	1.88E-17
CRS 812	Ursa Mud		U1324B-23H-5WR	199.80	1910	0.48	11.75	-22.65	1.08E-17
CRS 813	Ursa Mud		U1324B-10H-7WR	88.80	1800	0.55	9.96	-22.06	2.49E-17

Table 3.2: Permeability properties.

[a] CRS #: constant-rate-of-strain (CRS) consolidation test number
[b] MTD: 'X' means the sample comes from a mass transport deposit (MTD)
[c] Depth: depth of the center of the whole core sample in mbsf
[d] ρ_b: Logging-while-drilling (LWD) bulk density values from nearby where specimens were taken.

[e] n_i: *In-situ* porosity calculated from logging-while-drilling bulk density log assuming grain density of 2740 kg/m^3 and water density of 1024 kg/m^3.
[f] γ : fitting parameter (slope of porosity – permeability relationship)
[g] k_0: fitting parameter (y-axis intercept of porosity – permeability relationship)
[h] k_i: *in-situ* vertical permeability determined through extrapolation of individual log-linear relationship between vertical permeability and porosity back to *in-situ* porosity.

3.3.4 *In-situ* permeabilities

I obtained *in-situ* vertical permeabilities by extrapolating the individual vertical permeability – porosity relationships of samples (γ and k_0 from Table 3.2) back to the *in-situ* porosity (n_i) (Table 3.2), which is determined from logging-while-drilling bulk density log assuming a grain density of 2740 kg/m^3 and fluid density of 1024 kg/m^3. There is a discrepancy of about 2 to 5 porosity units between logging-while-drilling porosity and moisture and density porosity or porosity measured on the CRS specimen in the laboratory due to expansion of the cores as they are brought to the surface and due to drying processes during trimming of the CRS specimens. Porosity derived from logging-while-drilling bulk density log is the best indicator of in-situ conditions if reliable grain and water densities are known. The Ursa Mud *in-situ* permeabilities vary between $5.8 \cdot 10^{-19}$ m^2 to $1.1 \cdot 10^{-16}$ m^2 (Figure 3.7). Ursa Silt *in-situ* permeability is 8.5×10^{-16} m^2, which is more than one order of magnitude higher than Ursa Mud *in-situ* permeabilities at similar porosities (Figure 3.7).

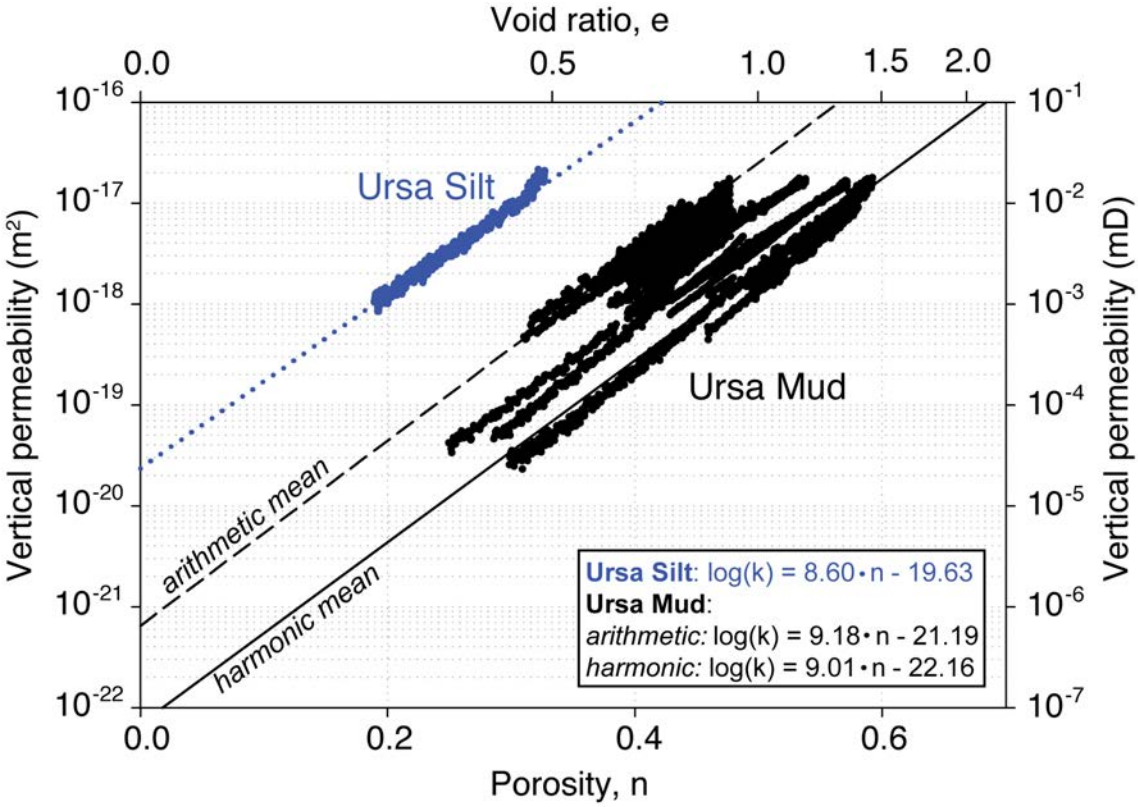

Figure 3.6: Predicted log-linear permeability – porosity relationships for Ursa Silt (blue) and Ursa Mud (black) samples from Ursa Basin (IODP Sites U1322 and U1324). Symbols are measured permeabilities. Dotted line is regression line of Ursa Silt permeability – porosity data. Dashed line represents arithmetic mean of 29 Ursa Mud samples whereas solid line represents harmonic mean of 29 Ursa Mud samples.

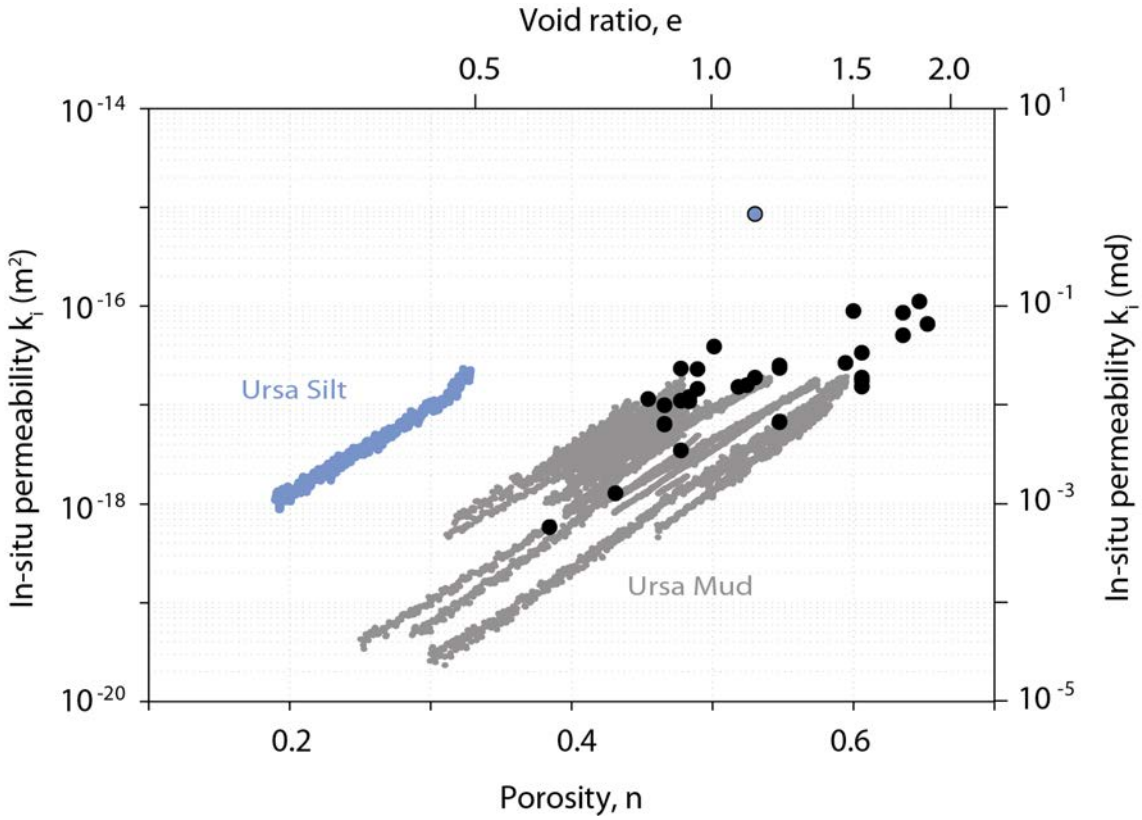

Figure 3.7: Predicted *in-situ* permeabilities of single Ursa Silt sample (dark blue) and 29 Ursa Mud samples (black). Individual log-linear permeability – porosity relationships of Ursa Silt (light blue) and Ursa Mud (gray) are extrapolated to *in-situ* porosity derived from logging-while-drilling (LWD) bulk density log (Table 3.2) to get *in-situ* permeability.

3.5 DISCUSSION

In-situ permeabilities of Ursa Mud follow the same log-linear trend as other published permeability data on natural mudstones (Figure 3.8). Dewhurst et al. (1999) measured permeability by constant-head method and inferred from consolidation tests on cores of London Clay that were drilled in 1987 near Bradwell (Essex, United Kingdom). The clay content of those London Clay cores varied between 27 and 66%. They grouped the samples into two fractions: cores with clay contents between 27 and 33% (stars around arithmetic mean in Figure 3.8) and cores with clay contents between 49 and 66% (stars below harmonic mean in Figure 3.8). Yang and Aplin (2007) measured permeability of 30 core samples that were collected from 14 North Sea wells, 8 Gulf of Mexico wells, and one Caspian Sea well (Figure 3.8). They used transient pulse decay method to measure permeability.

Ursa Mud *in-situ* permeabilities follow the same log-linear trend between permeability and porosity as the London Clay and mudstones from North Sea, Gulf of Mexico, and Caspian Sea, but only at higher porosities (Figure 3.8) because Ursa Mud samples were not buried as deeply as some of the mudstones published by Dewhurst et al. (1999) and Yang and Aplin (2007). The increase in permeability with decreasing clay content at a given porosity, as seen for the Ursa Mud and Ursa Silt, was also observed in the other two studies. The coarser cores of the London Clay line up with the arithmetic mean of the Ursa Mud permeabilities, whereas the fine-grained cores of London Clay have much lower permeabilities at the same porosity than the coarse fraction and plot below the harmonic mean of Ursa Mud permeabilities (Figure 3.8). Differences between permeabilities of London Clay, permeabilities on cores from the Gulf of Mexico, North Sea, and Caspian Sea and Ursa Mud/Silt permeabilities may be due to variations in mineralogy, particularly clay mineralogy. Different clay minerals have different specific

surface areas and different abilities to form a diffuse double layer resulting in different permeability trends (Robinson and Allam, 1998) (this is discussed in Chapter 6).

The experimentally-derived permeability results show a remarkably similar trend with porosity than *in-situ* permeabilities. Experimentally-derived permeabilities and *in-situ* permeabilities decline over two orders of magnitude between porosities of 0.4 and 0.6 (Figures 3.7 and 3.8). This means that for a given porosity the permeability observed at *in-situ* conditions in an intact sample is nearly equal than if a lithologically similar sample was taken from shallower depth (lower effective stress) and compressed to the porosity of the deeper sample. This can be seen in Figures 3.12 and 3.13, which show a comparison of the arithmetic and harmonic mean of the experimentally-derived permeability trends with the *in-situ* permeability profile with depth for each drill site (Site U1324 and U1322).

Clay fraction does not appear to be driving the permeability behavior (Figure 3.9). Specific surface area, measured on five Ursa Mud samples and the Ursa Silt sample by *Micromeritics Analytical Services* using gas adsorption (Brunauer Emmett Teller (BET) method) (Table 3.3), appears to decrease in the same matter as *in-situ* permeability does with porosity (Figure 3.10).

Mass transport deposits (MTDs), which are commonly observed in the Ursa Basin (Sawyer et al., 2009), do not seem have an effect on the permeability-porosity behavior either (Figure 3.11). In theory, MTDs are expected to have a lower permeability at a given porosity because they result from remolding via debris flows and remolding changes the soil fabric by collapsing a 'cardhouse' structure of clay particles to a preferred parallel alignment (Mitchell, 1993), which reduces permeability. But there is no significant difference in the *in-situ* permeability - porosity trend between MTDs or non-MTDs (Figure 3.11).

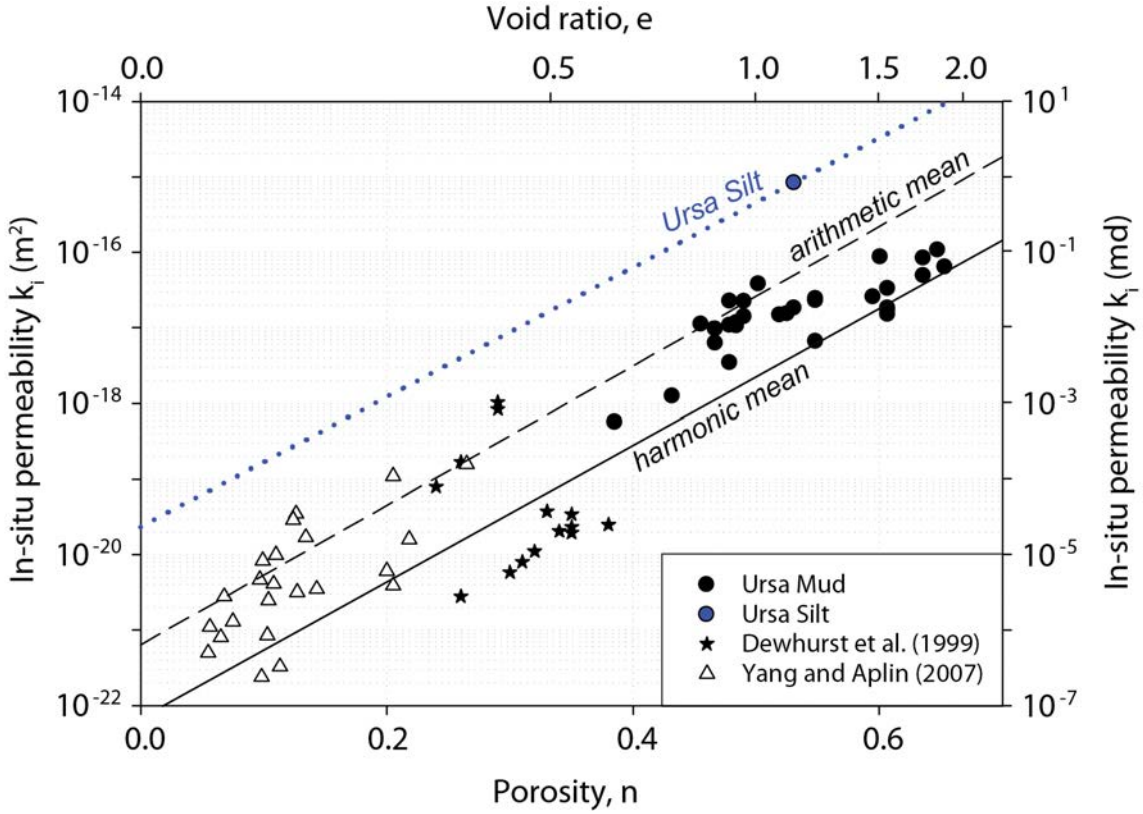

Figure 3.8: Comparison of *in-situ* Ursa permeabilities (Table 3.2) with previously published data (Dewhurst et al., 1999; Yang and Aplin, 2007). For Dewhurst et al. (1999) only direct permeability measurements are shown. For Yang and Aplin (2007) only vertical permeabilities are shown. Ursa Silt *in-situ* permeability is in blue, Ursa Mud *in-situ* permeabilities are in black.

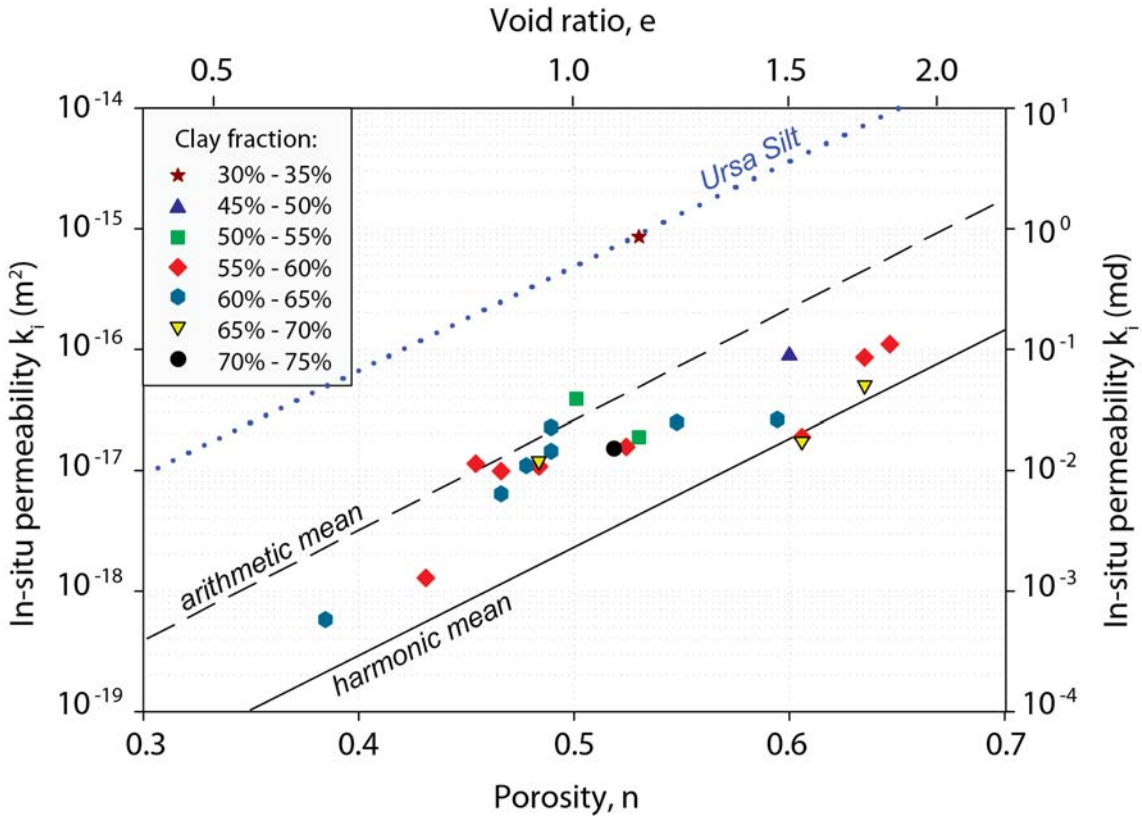

Figure 3.9: *In-situ* permeabilities versus porosity sorted by different clay fractions (< 2 μm) in 5% increments. Overlain are upper bound (arithmetic mean) and lower bound (harmonic mean) on experimental log-linear permeability – porosity relationships. *Note*: grain size analyses were measured by Sawyer et al. (2008) on a fraction of all specimens tested here (Table 3.1).

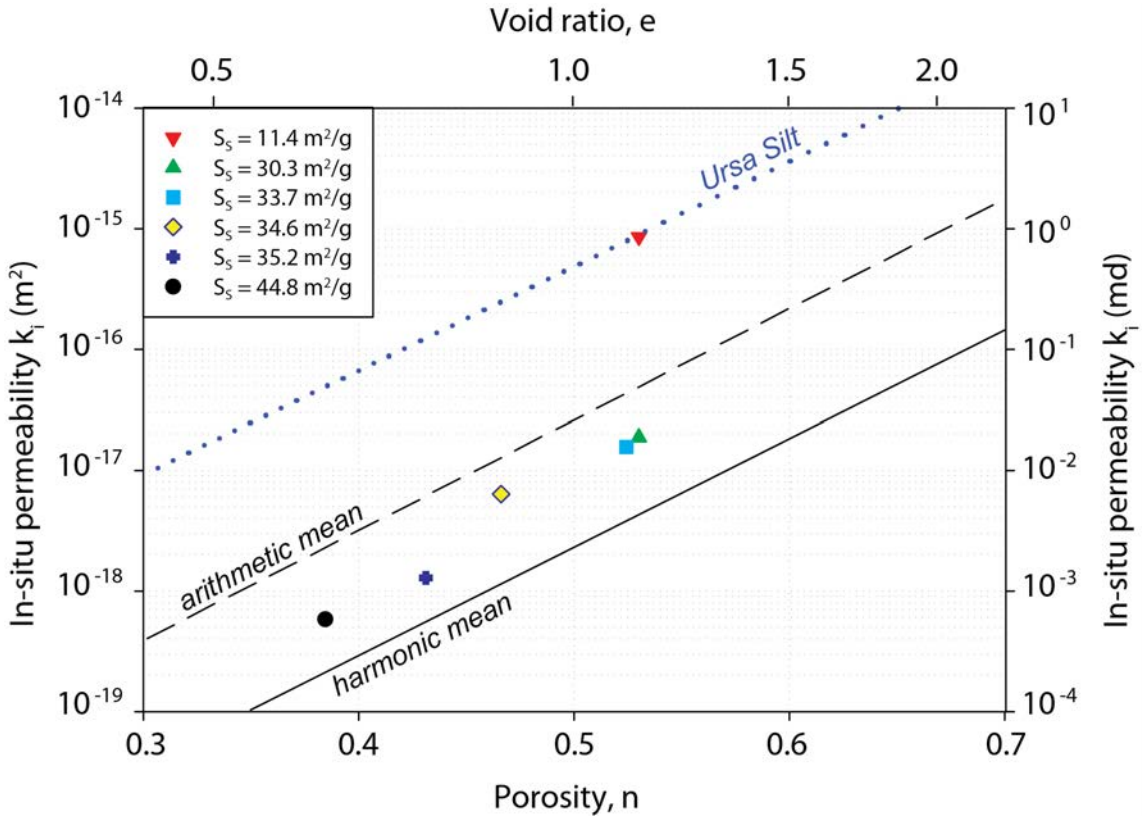

Figure 3.10: *In-situ* permeabilities versus porosity sorted by different specific surface areas. Overlain are upper bound (arithmetic mean) and lower bound (harmonic mean) on experimental log-linear permeability – porosity relationships. *Note*: specific surface area measurements were only performed on six specimens by using gas adsorption (Brunauer Emmett Teller (BET) method) (Table 3.3).

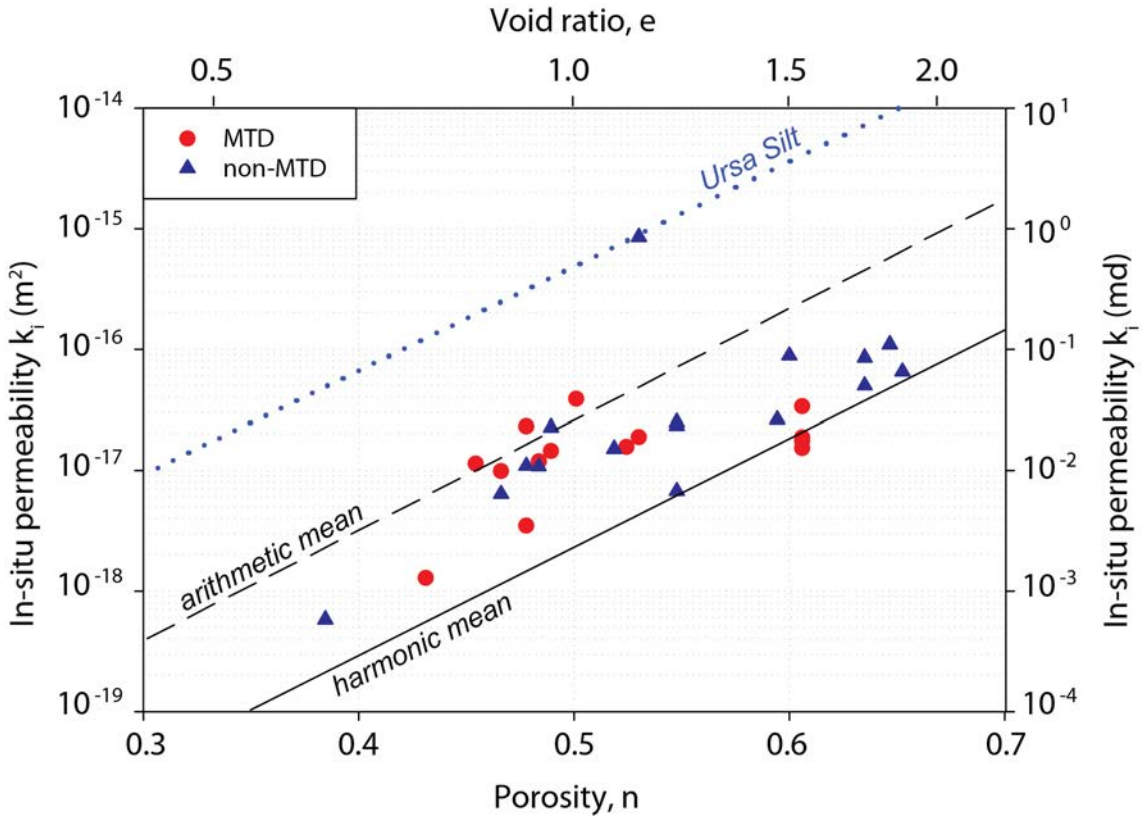

Figure 3.11: *In-situ* permeabilities versus porosity sorted by whether the sample comes from a mass transport deposit (MTD) or not (Table 3.2). Overlain are upper bound (arithmetic mean) and lower bound (harmonic mean) on experimental log-linear permeability – porosity relationships.

CRS #[a]	***Lithology***	***Hole-Core-Section***	***Depth[b] (mbsf)***	***S_S[c] (m^2/g)***
CRS 01, 02	Ursa Mud	U1324C-6H-3WR	304.04	34.6
CRS 05	Ursa Mud	U1324B-13H-7WR	117.26	33.7
CRS 06	Ursa Mud	U1324B-70X-6WR	578.15	44.8
CRS 07	Ursa Mud	U1324B-60X-2WR	476.84	35.2
CRS 08	Ursa Silt	U1324C-7H-1WR	406.02	11.4
CRS 807	Ursa Mud	U1324C-2H-4WR	105.26	30.3

Table 3.3: Specific surface area measurements of Ursa Mud and Ursa Silt samples.

[a] CRS #: constant-rate-of-strain (CRS) consolidation test number
[b] Depth: depth of the center of the whole core sample in mbsf
[c] S_S: measured by *Micromeritics* using Brunauer Emmett Teller (BET) method

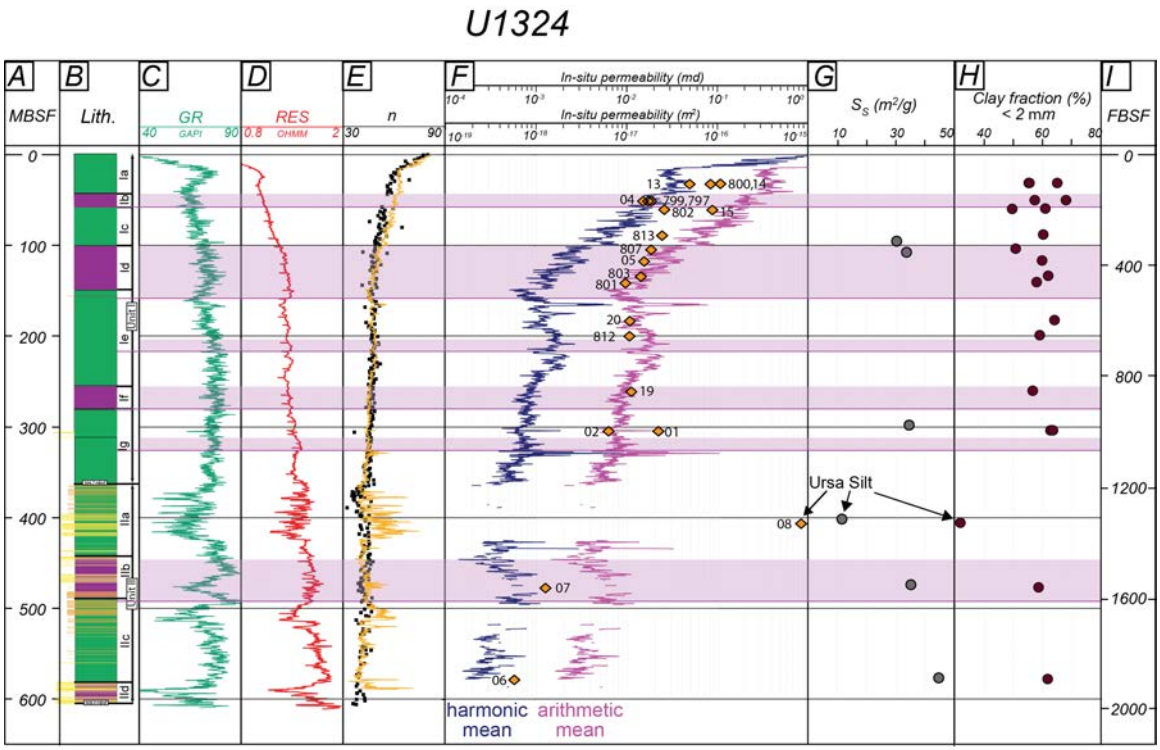

Figure 3.12: IODP Site U1324 (modified from Flemings et al., 2008). A) Depth in meters below seafloor (mbsf). B) Lithology, Mass Transport Deposits (MTDs) are delineated in purple, siltstones in orange, sandstones in yellow, and mudstones in green. C) Gamma Ray (GR) from logging-while-drilling (LWD) data. D) Resistivity (RES) log. E) Porosity interpreted from shipboard moisture and density (MAD) measurements (solid symbols). Porosity interpreted from logging-while-drilling (LWD) bulk density log assuming a grain density of 2740 kg/m^3 and water density of 1024 kg/m^3 (orange line). F) *In-situ* permeabilities are (symbols) and arithmetic mean and harmonic mean of permeability – porosity relationships. Both were calculated using log-derived porosity. Density log was filtered using the GR as an indicator of grain size. Numbers refer to CRS test number. G) Specific surface area measurements. H) Clay fraction < 2μm in percent (Sawyer et al., 2008). I) Depth in feet below seafloor (fbsf). Shaded areas across all logs represent locations of MTDs.

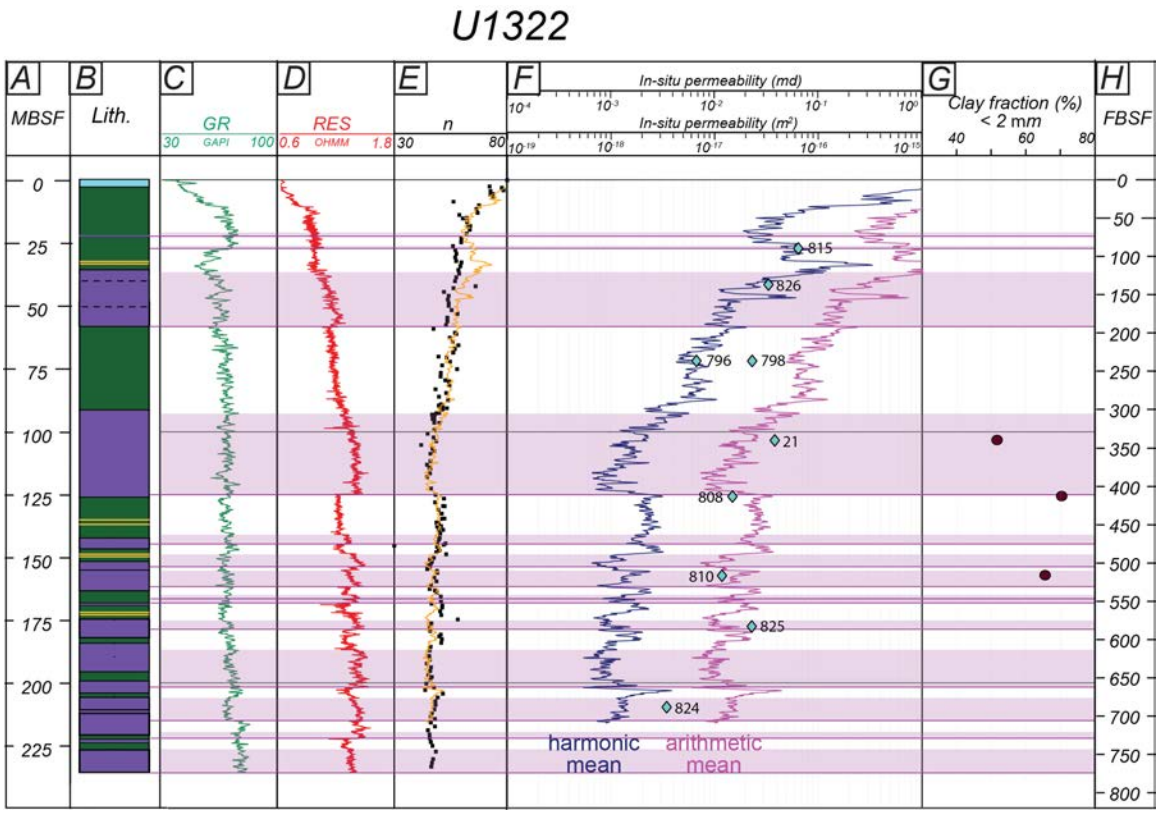

Figure 3.13: IODP Site U1322. A) Depth in meters below seafloor (mbsf). B) Lithology, Mass Transport Deposits (MTDs) are delineated in purple, siltstones in orange, sandstones in yellow, and mudstones in green. C) Gamma Ray (GR) from logging-while-drilling (LWD) data. D) Resistivity (RES) log. E) Porosity interpreted from shipboard moisture and density (MAD) measurements (solid symbols). Porosity interpreted from logging-while-drilling (LWD) bulk density log assuming a grain density of 2740 kg/m^3 and water density of 1024 kg/m^3 (orange line). F) *In-situ* permeabilities are (symbols) and arithmetic mean and harmonic mean of permeability – porosity relationships. Both were calculated using log-derived porosity. Density log was filtered using the GR as an indicator of grain size. Numbers refer to CRS test numbers. G) Clay fraction < 2μm in percent (Sawyer et al., 2008). H) Depth in feet below seafloor (fbsf). Shaded areas across all logs represent locations of MTDs.

Laboratory permeability measurements are often performed on small samples but then used in large-scale basin models. This requires an upscaling of permeability behavior from cm- scale to hundreds of meters scale. The most obvious way of upscaling permeability is to use an average, such as the arithmetic, geometric, or harmonic average (Tegnander and Gimse, 1998). Other possible upscaling techniques are described by Renard and LeLoc'h (1996). The 29 different Ursa Mud permeability-porosity relationships and *in-situ* permeabilities reflect the heterogeneity in the subsurface. High-permeability sand layers in a layered sediment column could, for example, significantly enhance the horizontal permeability (Davis and Fisher, 1994) but have very little impact on vertical fluid flow; thus, the effective vertical permeability of the layered sediment column is controlled by the low-permeability layers (Giambalvo et al., 2000). Therefore, the harmonic mean is a good indicator of upscaled vertical permeability and the arithmetic mean is a good indicator for upscaled horizontal permeability.

In order to estimate upward flow rates within the uppermost mudstone deposits at both drill sites (Site U1324 and U1322), I upscale the Ursa Mud *in-situ* permeabilities at both sites by obtaining the harmonic mean of *in-situ* permeabilities at each site, which are calculated from extrapolating the individual log-linear trend between permeability and porosity back to the *in-situ* porosity. The harmonic average of *in-situ* permeabilities is $7.45 \cdot 10^{-18}$ m^2 at Site U1324 and $1.69 \cdot 10^{-17}$ m^2 at Site U1322. Given the direct pore pressure measurements indicating an overpressure ratio of 0.7 at Site U1324 and 0.6 at Site U1322 (Flemings et al., 2008), I estimate pressure gradients of 6.25 MPa per kilometer and 5.0 MPa per kilometer at Site U1324 and U1322, respectively. Based on Darcy's Law I determine modern upward flow rates of 1.5 mm/yr at Site U1324 and 2.7 mm/yr at Site U1322. These flow rates are consistent with vertically upward flow rates of

approximately 4 mm/yr in Keathley Canyon, northern Gulf of Mexico and existing regional-scale models of flow in the northern Gulf of Mexico (Dugan, 2008).

Based on the estimated modern upward flow rates I can determine if the heat transport is diffusion- or advection-dominated. For thermal diffusion the Péclet number is defined as the product of velocity and system length divided by the thermal diffusivity. The thermal diffusivity is the thermal conductivity divided by the volumetric heat capacity. The Péclet number describes the ratio of rate of advection to rate of diffusion. In the context of transport of heat, the Péclet number is the product of Reynolds number and the Prandtl number. Given flow rate estimates of 1.5 mm/yr (Site U1324) and 2.7 mm/yr (Site U1322), an assumed volumetric heat capacity of $4.1796 \cdot 10^{-6}$ J/(m^3 K) (for water at 15 °C), thermal conductivities of 1.3 W/(m K) (Site U1324) and 1.15 W/(m K) (Site U1322), and a system length of 600 m (Site U1324) (Figure 3.12) and 230 m (Site U1322) (Figure 3.13), the Péclet numbers are $Pe = 9.1 \cdot 10^{-14}$ and $7.1 \cdot 10^{-14}$ at Sites U1324 and U1322, respectively. Results from both sites indicate strong diffusion-dominated transport.

The implication of these low Péclet numbers is that there is no heat transferred vertically by advection because the advective transport in the mudstones is negligible. Binh et al. (2009) obtained mean geothermal gradients from two-dimensional basin modeling of 1.83 °C/100m at Site U1324 and 2.3 °C/100m at Site U1322. They suggested that lateral flow of higher temperature fluids from regions at Site U1324 contribute to the slightly elevated geothermal gradient at Site U1322 compared to Site U1324. However, there is no heat transferred vertically at Site U1322. Therefore, other mechanisms must have caused higher temperature gradients at Site U1322 than at Site U1324.

3.6 CONCLUSIONS

I used 1D consolidation experiments to derive vertical permeability of mudstones from Sites U1324 and U1322 in the Ursa Basin, Gulf of Mexico. I find two type lithologies in the Ursa Basin: Ursa Mud and Ursa Silt. Both lithologies show a similar permeability decrease per given porosity change. However, vertical permeabilities at a given porosity vary over orders of magnitudes. *In-situ* permeabilities decrease similarly with porosity than the experimentally-derived permeability-porosity trend. Based on *in-situ* permeabilities and given pore pressure measurements I calculated upward flow rates between 1.5 and 2.7 mm/yr within the mudstones of Ursa Basin. These results have implications for drainage and fluid flow as well as solute and mass transport in the subsurface. Permeability is also an important control on the mechanics and morphology of accretionary wedges (Saffer and Bekins, 2002, 2006) as well as an key input parameters to basin models.

NOMENCLATURE

Symbol	*Name*	*Unit*
e	void ratio	dimensionless
g	acceleration due to gravity	m/s^2
H	specimen height	cm
H_0	initial specimen height	cm
K	hydraulic conductivity	m/s
k	intrinsic permeability	m^2
k_0	intercept in porosity vs. permeability relationship	m^2
k_i	*in-situ* permeability	m^2
n	porosity	dimensionless
n_i	*in-situ* porosity (derived from ρ_b)	dimensionless
Pe	Peclet number	dimensionless
S_s	specific surface area	m^2/g
$d\varepsilon/dt$	strain rate	strain/s
Δu	excess pore pressure	Pa
γ	slope in porosity vs. permeability relationship	m^2
γ_w	unit weight of water	$kg/m^2/s^2$
μ_w	dynamic fluid viscosity	Pa s
ρ_b	bulk density from logging-while-drilling (LWD)	kg/m^3
ρ_w	fluid density	kg/m^3

ACKNOWLEDGEMENTS

I thank the crew, technicians, and scientific staff of the *Joides Resolution* for their extraordinary efforts during Expedition 308. This work was funded by JOI/USSSP post cruise grant and by the Petroleum Research Fund (PRF #44476-AC8). This research used samples and data provided by the Integrated Ocean Drilling Program (IODP). IODP is sponsored by the U.S. National Science Foundation (NSF) and participating countries, administered by the Joint Oceanographic Institutions (JOI), Inc.

REFERENCES

Alt, J.C., and Teagle, D.A.H., 1999. The uptake of carbon during alteration of ocean crust. *Geochim. Cosmochim. Acta*, 63(10): 1,527-1,535.

Alt, J.C., 2004. Alteration of the upper oceanic crust: mineralogy, chemistry, and processes. *In* Davis, E.E., and Elderfield, H., eds., Hydrogeology of the Oceanic Lithosphere: Cambridge, Cambridge University Press, p. 706.

Anderson, R.N., and Hobart, M.A., 1976. The relation between heat flow, sediment thickness, and age in the Eastern Pacific. *J. Geophs. Res.*, 81: 2,968-2,989.

ASTM International, 2006. Standard test method for one-dimensional consolidation properties of saturated cohesive soils using controlled-strain loading (Standard D4186-06). *In* Annual Book of ASTM Standards (Vol. 04.08), ed., Soil and Rock (I): West Conshohocken, PA, American Society for Testing and Materials, p. 15.

Bickle, M., and Elderfield, H., 2004. Hydrothermal fluxes in a global context. *In* Davis, E.E., and Elderfield, H., eds., Hydrogeology of the Oceanic Lithosphere: Cambridge, Cambridge University Press, p. 706.

Binh, N.T.T., Tokunaga, T., Nakamura, T., Kozumi, K., Nakajima, M., Kubota, M., Kameya, H., and Taniue, M., 2009. Physical properties of the shallow sediments in late Pleistocene formations, Ursa Basin, Gulf of Mexico, and their implications for generation and preservation of shallow overpressures. *Marine and Petroleum Geology*, 26(4): 474-486, doi:10.1016/j.marpetgeo.2009.01.018.

Davis, E.E., and Fisher, A.T., 1994. On the nature and consequences of hydrothermal circulation in the Middle Valley sedimented rift: Inferences from geophysical and geochemical observations, Leg 139. *In* Motte, M.J., Davis, E.E., Fisher, A.T., and Slack, J.F., eds., Proceedings of the Ocean Drilling Program, Scientific Results, Volume 139: College Station, TX, Ocean Drilling Program, p. 695-717.

Davis, E.E., and Becker, K., 2004. Observations of temperature and pressure: constraints on ocean crustal hydrologic state, properties, and flow. *In* Davis, E.E., and Elderfield, H., eds., Hydrogeology of the Oceanic Lithosphere: Cambridge, Cambridge University Press, p. 706.

Dewhurst, D.N., Aplin, A.C., and Sarda, J.P., 1999. Influence of clay fraction on pore-scale properties and hydraulic conductivity of experimentally compacted mudstones. *Journal of Geophysical Research*, 104(B12): 29261-29274, doi:10.1029/1999JB900276.

Dugan, B., and Flemings, P.B., 2000. Overpressure and Fluid Flow in the New Jersey Continental Slope: Implications for Slope Failure and Cold Seeps. *Science*, 289(5477): 288-291.

Dugan, B., Flemings, P.B., Olgaard, D.L., and Gooch, M.J., 2003. Consolidation, effective stress, and fluid pressure of sediments from ODP Site 1073, US mid-

Atlantic continental slope. *Earth and Planetary Science Letters*, 215: 13-26, doi:10.1016/S0012-821X(03)00425-4.

Dugan, B., 2008. Fluid flow in the Keathley Canyon 151 Mini-Basin, northern Gulf of Mexico. *Marine and Petroleum Geology*, 25(9): 919-923, doi:10.1016/j.marpetgeo.2007.12.005.

Dugan, B., and Germaine, J., 2008. Near-seafloor overpressure in the deepwater Mississippi Canyon, northern Gulf of Mexico. *Geophysical Research Letters*, 35(L02304), doi:10.1029/2007GL032275.

Fisher, A.T., 2004. Rates of flow and patterns of fluid circulation. *In* Davis, E.E., and Elderfield, H., eds., Hydrogeology of the Oceanic Lithosphere: Cambridge, Cambridge University Press, p. 706.

Flemings, P.B., Behrmann, J.H., John, C.M., and Expedition 308 Scientists, 2006. Gulf of Mexico Hydrogeology, Proc. IODP, Volume 308: College Station, TX (Integrated Ocean Drilling Program Management International, Inc.), doi:10.2204/iodp.proc.308.2006.

Flemings, P.B., Long, H., Dugan, B., Germaine, J.T., John, C., Behrmann, J.H., Sawyer, D.E., and IODP Expedition 308 Scientists, 2008. Pore pressure penetrometers document high overpressure near the seafloor where multiple submarine landslides have occurred on the continental slope, offshore Louisiana, Gulf of Mexico. *Earth and Planetary Science Letters*, 269: 309-325, doi:10.1016/j.epsl.2007.12.005.

Garcia-Bengochea, I., Lovell, C.W., and Altchaeffl, A.G., 1979. Pore distribution and permeability of silty clays. *J. Geotech. Eng. Div., ASCE*, 105: 839-856.

Giambalvo, E.R., Fisher, A.T., Martin, J.T., Darty, L., and Lowell, R.P., 2000. Origin of elevated sediment permeability in a hydrothermal seepage zone, eastern flank of the Juan de Fuca Ridge, and implications for transport of fluid and heat. *J. Geophs. Res.*, 105(B1): 913-928.

Gibson, R.E., 1958. The progress of consolidation in a clay layer increasing in thickness with time. *Geotechnique*, 8: 171-182.

Grevemeyer, I., and Bartetzko, A., 2004. Hydrothermal aging of oceanic crust: inferences from seismic refraction and borehole studies. *In* Davis, E.E., and Elderfield, H., eds., Hydrogeology of the Oceanic Lithosphere: Cambridge, Cambridge University Press, p. 706.

Harris, R.N., and Chapman, D.S., 2004. Deep-seated oceanic heat flow, heat deficits, and hydrothermal circulation. *In* Davis, E.E., and Elderfield, H., eds., Hydrogeology of the Oceanic Lithosphere: Cambridge, Cambridge University Press, p. 706.

Harrison, W.J., and Summa, L.L., 1991. Paleohydrology of the Gulf of Mexico Basin. *American Journal of Science*, 291(2): 109-176.

Hermanrud, C., 1993. Basin modeling techniques - An overview. *In* Doré, A.G., ed., Basin Modelling: Advances and Applications, Norwegian Petroleum Society Spec. Publ. 3: New York, Elsevier, p. 1-34.

Jacobson, R.S., 1992. Impact of crustal evolution of changes of the seismic properties of the uppermost ocean crust. *Rev. Geophys.*, 30: 23-42.

Lambe, T.W., and Whitman, R.V., 1979. Soil Mechanics: SI Version. New York, Wiley, 553 p.

Leonards, G.H., 1962. Engineering Properties of Soils. New York, McGraw-Hill.

Long, H., Flemings, P.B., Germaine, J.T., Saffer, D.M., and Dugan, B., 2008. Data report: consolidation characteristics of sediments from IODP Expedition 308, Ursa Basin, Gulf of Mexico. *In* Flemings, P.B., Behrmann, J.H., and John, C.M., eds., Proc. IODP, Volume 308: College Station, TX, Proc. IODP, Sci. Results, p. 47, doi:10.2204/iodp.proc.308.204.2008.

Mitchell, J.K., 1993. Fundamentals of soil behavior. Hoboken, N.J., John Wiley & Sons.

Mottl, M.J., and Wheat, C.G., 1994. Hydrothermal circulation through mid-ocean ridge flanks: fluxes of heat and magnesium. *Geochim. Cosmochim. Acta*, 58: 2,225-2,237.

Orange, D.L., Saffer, D.M., Jeanjean, P., Al-Khafaji, Z., Humphrey, G., and Riley, G., 2003. Measurements and modeling of the shallow pore pressure regime at the Sigsbee Escarpment: Successful prediction of overpressure and ground-truthing with borehole measurements. *Leading Edge*, 22: 906-913.

Pittman, E.D., 1992. Relationship of porosity and permeability to various parameters derived from mercury injection-capillary pressure curves for sandstone. *AAPG Bulletin*, 76: 191-198.

Prior, D.B., and Suhayda, J.N., 1979. Application of infinite slope analysis to subaqueous sediment instability, Mississippi delta. *Engineering Geology*, 14(1): 1-10.

Prior, D.B., and Coleman, J.M., 1982. Active slides and flows in underconsolidated marine sediments on the slope of the Mississippi delta. *In* Saxov, S., and Nieuwenhuis, J.K., eds., Marine slides and other mass movements: New York, NY: Plenum Press, p. 21-49.

Renard, P., and LeLoc'h, G., 1996. A new upscaling technique for permeability of porous media: the simplified renormalization. *Comptes Rendus de l'Ac. des Sc. Serie II Fascicule*, 323(10): 859-864.

Robinson, R.G., and Allam, M.M., 1998. Effect of clay mineralogy on coefficient of consolidation. *Clays and Clay Minerals*, 46(5): 596-600, doi:10.1346/CCMN.1998.0460514.

Ruppel, C., Dickens, G.R., Castellini, D.G., Gilhooly, W., and Lizarralde, D., 2005. Heat and salt inhibition of gas hydrate formation in the northern Gulf of Mexico. *Geophys. Res. Lett.*, 32(L04605), doi:10.1029/2004GL021909.

Saffer, D.M., and Bekins, B.A., 2002. Hydrologic controls on the morphology and mechanics of accretionary wedges. *Geology*, 30(3): 271-274.

Saffer, D.M., and Bekins, B.A., 2006. An evaluation of factors influencing pore pressure in accretionary complexes: Implications for taper angle and wedge mechanics. *Journal of Geophysical Research*, 111(B04101), doi:10.1029/2005JB003990.

Sawyer, D.E., Flemings, P.B., Shipp, R.C., and Winker, C.D., 2007. Seismic geomorphology, lithology, and evolution of the late Pleistocene Mars-Ursa turbidite region, Mississippi Canyon area, northern Gulf of Mexico. *AAPG Bulletin*, 91(2): 215-234, doi:10.1306/08290605190.

Sawyer, D.E., Jacoby, R., Flemings, P.B., and Germaine, J.T., 2008. Data report: particle size analysis of sediments in the Ursa Basin, IODP Expedition 308 Sites U1324 and U1322, northern Gulf of Mexico. *In* Flemings, P.B., Behrmann, J.H., John, C.M., and the Expedition 308 Scientists, eds., Proc. IODP, Volume 308: College Station, TX, p. 20, doi:10.2204/iodp.proc.308.205.2008.

Sawyer, D.E., Flemings, P.B., Dugan, B., and Germaine, J.T., 2009. Retrogressive Failures Recorded in Mass Transport Deposits in the Ursa Basin, Northern Gulf of Mexico. *J. Geophs. Res.*, 114(B10102), doi: 10.1029/2008JB006159.

Scheidegger, 1974. The Physics of Flow Through Porous Media. Toronto, University of Toronto Press.

Schneider, F., Burrus, J., and Wolf, S., 1993. Modelling overpressures by effective-stress/porosity relationships in low-permeability rocks: Empirical artifice of physical reality? *In* Doré, A.G., ed., Basin Modelling: Advances and Applications, Norw. Pet. Soc. Spec. Publ. 3: New York, Elsevier, p. 333-341.

Schneider, J., Flemings, P.B., Dugan, B., Long, H., and Germaine, J.T., 2009. Overpressure and consolidation near the seafloor of Brazos-Trinity Basin IV, Northwest Deepwater Gulf of Mexico. *J. Geophys. Res.*, 114(B05102): 13, doi:10.1029/2008JB005922.

Sclater, J.G., Crowe, J., and Anderson, R.N., 1976. On the reliability of oceanic heat flow averages. *J. Geophs. Res.*, 81: 2,997-3,006.

Sharp, J.M., and Domenico, A., 1976. Energy transport in thick sequences of compacting sediment. *Geol. Soc. Am. Bull.*, 87: 390-400.

Smith, J.E., 1971. The dynamics of shale compaction and evolution of pore fluid pressure. *Math. Geol.*, 3: 239-263.

Spinelli, G.A., Giambalvo, E.R., and Fisher, A.T., 2004. Sediment permeability, distribution, and influence on fluxes in oceanic basement. *In* Davis, E.E., and

Elderfield, H., eds., Hydrogeology of the Oceanic Lithosphere: Cambridge, Cambridge University Press, p. 706.

Stein, C.A., and Stein, S., 1994. Comparison of plate and asthenospheric flow models for the thermal evolution of oceanic lithosphere. *Geophys. Res. Lett.*, 99: 3,081-3,095.

Tan, B., Germaine, J.T., and Flemings, P.B., 2006. Data Report: Consolidation and strength characteristics of sediments from ODP Site 1244, Hydrate Ridge, Cascadia continental margin. *In* Trehu, A.M., Bohrmann, G., Torres, M.E., and Colwell, F.S., eds., Proc. ODP, Sci. Results, Volume 204: College Station, TX.

Tegnander, C., and Gimse, T., 1998. Flow Simulations To Evaluate Upscaling of Permeability. *Math. Geol.*, 30(6): 717-731.

Terzaghi, K., and Peck, R.B., 1948. Soil mechanics in engineering practice. New York, Wiley.

Wheat, C.G., and Mottl, M.J., 2004. Geochemical fluxes through mid-ocean ridge flanks. *In* Davis, E.E., and Elderfield, H., eds., Hydrogeology of the Oceanic Lithosphere: Cambridge, Cambridge University Press, p. 706.

Yang, Y.L., and Aplin, A.C., 1998. Influence of lithology and compaction on the pore size distribution and modelled permeability of some mudstones from the Norwegian margin. *Marine and Petroleum Geology*, 15(2): 163-175, doi:10.1016/S0375-6742(03)00035-9.

Yang, Y.L., and Aplin, A.C., 2007. Permeability and petrophysical properties of 30 natural mudstones. *Journal of Geophysical Research*, 112(B03206), doi:10.1029/2005JB004243.

Chapter 4: Insights Into Pore-scale Controls on Mudstone Permeability Through Resedimentation Experiments[2]

ABSTRACT

At a given porosity, mudstone permeability increases by an order of magnitude for clay contents ranging from 57% to 36% clay (<2 μm). This increase in vertical permeability results from a dual-porosity system that develops through three mechanisms: (1) silt bridging preserves large pores, (2) stress bridges inhibit clay particle alignment, and (3) local clay particle compression within stress bridges alters pore size distribution. Uniaxial consolidation experiments on resedimented clay-silt mixtures illuminate how permeability varies as a function of clay fraction during burial. Backscattered electron microscope images show that silty mixtures have larger pores and fewer aligned clay particles than do more clay-rich mixtures. I describe the permeability of clay-silt mixtures with a geometric mean model. My method provides a promising framework for modeling of mudstone permeability as a function of clay fraction and porosity. How permeability and consolidation evolve during burial affects the ability of mudstones to seal CO_2 and hydrocarbons in the subsurface, how mudstones behave as gas reservoirs, and under what conditions mudstones will be overpressured. Dual-porosity systems have fundamentally different transient flow and solute transport behaviors.

[2]The full content of this chapter is published in *Geology* in 2011.

4.1 INTRODUCTION

Mudstones compose nearly 70% of the volume of sedimentary basins (Dewhurst et al., 1998), yet they are among the least studied of sedimentary rocks. Their low permeability and high compressibility contribute to overpressure around the world (Broichhausen et al., 2005). Mudstone reservoirs contain large volumes of natural gas that is now being economically extracted (Zoback et al., 2010). In addition, they serve as hydrocarbon traps and are employed as barriers in CO_2 sequestration and waste repositories. Despite their fundamental importance in geologic processes and as seals for anthropogenic-related storage, a systematic, process-based understanding of the interactions between porosity, compressibility, permeability, and pore size distribution in mudstones remains elusive (Dewhurst et al., 1999).

Three dominant approaches have been used to explain the permeability behavior of mudstones of different compositions during burial. First, permeability has been measured on core samples from natural mudstones. The influence of grain size distribution on permeability and pore size distribution has been studied on a variety of naturally occurring mudstones (Dewhurst et al., 1998, 1999; Yang and Aplin, 2007). Unfortunately, despite attempts to sample mudstone where only one parameter is changing (e.g. grain size), sample variability often results in more than one variable changing and consequently, there is large scatter in any porosity-permeability relationship developed. In addition, it is difficult to obtain sufficient numbers of samples for a systematic study.

A second approach is to predict permeability from either empirical relationships between permeability and porosity built from laboratory measurements (Tavenas et al., 1983; Yang and Aplin, 2010) or from theoretical models such as Hagen-Poiseuille (e.g. Yang and Aplin, 1998), Kozeny-Carman (e.g. Revil and Cathles, 1999; Chapuis and

Aubertin, 2003), or binary mixing models (e.g. Koltermann and Gorelick, 1995; Revil and Cathles, 1999). These studies generally rely on macroscale assumptions that relate bulk porosity to permeability and apply a correction factor related to either clay fraction or clay surface area. However, they try to develop an approximate, macroscale flow behavior that does not explore how the structure of mudstones controls flow.

The third approach, used here, is to study the permeability of laboratory-prepared mudstone samples. In this approach, composition is controlled and the behavior that results from changing only one parameter can be studied. Bandini and Sathiskumar (2009) determined the effects of silt content, void ratio, and effective confining stress on the permeability of sand-silt mixtures. Mondol et al. (2008a) explored the relationships between permeability and other petrophysical properties in smectite–kaolinite mixtures. Only three studies have examined permeability of materials with grain sizes comparable to those present in mudstones (Wagg and Konrad, 1990; Mondol et al., 2008b; Shafiee, 2008). However, these studies used binary grain size distributions.

I use resedimentation to study the permeability of mudstones of various grain size compositions. I admix silt-sized silica to a natural mudstone with a wide grain size distribution to describe the systematic variation of permeability with clay fraction. I use backscattered electron microscopy (BSE) on samples with a given stress path and stress level to address the relative change in packing and clay particle alignment associated with altering composition. Finally, I develop a new dual-porosity permeability model to describe the permeability of clay-silt mixtures with graded grain size distributions on the basis of clay content and porosity. The results are an important step toward developing a process-based understanding of the mechanics of consolidation and its consequent impacts on permeability.

4.2 SAMPLES AND EXPERIMENTAL TECHNIQUES

I use Boston Blue Clay (BBC), a mudstone that has been analyzed extensively in the geotechnical community (Sheahan, 1991; Santagata and Kang, 2007). It is an illitic glaciomarine clay (Kenney, 1964) composed of 57% clay-sized particles (<2 μm by mass) with a wide grain size distribution (BBC line, Figure 4.1A). Its mineralogic composition is dominated by illite + illite-smectite, muscovite, and trioctahedral mica, with lesser amounts of chlorite, hydrobiotite, and kaolinite. I admix silt-sized silica to dry BBC powder in five different mass ratios of BBC to silica: 100:00, 84:16, 75:25, 68:32, and 50:50. The resultant mixtures contain 57%, 52%, 48%, 44% and 36% clay, as determined by hydrometer analyses (Table 4.1, Figure 4.1A) (Standard D422-63, ASTM International, 2007). I then simulate natural sedimentation through a method called resedimentation (Sheahan, 1991; Santagata and Kang, 2007) (see Appendix 4): a sediment slurry is mixed at a particular water content and salinity and then uniaxially, incrementally loaded to a certain vertical effective stress (100 kPa in this study).

I derive vertical permeability using uniaxial, constant-rate-of-strain (CRS) consolidation experiments (Standard D4186-06, ASTM International, 2006) assuming linear soil theory. Specimens are consolidated to a maximum vertical effective stress of 2.4 MPa, which corresponds to a depth of ~250 m below the seafloor under hydrostatic conditions. During a CRS test, excess pore pressure builds up at the base of the specimen. The pressure difference between base and top of the sample, when coupled with strain rate, is used to calculate vertical permeability (ASTM International, 2006).

After the consolidation test, high-resolution BSE images are taken of subsamples of the CRS specimens on a field-emission scanning electron microscope (SEM). The samples are prepared using an argon-ion beam milling technique (Loucks et al., 2009),

% BBC : % Silt[a]	*% Clay*[b]	*Resed #*[c]	*CRS #*[d]	*GS #*[e]
100 : 00	57	Resed 017	CRS 046	GS 094
84 : 16	52	Resed 018	CRS 047	GS 096
75 : 25	48	Resed 019	CRS 048	GS 098
68 : 32	44	Resed 020	CRS 050	GS 100
50 : 50	36	Resed 021	CRS 051	GS 102
Silt[a]	10			GS 103

Table 4.1: Summary table of various tests performed on Boston Blue Clay (BBC) – silt mixtures.

[a] Silt: silt-sized silica (US MIN U SIL 40 purchased from US Silica)
[b] % Clay: clay fraction by mass measured in grain size analysis (for test number see this table, column 5)
[c] Resed #: resedimentation test number
[d] CRS #: constant-rate-of-strain (CRS) consolidation test number
[e] GS #: grain size analysis test number

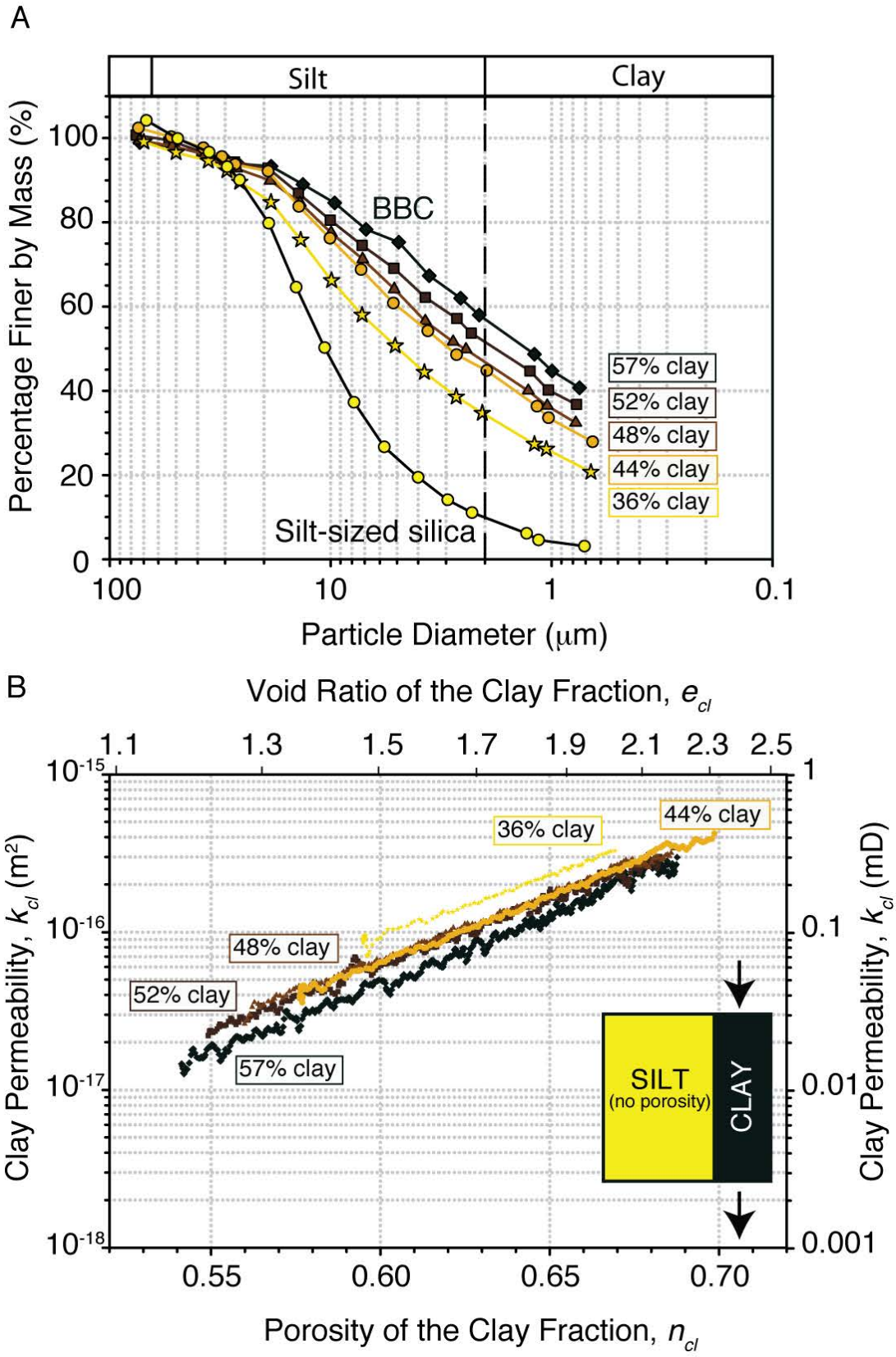
A
Silt
Clay
Percentage Finer by Mass (%)
100
80
60
40
20
0
BBC
57% clay
52% clay
48% clay
44% clay
36% clay
Silt-sized silica
100
10
1
0.1
Particle Diameter (μm)
B
Void Ratio of the Clay Fraction, e_{cl}
1.1
1.3
1.5
1.7
1.9
2.1
2.3
2.5
Clay Permeability, k_{cl} (m²)
10^{-15}
10^{-16}
10^{-17}
10^{-18}
36% clay
44% clay
48% clay
52% clay
57% clay
SILT
(no porosity)
CLAY
1
0.1
0.01
0.001
Clay Permeability, k_{cl} (mD)
0.55
0.60
0.65
0.70
Porosity of the Clay Fraction, n_{cl}

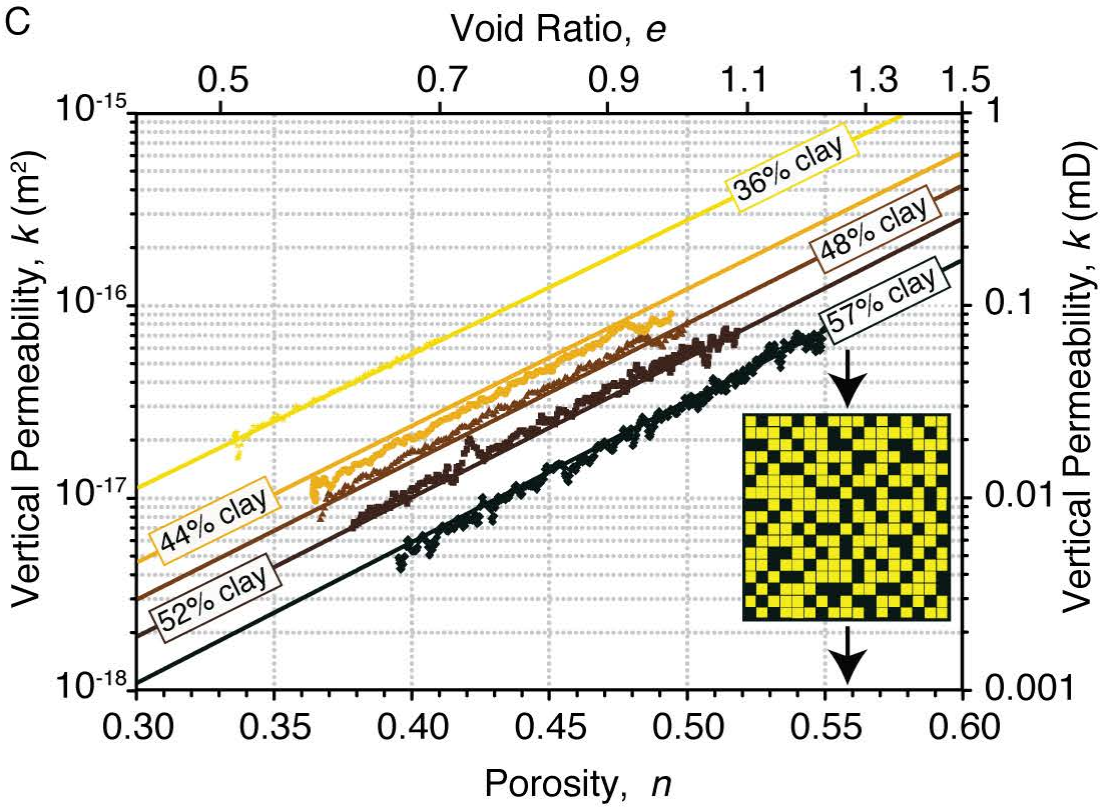

Figure 4.1: A: Grain size distributions for mixtures composed of natural Boston Blue Clay (BBC) and silt-sized silica (yellow circles) (Table 4.1). Diamonds = 57% clay (pure BBC), squares = 52% clay, triangles = 48% clay, orange circles = 44% clay, stars = 36% clay. Percentages represent fractions of solid mass <2 μm. B: Predicted clay permeabilities of BBC–silt mixtures derived from uniaxial constant-rate-of-strain consolidation tests (for test numbers see Table 4.1) using arithmetic mean model. Black = 57% clay (pure BBC), dark brown = 52% clay, light brown = 48% clay, orange = 44% clay, and yellow = 36% clay. C: Vertical permeabilities of BBC–silt mixtures derived from uniaxial constant-rate-of-strain consolidation tests (for test numbers see Table 4.1). Black = 57% clay (pure BBC), dark brown = 52% clay, light brown = 48% clay, orange = 44% clay, and yellow = 36% clay. Solid lines represent permeabilities predicted by our geometric mean model.

which avoids mechanical polishing and instead produces surfaces with only minor topographic variations using accelerated argon ions.

4.3 RESULTS

Vertical permeability (k) varies exponentially with porosity (n) in our clay-silt mixtures:

$$\log(k) = \gamma n + \log(k_0), \tag{4.1}$$

where γ is the slope and k_0 is the y intercept, ranging between 4 x 10^{-18} to 9 x 10^{-17} m^2 across all five clay fractions for porosities varying from 33% to 55% (Figure 4.1C). As clay content decreases, vertical permeability increases for a given porosity (Figure 4.1C). For example, permeability of the 57% clay sample is approximately one order of magnitude less than permeability of the 36% clay sample at any given porosity. A linear regression of porosity versus log permeability for each test shows that the y intercept (k_0), the projected permeability at a porosity of zero, increases linearly with decreasing clay content (Figure 4.1C; Table 4.1).

Electron microscopy illuminates the pore-scale effects that result from consolidation (Figure 4.2). The most clay-rich sample (57% clay) has small pores within the clay matrix (Figure 4.2A). The clay particles are aligned horizontally, perpendicular to the loading direction (vertical). In the intermediate mixture (48% clay), some larger pores are present near silt grains, and clay particles are aligned around silt grains (Figure 4.2B). The silt-rich sample (36% clay) has very large pores (5 μm) that are concentrated around silt grains, as well as zones of smaller pores more characteristic of the clay-rich sample (Figure 4.2C). In this silt-rich example, clay particles do not appear to be aligned

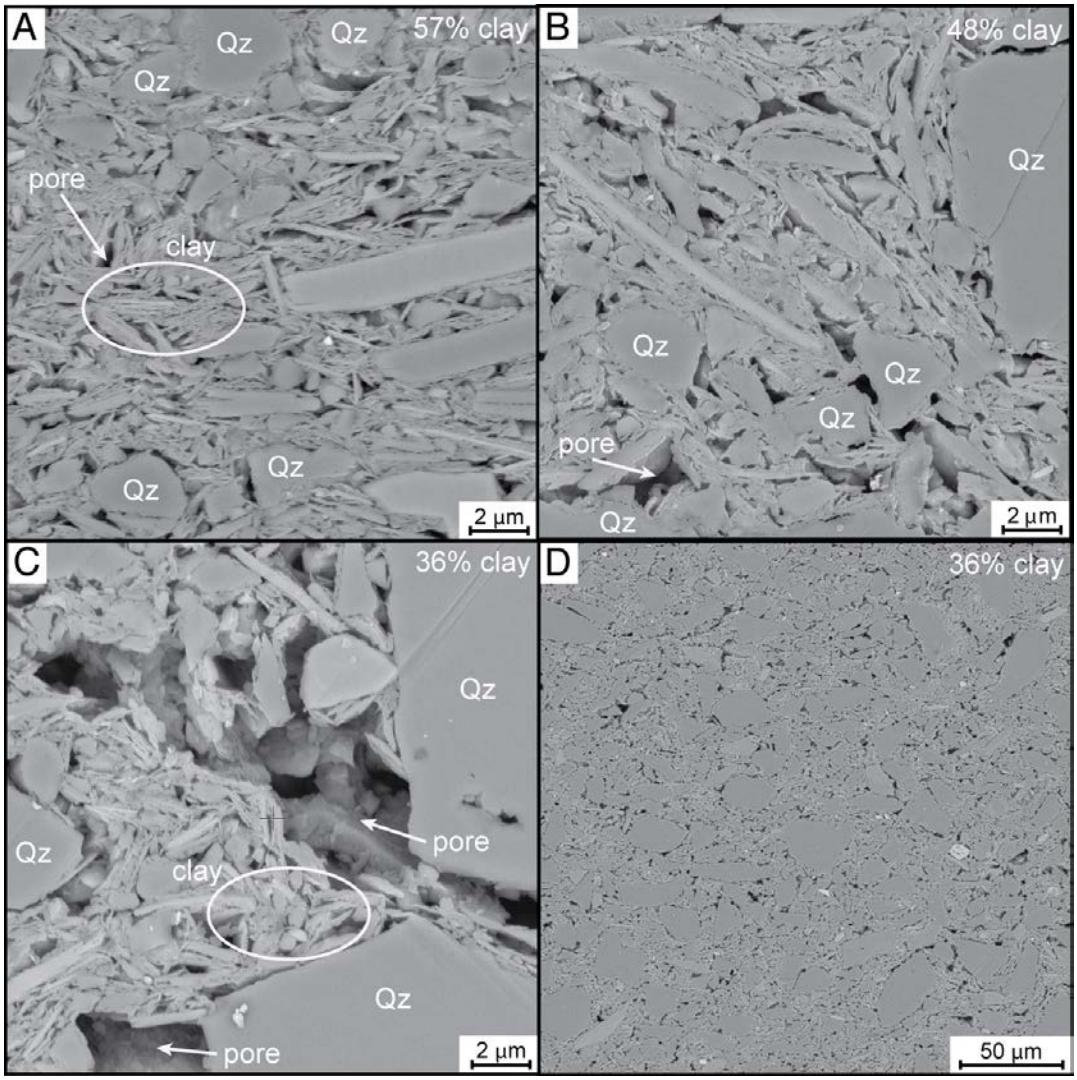

Figure 4.2: Backscattered electron microscope (BSE) images of Boston Blue Clay (BBC)–silt mixtures. Images were taken after consolidation to maximum vertical effective stress of 2.4 MPa. They represent vertical cross-section of sample. Qz-Quartz. A: 57% clay sample at magnification of 14,000 (SEM015_BSE_01_UT.tif). Circle indicates strong preferred alignment of clay particles. B: 48% clay sample at magnification of 14,000 (SEM017_BSE_03_UT.tif). C: 36% clay sample at magnification of 14,000 (SEM019_BSE_03_UT.tif). Circle indicates less preferential alignment of clay particles. Secondary electron image (see Figure A6.1 in Appendix 6) proves that darker spaces visible in BSE image are pore spaces. D: 36% clay sample at magnification of 1000 (SEM019_BSE_05_UT.tif).

far from silt grains; however, close to silt grains, clay particles show a preferred alignment around grains. A less-magnified view of the silt-rich sample shows that large pores are associated with clusters of silt grains (Figure 4.2D); grain-to-grain silt contacts (silt bridging) have preserved these large pores (Figure 4.3).

4.3.1 Permeability models

I initially assumed that the mudstone can be represented by a parallel zone model, which divides the clay and silt into individual layers. The effective vertical permeability (k_{eff}) is then described by an arithmetic mean model:

$$k_{eff} = cf_v(1-n)k_{cl} + \left[1 - cf_v(1-n)\right]k_{si}, \tag{4.2}$$

where cf_v is the fraction of the solid volume composed of clay-sized particles (<2 μm), which in combination with (1-n) represents the clay fraction with respect to the total volume. The subscripts cl and si are clay and silt, respectively. I then hypothesized that permeability of clay-silt mixtures is entirely controlled by a unique relationship between permeability of the clay fraction and its porosity. In this model, the only role of silt grains is to block flow. This system can be described as an impermeable fraction of zero porosity composed of silt grains and a permeable fraction composed of clay particles and all pore volume (Figure 4.1B, inset). Because the entire pore volume is in the clay fraction, flow is only controlled by porosity of the clay fraction (n_{cl}) (Figure 4.1B, inset), which is the void volume divided by the sum of the volumes of clay and voids. By assuming that silt has no porosity and is impermeable and combining equations 4.1 and 4.2 I find:

$$\log \frac{k_{eff}}{cf_v(1-n)} = \gamma_{cl} n_{cl} + \log(k_0^{cl}) . \quad (4.3)$$

The term on the left side is the effective permeability divided by the clay fraction of the total volume: it is the permeability of the clay-sized material alone, which I refer to as k_{cl}. If there is a unique relationship between permeability of the clay fraction and its porosity, then a semi-logarithmic plot of k_{cl} versus n_{cl} should collapse all data to a single line with a slope γ_{cl} and intercept k_0^{cl}. The data collapse considerably (Figure 4.1B); however, the 36% clay sample still has a permeability that is two times higher than the 57% clay sample at a given n_{cl} (Figure 4.1B). This suggests that the structure of the clay is altered by the presence of silt grains such that it is more permeable at a given n_{cl} for a lower clay content: there is interaction between the silt and clay.

A better approach is to assume that both the clay and silt fractions have porosity and contribute to flow. For example, in my silt-rich samples, large pores are present near clusters of silt grains, while outside of these areas, the pores are smaller and more homogeneous (Figure 4.2D). I model this system assuming that the mudstone is composed of randomly distributed clay domains with clay particles and small pores and silt domains with silt grains and large pores. The assumed random distribution of clay and silt domains can be observed in less magnified backscattered electron microscope images that show a better representation of the whole sample. Each domain has its own permeability–porosity relationship. Under these conditions, k_{eff} can be approximated by the geometric mean of the permeabilities of the clay and silt components:

$$k_{eff} = k_{cl}^{cf_v} \cdot k_{si}^{(1-cf_v)}, \quad (4.4)$$

where k_{cl} is the permeability of the clay domain and k_{si} is the permeability of the silt domain. By combining equations 4.1 and 4.4 and assuming that porosity in both domains is the same ($n = n_{cl} = n_{si}$) I find:

$$\log k_{eff} = \left[cf_v\gamma_{cl} + \left(1 - cf_v\right)\gamma_{si}\right]n + cf_v \log(k_0^{cl}) + \left(1 - cf_v\right)\log(k_0^{si}), \quad (4.5)$$

where the subscripts and superscripts cl and si are clay and silt, respectively. Equation 4.5 describes k_{eff} of a clay-silt mixture as a function of porosity by the permeability behavior of the two end members and knowledge of grain size (cf_v). I solve for the four unknown parameters with multivariable linear regression: $\log(k_0^{cl}) = -22.61$, $\gamma_{cl} = 8.15$, $\log(k_0^{si}) = -17.23$, and $\gamma_{si} = 6.43$. I then use equation 4.5 to predict permeabilities for the given clay fractions over the measured porosity range.

4.4 DISCUSSION

CRS experiments on resedimented material in combination with SEM images allow me to characterize how form, structure, and flow behavior of mudstones change with decreasing clay fraction. Silt bridges are more prevalent with decreased clay fraction, and this results in a network of force chains that redistribute the load; this preserves large pores during loading (e.g. Mueth et al., 1998) (Figures 4.2C and 4.2D). The clay particles within these large pores in the silt-rich samples are more loosely packed and protected from consolidation. As a result they undergo less alignment (circle, Figure 4.2C). In contrast, clay particles in clay-rich samples are more horizontally aligned due to grain size and density effects as well as flattening of elongated clay particles during consolidation (circle, Figure 4.2A). Clay particles are more consolidated where they are near silt grains within a force chain (Figures 4.2 and 4.3) and wrap around

silt grains (Figure 4.2B, top right corner); this results in a wider pore size distribution for a given porosity of the clay fraction for more silt-rich samples (Shafiee, 2008). The decreased alignment and the increased pore size distribution that results as clay fraction is decreased (Day-Stirrat et al., 2011) generate a less tortuous path for vertical flow; this results in an increase in permeability for a given porosity of the clay fraction.

I have captured this behavior with a dual-porosity model. One fraction of the sample is composed of a clay domain where small pores are homogeneously distributed within the matrix of strongly aligned clay particles and a few silt grains. The other fraction is composed of a silt domain where large pores are partially filled with other silt grains and clay particles. I assume that these domains are randomly distributed with the result that the effective permeability can be described as the geometric mean of its components.

The model provides a remarkably accurate prediction of the permeability variation with clay fraction (Figure 4.1C). This is true for permeability predictions over the constrained clay fractions. It still remains open how well the geometric mean model predicts permeabilities outside if this range, i.e. closer to the end-members (100% clay or 100% silt). This could be tested in the future by performing a consolidation test on the pure silt-sized silica that was added to the BBC in order to determine permeability-porosity relationship and compare with the permeability prediction based on the geometric mean model.

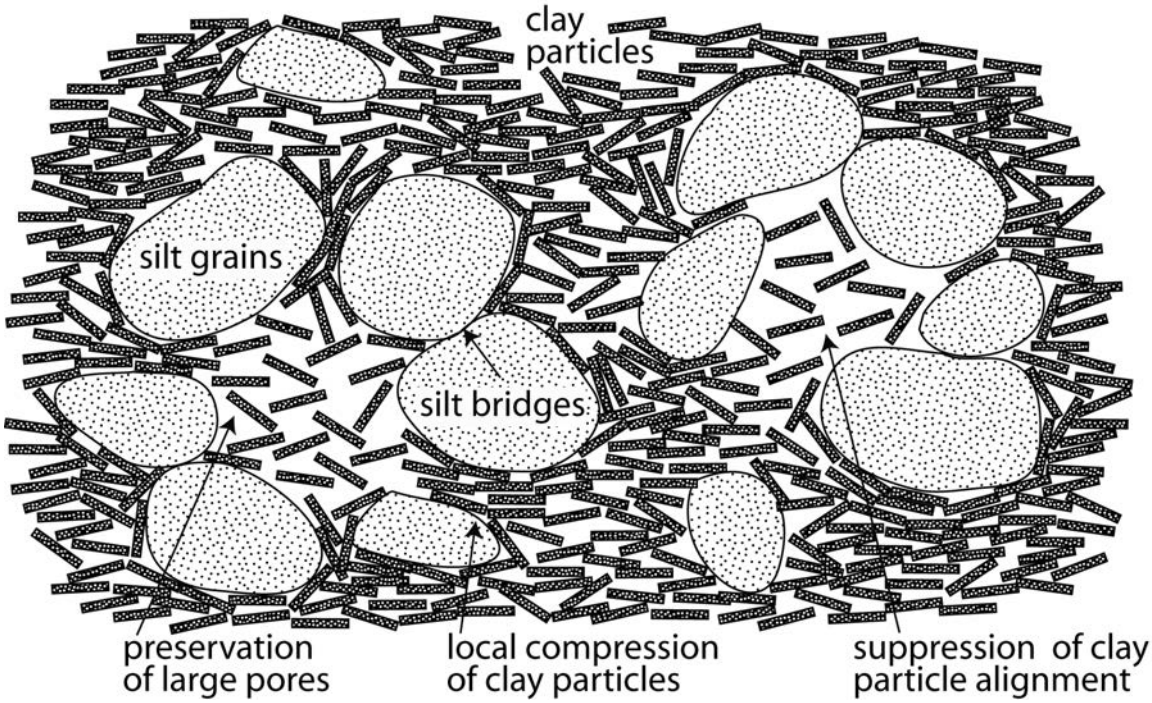

Figure 4.3: Three pore-scale mechanisms that contribute to dual-porosity structure. (1) silt bridging preserves large pores, (2) stress bridges inhibit horizontal clay-particle alignment, and (3) stress bridges enhance consolidation of clay matrix near silt grains, altering pore size distribution.

The model parameters (slope and intercept of end members) will vary with different mudstones depending on clay mineralogy, grain size distribution, and grain angularity. They can be determined if permeability is known from as few as two samples with different clay fractions. The model parameters depend on how the boundary between clay- and silt-sized particles is determined. In this study I use a clay-silt boundary at 2 μm as used by engineers. By using this division at 2 μm material that may not have physicochemical properties typical of clay minerals is knowingly included in the clay fraction while some clay minerals are included in the fine silt category (Hawkins and Pinches, 1992). In contrast, the sedimentological clay/silt boundary at 4 μm, which represents the upper limit of the size of particles that demonstrate cohesion, thus separating clay minerals from quartz grains, always results in non-clay minerals being present in the clay fraction (Hawkins and Pinches, 1992).

However, I find that if I define the clay-silt boundary as being at 4 μm as used by geologists/sedimentologists or if I define the fraction of clay solely by mineralogy (by X-ray diffraction), I predict permeability equally successfully. This means that my model is robust and produces very similar results if based on mineralogy, where mineralogy is often more common than grain size. For these examples, the modeled and measured permeabilities are on a 1:1 line with correlation coefficients of 0.96 and 0.99, respectively (see Figure A6.2 and Table A6.1 in Appendix 6), compared to a correlation coefficient of 0.96 for a clay-silt boundary at 2 μm. The success of the model prediction when based on mineralogy suggests that it will be possible to directly predict permeability behavior from *in-situ* logging because these tools determine mineralogy more easily than grain size distribution.

I made the assumption that the porosity of the clay fraction is equal within the clay and silt domains because it simplified my final effective permeability equation

(Equation 4.5) and because it proved remarkably effective. This simplification could be removed in the future if a methodology is developed to independently interpret the porosity of the clay and silt components.

My methodology is fundamentally different from most previous approaches used to predict permeability in mudstones. For example, some of the most influential papers on the impact of composition and grain size on mudstone permeability used packing models to determine a representative porosity and grain diameter, and these are then applied in Kozeny-Carmen-type equations (e.g. Revil and Cathles, 1999; Kolterman and Gorelick, 1995). Others relied on empirical correlations of permeability with clay fraction and porosity (e.g. Yang and Aplin, 2010). These approaches seek to approximate the permeability behavior of mudstones with a single macroscale relationship. In contrast, I have recognized that the microscale structure of mudstones controls the macroscale permeability and I have incorporated this structure (albeit simply) in my permeability model. This step is important because it opens the path toward a more complete understanding of flow behavior in mudstones. Dual-porosity systems will have complex interactions between the two domains and affect water flow and solute transport in mudstones by creating preferential flow (Gerke and Van Genuchten, 1993). This will affect leaching of fertilizer and pesticides from agricultural field soils, prediction of solute arrival times, and flow behavior during gas production.

4.5 CONCLUSIONS

I find that mudstone permeability increases with decreasing clay fraction due to the development of a dual-porosity system, where large pores between silt grains that act as high permeability pathways are preserved in addition to small pores within the clay matrix. Permeability of clay-silt mixtures can be effectively described by a geometric mean model. My results are an important step toward developing a model to predict mudstone behavior during burial that can be applied to carbon sequestration, hydrocarbon trapping, and an understanding of gas-shale behavior.

ACKNOWLEDGEMENTS

The University of Texas GeoFluids Consortium (supported by 12 energy companies) and the Schlanger Ocean Drilling Fellowship from the Consortium for Ocean Leadership provided funding. We thank Robert M. Reed for taking the backscattered electron images. This paper is The University of Texas Institute for Geophysics contribution #2383. Publication authorized by the Director, Bureau of Economic Geology, The University of Texas.

REFERENCES

ASTM International, 2006, Standard test method for one-dimensional consolidation properties of saturated cohesive soils using controlled-strain loading (Standard D4186-06), *in* Annual Book of ASTM Standards (Vol. 04.08), ed., Soil and Rock (I): West Conshohocken, PA, American Society for Testing and Materials, p. 15, doi:10.1520/D4186-06.

ASTM International, 2007, Standard test method for particle-size analysis of soils (Standard D422-63R07), *in* Annual Book of ASTM Standards (Vol. 04.08), ed., Soil and Rock (I): West Conshohocken, PA, American Society for Testing and Materials, p. 10-17, doi:10.1520/D0422-63R07.

Bandini, P., and Sathiskumar, S., 2009, Effects of Silt Content and Void Ratio on the Saturated Hydraulic Conductivity and Compressibility of Sand-Silt Mixtures: Journal of Geotechnical and Geoenvironmental Engineering, v. 135, no. 12, p. 1976-1980, doi:10.1061/(ASCE)GT.1943-5606.0000177.

Broichhausen, H., Littke, R., and Hantschel, T., 2005, Mudstone compaction and its influence on overpressure generation, elucidated by a 3D case study in the North Sea: International Journal of Earth Sciences, v. 94, no. 5-6, p. 956-978, doi:10.1007/s00531-005-0014-1.

Chapuis, R.P., and Aubertin, M., 2003, On the use of the Kozeny-Carman equation to predict the hydraulic conductivity of soils: Canadian Geotechnical Journal, v. 40, p. 616-628, doi:10.1139/T03-013.

Day-Stirrat, R.J., Schleicher, A.M., Schneider, J., Flemings, P.B., Germaine, J.T., and van der Pluijm, B.A., 2011, Preferred orientation of phyllosilicates: Effects of composition and stress on resedimented mudstone fabric: Journal of Structural Geology, v. 33, no. 9, p. 1347-1358, doi:10.1016/j.jsg.2011.06.007.

Dewhurst, D.N., Aplin, A.C., Sarda, J.P., and Yang, Y.L., 1998, Compaction-driven evolution of porosity and permeability in natural mudstones: An experimental study: Journal of Geophysical Research, v. 103, no. B1, p. 651-661, doi:10.1019/97JB02540.

Dewhurst, D.N., Aplin, A.C., and Sarda, J.P., 1999, Influence of clay fraction on pore-scale properties and hydraulic conductivity of experimentally compacted mudstones: Journal of Geophysical Research, v. 104, no. B12, p. 29261-29274, doi:10.1029/1999JB900276.

Gerke, H.H., and Van Genuchten, M.T., 1993, A dual-porosity model for simulating the preferential movement of water and solutes in structured porous media: Water Resources Research, v. 29, no. 2, p. 305-319, doi:10.1029/92WR02339.

Hawkins, A.B. and Pinches, G.M., 1992, Engineering description of mudrocks: Quaterly Journal of Engineering Geology, v. 25, p. 17-30.

Kenney, T.C., 1964, Sea-level movements and the geologic histories of the post-glacial marine soils at Boston, Nicolet, Ottawa and Oslo: Geotechnique, v. 14, no. 3, p. 203-230, doi:10.1680/geot.1964.14.3.302.

Koltermann, C.E., and Gorelick, S.M., 1995, Fractional packing model for hydraulic conductivity derived from sediment mixtures: Water Resources Research, v. 31, no. 12, p. 3283-3297, doi:10.1029/95WR02020.

Loucks, R.G., Reed, R.M., Ruppel, S.C., and Jarvie, D.M., 2009, Morphology, genesis, and distribution of nanometer-scale pores in siliceous mudstones of the Mississippian Barnett Shale: Journal of Sedimentary Research, v. 79, no. 12, p. 848-861, doi:10.2110/jsr.2009.092.

Mondol, N.H., Bjørlykke, K., and Jahren, J., 2008a, Experimental compaction of clays: relationship between permeability and petrophysical properties in mudstones: Petroleum Geoscience, v. 14, p. 319-337, doi:10.1144/1354-079308-773.

Mondol, N.H., Fawad, M., Jahren, J., and Bjørlykke, K., 2008b, Synthetic mudstone compaction trends and their use in pore pressure prediction: First Break, v. 26, p. 43-51, doi:10.3997/1365-2397.2008018.

Mueth, D.M., Jaeger, H.M., and Nagel, S.R., 1998, Force distribution in a granular medium: Physical Review E, v. 57, p. 3164-3169, doi:10.1103/PhysRevE.57.3164.

Revil, A., and Cathles, L.M., 1999, Permeability of shaly sands: Water Resources Research, v. 35, no. 3, p. 651-662, doi:10.1029/98WR02700.

Santagata, M.C., and Kang, Y.I., 2007, Effects of geologic time on the initial stiffness of clays: Engineering Geology, v. 89, p. 98-111, doi: 10.1016/j.enggeo.2006.09.018.

Shafiee, A., 2008, Permeability of compacted granule - clay mixtures: Engineering Geology, v. 97, p. 199-208, doi:10.1016/j.enggeo.2008.01.002.

Sheahan, T.C., 1991, An experimental study of the time-dependent undrained shear behavior of resedimented clay using automated stress path triaxial equipment [Ph.D. thesis]: Cambridge, Massachusetts Institute of Technology.

Tavenas, F., Jean, P., Leblond, P., and Leroueil, S., 1983, The permeability of natural soft clays. Part 2: Permeability characteristics: Canadian Geotechnical Journal, v. 20, p. 645-660, doi:10.1139/t83-073.

Wagg, T.B., and Konrad, J.-M., 1990, Index properties of clay-silt mixtures, 43rd Canadian Geotechnical Conference, Volume 2: Québec City, Canada, p. 705-710.

Yang, Y., and Aplin, A.C., 2010, A permeability-porosity relationship for mudstones: Marine and Petroleum Geology, v. 27, p. 1692-1697, doi:10.1016/j.marpetgeo.2009.07.001.

Yang, Y.L., and Aplin, A.C., 1998, Influence of lithology and compaction on the pore size distribution and modelled permeability of some mudstones from the Norwegian margin: Marine and Petroleum Geology, v. 15, no. 2, p. 163-175, doi:10.1016/S0375-6742(03)00035-9.

Yang, Y.L., and Aplin, A.C., 2007, Permeability and petrophysical properties of 30 natural mudstones: Journal of Geophysical Research, v. 112, no. B03206, doi:10.1029/2005JB004243.

Zoback, M.D., Kitasei, S., and Copithorne, B., 2010, Addressing the environmental risks from shale gas development: Briefing Paper 1: Washington, D.C., Worldwatch Institute, 19 p.

Chapter 5: Deformation and Transport Processes of Resedimented Mudstones From the Shikoku Basin, IODP Expedition 322

ABSTRACT

I use uniaxial consolidation experiments on resedimented samples of mudstones from offshore Japan to analyze the permeability and compressibility evolution during consolidation for natural mudstones with varying grain size distribution and to develop a predictive coupled permeability-compressibility model. I prepare mixtures composed of varying proportions of silt-sized silica and a marine mudstone from Site C0011 drilled seaward of the Nankai Trough during Integrated Ocean Drilling Program (IODP) Expedition 322. At a given porosity, vertical permeability increases by two orders of magnitude and compression index decreases from 0.36 to 0.24 for sediment mixtures with 59% to 34% clay (<2 μm) by mass. Backscattered electron microscope images show that pores in clay-rich samples are elongated and crescent-shaped whereas pores in silt-rich samples are larger, jagged pores that are preserved in compaction shadows and which largely contribute to higher permeability. I develop a generalized model to describe the evolution of mudstone permeability, compressibility, and hence hydraulic diffusivity (coefficient of consolidation) with vertical effective stress and as a function of grain size during burial. Understanding how compressibility and permeability of marine mudstones evolve during burial is important in order to constrain key input parameters for basin models such as porosity – effective stress and permeability – porosity relationships and to improve pore pressure predictions as well as predictions of morphology, geometry, and pore fluid pressures in thrust belt systems.

5.1 INTRODUCTION

Mudstones comprise about 60 – 70% of the basin-fill in sedimentary basins. Most hydrocarbon reserves are found in sedimentary basins (Vasseur et al., 1995). A better understanding of deformation and fluid flow in mudstones is fundamental for the identification and exploration of petroleum reserves. The low permeability and high compressibility of mudstones contribute to overpressure around the world (Broichhausen et al., 2005). In addition, mudstones are employed as barriers in CO_2 sequestration and waste repositories.

Researchers have tried to understand and predict mechanical compression of mudstones for decades. Mondol et al. (2007) compiled the large variation in compression trends of mudstones and shales. The evolution of porosity with depth is mostly described by exponential or power law functions, which are empirical. Perhaps the best known example was presented by Athy (1930). However, several published results have shown that constants in these empirical relationships may vary over an order of magnitude for different mudstones. A more robust approach was developed in the field of soil mechanics based on Terzaghi's (1925) principle of effective stress; this approach assumes that mechanical compression of soils and sediments is driven only by effective stress on the sediment's solid matrix (Smith, 1971). This approach, even though developed for civil engineering purposes in the shallow subsurface, applies reasonably well to mudstones from greater depth if they are not highly affected by diagenesis.

Compression behavior, or the relation of stress to strain, is affected by grain size and mineralogy. Compression coefficients, which describe the decline in porosity for a given increase in effective stress, are related to liquid limit and liquid limit, in turn, correlates with grain size (Skempton, 1970; Burland, 1990; Aplin et al., 1995; Chandler, 2000; Yang and Aplin, 2004).

Intact cores as well as laboratory-prepared samples have been used to analyze compression and permeability behavior of mudstones. Dewhurst et al. (1998; 1999) and Yang and Aplin (2007) studied the influence of grain size distribution on permeability and pore size distribution on a variety of naturally occurring mudstones. Others used synthetically prepared sediment mixtures to determine the effects of silt content, void ratio, and effective confining stress on permeability (Mondol et al., 2008; Bandini and Sathiskumar, 2009). However, these studies used synthetic materials with bimodal grain size distributions. The only two studies that used laboratory-prepared but natural mudstones, with a wide grain size distribution are Clennell et al. (1999) and Schneider et al. (2011). Clennell et al. (1999) studied the permeability anisotropy of a remolded natural clay from the Chile Triple Junction accretionary complex. In contrast to the single natural mudstone data set from Clennell et al. (1999), Schneider et al. (2011) systematically prepared five mixtures composed of varying fractions of Boston Blue Clay and silt to study the grain size effect on permeability.

Here, I follow our approach (Schneider et al., 2011) to prepare natural mudstone samples in the laboratory by using the resedimentation method (Sheahan, 1991; Santagata and Kang, 2007) and adding silt-sized silica to the mudstone in varying proportions. But instead of using a glacial clay like Boston Blue Clay I use a mudstone with a wide grain size distribution and a large smectite content from a deep marine continental margin seaward of the deformation front. The high smectite content has a large control on the compression and permeability behavior. A marine, deepwater mudstone is more directly applicable to pore pressure predictions and basin modeling than a glacial clay.

I prepare the marine mudstone samples using a method called resedimentation as described by Schneider et al. (2011). This approach allows me to prepare homogenous and undisturbed samples in order to systematically study the compression and

permeability behavior of marine mudstones. There are more and more data sets that relate variations in sedimentological and mineralogical properties of mudstones to variations in compaction parameters. Aplin et al. (1995) noticed that systematic studies such as Vasseur et al. (1995) are important for determining fundamental rheological properties of mudstones. Vasseur et al. (1995) compacted reworked kaolinite samples under various loads in oedometric conditions and performed microscopic and macroscopic measurements. Among those were transmission electron microscopy, mercury porosimetry, specific surface area, hydraulic and thermal conductivity. Their goal was to qualitatively and quantitatively understand behavior of kaolinite with respect to parameters such as permeability, porosity, mechanical and thermal properties. However, Vasseur et al. (1995) only considered kaolinite and not more complex mineralogies that are found in nature.

Here I ad-mix silt-sized silica in varying proportions to a natural, marine mudstone from offshore Japan (hereafter called Nankai mudstone) to describe the systematic variation of permeability and compressibility with clay fraction. I then use backscattered electron microscope images to analyze the microstructure and address the relative change in clay particle alignment associated with altering composition. Finally, I develop a new, coupled compressibility – permeability model that predicts porosity, permeability, coefficient of volume compressibility, and coefficient of consolidation of any Nankai– silt mixture as a function of clay fraction and vertical effective stress or depth if pore fluid pressures are known.

5.2 GEOLOGIC SETTING

The Shikoku Basin is located southwest of Japan and has been target for several Integrated Ocean Drilling Program (IODP) expeditions that are part of the Nankai Trough Seismogenic Zone Experiment (NanTroSEIZE) project. This study focuses on the IODP Expedition 322, which sampled and logged the incoming sedimentary strata and uppermost igneous basement of the Shikoku Basin, seaward of the Nankai Trough (Underwood et al., 2010). The expedition was aimed at understanding the initial pre-subduction conditions because the down-dip evolution of the initial properties of the sediment is what ultimately changes slip behavior along the plate interface from aseismic to seismic (Vrolijk, 1990; Hyndman et al., 1997; Moore and Saffer, 2001). Two sites were drilled during Expedition 322 along the Kumano Transect: Site C0011 on the northwestern flank of the bathymetric high called Kashinosaki Knoll (Figure 5.1) and Site C0012 near the crest of the seamount (Figure 5.1, 5.2). I only show Site C0011.

During the early to middle Miocene, the Shikoku Basin formed as part of the Philippine Sea plate (Okino et al., 1994; Kobayashi et al., 1995) which is currently moving toward the northwest beneath the Eurasian plate (Figure 5.2), roughly orthogonal to the axis of the Nankai Trough, at a rate of ~4 to 6 cm yr^{-1} (Seno et al., 1993; Miyazaki and Heki, 2001) (Figure 5.1). Deposits within the Shikoku Basin and the overlying Quaternary trench wedge are actively accreting at the deformation front (Figure 5.2) (Tobin et al., 2009).

At Site C0011, measurement-while-drilling (MWD) and logging-while-drilling (LWD) data was collected at the end of Expedition 319 in Hole C0011A while a 536 m thick succession was cored in Hole C0011B during Expedition 322. The Shikoku Basin facies consists of three sub facies. Coring started at 340 mbsf, and thus the shallow Lithologic Unit I, which is composed of hemipelagic mud and thin volcanic ash beds of

the upper Shikoku Basin facies, was not cored during Expedition 322. However, it was cored during Expedition 333. The cored succession below the upper Shikoku Basin facies includes middle Shikoku Basin facies consisting of volcaniclastic and muddy turbidites as well as mass transport deposits and hemipelagic sediments, lower Shikoku Basin hemipelagic facies, lower Shikoku Basin turbidite facies, and volcaniclastic-rich facies. The age at the bottom of the cored succession is poorly constrained within the range of middle Miocene (~14.0 Ma). The igneous basement lies at ~1050 mbsf.

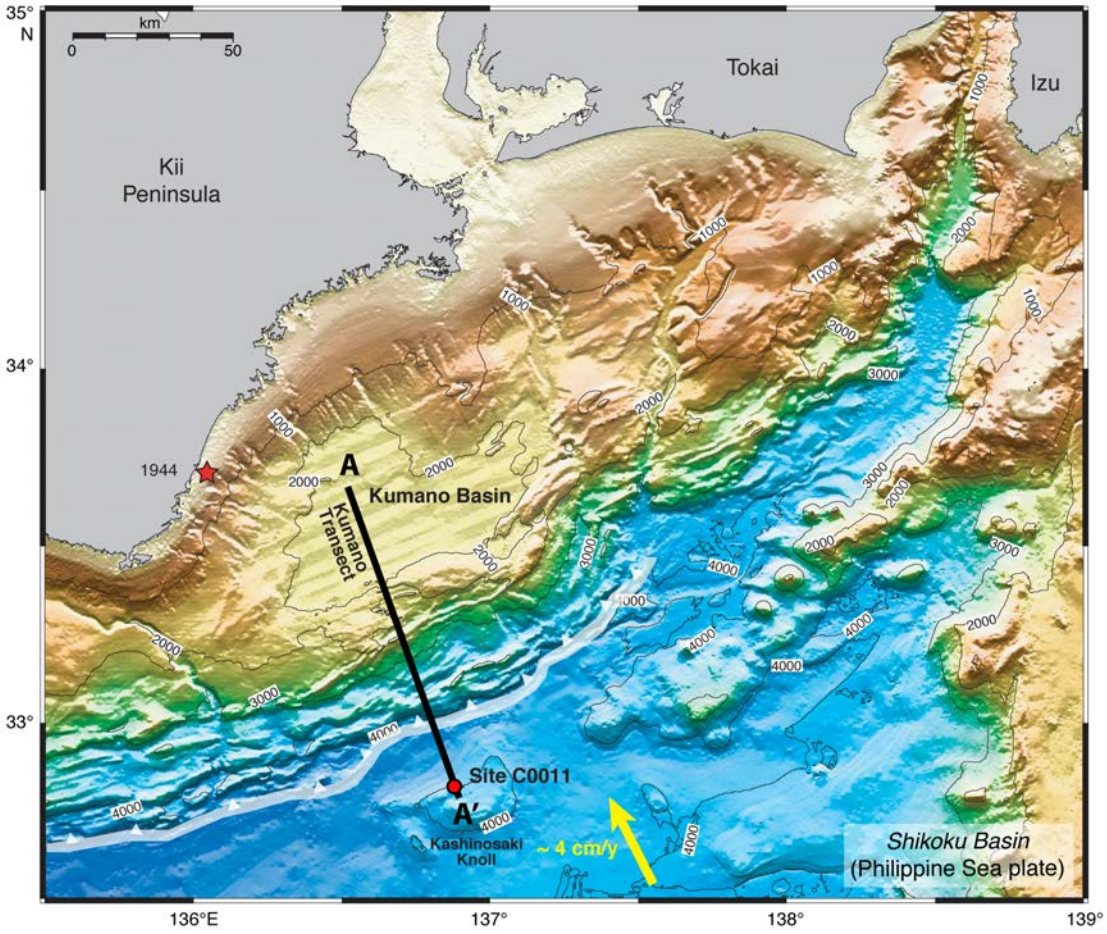

Figure 5.1: Bathymetry map with IODP Site C0011 drilled during IODP Expedition 322 (after Underwood et al., 2009). Black line indicates seismic line from Kumano Basin to Kashinosaki Knoll (A to A') in the Shikoku Basin as shown in Figure 5.2. White transparent line indicates deformation front. Arrow shows convergence vector between Philippine Sea plate and Japanese Islands (Eurasian plate).

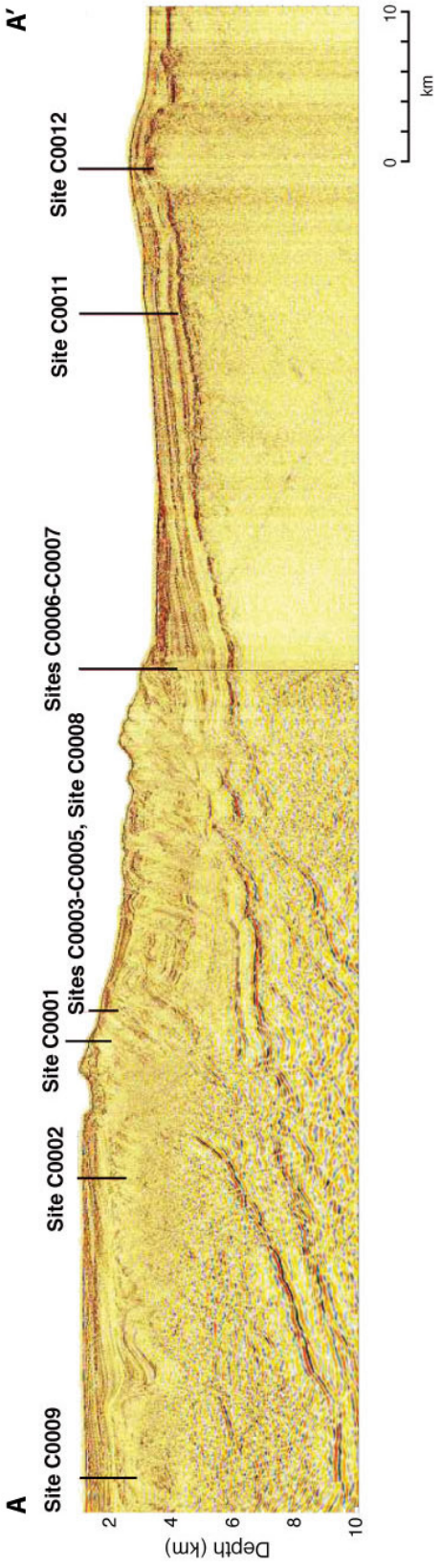

Figure 5.2: Spliced composite seismic line from A to A' across Nankai Trough along Kumao transect (after Underwood et al., 2009). Representative depth section shown here is from NanTroSEIZE 3-D data volume (Moore et al., 2009) and Line 95 from IFREE mini 3-D seismic survey (Park et al., 2008). Projected positions of Stage 1 drill sites as well as Stage 2 drill sites (Site C0011 and C0012) are shown. Focus of this study is on Site C0011, located on the incoming Philippine Sea plate, seaward of the Nankai Trough.

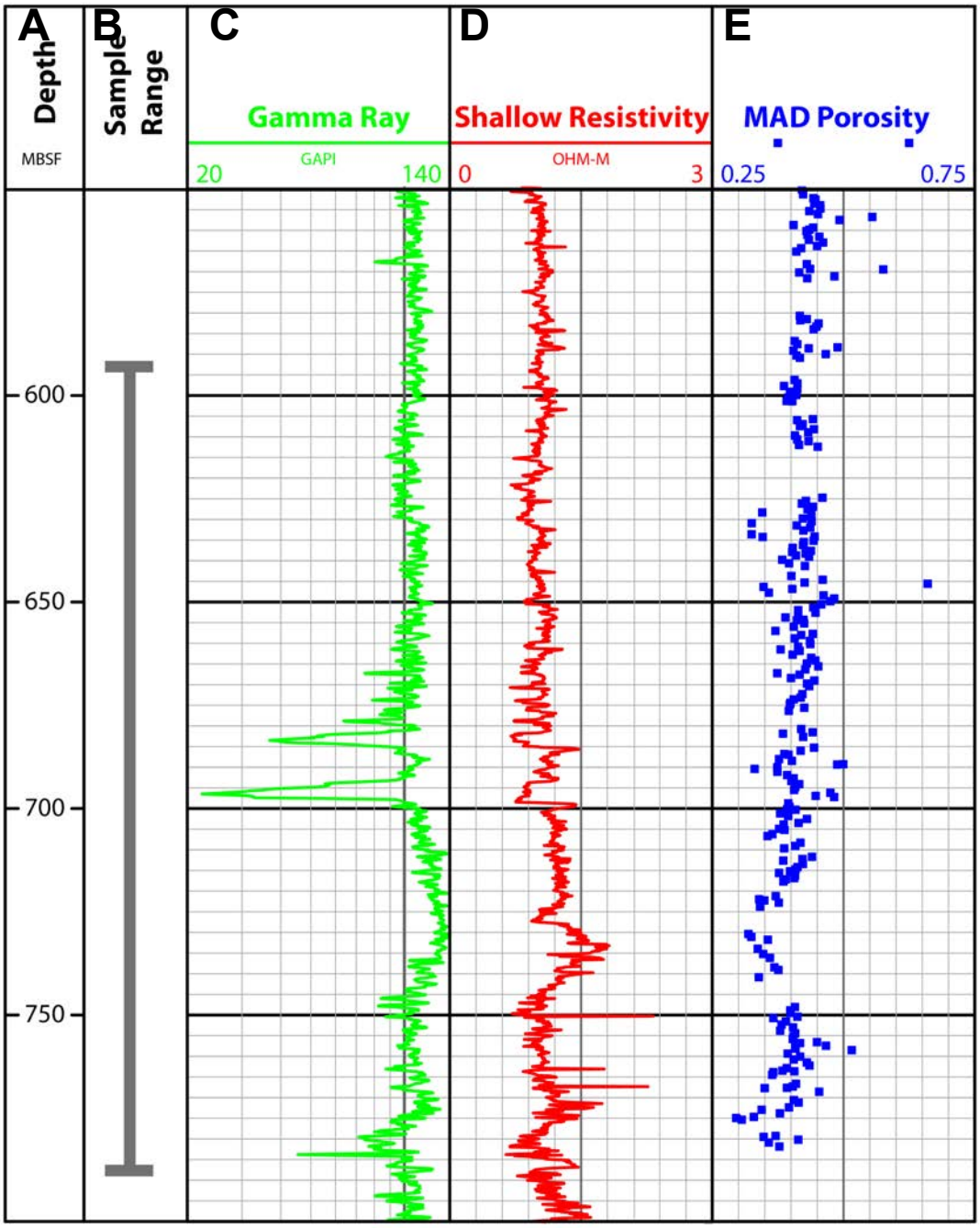

Figure 5.3: Logging and shipboard sample measurements from Site C0011. A) Depth in meters below seafloor (mbsf). B) Depth range over which Nankai mudstone, which is combined to a single batch, was collected. The Nankai mudstone is from the lower Shikoku Basin hemipelagic facies. C) Gamma Ray log. D) Resistivity log. E) Porosity from moisture and density measurements.

5.3 SAMPLES AND EXPERIMENTAL TECHNIQUES

The Nankai mudstone was collected during IODP Expedition 322 from the lower Shikoku Basin hemipelagic facies, cores 31R to 58R at Site C0011B, corresponding to depths of 586.8 mbsf to 774.69 mbsf (Figure 5.3). The samples were preferentially taken from mud-prone, homogeneous sections as large bulk material. Shipboard, the material was dumped into a bucket and ultimately 25 kg of the material were delivered to The University of Texas for analysis. I air-dried the material on large trays at room temperature. When the mass remained constant, I ground small amounts at a time in a ball grinder, sieved and then homogenized it in two 5-gallon buckets. Because this material is the first processed Nankai batch, it is termed Nankai series I. For the remainder of this thesis, I refer to this material as Nankai mudstone. Then I ad-mixed silt-sized silica (MIN U SIL 40) from US Silica to the baseline batch of Nankai mudstone in the following proportions of mud to silica: 100:00, 88:12, 76:24, 64:36, 52:48, and 40:60, resulting in samples with 59%, 54%, 51%, 43%, 39%, and 34% clay-sized particles by mass (Table 5.1). These fractions were determined from grain size analyses using the hydrometer method in accordance to ASTM D422-63 guidelines (ASTM International, 2007) (Figure 5.4). The average specific gravity of the Nankai mudstone is 2680 kg/m^3, based on moisture and density (MAD) measurements onboard the *JOIDES Resolution*. The mineralogic composition of the pure Nankai mud was measured by *Macaulay Scientific Consulting LTD* in Aberdeen, UK. Both whole rock and <2μm clay fraction analyses were performed by X-ray powder diffraction (XRPD). The bulk sample contains quartz, feldspars, minor calcite, pyrite, and halite and clay minerals (Figure 5.5A). The fraction < 2μm is dominated by smectite with lesser amounts of illite, chlorite and kaolinite (Figure. 5.5B).

% Nankai : % Silt[a]	*% Clay*[b]	*Resed #*[c]	*CRS #*[d]	*GS #*[e]
100 : 00	59	Resed 062 T	CRS 090	GS 147
88 : 12	54	Resed 051 B	CRS 091	GS 148
76 : 24	51	Resed 052 T	CRS 093	GS 149
64 : 36	43	Resed 054 T	CRS 094	GS 150
52 : 48	39	Resed 056 T	CRS 089	GS 146
40 : 60	34	Resed 059 T	CRS 088	GS 145
Silt[a]	10			GS 103

Table 5.1: Summary table of various tests performed on Nankai mudstone – silt mixtures.

[a] Silt: silt-sized silica (US MIN U SIL 40 purchased from US Silica)
[b] % Clay: clay fraction by mass measured in grain size analysis (for test number see this table, column 5)
[c] Resed #: resedimentation test number; 'T' and 'B' refer to top and bottom specimen out of the two specimens per resedimentation batch
[d] CRS #: constant-rate-of-strain (CRS) consolidation test number
[e] GS #: grain size analysis test number

A

Quartz	*Plagioclase*	*K-feldspar*	*Calcite*	*Pyrite*	*Halite*	*Muscovite*
23.5	11.4	4.5	1.2	1.1	0.3	2.6

Illite	*Smectite*	*Kaolinite*	*Chlorite*	*Total*
5.8	44.7	1.2	3.8	100.1

B

Chlorite	*Kaolinite*	*Illite*	*Smectite*	*% Expandibility*
3	1	11	85	80

Table 5.2: Mineralogy of Nankai mudstone (Resed 062, CRS 090). A) Mineralogy of whole rock as weight percent determined using the reference intensity ratio (RIR) method (Hillier, 2000). B) Mineralogy of clay fraction smaller than 2 μm expressed as relative weight percent.

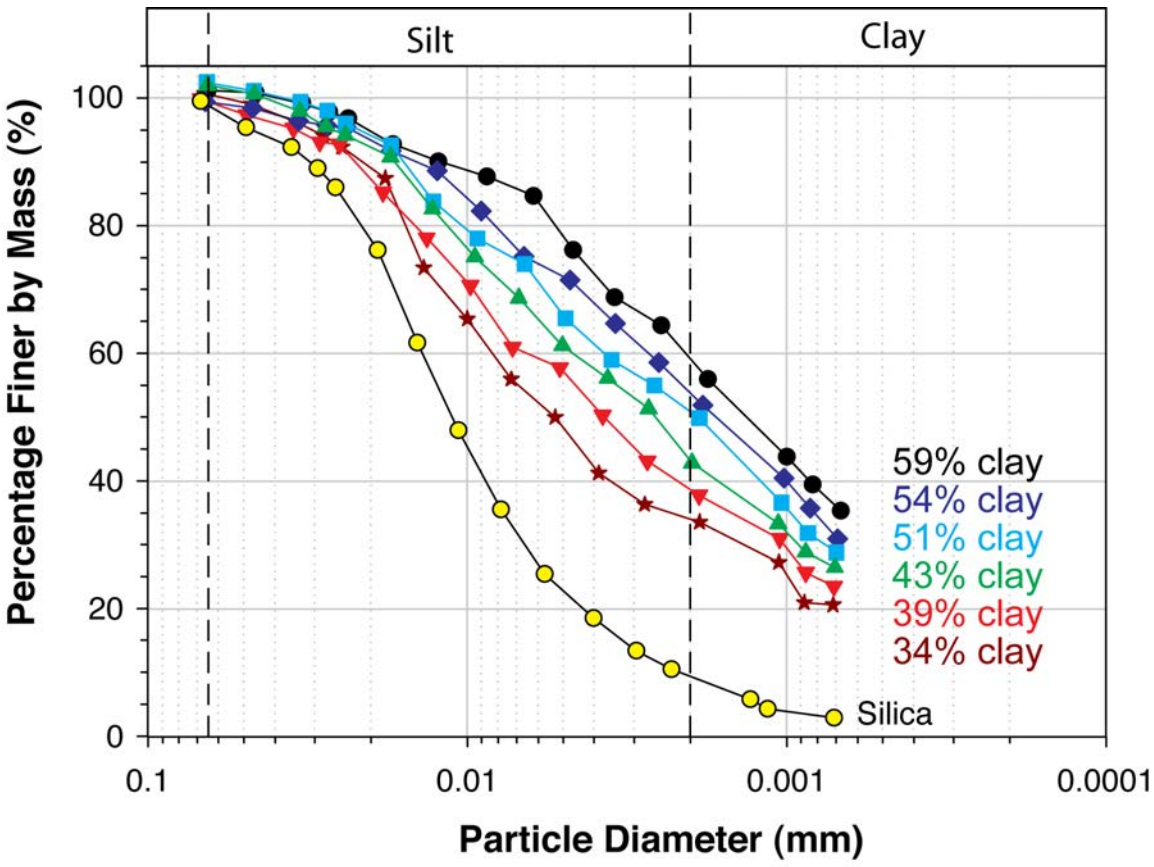

Figure 5.4: Grain size distributions of six Nankai-silt mixtures measured using the hydrometer method in accordance to ASTM D422-63 guidelines (Table 5.1) (ASTM, 2007). Black circles = 59% clay (pure Nankai mudstone); diamonds = 54% clay; squares = 51% clay; triangle pointing upward = 43% clay; triangle pointing downward = 39% clay; stars = 34% clay; yellow circles = silt-sized silica that is added to Nankai mudstone in different proportions. All percentages are by mass. The boundary between clay- and silt-sized particles is defined to be at 2 μm.

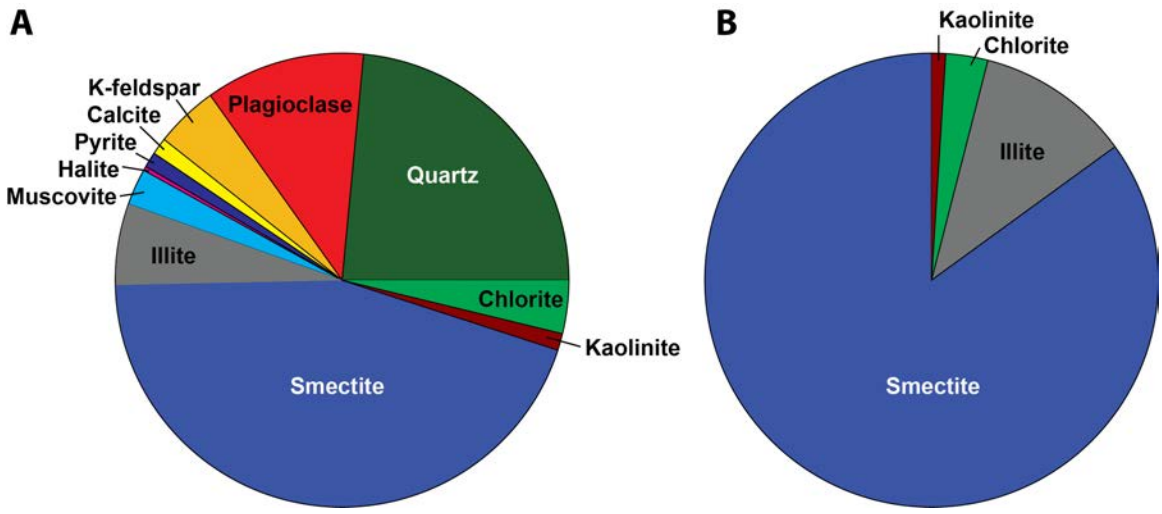

Figure 5.5: Mineralogy of Nankai mudstone measured through X-ray powder diffraction by *Macaulay Scientific Consulting LTD* (Table 5.2). A) Mineralogy of whole rock determined using the reference intensity ratio (RIR) method (Hillier, 2000). B) Mineralogy of clay fraction smaller than 2 μm expressed as relative weight percent.

I prepared the Nankai-silt mixtures in the laboratory with a method called resedimentation, which allows me to prepare undisturbed and homogenous samples in the laboratory under controlled stress conditions. Details of resedimentation can be found in Schneider et al. (2011) and in Appendix 4. Once the samples were resedimented to a maximum total stress of 100 kPa, I extruded the samples and trimmed them into a confinement ring for uniaxial, constant-rate-of-strain (CRS) consolidation testing to continuously measure compressibility and permeability as a function of vertical effective stress. I performed the CRS tests in accordance to ASTM Standard D4186-06 (ASTM International, 2006) (see Appendix 5). After consolidation to a maximum vertical effective stress of 20 MPa, high-resolution backscattered electron images were taken of subsamples of the CRS specimens on a field-emission scanning electron microscope. The samples were prepared using an argon-ion beam milling technique (Loucks et al., 2009).

5.4 RESULTS

5.4.1 Resedimentation

All six compression curves from resedimentation experiments are shown in Figure 5.6 (Table 5.3). Each data point represents the void ratio and applied vertical stress at the end of a stress increment. The first digitally measured void ratio (at 2.6 kPa) systematically decreases from 2.50 to 1.57 for specimens with 59% and 34% clay by mass. The compression index (C_c), defined as the change in void ratio over the change in log of vertical effective stress (here calculated between 2.6 kPa and 100 kPa), decreases from 0.63 to 0.37 for specimens with 59% and 34% clay. This shows that the samples become stiffer the more silica they contain.

% Nankai : % Silt[a]	*Resed #*[b]	*e*[c] *at 2.60 kPa*	*e at 5.22 kPa*	*e at 10.46 kPa*	*e at 20.95 kPa*	*e at 41.92 kPa*	*e at 68.15 kPa*	*e at 99.62 kPa*	*e at 24.88 kPa*
100 : 00	Resed 062 T	2.50	2.32	2.13	1.96	1.77	1.63	1.51	1.57
88 : 12	Resed 051 B	2.39	2.20	2.03	1.85	1.67	1.54	1.43	1.44
76 : 24	Resed 052 T	2.20	2.06	1.89	1.72	1.51	1.40	1.30	1.31
64 : 36	Resed 054 T	1.92	1.78	1.62	1.49	1.34	1.22	1.17	1.18
52 : 48	Resed 056 T	1.65	1.53	1.40	1.28	1.18	1.10	1.04	1.04
40 : 60	Resed 059 T	1.57	1.45	1.31	1.20	1.10	1.03	0.98	0.98

Table 5.3: Resedimentation results for Nankai mudstone – silt mixtures.

[a] Silt: silt-sized silica (US MIN U SIL 40 purchased from US Silica)
[b] Resed #: resedimentation test number; 'T' and 'B' refer to top and bottom specimen out of the two specimens per resedimentation batch
[c] e: void ratio at varying vertical effective stresses

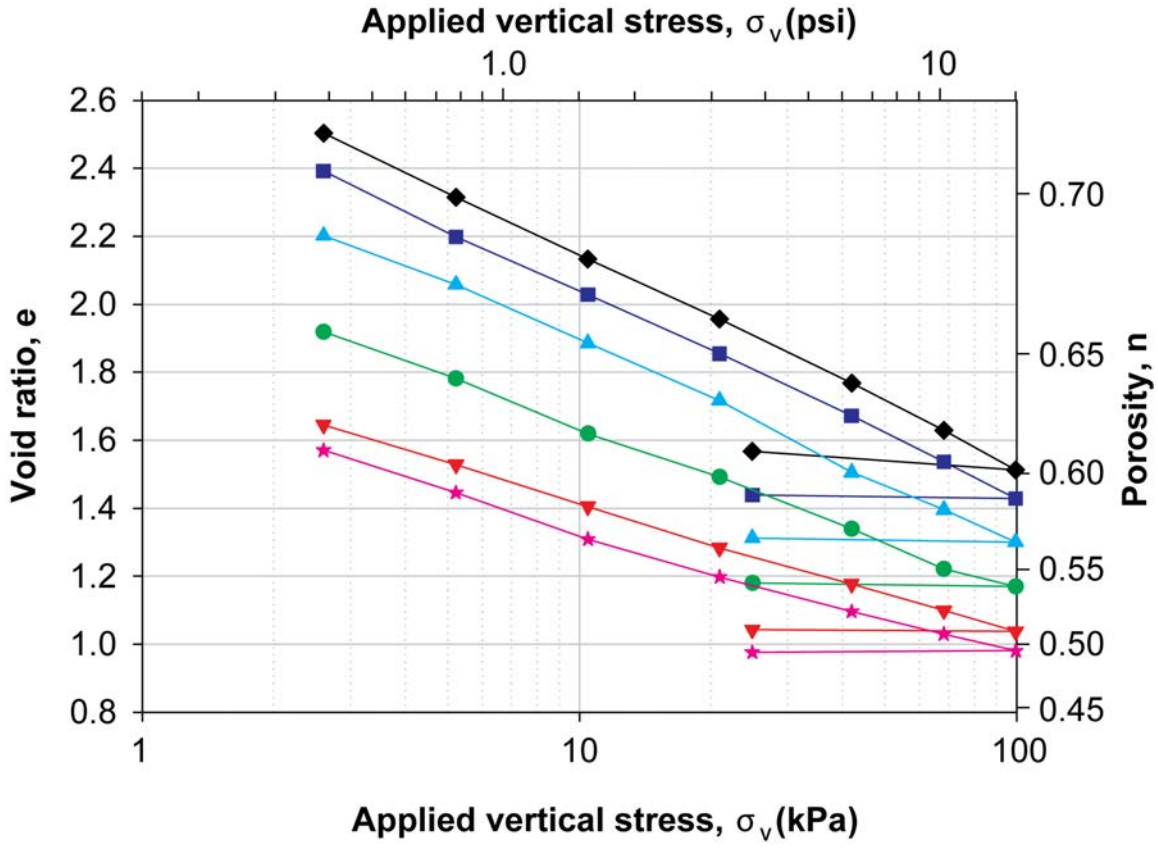

Figure 5.6: Resedimentation results (Table 5.3). Each data point represents the void ratio at the end of an individual load increment. Each load increment is left on the slurry till the end of primary consolidation. At the end of the test (after last load increment), the void ratio is measured using the wet and dry mass and assumed grain density of 2680 kg/m^3. Based on the vertical deformation, void ratio is then backtracked to previous load increments. Black diamonds = 59% clay (pure Nankai mudstone); dark blue squares = 54% clay; light blue triangles = 51% clay; green circles = 43% clay; red triangles pointing downward = 39% clay; pink stars = 34% clay.

5.4.2 Compression and permeability behavior

I measured evolution of compressibility and permeability with vertical effective stress of all six Nankai-silt mixtures using uniaxial, constant-rate-of-strain (CRS) consolidation tests. The initial void ratio in CRS tests, equivalent to the void ratio at the end of resedimentation, decreases from 1.63 to 0.97 for mixtures with 59% to 34% clay (Figure 5.7). The decrease in void ratio is due to the reduction in pore space, which is large for fine-textured clays but less for sediments composed of larger solid grains. All compression curves show an inflection point at 100 kPa, which is the preconsolidation stress equivalent to the stress the samples were preloaded to in the resedimentation experiments. The preconsolidation stress separates the elastic behavior represented by the flat part of the compression curve, where deformation is reversible, from the elasto-plastic behavior represented by the steep part of the compression curve, where deformation is irreversible. The lower the clay content, the stiffer the sediments are and the flatter is the elasto-plastic part of the consolidation curve (Figure 5.7). The compression index (C_c), the change in void ratio over change in log of vertical effective stress, is not constant over stress; instead, it decreases with vertical effective stress, particularly for clay-rich samples.

Vertical permeability is commonly known to vary exponentially with porosity. Thus, on a log-linear plot the log of permeability decreases linearly with porosity (Figure 5.8):

$$\log(k) = \gamma n + \log(k_0), \tag{5.1}$$

where γ is the slope of the log-linear relationship between permeability and porosity and k_0 is the y-intercept at a porosity of zero. Vertical permeability increases with decreasing clay fraction (Figure 5.8). There is a difference of almost two orders of magnitudes at a

given porosity between samples with 59% clay and samples with 34% clay. The values shown here are a 15-point moving average because more noise is introduced as the reading time gets shorter. Still irregularities in the measurements are present which could be slow transient effects. The smaller-scale ups and downs are due to the pumps. The larger-scale bends in the curves (over larger porosity ranges) are due to partial pressure losses, where the base pressure slightly dropped or leveled out instead of a steady increase. This causes the ratio of overpressure to applied total load to decrease, which in turn affects the permeability calculation.

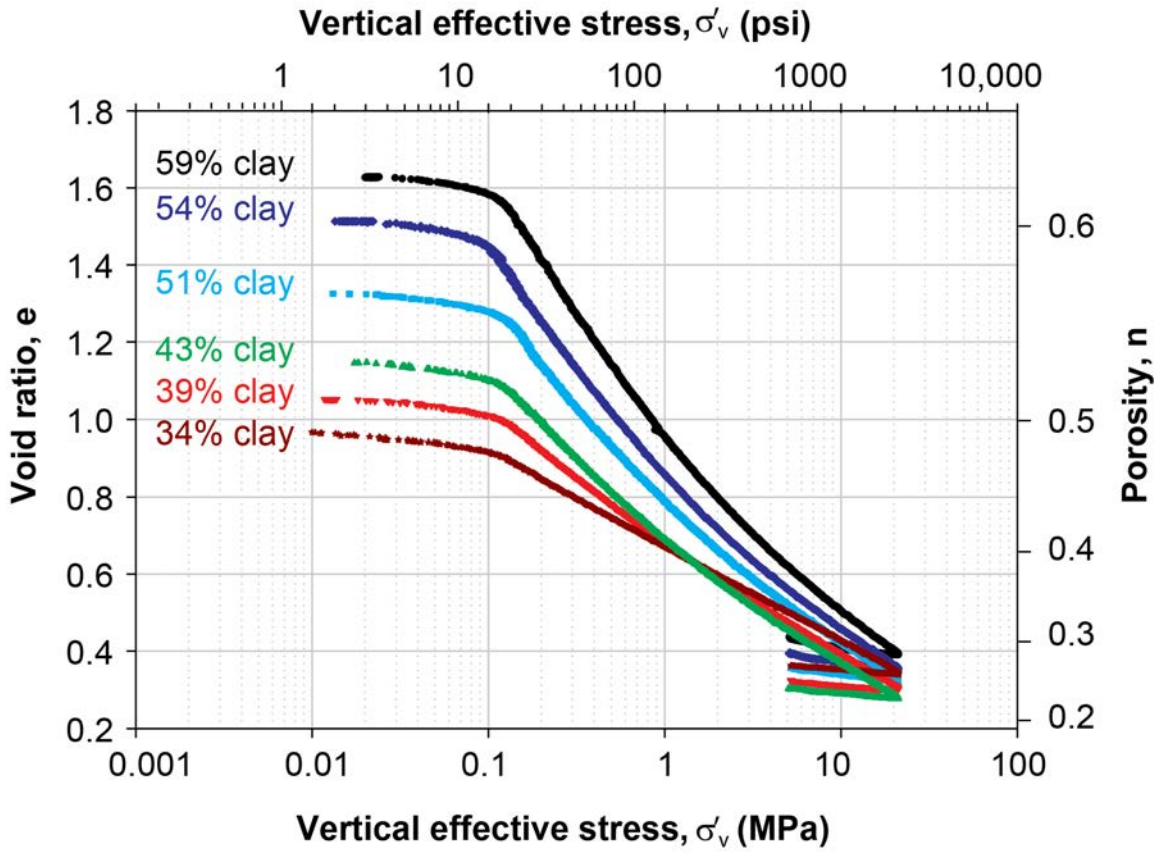

Figure 5.7: Compression curves of six Nankai-silt mixtures from uniaxial constant-rate-of-strain consolidation tests (Table 5.1). All samples were consolidated to a maximum vertical effective stress of 20 MPa. Black circles = 59% clay (pure Nankai mudstone); dark blue diamonds = 54% clay; light blue squares = 51% clay; green triangle pointing upward = 43% clay; red triangle pointing downward = 39% clay; brown stars = 34% clay.

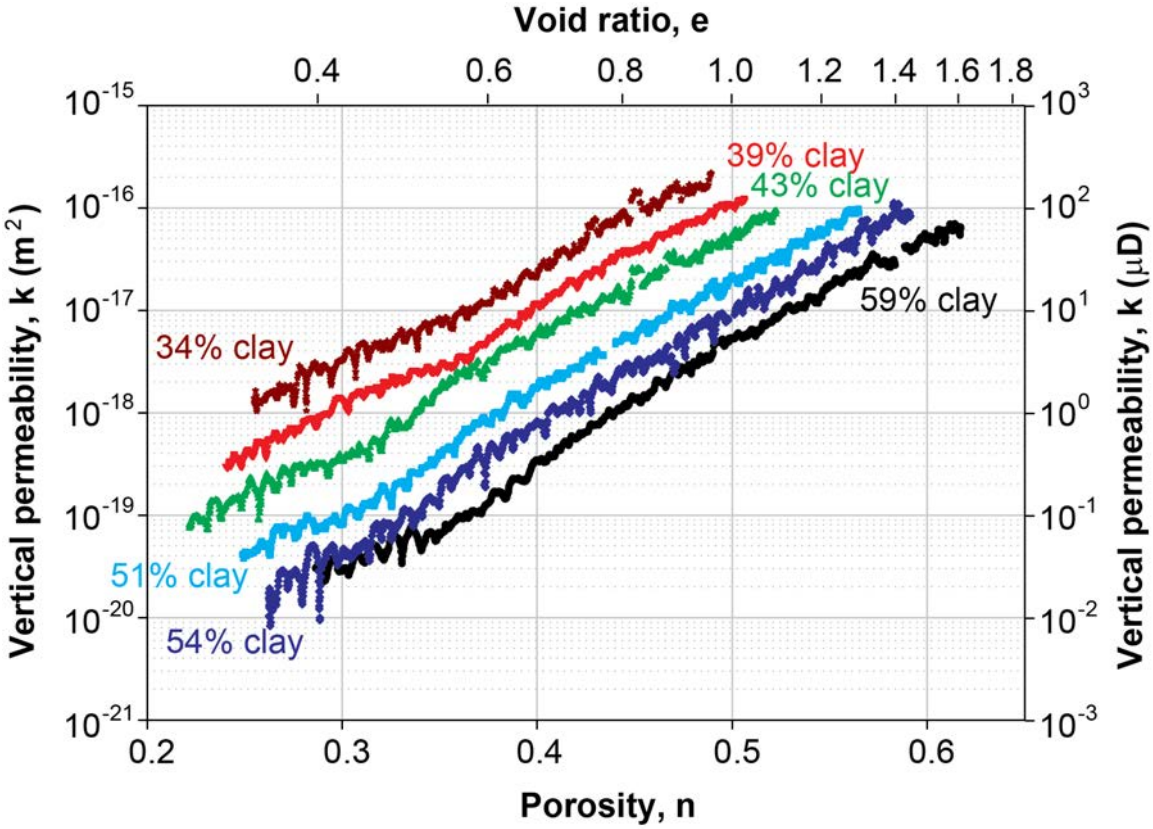

Figure 5.8: Permeability – porosity relationships of six Nankai-silt mixtures derived from uniaxial, constant-rate-of-strain consolidation experiments (Table 5.1). Black circles = 59% clay (pure Nankai mudstone); dark blue diamonds = 54% clay; light blue squares = 51% clay; green triangle pointing upward = 43% clay; red triangle pointing downward = 39% clay; brown stars = 34% clay.

5.4.3 Permeability model

Schneider et al. (2011) showed that a geometric mean model accurately predicts permeability of clay-silt mixtures as a function of porosity and clay fraction. Their model assumes the rock to be composed of two fractions: one rock fraction is composed of silt where large pores are present and most of the flow occurs, whereas the other rock fraction is composed of clay where small pores are present and flow is limited. Each rock fraction has its own permeability – porosity relationship. Under these conditions, the effective permeability of clay-silt mixtures can be approximated by the geometric mean of the permeabilities of the clay (k_{cl}) and silt (k_{si}) components and can be written as:

$$\log k_{eff} = \left[cf_v \gamma_{cl} + \left(1 - cf_v\right)\gamma_{si}\right] n + cf_v \log(k_0^{cl}) + \left(1 - cf_v\right)\log(k_0^{si}), \tag{5.2}$$

where subscripts and superscripts cl and si stand for clay and silt, respectively and cf_v is the volumetric clay fraction calculated from the clay fraction by mass (cf_m), measured by hydrometer analyses, as follows:

$$cf_v = 1 - \frac{\rho_g}{\rho_{Qz}} \cdot \left(1 - cf_m\right), \tag{5.3}$$

where ρ_g and ρ_{Qz} are grain density and density of silt/quartz, respectively.

The fundamental assumption in our model is that the porosity in the volume element that contains the fine fraction is equal to the porosity in the element that contains the coarse fraction. I determine slopes and intercepts of linear relationships between log of permeability and porosity for all six Nankai-silt mixtures (Table 5.4). Then I use Schneider et al.'s (2011) approach to determine the model parameters specific for the Nankai mudstone system with multivariable linear regression of the experimental data

(see Appendix 3): $\log(k_0^{cl}) = -27.53$, $\gamma_{cl} = 14.50$, $\log(k_0^{si}) = -16.92$, and $\gamma_{si} = 7.40$. I then use Equation 5.2 and the determined model parameters to predict vertical permeability of Nankai-silt mixtures for the given clay fractions over the measured porosity range (Figure 5.9).

% Nankai : % Silt[a]	*CRS #*[b]	γ	$\log(k_0)$
100 : 00	CRS 90	11.1	-22.9
88 : 12	CRS 91	11.6	-22.8
76 : 24	CRS 93	11.2	-22.3
64 : 32	CRS 94	10.5	-21.5
52 : 48	CRS 89	9.9	-21.0
40 : 60	CRS 88	9.8	-20.5

Table 5.4: Slopes (γ) and intercepts (k_0) of linear relationships between log of permeability and porosity determined by linear regression of experimental data.

[a] Silt: silt-sized silica (US MIN U SIL 40 purchased from US Silica)
[b] CRS #: constant-rate-of-strain (CRS) consolidation test number

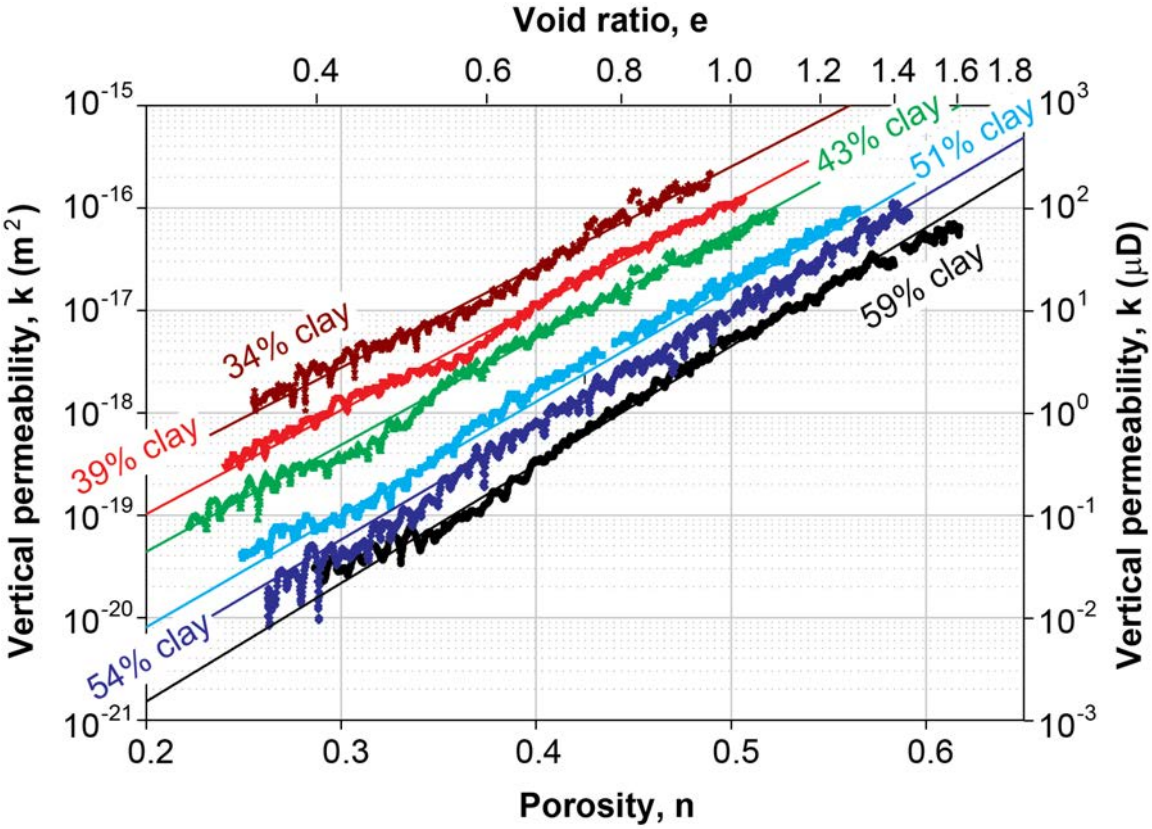

Figure 5.9: Permeability prediction from geometric mean model (solid lines) and permeability derived from uniaxial constant-rate-of-strain consolidation tests (Table 5.1) (symbols). Black circles = 59% clay (pure Nankai mudstone); dark blue diamonds = 54% clay; light blue squares = 51% clay; green triangle pointing upward = 43% clay; red triangle pointing downward = 39% clay; brown stars = 34% clay.

5.4.4 Compression model

The CRS data show concave up profiles when void ratio is plotted against the log of vertical effective stress, which is a characteristic behavior of mudstones that have been compressed over a large range of effective stress (0-20 MPa). Long et al. (2011) compared four different approaches to describe the compression behavior of mudstones. They found that the relationship proposed by Butterfield (1980) captures the rapid void ratio decrease at low effective stresses best and predicts reasonably well void ratios at high effective stresses. Butterfield (1980) suggested that the concave up profile when void ratio is plotted against log of vertical effective stress could be described by setting specific volume ($v = e+1$) equal to change in vertical effective stress (σ'_v):

$$\frac{dv}{v} = -C\frac{d\sigma'_v}{\sigma'_v} \tag{5.4}$$

Equation 5.4 can be solved for the variation in specific volume (v) with vertical effective stress by integration:

$$v = v_0\left(\sigma'_v\right)^C, \tag{5.5}$$

where v_0 is the specific volume at a vertical effective stress of unity (1 MPa). v_0 and C can be constrained through linear regression of specific volume and vertical effective stress on a log-log plot.

I apply this method to all six CRS data sets and determine v_0 and C for each Nankai-silt mixture (Table 5.5). Predicted compression curves agree well with the elasto-plastic part of the measured compression curves (Figure 5.10A). A comparison of the resedimentation compression data (from Figure 5.6) with the extrapolation of the elasto-

plastic deformation to low stresses (Figure 5.10A) by using the compression model shows that the model holds over a wide vertical effective stress range (Figure 5.10B). Only for high clay fractions, where the concave upward shape of the virgin consolidation curve is more pronounced, the compression model starts to overpredict void ratio at a given vertical effective stress (Figure 5.10B).

In order to predict v_0 and C for other clay fractions than tested here, I develop relationships between v_0 and volumetric clay fraction (cf_v) and between C and volumetric clay fraction (cf_v) (Figure 5.11). v_0 varies nonlinearly with clay fraction (Figure 5.11A):

$$v_0 = 5.5602 cf_v^2 - 3.8943 cf_v + 2.352 . \quad (5.6)$$

Following Equation 5.6, specific volume at 1 MPa (v_0) has a minimum of 1.66 at a clay fraction of 0.34 (Figure 5.11A). Given the fact that initial void ratio decreases and stiffness increases with decreasing clay fraction, which causes a void ratio minimum at high vertical effective stresses as a function of clay fraction, such a minimum in the specific volume is possible. However, the specific volume of 2.35 at zero clay fraction, which corresponds to a void ratio of 1.35 and porosity of 0.57, seems too high. The porosity in an ideal cubic packing of equally sized spheres is 0.47. In this study though, the silt particles are not all equally sized and perfect spheres and a rhombohedral packing is more likely in nature than a cubic packing. So I would expect any porosity between 0.2 and 0.47, equivalent to specific volumes at zero clay fraction of 1.26 and 1.89, respectively. The relationship between v_0 and cf_v basically reflects the packing structure.

In contrast, C linearly decreases with increasing clay fraction (Figure 5.11B):

$$C = -0.188 cf_v - 0.009 . \quad (5.7)$$

% Nankai : % Silt[a]	*CRS #*[b]	v_0[c]	*C*[d]
100 : 00	CRS 90	1.97	-0.119
88 : 12	CRS 91	1.87	-0.109
76 : 24	CRS 93	1.80	-0.102
64 : 32	CRS 94	1.70	-0.094
52 : 48	CRS 89	1.68	-0.083
40 : 60	CRS 88	1.67	-0.069

Table 5.5: Constrained parameters v_0 and C from log-log plot of specific volume and vertical effective stress after Butterfield (1980). Specific volume is equal to void ratio plus one.

[a] Silt: silt-sized silica (US MIN U SIL 40 purchased from US Silica)
[b] CRS #: constant-rate-of-strain (CRS) consolidation test number
[e] v_0: specific volume at a vertical effective stress of unity (1 MPa); factor in Equation 5.5
[d] C: fitting parameter; exponent in Equation 5.5

Because C is the power to which the vertical effective stress is raised in its relationship to specific volume (Equation 5.5), a higher absolute value of C means an increased curvature, i.e. the rate at which specific volume decreases with increasing vertical effective stress slows down with consolidation. For low clay contents, however, the rate at which specific volume decreases with vertical effective stress is nearly constant. This behavior is captured by the linear relationship between C and cf_v, which predicts a value of almost zero for C in case of a pure silt (clay fraction equals zero). This relationship between C and cf_v basically reflects the compressibility of the samples.

The dependencies of v_0 and C on cf_v allow me to predict void ratio over a large effective stress range for possibly any clay fraction of Nankai-silt mixtures by writing v as e+1 and solving for e (see Appendix 3):

$$e = v_0 \left(\sigma_v^{'}\right)^C - 1, \tag{5.8}$$

where v_0 and C are the functions in Equation 5.6 and 5.7, respectively. However, an extrapolation of this model to clay fractions outside of the constrained data range as shown in Figure 5.11 should be considered with caution because the validity of the model at clay fractions outside the measurement range is not proven at this point.

5.4.5 Predictive model

I develop a model that predicts vertical permeability, coefficient of volume compressibility, and coefficient of consolidation of any Nankai-silt mixture with vertical effective stress, or depth if pore fluid pressures are known, by coupling the geometric

mean permeability model after Schneider et al. (2011) and the compression model after Butterfield (1980) and Long et al. (2011).

To describe permeability as a function of vertical effective stress I substitute Equation 5.7 into 5.2 and convert void ratio to porosity ($n = \frac{e}{e+1}$):

$$\log k_{eff} = \left[1 - \left(v_0 (\sigma'_v)^C\right)^{-1}\right] \cdot \left[cf_v \gamma_{cl} + (1 - cf_v)\gamma_{si}\right] + cf_v \log(k_0^{cl}) + (1 - cf_v)\log(k_0^{si}), \quad (5.9)$$

where v_0 and C are described by Equations 5.6 and 5.7, respectively. The coefficient of volume compressibility can be described as (after Butterfield, 1980):

$$m_v = -\frac{1}{v}\frac{dv}{d\sigma'_v} = -\frac{1}{v}\frac{dv}{d(\log\sigma'_v)}\frac{d(\log\sigma'_v)}{d\sigma'_v} = C\frac{1}{\sigma'_v}, \quad (5.10)$$

where C is described by Equation 5.7. This relationship shows that m_v is linearly dependent on clay fraction. The coefficient of consolidation (C_v) is the ratio between intrinsic permeability (k) and the coefficient of volume compressibility (m_v):

$$C_v = \frac{k\mu}{m_v}, \quad (5.11)$$

where μ is dynamic viscosity assumed to be 0.001002 Pa s. m_v has to be divided by 10^3 to convert from kPa to Pa to maintain dimensional homogeneity. The predictions of k, m_v, and C_v over stress are shown for the six Nankai-silt mixtures that were analyzed in this study in Figure 5.12. Vertical permeability changes significantly more with a change in clay fraction of 25% than does the coefficient of volume compressibility, resulting in large difference in C_v. The coarsest sample first increases in C_v and then stays constant, whereas the most fine-grained sample gradually decreases in C_v.

A

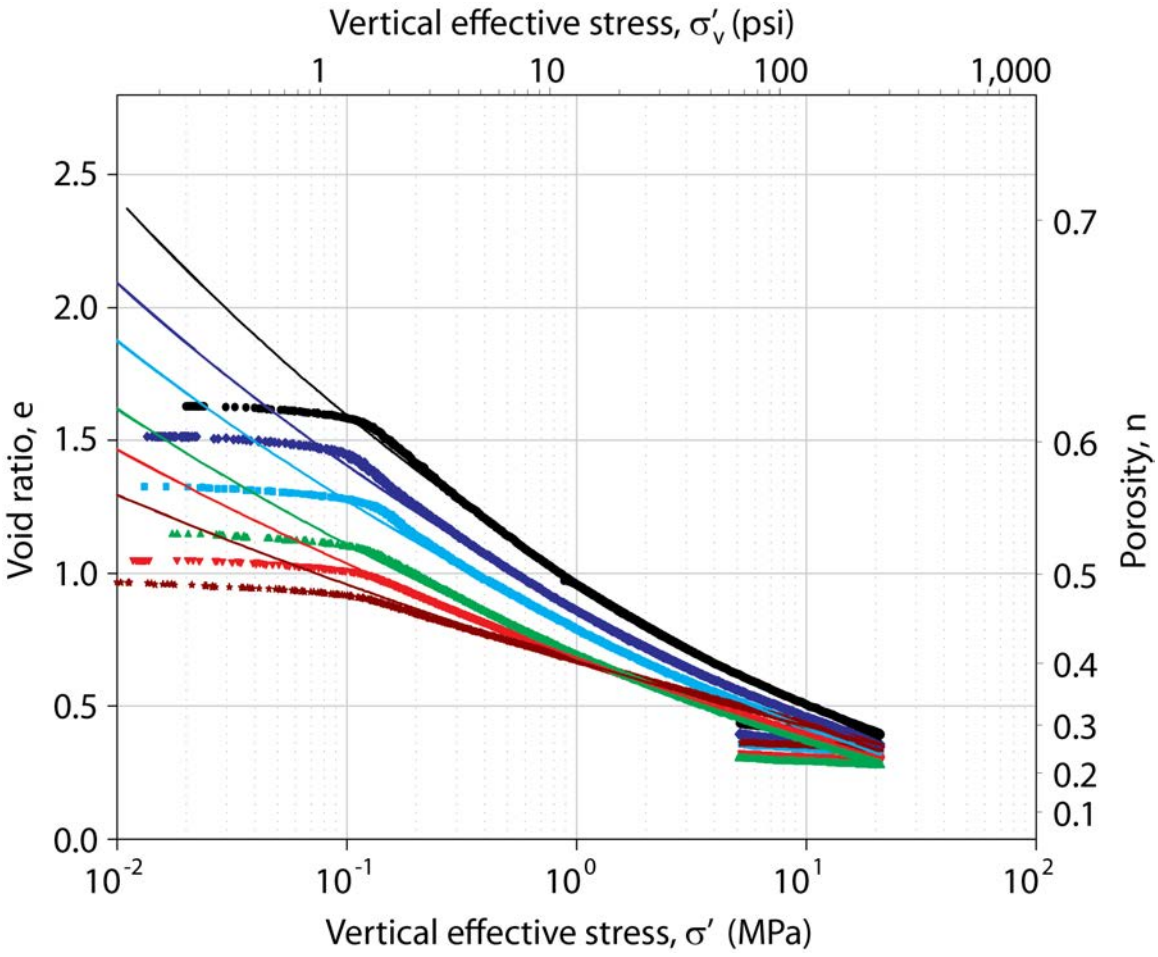
Vertical effective stress, σ′v (psi)
1
10
100
1,000
2.5
2.0
1.5
1.0
0.5
0.0
Void ratio, e
0.7
0.6
0.5
0.4
0.3
0.2
0.1
Porosity, n
10-2
10-1
100
101
102
Vertical effective stress, σ′ (MPa)

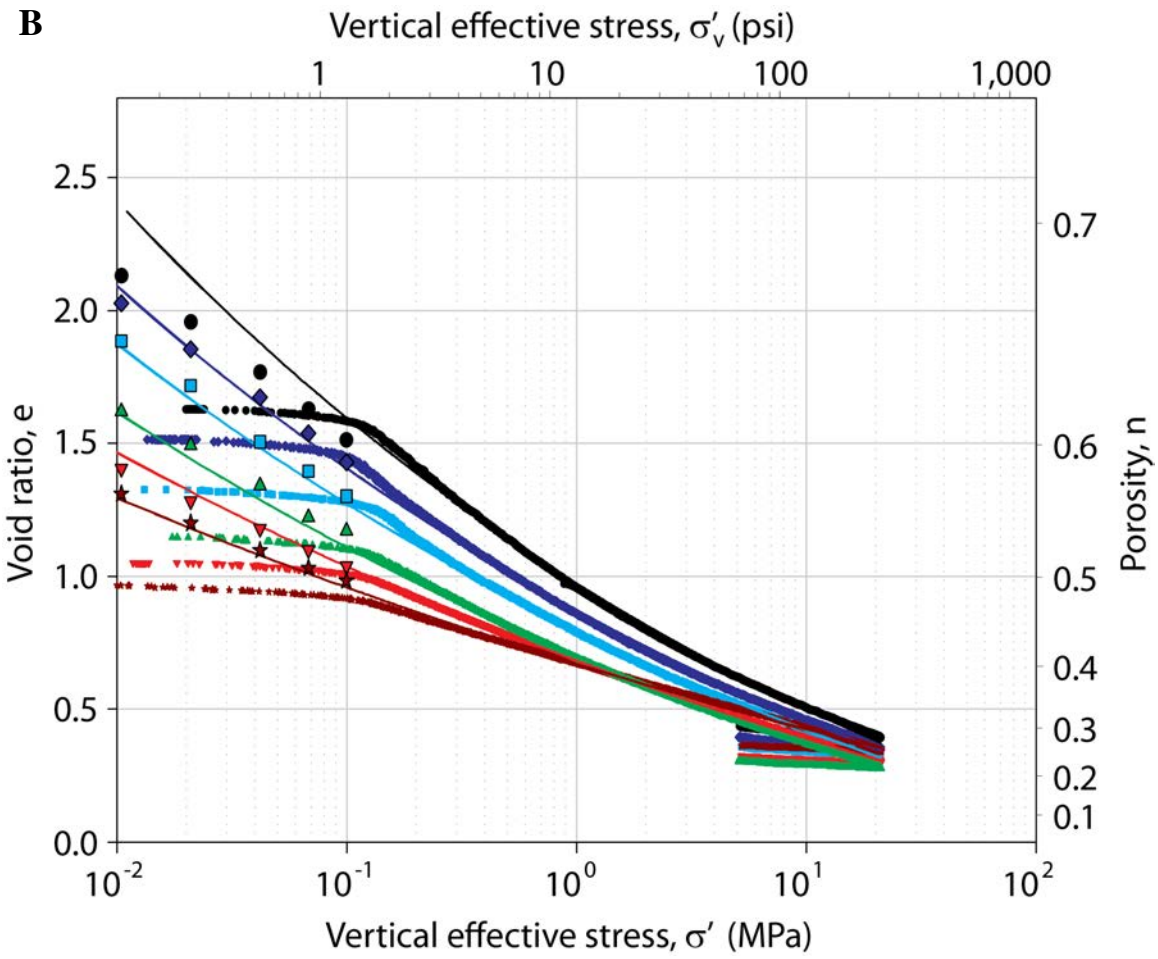

Figure 5.10: Prediction of compression behavior of six Nankai-silt mixtures along virgin consolidation based on Long et al.'s (2011) model. A) Comparisons of predicted compression behaviors with measured compression curves. B) Comparison of predicted compression behaviors with resedimentation data (from Figure 5.6, Table 5.3) at low vertical effective stresses. Black circles = 59% clay (pure Nankai mudstone); dark blue diamonds = 54% clay; light blue squares = 51% clay; green triangle pointing upward = 43% clay; red triangle pointing downward = 39% clay; brown stars = 34% clay.

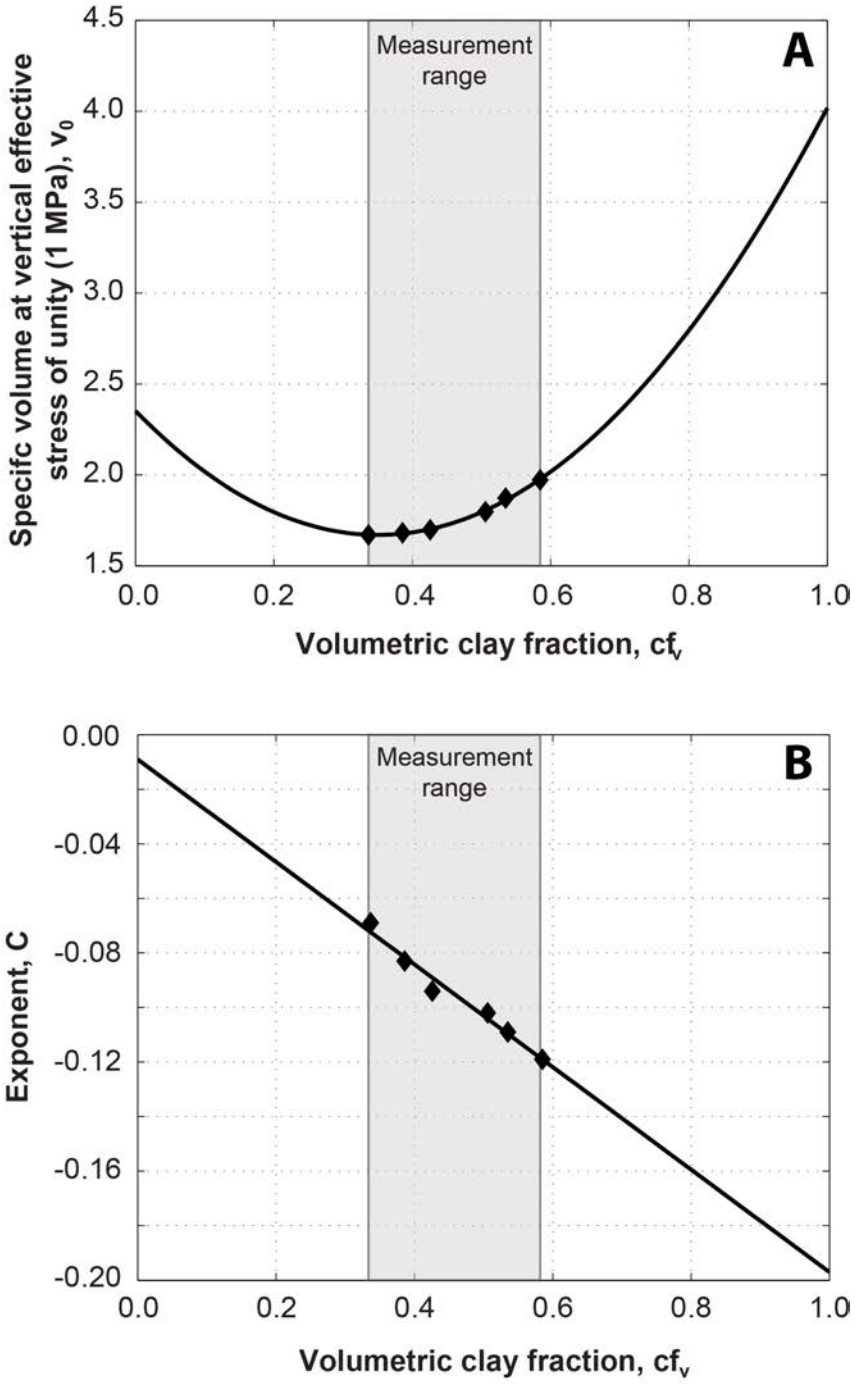

Figure 5.11: Variation of parameters in Long et al.'s (2011) model with volumetric clay fraction (Tables 5.1, 5.5). A) Relationship between v_0 and volumetric clay fraction (cf_v). B) Relationship between exponent C and volumetric clay fraction (cf_v). Measurement range over which model is constrained is indicated by the gray box.

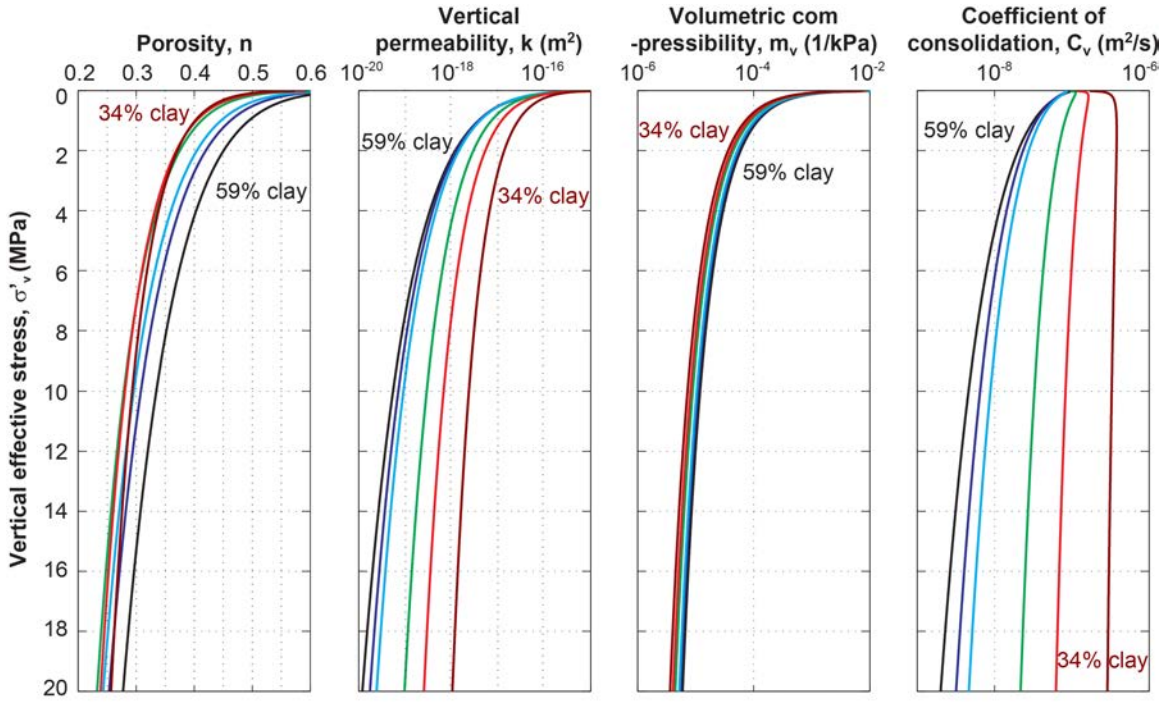

Figure 5.12: Generalized predictive model for six measured clay fractions. From left to right: porosity, vertical permeability, coefficient of volume compressibility, and coefficient of consolidation versus vertical effective stress. Black = 59% clay, dark blue = 54%, light blue = 51%, green = 43%, red = 39%, brown = 34%.

5.5 DISCUSSION

A comparison of the laboratory compression curve of Nankai mudstone with the *in-situ* void ratio – vertical effective stress trend is shown in Figure 5.13. The field compression curve (black symbols), derived from moisture and density void ratios and vertical effective stresses assuming hydrostatic conditions in the subsurface, shows a stronger void ratio reduction for a given effective stress interval than the lab compression curve (black line) does. Specifically, over the depth from which resedimentation material was collected (587 to 775 mbsf), *in-situ* porosity declines 45 to 35% and vertical effective stress increases from 5.9 to 7.7 MPa at hydrostatic pore pressure. In contrast, during resedimentation and uniaxial consolidation in the laboratory, porosity declines from 37.5 to 35.5% over this vertical effective stress range (Figure 5.13). The *in-situ*, or field compression curve converges to the experimental curve at vertical effective stresses of 8.8 MPa, which is equivalent to the effective stress at the bottom of Hole C0011B (880 mbsf).

Burland (1990) compared *in-situ* compression lines (sedimentation compression line, SCL) of various clays with compression lines of reconstituted clays (intrinsic compression line, ICL) and found that they are parallel to each other. He showed that the vertical effective stress of the SCL is five times greater than the vertical effective stress of the ICL. Burland (1990) interpreted that the material in the field was stronger because of a difference in fabric and stronger particle bonding in the intact material (Burland, 1990). My results (Figure 5.13) do not show this behavior. Instead, my results show that at a porosity of about 55% the vertical effective stress of the SCL (4.8 MPa) is one order of magnitude greater than the vertical effective stress of the ICL (0.48 MPa). This difference in effective stress between SCL and ICL declines with increasing effective

stress to where both are identical at a vertical effective stress of 8.8 MPa, which is equivalent to the bottom of Hole C001B.

A comparison between Burland's (1990) study and these results on Nankai mudstone should be done with caution though because the stress conditions of the materials are different. The shallow geotechnical sediments in studies by Burland were all overconsolidated either due to stress unloading by erosion or by aging at constant effective stress, whereas the Nankai mudstone is normally consolidated and still undergoes primary consolidation strains.

There are three possible explanations though for why the *in-situ* and laboratory-derived compression curves of the Nankai mudstone are so different. First, the composition of the resedimented Nankai mudstone is an average of compositions over the sampled depth range from 587 to 775 mbsf (Figure 5.3). In contrast, the *in-situ* material varies compositionally as layering and heterogeneities occur over the samples 200 meters. Specifically, the lowest *in-situ* porosity samples from around 730 and 775 mbsf appear to be low because they represent highs in the gamma ray (GR) log (Figure 5.3). Thus, it is possible that there are significant compositional variations downhole and this could impact the *in-situ* compression behavior. However, it is not likely that such a dramatic difference in compression curves is caused by the compositional variations in the field versus the averaged composition in resedimentation.

Second, without knowing *in-situ* pore fluid pressures I do not know *in-situ* vertical effective stresses. Thus, I can only make estimates of the *in-situ* vertical effective stresses based on different assumptions. Overpressure in the subsurface would reduce the vertical effective stress. However, a constant pore pressure ratio (λ^*), which is the ratio of overpressure to hydrostatic vertical effective stress, over depth would just move the field curve along the vertical effective stress axis to lower stresses as shown in Figure

5.13 for the example of $\lambda^* = 0.9$. A constant overpressure ratio would not change the slope of the field curve. Only a decreasing pore pressure ratio with depth would match the laboratory compression curve. An actual pore pressure ratio of $\lambda^* = 0.9$ would be required at shallow depths decreasing to hydrostatic conditions at the bottom of the hole in order to match the field curve with the laboratory curve over large stress ranges (Figure 5.13). This scenario with significant overpressure so close to the seafloor (about 40 mbsf) and no overpressure at larger depths is unlikely.

The third and most plausible explanation is based on the fact that here I am studying mudstones at high geologic stresses as opposed to lower effective stresses mostly considered in civil engineering. Burland (1990) did state that SCL and ICL are parallel only between approximately 10 kPa and 1000 kPa, the effective stress range over which most of the clays for civil engineering purposes are constrained. For effective stresses larger than 1000 kPa SCL and ICL tend to converge. The *in-situ* void ratio measurements available at this time and shown in Figures 5.3 and 5.13 start at a depth of 340 mbsf, equivalent to a vertical effective stress of about 3.5 MPa under hydrostatic conditions. This effective stress is already larger than the 1 MPa threshold where field compression and laboratory compression curve would start to converge as described by Burland (1990). In summary, the difference between field and laboratory compression behavior is still unclear and needs to be explored in more detail in future studies.

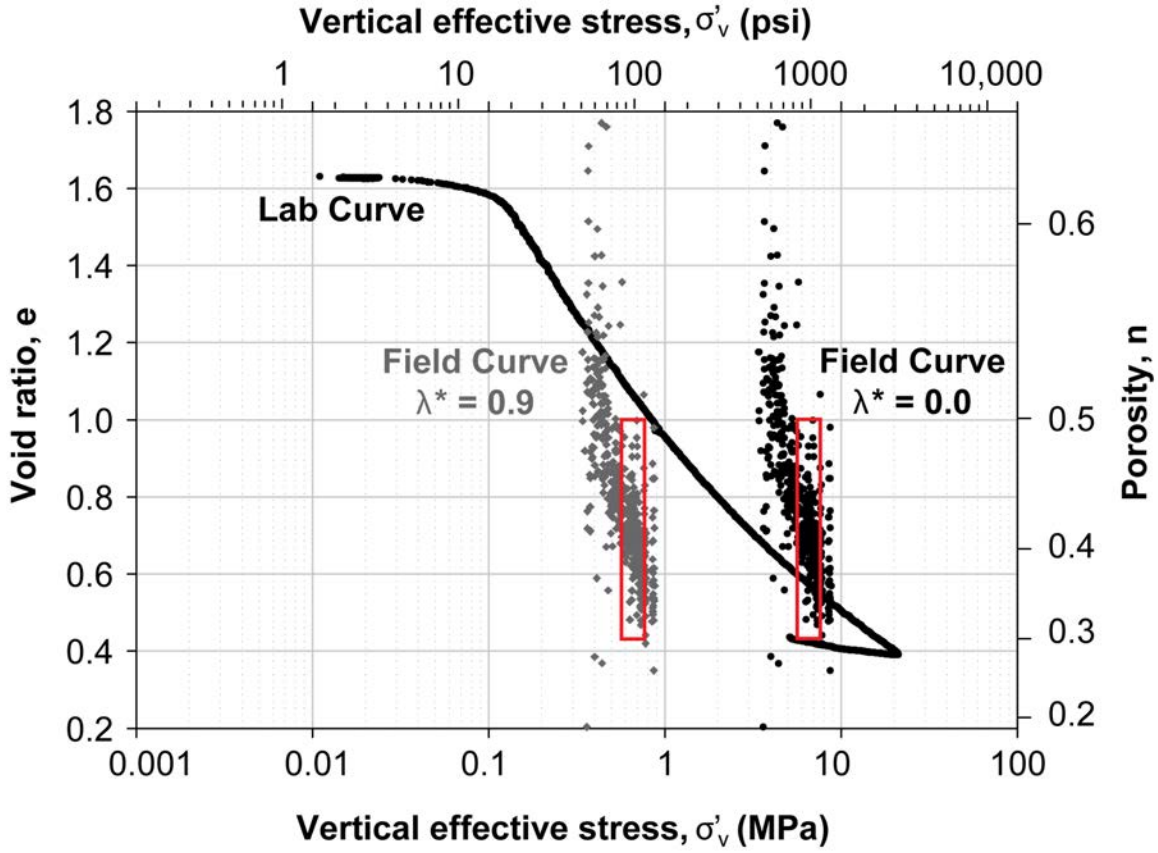

Figure 5.13: Comparison between field compression curve and laboratory-derived compression curve (CRS 090). Void ratios of field curves were calculated from moisture and density porosity data (as shown in Figure 5.3). Black field curve refers to void ratio – based overpressure prediction assuming hydrostatic conditions, i.e. overpressure ratio (ratio of overpressure to hydrostatic vertical effective stress) $\lambda^* = 0.0$. Gray field curve refers to void ratio – based overpressure prediction assuming overpressure ratio $\lambda^* = 0.9$. Red boxes indicate porosity range over which data is constrained at effective stresses that are equivalent to the depth samples were collected from assuming either $\lambda^* = 0.0$ or $\lambda^* = 0.9$.

The compression and permeability results of resedimented Nankai – silt mixtures show similar trends as other published results on samples prepared by techniques similar to resedimentation. Among those samples are for example mixtures of kaolinite and smectite (Mondol et al., 2008), kaolinite and silt (Mondol, 2009), smectite and silt (Mondol et al., 2010), as well as a silty clay and remolded natural clay (Clennell et al., 1999). Clennell et al. (1999) studied the permeability anisotropy of four consolidated clays. Here, I only show the two clays that are most comparable to natural clays. The silty clay is an artificial test clay developed to simulate a typical marine clay (Karig and Hou, 1992) and the remolded natural clay (Clennell et al., 1999) was recovered during Ocean Drilling Program (ODP) Leg 141 from the Chile Triple Junction accretionary complex and remolded at 125% of the liquid limit. A remolded clay has its natural internal structure modified or disturbed to where flocculated aggregations are broken down, shear planes are destroyed, large pores are eliminated, and a more homogeneous fabric is produced (Mitchell, 1993). Both clays have initial porosities similar to the coarsest Nankai – silt mixture (34% clay) (Figure 5.14). However, the porosity of the natural clay declines more with increasing effective stress than the silty clay because it is almost entirely composed of clay minerals, whereas the silty clay has 50% silt-grade quartz. For vertical effective stresses larger than 5 MPa, the compression curves of both clays (only shown for loading curve) bound the compression curves of Nankai-silt mixtures (Figure 5.14).

The compression curves of Nankai –silt mixtures have similar slopes as the smectite – kaolinite mixtures (Mondol et al., 2008) and fit in between the 100% kaolinite and 60% kaolinite – 40% smectite mixture (Mondol et al., 2008) (Figure 5.14). This is not surprising as the Nankai mudstone is mostly composed of smectite and silt (Figure 5.5). The silt in the Nankai mudstone is comparable in grain size to the kaolinite in

Mondol et al.'s (2008) mixtures because kaolinite has the largest clay particle size out of the four main clay mineral groups (kaolinite, illite, chlorite, and smectite). In contrast, the kaolinite – silt mixtures (Mondol, 2009) show very different slopes across the compression curves. The 51% clay sample of the Nankai – silt mixtures shows a similar trend as the 50% silt – 50% kaolinite at high effective stresses. However, at low effective stresses the porosity of the 51% sample is higher due to the larger amount of small-sized smectite minerals.

The porosity – permeability relationships of Nankai – silt mixtures fall right in the middle of all mentioned studies. In general, the trends of the Nankai – silt mixtures are steeper than other published results and most similar to the pure smectite of Mondol et al. (2008) (Figure 5.15). I hypothesize that mineralogy is the reason for the different porosity - permeability trends. Smectite shows the largest decrease in permeability at a given porosity out of all clay minerals and mixtures shown here (Figure 5.15). This is due to its small particle size, large surface area, and small pore size (Mesri and Olson, 1971; Mondol et al., 2008). In addition, the amount of bound water (double layers) may also play a role, depending on the pore water composition (Mondol et al., 2008). The permeability of kaolinite decreases less with porosity than the permeability of smectite (Mondol et al., 2008) (Figure 5.15) and less than the permeability of silt (Mondol, 2009) (Figure 5.15). This means if one mixes kaolinite and silt, the permeability difference between both mineralogies decreases with decreasing porosity (converging trend), whereas if one mixes smectite with silt, the permeability difference increases with decreasing porosity (diverging trend) as observed by Mondol et al. (2010). Since my samples are mostly composed of smectite and silt (Figure 5.5) my results agree with Mondol et al.'s (2010) results with respect to the slope of the porosity – permeability

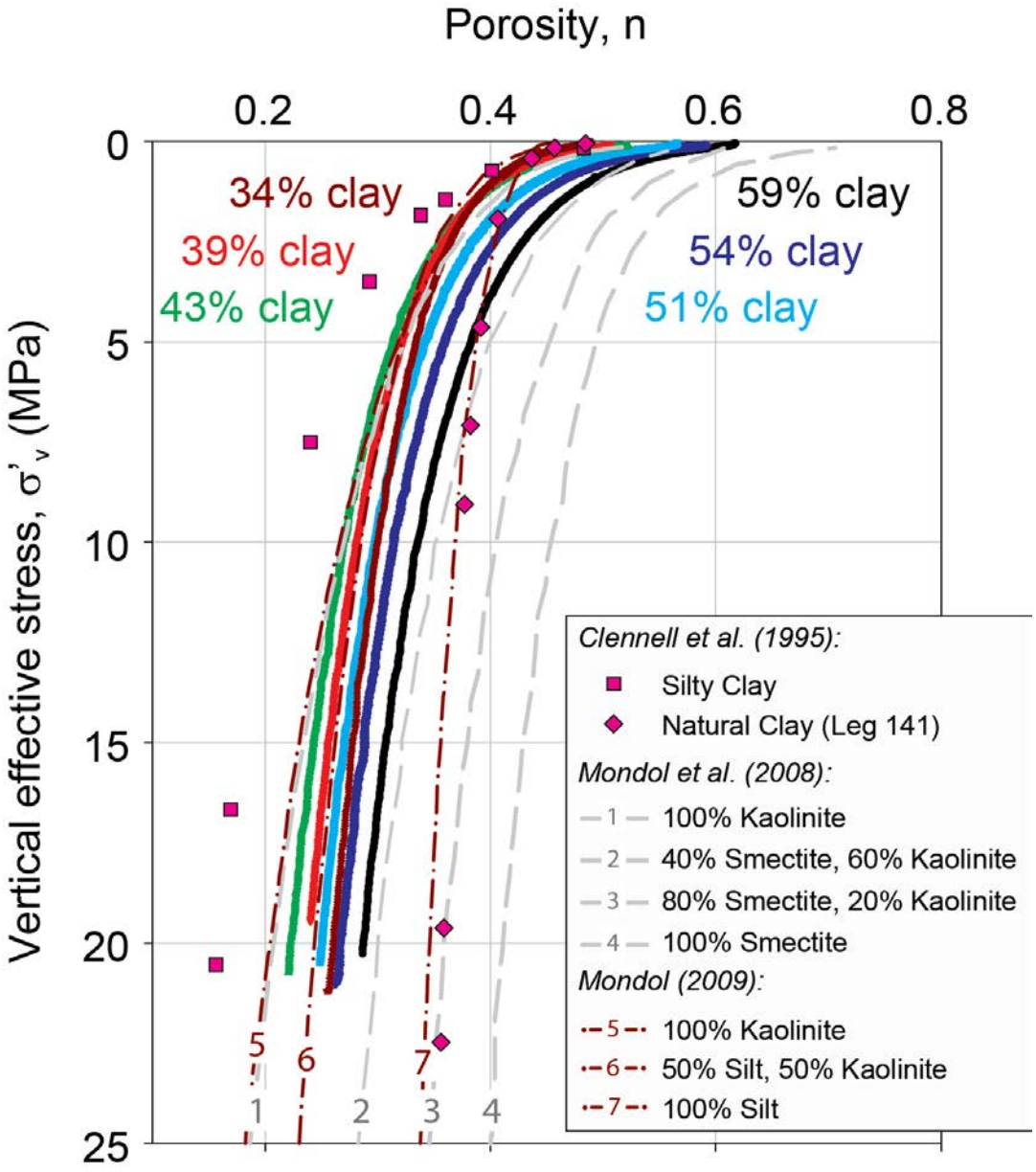

Figure 5.14: Comparison of compression behaviors of Nankai – silt mixtures through uniaxial constant-rate-of-strain consolidation tests (Table 5.1) with those of other laboratory-prepared mudstones. Clennell et al. (1999) performed constant-rate-of-flow permeability tests at various stresses in a modified oedometer setup on four different clays. Shown here are the results for a silty clay and a natural clay collected during ODP Leg 141. Studies on kaolinite – smectite mixtures, and kaolinite – silt mixtures were published by Mondol et al. (2008) and Mondol (2009), respectively.

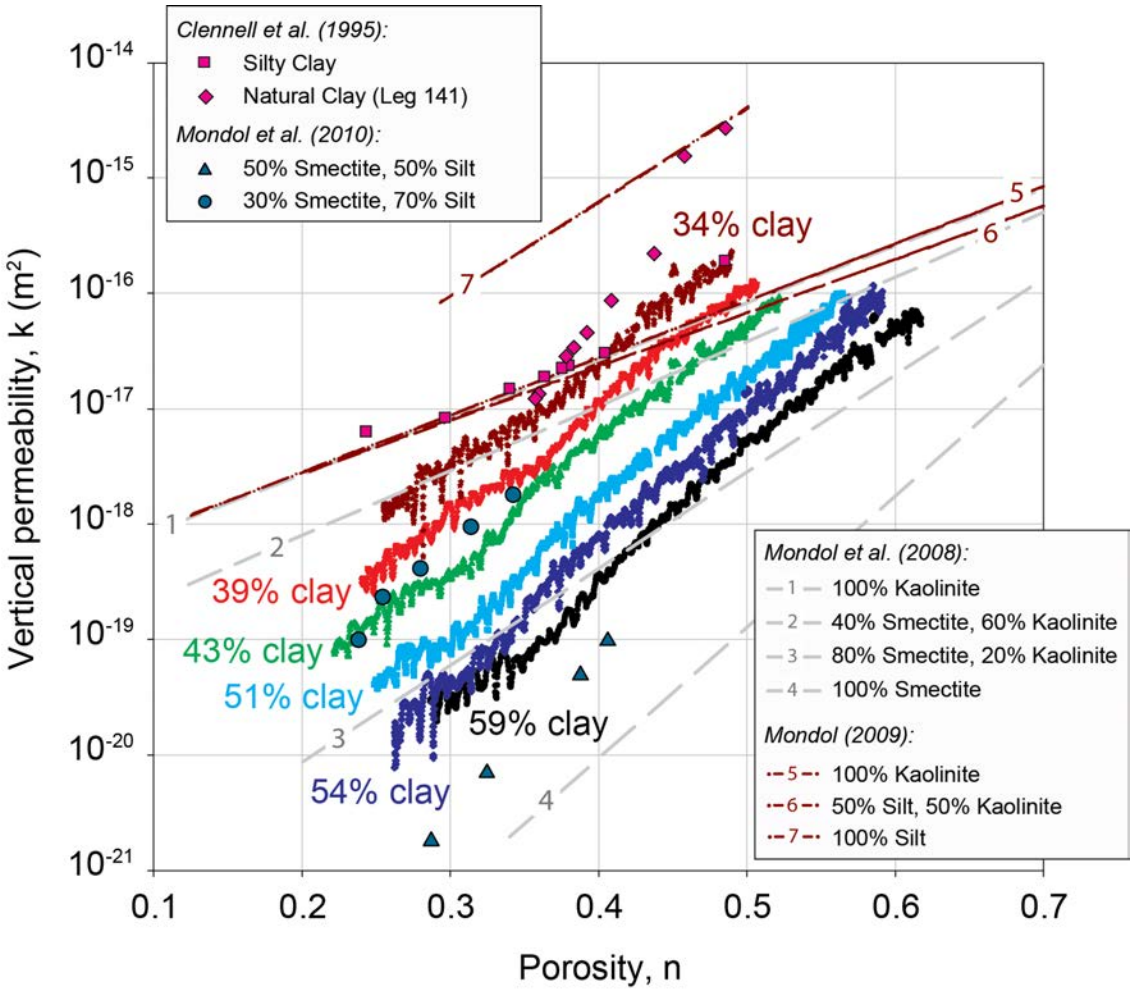

Figure 5.15: Comparison of porosity – permeability trends of Nankai – silt mixtures derived from uniaxial constant-rate-of-strain consolidation tests (Table 5.1) with those of other laboratory-prepared mudstones. Clennell et al. (1999) performed constant-rate-of-flow permeability tests at various stresses in a modified oedometer setup on four different clays. Shown here are the results for a silty clay and a natural clay collected during ODP Leg 141. Studies on kaolinite – smectite mixtures, kaolinite – silt mixtures, and smectite – silt mixtures were published by Mondol et al. (2008), Mondol (2009), and Mondol et al. (2010), respectively.

relationship. Absolute permeabilities in Mondol et al. (2010) are lower though than permeabilities of Nanaki – silt mixtures for comparable clay fractions. Despite the different techniques among all studies (transient pulse decay, oedometer permeameter, constant-rate-of-strain, modeling), I do not believe that the experimental approach has a large affect on the permeability - porosity trends. Dewhurst et al. (1996) showed that measurements of permeability using the constant-rate-of-strain and flow pump tests gave almost identical results. Thus, at this point I do not understand why Mondol's et al. (2010) permeabilities are lower than permeabilities of Nankai-silt mixtures for comparable clay fractions.

In contrast to compressibility and permeability measurements on samples that were prepared in the laboratory, other studies built geological databases with compression and permeability information on hundreds of cores from around the world. These datasets are then used to describe mudstone relationships that are constrained over a large range of mudstones with varying properties (e.g. composition, clay fraction size) (Yang and Aplin, 2004; Yang and Aplin, 2010). Figures 5.16 and 5.17 show a comparison of compression and permeability behavior of the resedimented Nankai – silt mixtures and predicted compression and permeability behavior from field-derived models using the same clay fractions as in the Nankai – silt mixtures. Field-derived models are constrained over large depths (up to 3500 mbsf) corresponding to effective stresses of about 35 MPa under hydrostatic conditions. Because neither of the Yang and Aplin studies clearly defines clay fraction, I use clay fraction by mass to substitute into their models.

The conceptual approach used in Yang and Aplin's (2004) compression model is very similar to my approach. However, my measured compression curves show that the compression behavior cannot be captured with a linear void ratio – log effective stress

relationship. Thus, instead of using Burland's (1990) assumption that void ratio is proportional to the log of effective stress, I use a different compression model that fits v_0 and C to clay fractions of systematically prepared samples with known compositions. Yang and Aplin's (2004) compression model predicts for the same clay fractions of the Nankai-silt mixtures slightly higher initial porosities and a less pronounced porosity reduction at low stresses (Figure 5.16). As a result, at high effective stresses, porosities predicted by Yang and Aplin (2004) are lower than measured porosities for the same clay fractions in this study. The vertical effective stress where both measurement and prediction agree is highest for the 43% clay sample (at 14 MPa) and decreases for both decreasing and increasing clay fractions. This behavior is due to a so called cross-over which is discussed in the next section. The difference in compression behaviors is due to a simplification in Yang and Aplin's (2004) model. The clay fraction in their model, which the compression trend is dependent on, is averaged over a compilation of geological samples with various mineralogies from the North Sea and Gulf of Mexico. Different clay minerals have not only different particle sizes, thus affecting clay content, but also different plasticities and likelihood to keep bound water, which affects compression but also permeability behavior. In contrast, I use mudstone mixtures of exactly the same components, just with varying clay-size fraction.

Despite the differences mentioned above, I predict permeabilities for the Nankai-silt mixtures measured here using Yang and Aplin's (2010) permeability-porosity model. The predicted permeabilities for the same clay fractions are in general about five times lower than the measured permeabilities at a given porosity. Also, my porosity – permeability trends are straight whereas Yang and Aplin's (2010) model predicts converging trends at both low and high porosities. Again, this difference in measurement and prediction appears to be due to a mineralogical effect. Yang and Aplin (2010) used a

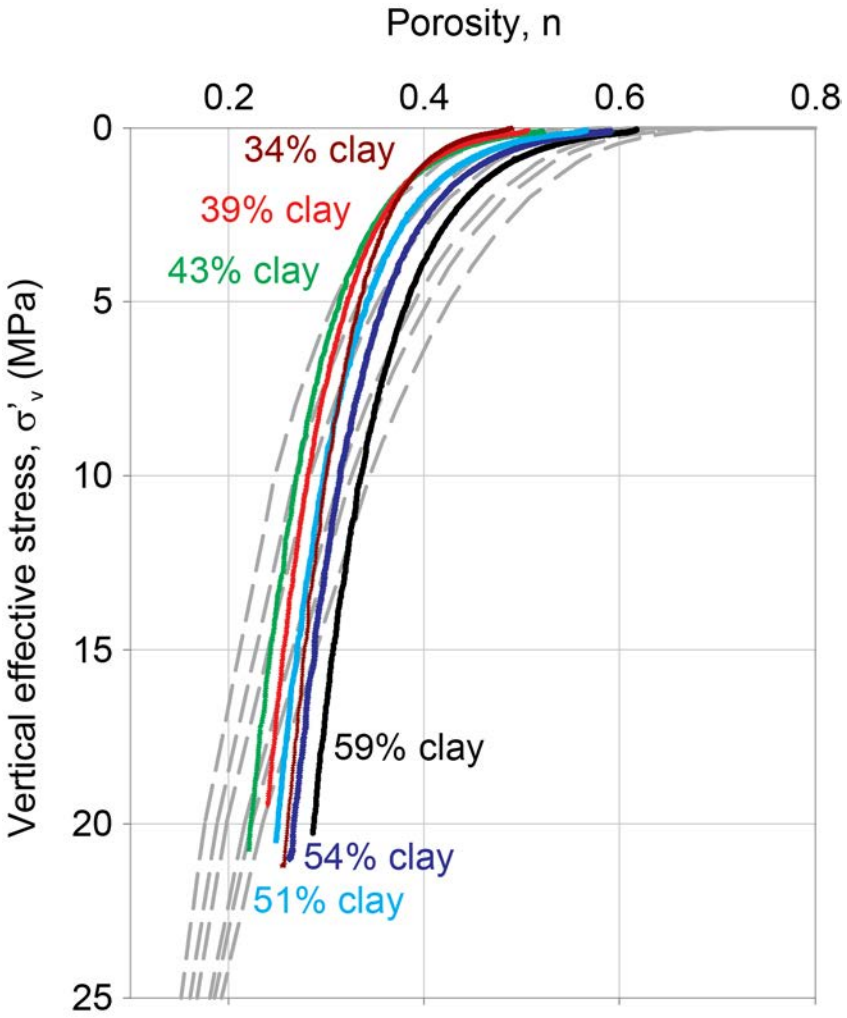

Figure 5.16: Comparison of compression curves of Nankai – silt mixtures through uniaxial constant-rate-of-strain consolidation tests (Table 5.1) with predicted compression curves using Yang and Aplin's (2004) compression model. Yang and Aplin's (2004) porosity – effective stress model is applied to the same clay fractions tested in Nankai-silt mixtures (gray dashed lines). Their compression model based on the effective stress principle established in soil mechanics by Terzaghi (1943), Skempton (1970), and Burland (1990) and was constrained by a large geological database.

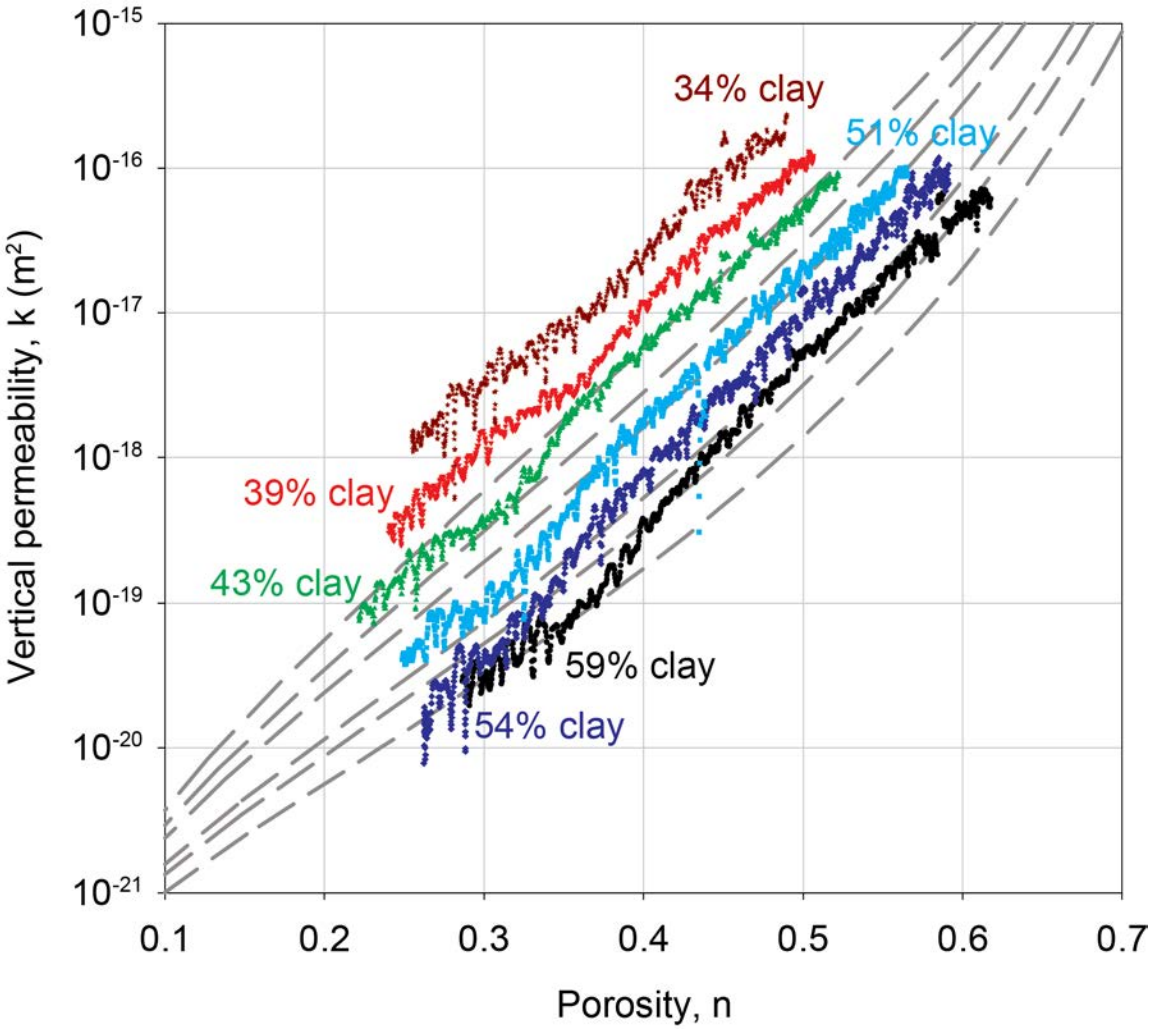

Figure 5.17: Comparison of porosity – permeability trends of Nankai – silt mixtures derived from uniaxial constant-rate-of-strain consolidation tests (Table 5.1) with predicted n – log k relationships using Yang and Aplin's (2010) permeability – porosity model. Yang and Aplin's (2004) permeability – porosity model is applied to the same clay fractions tested in Nankai-silt mixtures (gray dashed lines).Their permeability – porosity model was constrained by 376 data points measured with different methods on samples that were collected by different techniques from various regions.

compilation of cores from North Sea, Caspian Sea, Gulf of Mexico, and London Clay as well as reconstituted residual sediments and smectite in concentrated NaCl solution based on six different published studies to derive their model parameters. The actual porosity – permeability data Yang and Aplin's (2010) model is constrained over show large scatter.

The idea of predicting porosity and permeability of sediment mixtures during burial from the end-member compositions is similar to the approach used in dual-component models. Dual-component models describe consolidation and permeability equations assuming either an ideal or fractional packing model to derive properties of a mixture from properties of end-members and their respective volumetric contents (Koltermann and Gorelick, 1995; Revil and Cathles, 1999; Revil et al., 2002). These models predict a porosity and permeability minimum at a critical clay fraction, which shifts to higher clay fractions for increasing burial (Koltermann and Gorelick, 1995). This minimum reflects the packing where the large grains are touching and the small grains lie within the interstices of the large grains.

A porosity minimum also occurs in the Nankai - silt mixtures, at a volumetric clay fraction of 0.43 for vertical effective stresses higher than 2 MPa (Figure 5.18). The porosity minimum slowly develops with increasing vertical effective stress (Figure 5.18) and is not visible at low vertical effective stresses. At a vertical effective stress of 0.2 MPa, porosity consistently increases with clay fraction. At a stress of 2 MPa, porosity decreases to a volumetric clay fraction of 0.38 and either stays constant or further decreases until porosity increases again for clay contents larger than 0.43 (Figure 5.18). At another order of magnitude higher in effective stress, porosity has a minimum at 0.43. Based on observations by Koltermann and Gorelick (1995) and references therein, who showed that the porosity minimum shifts to higher clay fractions during consolidation, I hypothesize that a porosity minimum in my Nankai-silt mixtures is possibly present at

low effective stresses. However, it cannot be resolved in my data set. I would need more samples with lower clay fractions in order to show the potential porosity minimum at low vertical effective stresses.

The presence of a porosity minimum is consistent with a cross-over in compression curves; the compression curves of the three coarsest Nankai – silt mixtures plot at the same void ratio and vertical effective stress of approximately 1.5 MPa (Figure 5.7). Two competing processes cause this cross-over: 1) initial void ratio drops with decrease in clay fraction and 2) stiffness increases with decease in clay fraction, i.e. virgin consolidation line becomes flatter. Skempton (1970) already showed compaction curves for argillaceous sediments and noticed that finer grained muds (higher liquid limit) have higher initial void ratios, but compact more rapidly than coarser grained muds.

The fact that the cross-over occurs at a vertical effective stress of 1.5 MPa actually indicates that a porosity minimum should also be present at 2 MPa as observed in Figure 5.18. However, due to the larger sampling interval between measured clay fractions, the minimum is not as clear as at a vertical effective stress of 20 MPa. The cross-over indicates a transition from a matrix-supported to a grain-supported system equivalent to the transition from sandy shale to clayey sand domain in Revil et al. (2002).

Despite the porosity minimum, a minimum in permeability, as documented by Revil et al. (2002) as well as Koltermann and Gorelick (1995), and a minimum in compressibility cannot be observed in the Nankai mudstones (Figures 5.19, 5.20). Instead, coefficient of volume compressibility is relatively constant over varying clay fractions with the compressibility at 0.2 MPa being the largest and at 20 MPa being the smallest (Figure 5.19). Permeability at 0.2 MPa decreases slightly with increasing clay fraction (Figure 5.20). With increasing vertical effective stress the drop in permeability with clay fraction increases (Figure 5.20). Figure 5.20 indicates that the tortuosity, which

strongly affects permeability, increases with increasing vertical effective stress and clay fraction.

The absence of a minimum in compressibility and permeability could possibly be a result of the wide grain size distributions of Nankai – silt mixtures resulting in a different packing than the ideal or fractional packing assumed in dual-component models. This is in contrast to most of the dual-component models and the work on particle packing, which were developed for binary particle distributions (Koltermann and Gorelick, 1995).

Ideal packing, as assumed by Revil and Cathles (1999) and Revil et al. (2002), reproduces the observed porosity and permeability behavior if the ratio between coarsest and finest grain size is large, like in the case of sand and shale (Revil and Cathles, 1999). However, ideal packing might not succeed in approximating porosity and permeability behavior for natural geologic materials like the Nankai- silt mudstones, which are mixtures of silt-sized and clay-sized particles, in which grain size diameters vary widely and grain shapes are not perfect spheres. The smaller the diameter ratio, the more the porosity minimum occurs at higher porosity values (Koltermann and Gorelick, 1995) resulting in a less pronounced minimum. Similarly, the minima in compressibility and especially permeability appear to have been erased due to the smaller range in particle sizes, wide grain size distributions, and various grain shapes and angularities. These properties might cause different packing than ideal or fractional packing as assumed in dual-component models.

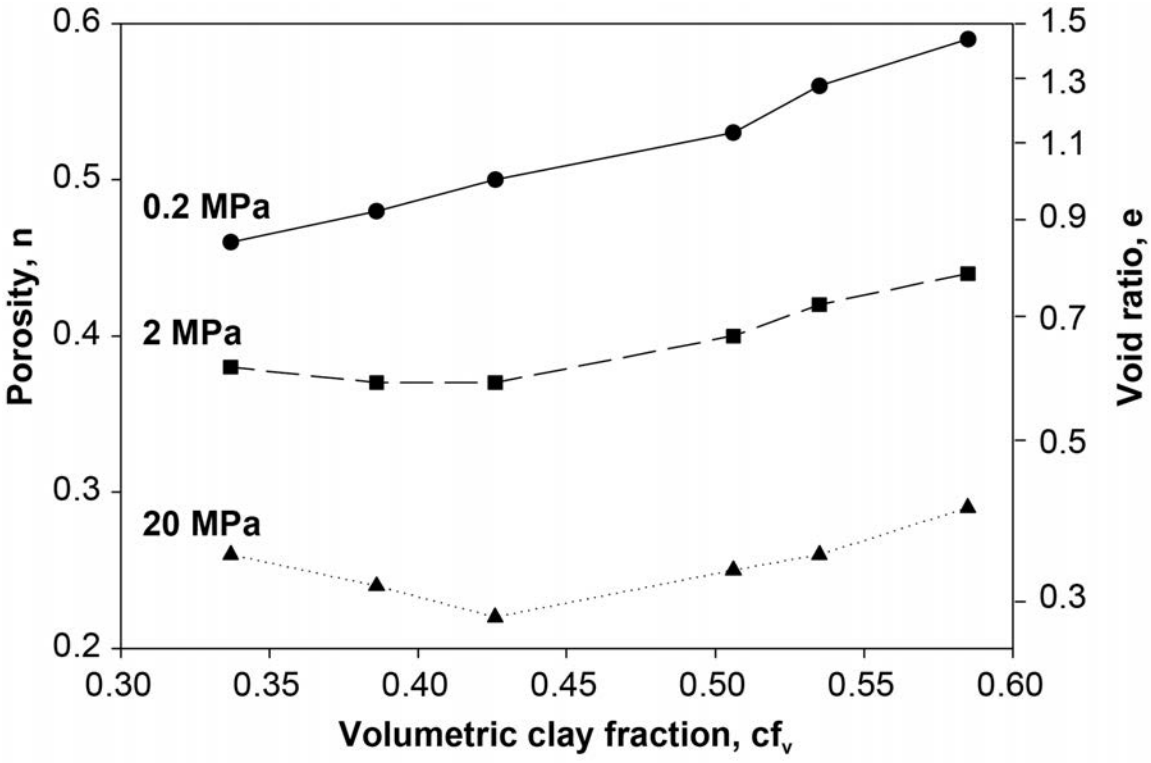

Figure 5.18: Porosity versus volumetric clay fraction at varying vertical effective stresses: 0.2 MPa (circles and solid line), 2 MPa (squares and dashed line), and 20 MPa (triangles and dotted line). A porosity minimum develops with increasing vertical effective stress.

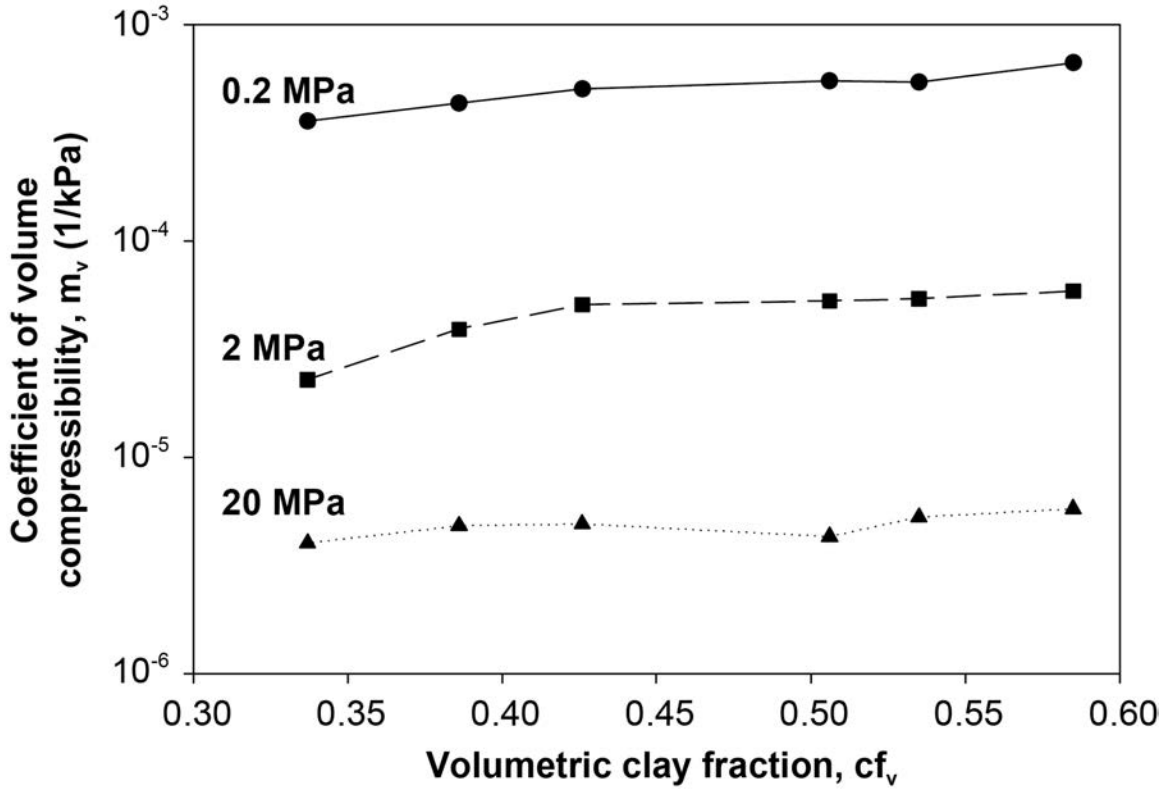

Figure 5.19: Coefficient of volume compressibility versus volumetric clay fraction at varying vertical effective stresses: 0.2 MPa (circles and solid line), 2 MPa (squares and dashed line), and 20 MPa (triangles and dotted line). A minimum coefficient of volume compressibility does not develop with increasing vertical effective stress.

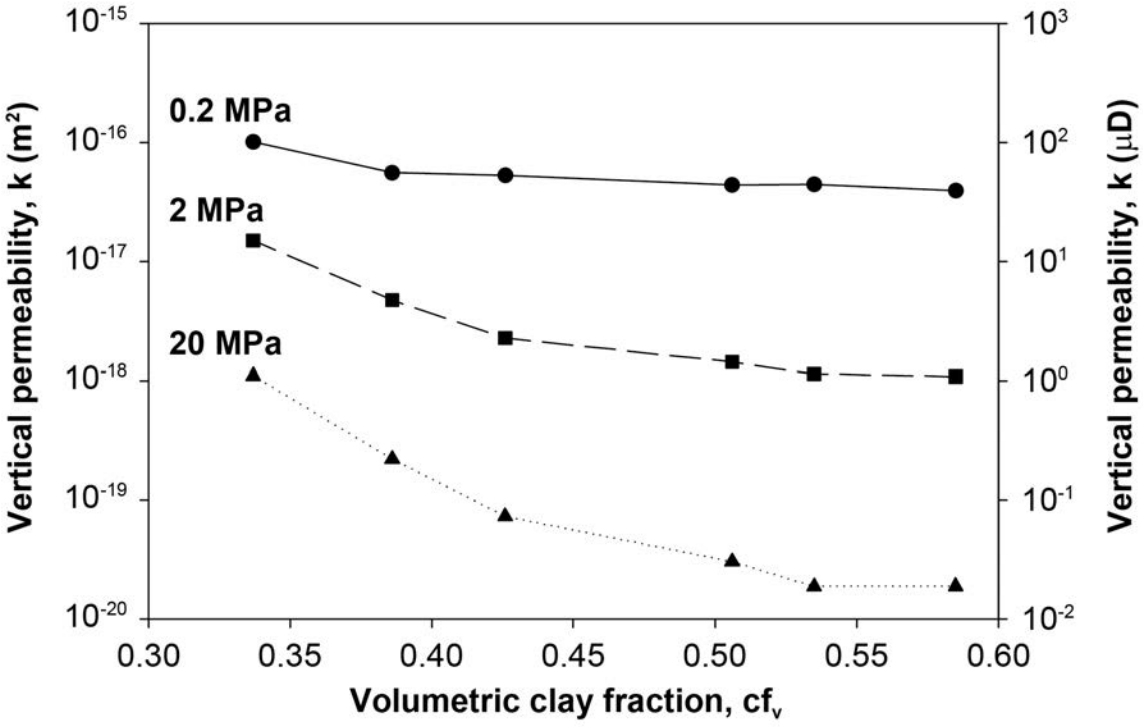

Figure 5.20: Vertical permeability versus volumetric clay fraction at varying vertical effective stresses: 0.2 MPa (circles and solid line), 2 MPa (squares and dashed line), and 20 MPa (triangles and dotted line). A permeability minimum does not develop with increasing vertical effective stress.

The geometric model works well for Nankai – silt mixtures because it reflects a dual-porosity system (Figure 5.21) as observed in the samples: small pores (on the order of 0.1 μm) within the clays where flow is limited and large pores within the silts where most of the flow occurs. Permeability is controlled by large pores (up to 5 μm in diameter), which form high permeability pathways. However, the smaller pores interact with the larger pores at a smaller rate resulting in different solute transport and longer times for the depletion of a reservoir, for example.

Different pore structures can be identified in the scanning electron images (Figure. 5.22). In the pure Nankai mudstone, most of the pores are either elongated pores between similarly oriented clay sheets or triangular to crescent-shaped pores in folded clays, particular in between smectites (Figures 5.22A, B). Only where silt grains touch other silt grains silt bridges are formed and larger jagged pores can be preserved in compaction shadows (Figures 5.22A, B). The nomenclature for pore types is adapted from Heath et al. (2011). Far away from large grains, the clay particles have undergone reorientation from an assumed random orientation of floccs (e.g. O'Brien, 1971) and show a preferred alignment that is perpendicular to the applied vertical load. However, in the vicinity of larger particles such as silt grains or muscovite, smaller clay particles are compressed against the large particles and folded in response to the local stress field. In the coarser Nankai – silt mixtures with 39% and 34% clay, the pores are much larger than in the sample with 59% clay because more grain-to-grain contacts are present prohibiting clay particles from aligning and filling in pores in between silt grains (Figures 5.22I- L). Smectites are shielded from the applied stress as can be seen by the wavy texture at a clay fraction of 34% (Figure 5.22K, L). Most of the pores are large jagged pores around silt grains, which are the pathways that are easily accessible to flow and, thus, control the permeability. There is a gradual increase in mean pore size with decreasing clay fraction.

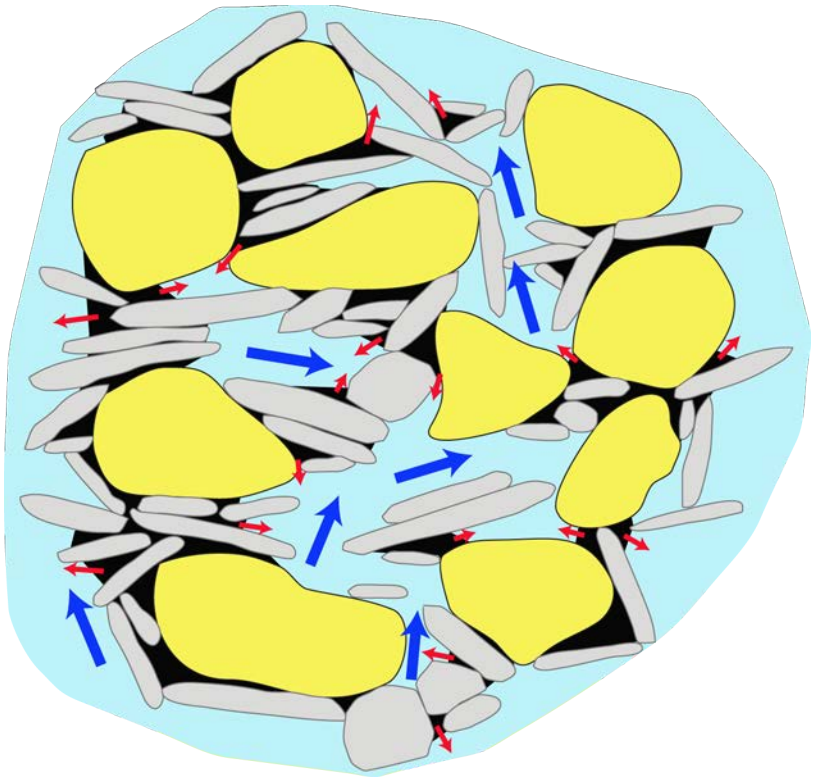

Figure 5.21: Cartoon illustrating the dual-porosity system. Most of the flow (blue arrows) occurs through large pores (light blue). Limited flow (red arrows) occurs at slower rates through small pores (black), which interact with large pores.

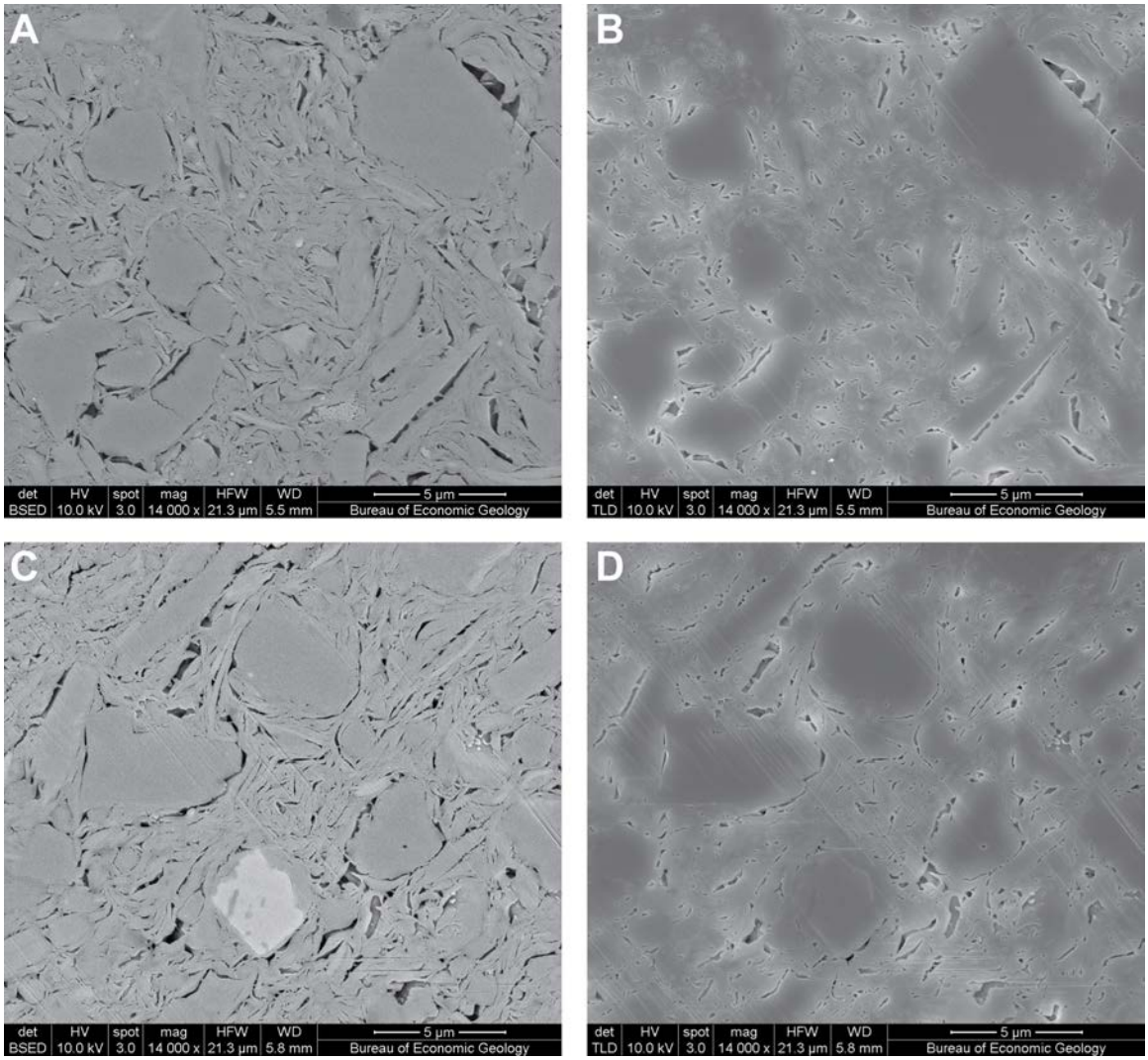

Figure 5.22: Scanning electron microscope images of Nankai –silt mixtures at maximum vertical effective stress of 20 MPa. Images represent vertical cross-section, i.e. load was applied from the top of the images. Left column are backscattered electron images. Right column are secondary electron images. A, B) Pure Nankai mudstone (59% clay) (SEM041_BSE_02b_UT.tif and SEM041_TLSE_02b_UT.tif). C, D) 54% clay. (SEM042_BSE_02b_UT.tif and SEM041_TLSE_02b_UT.tif)

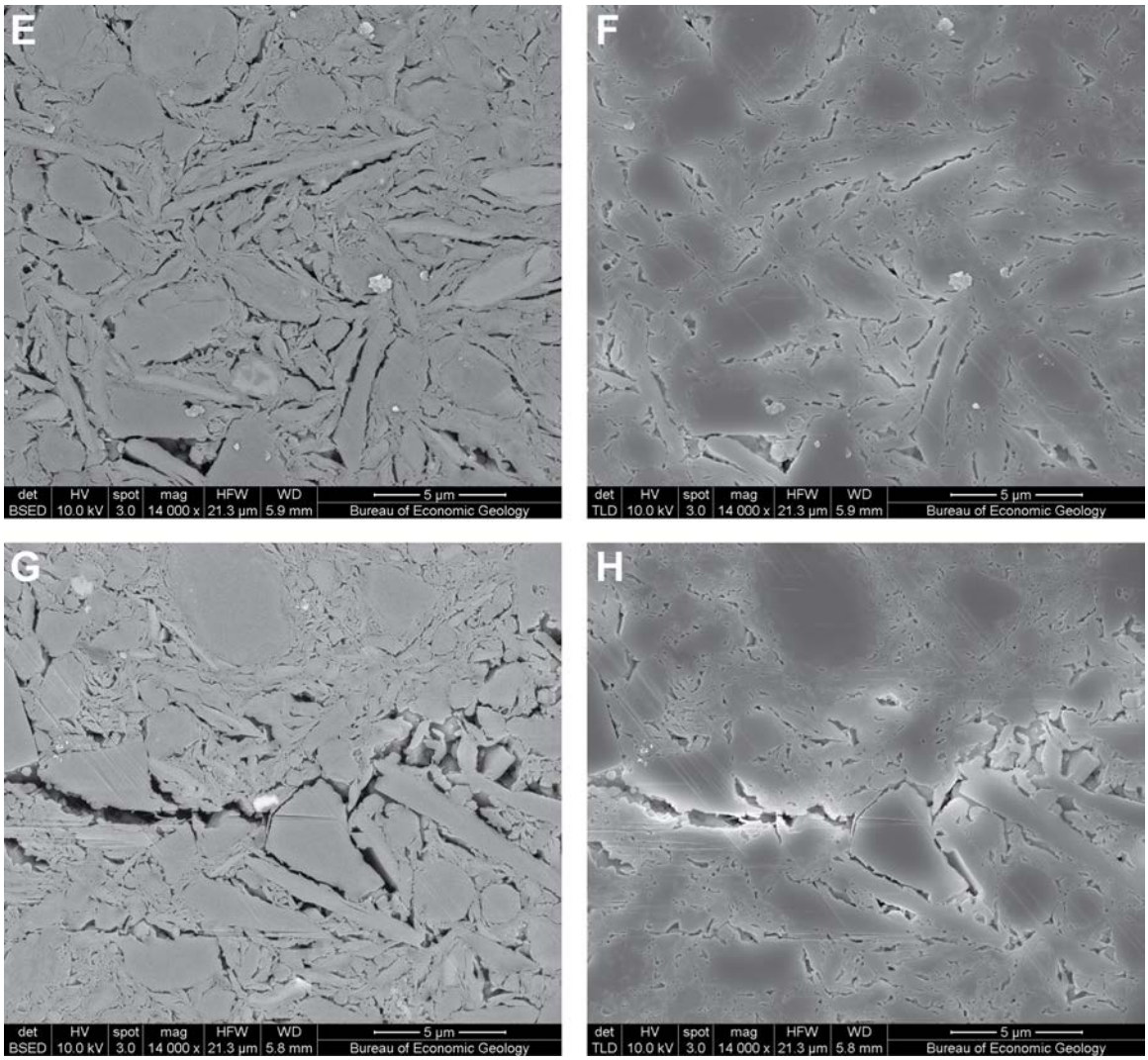

Figure 5.22: Continued. Scanning electron microscope images of Nankai –silt mixtures at maximum vertical effective stress of 20 MPa. Images represent vertical cross-section, i.e. load was applied from the top of the images. Left column are backscattered electron images. Right column are secondary electron images. E, F) 51% clay (SEM043_BSE_03b_UT.tif and SEM043_TLSE_03b_UT.tif). G, H) 43% clay (SEM044_BSE_03b_UT.tif and SEM044_TLSE_03b_UT.tif).

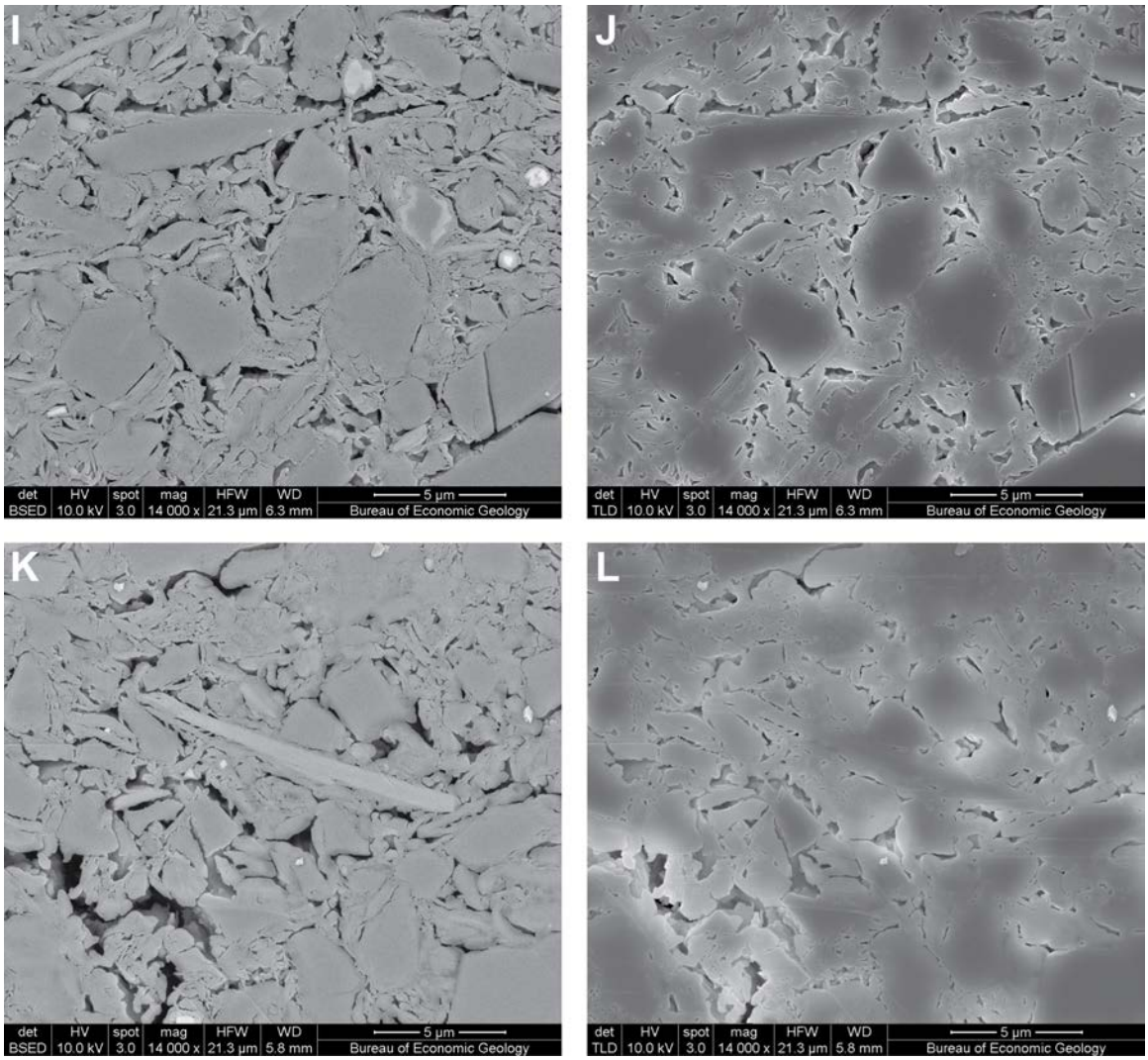

Figure 5.22: Continued. Scanning electron microscope images of Nankai –silt mixtures at maximum vertical effective stress of 20 MPa. Images represent vertical cross-section, i.e. load was applied from the top of the images. Left column are backscattered electron images. Right column are secondary electron images. I, J) 39% clay (SEM045_BSE_02b_UT.tif and SEM045_TLSE_02b_UT.tif). K, L) 34% clay (SEM046_BSE_01b_UT.tif and SEM046_TLSE_01b_UT.tif).

The coupled compressibility-permeability model developed in this study allows me to predict porosity, permeability, compressibility, and coefficient of consolidation for Nankai mudstones with varying clay fractions as a function of vertical effective stress or depth (if pore fluid pressures are known). The derived model parameters are mudstone specific but can be constrained for other materials if at least two uniaxial consolidation tests and information about material are available. In case of the compression part of the coupled model, more than two consolidation tests would significantly improve the prediction due to the non-linear relationship between v_0 and clay fraction (cf_v). Because of its universal application the couple permeability-compressibility model has large implications. It helps to constrain key input parameters for basin models and improve pore pressure predictions as well as accretionary wedge models, which predict morphology, geometry, and pore fluid pressures in the accretionary prisms.

5.6 CONCLUSIONS

I find that clay-rich, smectitic mudstones are more compressible and have a lower permeability at a given vertical effective stress than silt-rich mudstones due to the intensified loss of large pores at low stresses. I developed a generalized model that predicts porosity, permeability, compressibility, and thus hydraulic diffusivity (coefficient of consolidation) of marine mudstones with varying grain sizes from offshore Japan as a function of vertical effective stress or depth if pore fluid pressures are known. These results have large geologic implications and apply to carbon sequestration, basin models, pore pressure predictions, and predictions of geometry and morphology of thrust belts and pore pressure distribution in thrust belts.

NOMENCLATURE

Symbol	*Name*	*Unit*
cfv	volumetric clay fraction (< 2 μm)	dimensionless
C	exponent in Long et al.'s (2011) model	dimensionless
C_v	hydraulic diffusivity	m^2/s
C_c	compression index	MPa^{-1}
e	void ratio	dimensionless
k	vertical permeability	m^2
k_0	y-intercept of log-linear relationship between permeability and porosity	m^2
k_0^{cl}	model parameter: y-intercept of log-linear relationship between permeability and porosity for pure clay	m^2
k_0^{si}	model parameter: y-intercept of log-linear relationship between permeability and porosity for pure silt	m^2
k_{eff}	effective permeability based on geometric mean model	m^2
m_v	coefficient of volume compressibility	kPa^{-1}
n	porosity	dimensionless
v	specific volume	dimensionless
v_0	specific volume at vertical effective stress of 1 MPa (based on Long et al.'s (2011) model)	dimensionless
γ	slope of log-linear relationship between permeability and porosity	m^2
γ_{cl}	model parameter: slope of log-linear relationship between permeability and porosity for pure clay	m^2
γ_{si}	model parameter: slope of log-linear relationship between permeability and porosity for pure silt	m^2
λ^*	overpressure ratio	dimensionless
μ	dynamic viscosity	Pa s
σ_v	applied vertical stress	MPa
σ'_v	vertical effective stress	MPa

ACKNOWLEDGEMENTS

The University of Texas GeoFluids Consortium (supported by 11 energy companies) and the Schlanger Ocean Drilling Fellowship from the Consortium for Ocean Leadership provided funding. We thank Robert M. Reed for taking the backscattered electron images.

REFERENCES

Aplin, A.C., Yang, Y.L., and Hansen, S., 1995. Assessment of beta, the compression coefficient of mudstones and its relationship with detailed lithology. *Marine and Petroleum Geology*, 12(8): 955-963, doi:10.1016/0264-8172(95)98858-3.

ASTM International, 2006. Standard test method for one-dimensional consolidation properties of saturated cohesive soils using controlled-strain loading (Standard D4186-06). *In* Annual Book of ASTM Standards (Vol. 04.08), ed., Soil and Rock (I): West Conshohocken, PA, American Society for Testing and Materials, p. 15, doi:10.1520/D4186-06.

ASTM International, 2007. Standard test method for particle-size analysis of soils (Standard D422-63R07). *In* Annual Book of ASTM Standards (Vol. 04.08), ed., Soil and Rock (I): West Conshohocken, PA, American Society for Testing and Materials, p. 10-17, doi:10.1520/D0422-07.

Athy, L.F., 1930. Density, porosity, and compaction of sedimentary rocks. *Am. Assoc. Pet. Geol. Bull.*, 14: 1-22.

Bandini, P., and Sathiskumar, S., 2009. Effects of Silt Content and Void Ratio on the Saturated Hydraulic Conductivity and Compressibility of Sand-Silt Mixtures. *Journal of Geotechnical and Geoenvironmental Engineering*, 135(12): 1976-1980, doi:10.1061/(ASCE)GT.1943-5606.0000177.

Broichhausen, H., Littke, R., and Hantschel, T., 2005. Mudstone compaction and its influence on overpressure generation, elucidated by a 3D case study in the North Sea. *International Journal of Earth Sciences*, 94(5-6): 956-978, doi:10.1007/s00531-005-0014-1.

Burland, J.B., 1990. On the compressibility and shear strength of natural clays. *Geotechnique*, 40(3): 329-378.

Butterfield, R., 1980. A natural compression law for soils (an advance on e-logp'). *Geotechnique*, 29: 469-480.

Chandler, R.J., 2000. Clay Sediments in Depositional Basins: the Geotechnical Cycle. *Quaterly Journal of Engineering Geology and Hydrogeology*, 33: 7-39.

Clennell, M.B., Dewhurst, D.N., Brown, K.M., and Westbrook, G.K., 1999. Permeability anisotropy of consolidated clays. *In* Aplin, A.C., Fleet, A.J., and Macquaker, J.H.S., eds., Muds and Mudstones: Physical and Fluid Flow Properties, Volume 158: London, The Geological Society of London, p. 79-96.

Dewhurst, D.N., Brown, K.M., Clennell, M.B., and Westbrook, G.K., 1996. A comparison of the fabric and permeability anisotropy of consolidated and sheared silty clay. *Engineering Geology*, 42(4): 253-267, doi:10.1016/0013-7952(95)00089-5.

Dewhurst, D.N., Aplin, A.C., Sarda, J.P., and Yang, Y.L., 1998. Compaction-driven evolution of porosity and permeability in natural mudstones: An experimental study. *Journal of Geophysical Research*, 103(B1): 651-661, doi:10.1019/97JB02540.

Dewhurst, D.N., Aplin, A.C., and Sarda, J.P., 1999. Influence of clay fraction on pore-scale properties and hydraulic conductivity of experimentally compacted mudstones. *Journal of Geophysical Research*, 104(B12): 29261-29274, doi:10.1029/1999JB900276.

Heath, J.E., Dewers, T.A., McPherson, B.J.O.L., Petrusak, R., Chidsey, T.C., Rinehart, A.J., and Mozley, P.S., 2011. Pore networks in continental and marine mudstones: characteristics and controls on sealing behavior. *Geosphere, Advances in 3D imaging and and analysis of geomaterials themed issue*, 7(2): 429-454, doi:10.1130/GES00619.1.

Hillier, S., 2000. Accurate quantitative analysis of clay and other minerals in sandstones by XRD: comparison of a Rietveld and a reference intensity ratio (RIR) method and the importance of sample preparation. *Clay Minerals*, 35(1): 291-302.

Hyndman, R.D., Yamano, M., and Oleskevich, D.A., 1997. The seismogenic zone of subduction thrust faults. *Island. Arc*, 6: 244-260.

Karig, D.E., and Hou, G., 1992. High-stress consolidation experiments and their geologic implications. *Journal of Geophysical Research*, 97(B1): 289-300, doi:10.1029/91JB02247.

Kobayashi, K., Kasuga, S., and Okino, K., 1995. Shikoku Basin and its margins. *In* Taylor, B., ed., Backarc Basins: Tectonics and Magmatism: New York, Plenum, p. 381-405.

Koltermann, C.E., and Gorelick, S.M., 1995. Fractional packing model for hydraulic conductivity derived from sediment mixtures. *Water Resources Research*, 31(12): 3283-3297, doi:10.1029/95WR02020.

Long, H., Flemings, P.B., Germaine, J.T., and Saffer, D.M., 2011. Consolidation and overpressure near the seafloor in the Ursa Basin, Deepwater Gulf of Mexico. *Earth and Planetary Sceince Letters*, 305: 11-20, doi:10.1016/j.epsl.2011.02.007.

Loucks, R.G., Reed, R.M., Ruppel, S.C., and Jarvie, D.M., 2009. Morphology, genesis, and distribution of nanometer-scale pores in siliceous mudstones of the Mississippian Barnett Shale. *Journal of Sedimentary Research*, 79(12): 848-861, doi:10.2110/jsr.2009.092.

Mesri, G., and Olson, R.E., 1971. Mechanisms controlling the permeability of clays. *Clays and Clay Minerals*, 19: 151-158.

Mitchell, J.K., 1993. Fundamentals of soil behavior. Hoboken, N.J., John Wiley & Sons.

Miyazaki, S., and Heki, K., 2001. Crustal velocity field of southwest Japan: subduction and arc-arc collision. *Journal of Geophysical Research*, 106(B3): 4305-4326, doi:10.1029/2000JB900312.

Mondol, N.H., Bjørlykke, K., Jahren, J., and Høeg, K., 2007. Experimental mechanical compaction of clay mineral aggregates - Changes in physical properties of mudstones during burial. *Marine and Petroleum Geology*, 24: 289-311, doi:10.1016/j.marpetgeo.2007.03.006.

Mondol, N.H., Bjørlykke, K., and Jahren, J., 2008. Experimental compaction of clays: relationship between permeability and petrophysical properties in mudstones. *Petroleum Geoscience*, 14: 319-337, doi:10.1144/1354-079308-773.

Mondol, N.H., 2009, Porosity and permeability development in mechanically compacted silt-kaolinite mixtures, SEG Houston 2009 International Exposition and Annual Meeting: Houston, Society of Economic Geologists.

Mondol, N.H., Jahren, J., Berre, T., Grande, L., and Bjørlykke, K., 2010, Permeability anisotropy in mudstones - an experimental study, Search and DIscover Article #40649, AAPG Annual Convention and Exhibition: New Orleans, Louisiana, American Association of Petroleum Geologists.

Moore, G.F., Park, J.-O., Bangs, N.L., Gulick, S.P., Tobin, H.J., Nakamura, Y., Sato, S., Tsuji, T., Yoro, T., Tanaka, H., Uraki, S., Kido, Y., Sanada, Y., Kuramoto, S., and Taira, A., 2009. Structural and seismic stratigraphic frameworkof the NanTroSEIZE Stage 1 transect. *In* Kinoshita, M., Tobin, H., Ashi, J., Kimura, G., Lallemand, S.E., Screaton, E., Curewitz, D., Masago, H., Moe, K.T., and the Expedition 314/315/316 Scientists, eds., Proc. IODP 314/315/316: Washington, DC, Integrated Ocean Drilling Program Management International, Inc., doi:10.2204/iodp.proc.314315316.102.2009.

Moore, J.C., and Saffer, D., 2001. Updip limit of the seismogenic zone beneath the accretionary prism of southwest Japan: an effect of diagenetic to low-grade metamorphic processes and increasing effective stress. *Geology*, 29(2): 183-186, doi:10.1130/0091-7613(2001)029<0183:ULOTSZ>2.0.CO;2.

O'Brien, N.R., 1971. Fabric of kaolinite and illite floccules. *Clays and Clay Minerals*, 19: 353-359.

Okino, K., Shimakawa, Y., and Nagaoka, S., 1994. Evolution of the Shikoku Basin. *J. Geomagn. Geoelectr.*, 46: 463-479.

Park, J.-O., Tsuru, T., No, T., Takizawa, K., Sato, S., and Kaneda, Y., 2008. High-resolution 3D seismic reflection survey and prestack depth imaging in the Nankai Trough off southeast Kii Peninsula. *Butsuri Tansa*, 61: 231-241 (in Japanese with English abstract).

Revil, A., and Cathles, L.M., 1999. Permeability of shaly sands. *Water Resources Research*, 35(3): 651-662, doi:10.1029/98WR02700.

Revil, A., Grauls, D., and Brévart, O., 2002. Mechanical compaction of sand/clay mixtures. *Journal of Geophysical Research*, 107(B11): 2293, doi:10.1029/2001JB000318.

Santagata, M.C., and Kang, Y.I., 2007, Effects of geologic time on the initial stiffness of clays: Engineering Geology, v. 89, p. 98-111, doi: 10.1016/j.enggeo.2006.09.018.

Schneider, J., Flemings, P.B., Day-Stirrat, R.J., and Germaine, J.T., 2011. Insights into pore-scale controls on mudstone permeability through resedimentation experiments. *Geology*, 39(11): 1011-1014, doi:10.1130/G32475.1.

Seno, T., Stein, S., and Gripp, A.E., 1993. A model for the motion of the Philippine Sea Plate consistent with NUVEL-1 and geological data. *Journal of Geophysical Research*, 98(B10): 17941-17948, doi:10.1029/93JB00782.

Sheahan, T.C., 1991, An experimental study of the time-dependent undrained shear behavior of resedimented clay using automated stress path triaxial equipment [Ph.D. thesis]: Cambridge, Massachusetts Institute of Technology.

Skempton, A.W., 1970. The consolidation of clays by gravitational compaction. *J. Geol. Soc. London*, 125: 373-411.

Smith, J.E., 1971. The dynamics of shale compaction and evolution of pore fluid pressure. *Math. Geol.*, 3: 239-263.

Terzaghi, K., 1925. Erdbaumechanik auf bodenphysikalischer Grundlage. Leipzig, 399 p.

Terzaghi, K., 1943. Theoretical Soil Mechanics. London, Chapman and Hall, 510 p.

Tobin, H.J., Kinoshita, M., Ashi, J., Lallemant, S., Kimura, G., Screaton, E., Thu, M.K., Masago, H., Curewitz, D., and Expedition 314/315/316 Scientists, 2009. NanTroSEIZE Stage 1 expeditions: introduction and synthesis of key results, Proc. IODP, Volume 314/315/316: Washington, DC, Integrated Ocean Drilling Program Management International, Inc., doi:10.2204/iodp.proc314315316.101.2009.

Underwood, M.B., Saito, S., Kubo, Y., and the Expedition Scientists, 2009. NanTroSEIZE Stage 2: subduction inputs. *IODP Prel. Rept.*, 322, doi:10.2204/iodp.pr.322.2009.

Underwood, M.B., Saito, S., Kubo, Y., and IODP Expedition 322 Scientists, 2010. IODP Expedition 322 drills two sites to document inputs to the Nankai Trough subduction zone. *Scientific Drilling*, 10: 14-25, doi:10.2204/iodp.sd.10.02.2010.

Vasseur, G., Djeran-Maigre, I., Grunberger, D., Rousset, G., Tessier, D., and Velde, B., 1995. Evolution of structural and physical parameters of clays during experimental compaction. *Marine and Petroleum Geology*, 12(8): 941-954.

Vrolijk, P., 1990. On the mechanical role of smectite in subduction zones. *Geology*, 18: 703-707.

Yang, Y., and Aplin, A.C., 2010. A permeability-porosity relationship for mudstones. *Marine and Petroleum Geology*, 27: 1692-1697, doi:10.1016/j.marpetgeo.2009.07.001.

Yang, Y.L., and Aplin, A.C., 2004. Definition and practical application of mudstone porosity-effective stress relationships. *Petroleum Geoscience*, 10(2): 153-162.

Yang, Y.L., and Aplin, A.C., 2007. Permeability and petrophysical properties of 30 natural mudstones. *Journal of Geophysical Research*, 112(B03206), doi:10.1029/2005JB004243.

Chapter 6: Comparison of Boston Blue Clay and Nankai Mudstone

6.1 Introduction

Compressibility and permeability of mudstones is controlled by several parameters such as particle size and shape, and mineralogy. I showed compression and permeability behaviors of two different mudstones, Boston Blue Clay (Chapter 4 and Appendix 1) and Nankai mudstone (Chapter 5 and Appendix 2). But without a direct comparison it is difficult to understand the similarities and differences in their geomechanical behaviors and the cause for them. So here I want to compare both mudstones (BBC and Nankai mudstone) in their index parameters as well as their compression and permeability results and provide an explanation for why their behaviors are so different.

6.2 Comparing Results

Boston Blue Clay (BBC) is collected from different sites in the vicinity of Boston, Massachusetts, and thus has been subject to many investigations and studies at the Massachusetts Institute of Technology (MIT). Each amount of collected material is dried, ground, sieved, and homogenized and forms a new batch. Because each batch might have slightly different properties, reference tests are performed at MIT and each batch gets a series number assigned. The batch used in this research is referred to as BBC series IV.

Nankai mudstone was collected during Integrated Ocean Drilling Program (IODP) Expedition 322 from Hole C0011B on the seaward side of the Nankai Trough, offshore Japan, in a water depth of 4049 meters. Specifically, the mudstone was collected from a depth range between 586.8 to 774.7 mbsf. Because this mudstone is the first batch at The University of Texas at Austin that is collected, dried, ground, sieved, and

homogenized the Nankai mudstone is termed Nankai series I. For the remainder of this thesis, I refer to this material as Nankai mudstone.

6.2.1 Index properties

The grain size distribution is almost identical for two very different materials (Boston Blue Clay (BBC) and Nankai mudstone) from very different depositional environments. Grain size distributions were determined using the hydrometer method in accordance to ASTM D422-63 guidelines (ASTM International, 2007). Both mudstones are composed only of silt- and clay-sized particles and have similar fractions of particles smaller than 2 μm (by mass): BBC has 57% whereas Nankai mudstone has 59% (Table 6.1, Figure 6.1).

The mineralogy of both mudstones was determined through powder x-ray diffraction by *Macaulay Scientific Consulting LTD*. BBC is composed of quartz, plagioclase, muscovite, feldspar, tri-mica with lesser amounts of illite and illite-smectite mixed layer, hydrobiotite, chlorite, kaolinite, and remaining constituents (Table 6.2) (Figure 6.2A). Nankai mudstone contains a comparable amount of quartz, but less plagioclase and feldspar. Instead it is composed of a large amount of smectite with smaller amounts of illite, chlorite and kaolinite (Figure 6.2B).

Sample	*% Clay* [a]	*Resed #* [b]	*CRS #* [c]	*GS #* [d]
BBC	57	Resed 017	CRS 046	GS 094
Nankai	59	Resed 062 T	CRS 090	GS 147

Table 6.1: Summary table of various tests performed on Boston Blue Clay (BBC) and Nankai mudstone.

[a] % Clay: clay fraction by mass measured in grain size analysis (for test number see this table, column 5)
[b] Resed #: resedimentation test number; 'T' refers to top specimen out of the two specimens per resedimentation batch
[c] CRS #: constant-rate-of-strain (CRS) consolidation test number
[d] GS #: grain size analysis test number

Sample	*Quartz*	*Plagioclase*	*K-feldspar*	*Calcite*	*Dolomite*	*Pyrite*
BBC	21.3	20.5	8.2	0.5	0.8	0.0
Nankai	23.5	11.4	4.5	1.2	0.0	1.1

Halite	*Amphibole*	*Muscovite*	*Illite*	*Smectite*	*Illite + Illite-Smectite*
0.2	3.8	13.8	N/A	N/A	7.3
0.3	0.0	2.6	5.8	44.7	50.5

Kaolinite	*Chlorite*	*Tri-mica*	*Hydrobiotite*	*Talc*	*Total*
2.9	6.2	9.2	5.4	0.0	100.1
1.2	3.8	0.0	0.0	3.8	100.1

Table 6.2: Whole rock mineralogy as weight percent of Boston Blue Clay (BBC) (Resed 017, CRS 046) and Nankai mudstone (Resed 062, CRS 090) determined using the reference intensity ratio (RIR) method (Hillier, 2000).

The specific surface area, measured by *Micromeritics Analytical Services* using gas adsorption (Brunauer Emmett Teller (BET) method), is 32.3 m^2/g for Nankai mudstone and 23.9 m^2/g for BBC (Table 6.3). The slightly increased specific surface area of Nankai mudstone results from the increased amount of smectite. Smectite has a small particle size and, thus, adds to the specific surface area. However, the specific surface area of the Nankai mudstone is not as high as expected given the large amount of smectite in the sample. This is possibly a result of the technique used for the specific surface area measurement as described in more detail at the end of this chapter.

Atterberg limits such as liquid limit (*LL*), plastic limit (*PL*) and plasticity index (*PI*) are used to characterize the fine-grained fraction of soils and, together with other soil properties, to correlate with engineering behavior such as compressibility, hydraulic conductivity, intrinsic permeability, and shear strength, for example. Liquid and plastic limit are water contents that separate different consistency states from each other. I performed the multipoint liquid limit method (ASTM International, 2005) using a hand-operated liquid limit device, also called Casagrande cup. I determined the plastic limit by the hand method (ASTM International, 2005). The plasticity index is the range of water content over which the soil behaves plastically. It is also numerically the difference between the liquid limit and the plastic limit. The Atterberg limits are listed in Table 6.4. The liquid limit is significantly larger for Nankai mudstone than for BBC whereas plastic limits are relatively similar. Thus, the plasticity chart shows a low plasticity for BBC and high plasticity for Nankai mudstone (Figure 6.3). Nankai mudstone attracts water and needs more water to get to the same consistency state as the BBC.

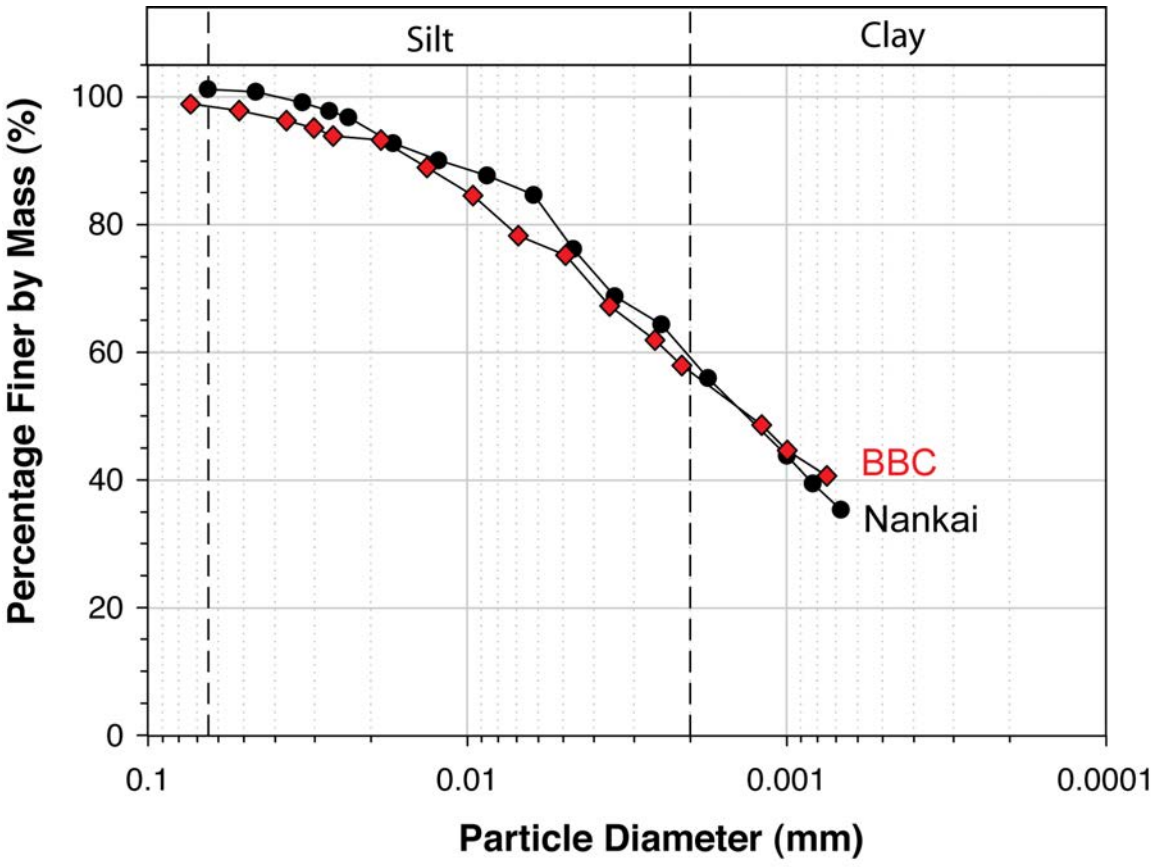

Figure 6.1: Comparison of grain size distributions determined through hydrometer analysis of Boston Blue Clay (BBC) (red) and Nankai mudstone (black) (Table 6.1).

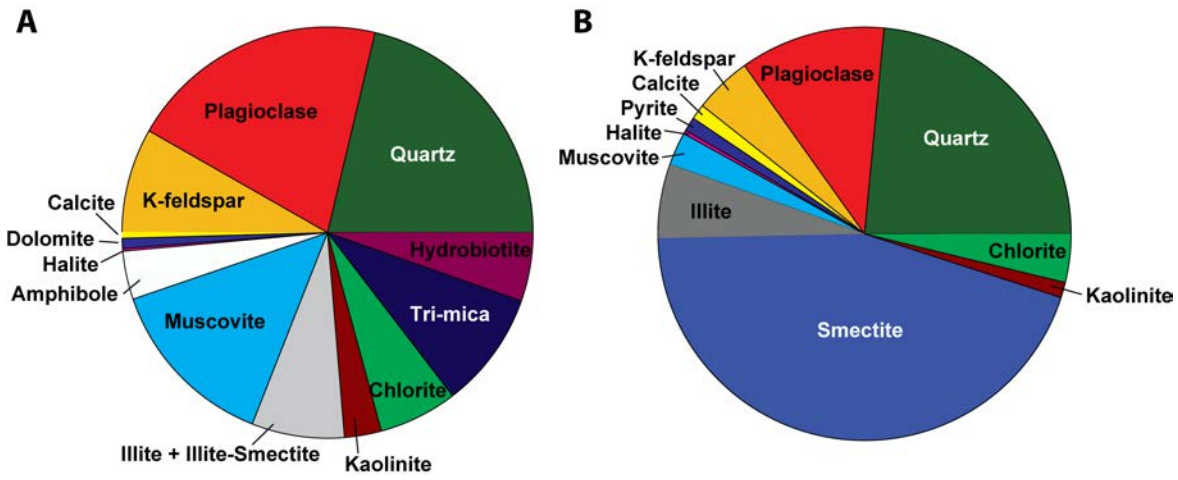

Figure 6.2: Comparison of whole rock mineralogies by percent (Table 6.2) of A) Boston Blue Clay (BBC) and B) Nankai mudstone. Mineralogy (X-Ray Powder Diffraction) was measured by *Macaulay Scientific Consulting LTD* using the reference intensity ratio (RIR) method (Hillier, 2000).

Mudstone	*Specific surface area (m^2/g)*
BBC	23.89
Nankai	32.26

Table 6.3: Comparison of specific surface areas of Boston Blue Clay (BBC) and Nankai mudstone. Specific surface areas were measured by *Micromeritics Analytical Services* using gas adsorption (Brunauer Emmett Teller (BET) method).

Mudstone	*Liquid Limit (%)*	*Plastic Limit (%)*	*Plasticity Index (%)*
BBC	46	23	23
Nankai	68	29	39

Table 6.4: Comparison of Atterberg Limits of Boston Blue Clay (BBC) and Nankai mudstone.

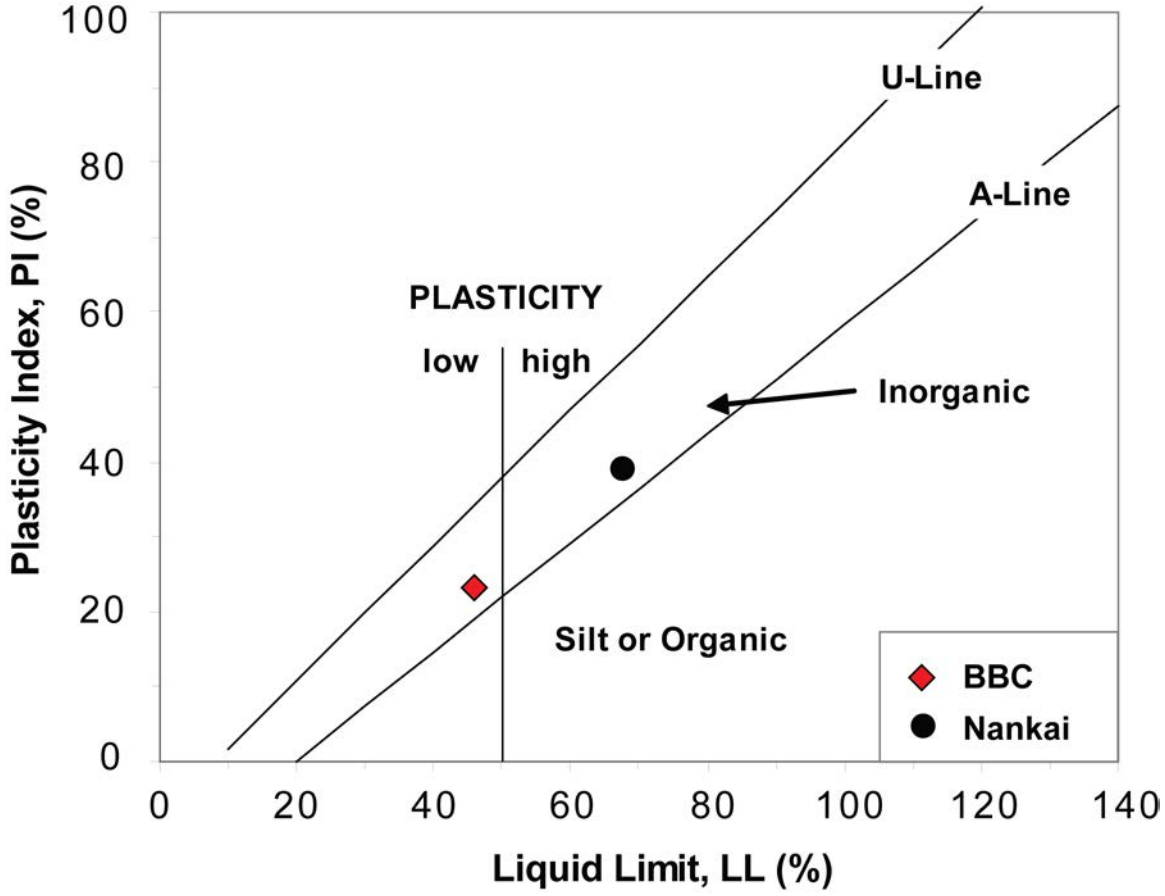

Figure 6.3: Comparison of plasticity states of Boston Blue Clay (BBC) (red) and Nankai mudstone (black). Plasticity index is the difference between liquid limit and plastic limit (see Table 6.4 for measurements).

6.2.2 Compression and permeability behavior

The compression and permeability behaviors are measured in uniaxial constant-rate-of-strain consolidation tests in accordance to ASTM Standard D4186-06 (ASTM International, 2006). The compression behavior is quite different for BBC and Nankai mudstone (Figure 6.4) except the preconsolidation stress at 100 kPa, which both compression curves have in common because both materials were resedimented to the same stress. The initial void ratio of BBC (1.23) is much lower than that of Nankai mudstone (1.63). The compression index of BBC is 0.35. Because the compression curve of Nankai mudstone is concave up, C_c is not constant with effective stress. At a similar stress range as for BBC (between 200 kPa and 1000 kPa) C_c of Nankai mudstone is approximately 0.65, almost twice the C_c of BBC. However, with higher stresses, C_c decreases. It appears from Figure 6.4 that if the BBC was consolidated to higher vertical effective streses, equivalent to those of the Nankai mudstone, both compression curves would cross-over at a vertical effective stress of approximately 10 MPa.

The log of permeability decreases linearly with decreasing porosity for both mudstones. However, the permeability – porosity trend of BBC is significantly different from the trend of Nankai mudstone (Figure 6.5). Permeability of BBC is larger than permeability of Nankai mudstone at a given porosity. The slope (γ) and the y-intercept $\log(k_0)$ of the log-linear relationship between permeability and porosity are smaller for BBC than for Nankai mudstone (Table 6.5) causing a divergence of both permeability trends with reduction in porosity. This means the difference between both vertical permeabilities at a given porosity increases with increasing consolidation (Figure 6.5).

Mudstone	γ	$log(k_0)$
BBC	7.6	-20.3
Nankai	11.1	-22.9

Table 6.5: Comparison of permeability properties of Boston Blue Clay (BBC) and Nankai mudstone.

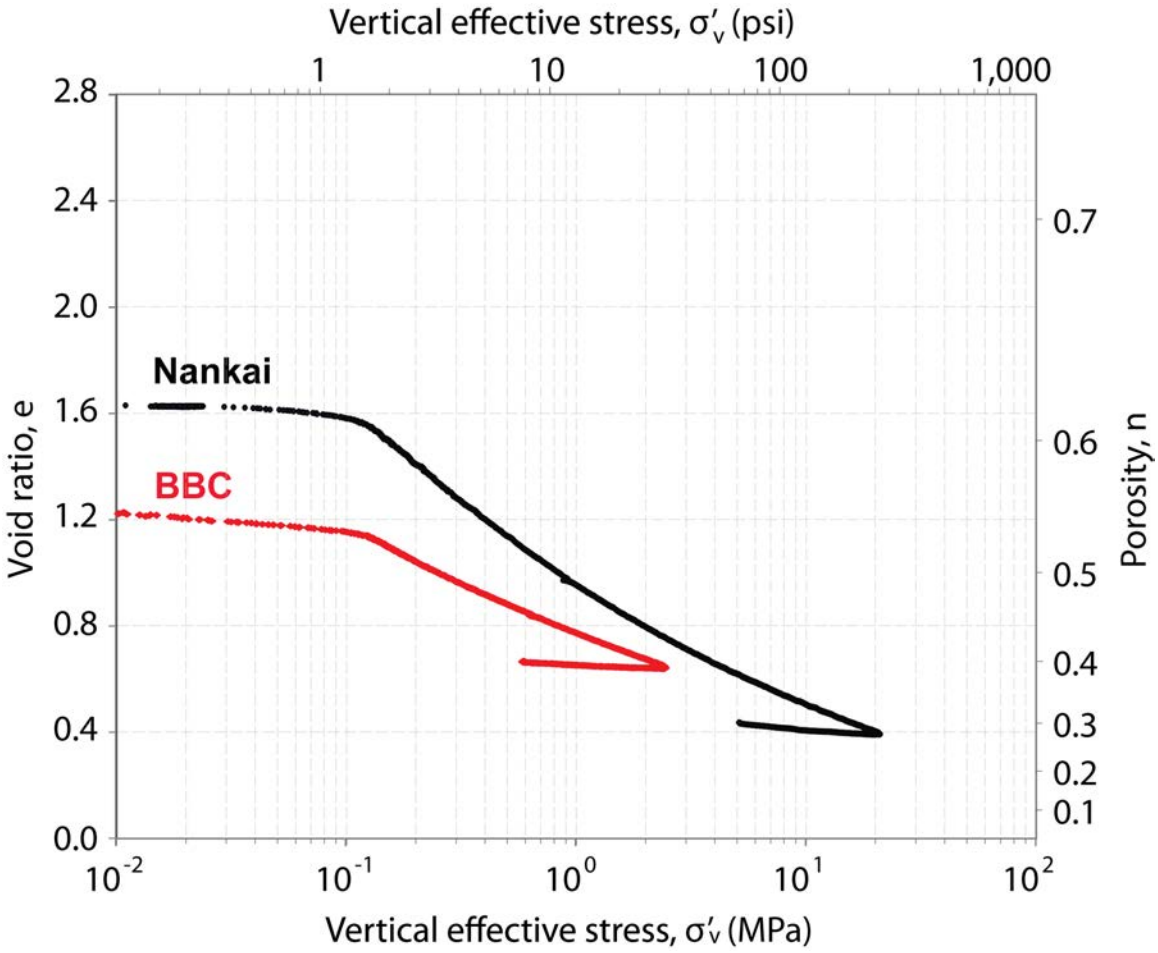

Figure 6.4: Comparison of compression curves of Boston Blue Clay (BBC) (red) and Nankai mudstone (black) determined through unaxial constant-rate-of-strain consolidation tests (Table 6.1). BBC was consolidated to 2.4 MPa, whereas Nankai was consolidated to 20 MPa. Both materials were resedimented to 100 kPa prior to uniaxial consolidation in constant-rate-of-strain load frame.

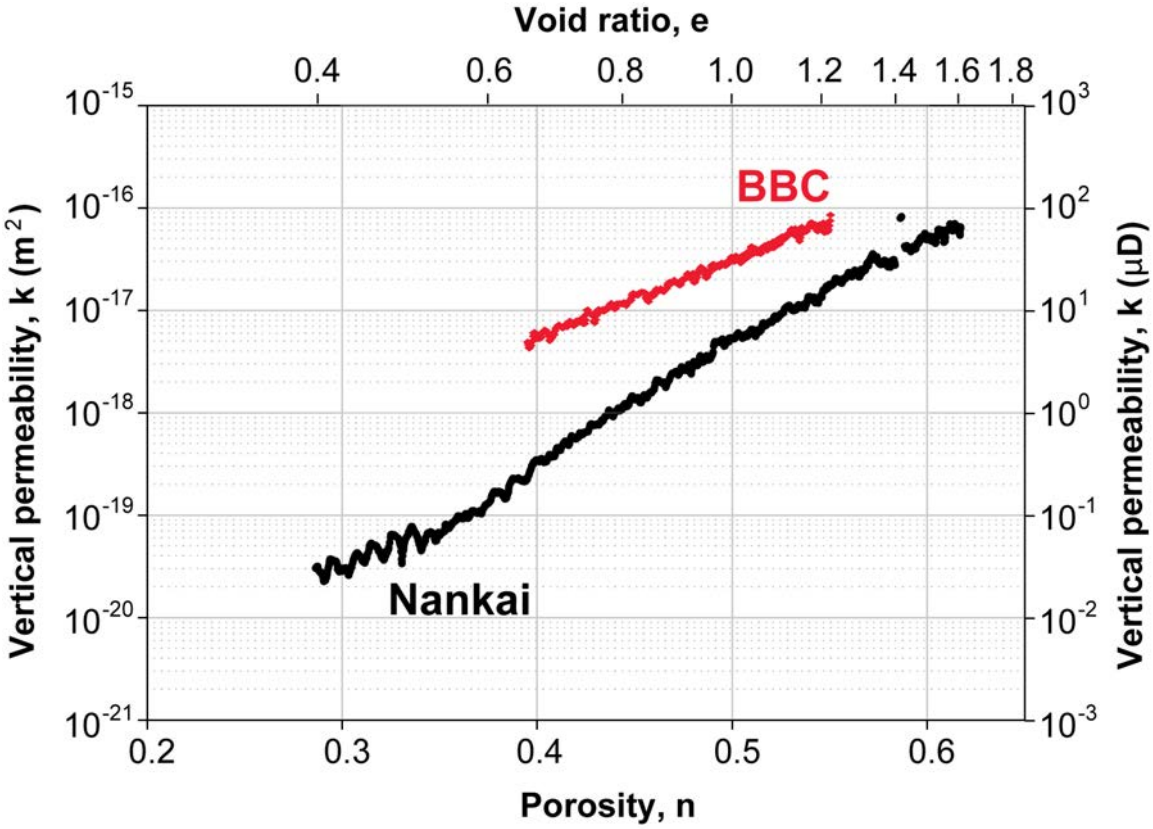

Figure 6.5: Comparison of permeability – porosity relationship of Boston Blue Clay (BBC) (red) and Nankai mudstone (black) derived from uniaxial constant-rate-of-strain consolidation experiments (Table 6.1).

Due to the large difference in vertical permeability and compressibility between BBC and Nankai mudstone, the coefficient of consolidation (C_v), which is the ratio of vertical permeability to coefficient of volume compressibility and dynamic viscosity, is drastically different. C_v of BBC slightly increases with vertical effective stress from about $8 \cdot 10^{-8}$ m^2/s at effective stresses close to 0 MPa to $1.7 \cdot 10^{-7}$ m^2/s at effective stresses larger than 2 MPa (Figure 6.6). In constrast, C_v of Nankai mudstone decreases with effective stress from $6 \cdot 10^{-8}$ m^2/s at effective stresses close to 0 MPa and approaches a constant value of $7 \cdot 10^{-9}$ m^2/s for effective stresses larger than 5 MPa (Figure 6.6).

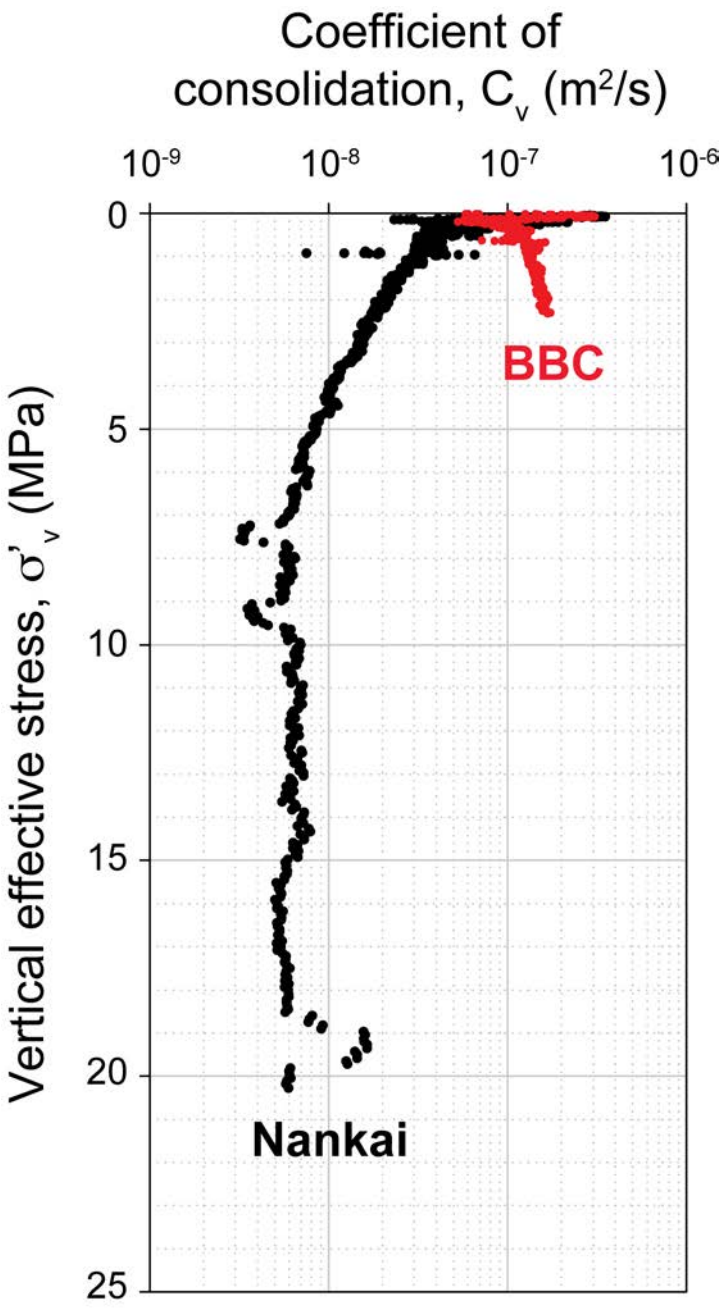

Figure 6.6: Comparison of coefficient of consolidation of Boston Blue Clay (BBC) (red) and Nankai mudstone (black) derived from uniaxial constant-rate-of-strain consolidation tests (Table 6.1).

6.3 DISCUSSION

Boston Blue Clay (BBC) and Nankai mudstone are mudstones from very different depositional environments. BBC is a glacio-marine meltwater deposit. Glaciers were advancing and receding across the Boston area during glacial and interglacial periods. The last major ice sheet retreated 15,000 years ago. As the climate changed to warmer temperatures, glaciers melted causing meltwater streams loaded with glacial clays, muds, and sands flowing away from the edges of glaciers (Phipps, 1964). Due to the release of water from melting glaciers and the isostatic rebound, sea level rose to about +60 feet 14,000 years ago (Kaye and Barghoorn, 1964) allowing deposition of marine sediments. Large amounts of debris including gravel and sand were deposited at edge of the glacier. The rock dust and clays, however, were carried into the ocean by glacial streams, deposited in a sedimentary basin (Phipps, 1964), and formed up to 100 feet thick layers of Boston Blue Clay in some places (Mencher et al., 1968), underlying almost all of Boston and Boston Harbor (Kaye and Barghoorn, 1964). Due to its glacio-marine origin BBC was deposited in saline water but with the influence of fresh meltwater. Thus, salinities of depositional environment were lower than they were for the Nankai mudstone. BBC derives its mineralogy from the Canadian Shield source rock through erosion and transport by glaciers. BBC clay minerals are mostly illite and chlorite, where illite resists chemical weathering and is common on most continental soils and chlorite is a typical product of physical weathering of plutonic and metamorphic rocks as well as shales (Biscaye, 1965). The amount of chlorite tends to increase toward higher latitude where physical weathering predominates (Biscaye, 1965).

Nankai mudstone is a hemipelagic sediment deposited in 4049 m of water column seaward of the Nankai Trough. These fine sediments are transported by suspension. Suspended sediment in most deep-marine environments is transported by a dynamic

combination of surface currents, bottom currents, gravity flows, and biologic resuspension (Gorsline, 1984). The fine-grained suspended sediment was eroded from the Izu-Bonin volcanic arc, the Izu-Honshu collision zone, and the Outer Zone of Kyushu and Shikoku, and homogenized by mixing in the water column (Underwood and Steurer, 2003). The smectite in the Lower Shikoku Basin results from an alteration of volcanic ash mostly coming from the Izu-Bonin volcanic arc. The enrichment of smectite during the early Pliocene and late Miocene is because of a weaker Kuroshio current, which flows toward the Izu-Bonin volcanic arc in the NE and drives surface water transport off the SE coast of Kyushu and Shikoku (Underwood and Steurer, 2003). About 3 Ma years ago, the Central America Seaway closed off, triggering an intensification of the Kuroshio current (Underwood and Steurer, 2003). This resulted in a stronger and deeper flow of surface water toward the NE causing the flux of smectite from Izu-Bonin volcanic arc to dampen (Underwood and Steurer, 2003). Due to a potentially lower geothermal gradient, as observed at another drill site further SW (Site 1177 along the Muroto Transect) (Underwood and Steurer, 2003), the smectite-to-illite transition (diagenesis) did not happen resulting in higher preserved smectite contents than for example at drill sites closer to the accretionary prism.

Despite the very different mineralogies, both mudstones (BBC and Nankai mudstone) have very similar fractions of particles smaller than 2 μm by mass. However, their compression and permeability behavior is significantly different. Thus, the reason for the large discrepancy in compression and permeability behavior must lie in the fraction smaller than 2 μm. But settling tests like hydrometer analyses cannot resolve grain sizes smaller than several hundred nanometers. Therefore, other techniques or parameters need to be considered.

Assuming a perfect sphere model and grain densities of 2780 and 2680 kg/m^3 for BBC and Nankai mudstone, respectively, the average particle diameters that reflect the measured specific surface areas (S_S), the ratio of particle surface to its mass, of 24 m^2/g and 32 m^2/g are 0.09 and 0.07 μm for BBC and Nankai mudstone, respectively. The grain density was measured for the BBC and derived from moisture and density data by averaging all measurements over the constrained depth range in case of the Nankai mudstone. This averaged grain density of 2680 kg/m^3 appears to be small and should be measured on the Nankai mudstone in the future. The theoretical smaller average particle diameter indicates that Nankai mudstone must have a much larger fraction smaller than what can be observed in the hydrometer analyses in order to decrease the average particle diameter. By binning the grain size fraction > 2 μm into smaller bins and calculating the specific surface areas of all bins scaled by their respective mass fractions I can estimate the specific surface area of the fraction < 2 μm by comparing with the measured S_S value of the whole rock. The S_S of the < 2 μm fraction would be 39 m^2/g for the BBC and 50 m^2/g for the Nankai mudstone. This shows that a lot of the surface area is hidden in the smallest fractions. The high specific surface area of the < 2 μm fraction of the Nankai mudstone is caused by the high amount of smectite, which has a much larger specific surface area (on the order of 800 m^2/g) than illite (on the order of 80 m^2/g) or kaolinite (on the order of 10 m^2/g) as discussed in the next paragraph. Aplin et al. (1995) showed that smectite-rich sediments have an extraordinary high content of < 0.1 μm fraction (80%).

Specific surface area of clay minerals depends on particle sizes and swelling capacities. Kaolinite, for example, has the largest particle size whereas smectite has the smallest out of all clay minerals. Smectite is also an expandable clay mineral, which significantly increases its diffuse double layer when expanded, thus, providing additional

surface area that other clay minerals at similar size do not have. Smectite is a 2:1 layer mineral, where a central gibbsite sheet is embedded between two silicon tetrahedral sheets, with very weak bonding between the 2:1 layer sheets allowing water, organic compounds and exchangeable ions to enter between layer sheets resulting in a high swelling capacity (Fjaer et al., 2008). The specific surface area associated with the interlayer space is between 500 and 700 m^2/g (Fjaer et al., 2008). The fact that Nankai mudstone is composed of a large amount of smectite (more than half of the whole rock) (Figure 6.2) indicates that it should have a large specific surface area, which might control the compression and permeability behavior.

However, the specific surface area measurements for BBC and Nankai mudstone are much smaller than expected with 24 and 32 m^2/g, respectively. They do compare well though with S_S of similar soils also measured by gas adsorption as summarized by Santamarina et al. (2002). However, there is a large discrepancy between S_S measured by gas adsorption and other methods such as methylene blue as discussed by Santamarina et al. (2002). Gas adsorption measurements are biased by the molecular size of adsorbate relative to the size of small pores and crevices (pores smaller than the adsorbent). They are performed on dry specimens as opposed to wet specimens in the methylene blue spot test (Santamarina et al., 2002). Molecules of the selected gas, here Nitrogen molecules, cannot cover the interlayer surface in expansive layer–silicates (such as smectite-rich clays) which remain tightly bound under dry conditions, resulting in low S_S values. Therefore, the measured S_S is significantly lower than the surface exposed in wet conditions.

In contrast, the methylene blue spot test is a wet procedure and results in higher S_S values for swelling clays as interlayer surfaces can be reached by exchangeable ions after hydration (Santamarina et al., 2002). For example, the S_S of Gulf of Mexico clay, which

might be comparable with Nankai mudstone, is 40 m^2/g if measured by gas adsorption and 230 m^2/g if measured by methylene blue (Santamarina et al., 2002). Thus, for swelling clays the difference in S_S determined with either dry or wet measurement conditions is significant but not for nonswelling clays. This means that the measured value of 32 m^2/g in case of the smectite-rich Nankai mudstone underpredicts the real value by far. Unfortunately, a S_S measurement using the wet measurement conditions is not available at this time.

However, specific surface area can be estimated from index properties. Mitchell (1993) stated that the Atterberg limits (liquid limit and plastic limit) reflect the specific surface of the soil, the thickness of the diffuse double layer, and the fabric. Farrar and Coleman (1967) developed a relationship between liquid limit and specific surface area based on nineteen British clays with varying liquid limits:

$$S_S = 1.8 \cdot LL - 34, \tag{6.1}$$

where LL is liquid limit in percent. Here I use equation 6.1 to get a better estimate of the real S_S of the two mudstones tested. The estimated specific surface areas are 48.8 m^2/g for BBC and 88.4 m^2/g for Nankai mudstone. Both values are at least twice the measured values of 24 m^2/g and 32 m^2/g, respectively.

Santamarina et al. (2002) presented another way to calculate S_S for spheres and platy particles from grain size distributions and slenderness of particles, which is the ratio of length to thickness of a particle. However, this approach cannot be used for BBC and Nankai mudstone due to lack of information. The equations proposed by Santamarina et al. are functions of the coefficient of uniformity, which is the ratio of particle diameter corresponding to 60% passing (D60) to particle diameter corresponding to 10% passing

(D10). Because there is no grain size information available at really low particle diameters for both BBC and Nankai mudstone, D10 cannot be determined for either mudstone.

The only parameters, which could be measured and provided a dramatic difference between both mudstones, were the Atterberg Limits. Liquid limit (LL) is significantly larger for Nankai mudstone than for BBC (Table 6.4) resulting in a large difference in plasticity index given the fact that plastic limit increased only slightly for Nankai mudstone. The large plasticity index means that Nankai mudstone behaves plastically over a larger range of water contents. Atterberg Limits are closely related to specific surface area and control the compression and permeability behavior.

Santamarina et al. (2002) use the Kozeny-Carman equation expressed in terms of specific surface area in order to calculate permeability. Permeability is inversely related to the square of specific surface area. Thus, permeability is strongly controlled by the clay fraction. The links between Atterberg limits and permeability with S_S suggest that various engineering properties such as compression index (C_c) and coefficient of consolidation (C_v) must be correlated to S_S (Santamarina et al., 2002).

Therefore, the increased specific surface area of Nankai mudstone must be related to the faster drop in porosity with vertical effective stress, as observed in Figure 6.4, and the greater permeability decrease for a given porosity interval, as observed in Figure 6.5, than BBC resulting in very different coefficient of consolidation (C_v) behaviors (Figure 6.6). Commonly it is assumed that both coefficient of volume compressibility (m_v) and permeability (k) rapidly decrease with increasing effective stress, so that the ratio (k/m_v) and, hence, C_v is fairly constant over a wide range of consolidation pressures (Terzaghi and Peck, 1967). However, this is not the case as shown by Robinson and Allam (1998). C_v increases with increasing consolidation pressure for kaolinite, illite, and powdered

quartz but decreases for montmorillonite (Robinson and Allam, 1998). This is consistent with the observed decrease in C_v for the smectite-rich Nankai mudstone and an increase for the smectite-poor BBC. Abeele (1986) showed in the 1980s that C_c and permeability change index increase as the proportion of smectite increases, thus, resulting in a decrease in C_v for high smectite contents. An addition of only 6% smectite to a sandy silt mixture revealed permeabilities nearly equal to the permeability of a pure bentonite (Abeele, 1986).

The response of C_v to an increase in vertical effective stress in clays is governed by the mechanical and physicochemical factors that govern the compressibility (Robinson and Allam, 1998). For kaolinite, illite, and powdered quartz the virgin consolidation is controlled by mechanical effects, which are particle interactions controlled by physical properties of mineral particles, that is, their strength and flexibility and by surface friction (Robinson and Allam, 1998). In contrast, for montmorillonite or smectite-rich clays physicochemical effects, which are interactions between particles especially through diffuse double layers, control virgin consolidation behavior (Robinson and Allam, 1998). This means that the C_v trend of smectite-rich clays is highly dependent on the pore fluid. If water is used as the pore fluid C_v decreases with increasing consolidation pressure. But when using a nonpolar fluid the diffuse double layer formation around clay particles is suppressed causing C_v to increase with increasing consolidation pressure. Then only mechanical effects control the virgin consolidation behavior. Because I used a saline brine for the Nankai mudstone during resedimentation (salinity of 35g/l) the pore fluid is highly polar causing physicochemical effects to control the compression behavior of Nankai mudstone resulting in a decreasing C_v trend with increasing vertical effective stress. In contrast to the Nankai mudstone, BBC is composed of no smectite and only 7.3 % illite and illite-smectite mixed layer, thus, mechanical effects control the compression

behavior resulting in an increasing C_v trend with increasing vertical effective stress. The different governing mechanisms, mechanical versus physicochemical effects, also explain the different curvatures of the compression curves. Physicochemical effects seem to cause a concave upward shape (Figure 6.4) whereas mechanical effects seem to cause a more constant C_c.

6.4 CONCLUSIONS

Compressibility, permeability and coefficient of consolidation are driven by the clay mineralogy. The high smectite content in the Nankai mudstone provides a large specific surface area due to the smaller particle size and additional interlayer surfaces that can be reached by water and exchangeable ions causing a high plasticity of the Nankai mudstone. Due to the high smectite content a large diffuse double layer can be formed around clay particles within the Nankai mudstone causing physicochemical effects to control virgin compression behavior instead of mechanical effects in the case of BBC. Thus, compressibility and permeability of Nankai mudstone decrease faster with vertical effective stress and porosity, respectively, than BBC resulting in a decrease in C_v as opposed to an increase for BBC. It is important to consider clay mineralogy as well and grain size distributions as predictions of geomechanical behavior of mudstones could otherwise be off by orders of magnitudes.

REFERENCES

Abeele, W.V., 1986. The influence if bentonite on the permeability of sandy silts. *Nuclear and Chemical Waste Management*, 6(1): 81-88. doi:10.1016/0191-815X(86)90091-4.

Aplin, A.C., Yang, Y.L., and Hansen, S., 1995. Assessment of beta, the compression coefficient of mudstones and its relationship with detailed lithology. *Marine and Petroleum Geology*, 12(8): 955-963. doi:10.1016/0264-8172(95)98858-3.

ASTM International, 2007. Standard test method for particle-size analysis of soils (Standard D422-63R07). *In* Annual Book of ASTM Standards (Vol. 04.08), ed., Soil and Rock (I): West Conshohocken, PA, American Society for Testing and Materials, p. 10-17, doi:10.1520/D0422-07.

ASTM International, 2006. Standard test method for one-dimensional consolidation properties of saturated cohesive soils using controlled-strain loading (Standard D4186-06). *In* Annual Book of ASTM Standards (Vol. 04.08), ed., Soil and Rock (I): West Conshohocken, PA, American Society for Testing and Materials, p. 15, doi:10.1520/D4186-06.

ASTM International, 2005, Standard Test Methods for Liquid Limit, Plastic Limit, and Plasticity Index of Soils (Standard D4318-05), *in* Annual Book of ASTM Standards (Vol. 04.08), ed., Soil and Rock (I): West Conshohocken, PA, American Society for Testing and Materials, p. 16.

Biscaye, P.E., 1965. Mineralogy and sedimentation of recent deep-sea clays in the Atlantic Ocean and adjacent seas and oceans. *Geol. Soc. Am. Bull.*, 76(7): 803-832. doi:10.1130/0016-7606(1965)76[803:MASORD]2.0.CO;2.

Farrar, D.M., and Coleman, J.D., 1967. The correlation of surface area with other properties of nineteen British clays. *Journal of Soil Science*, 18(1): 118-124.

Fjaer, E., Holt, R.M., Horsrud, P., Raaen, A.M., and Risnes, R., 2008. Petroleum related rock mechanics. Amsterdam, Netherlands, Elsevier.

Gorsline, D.S., 1984. A review of fine-grained sediment origins, characteristics, transport, and deposition. *In* Stow, D.A.V., and Piper, D.J.W., eds., Fine-grained sediments, Volume 15, Geol. Soc. Spec. Publ., p. 17-34.

Hillier, S., 2000. Accurate quantitative analysis of clay and other minerals in sandstones by XRD: comparison of a Rietveld and a reference intensity ratio (RIR) method and the importance of sample preparation. *Clay Minerals*, 35(1): 291-302.

Kaye, C.A., and Barghoorn, E.S., 1964. Late Quaternary sea-level change and crustal rise at Boston Harbor, Massachusetts, with notes on the autocompaction of peat. *Geological Soc. America Bulletin*, 75(2): 63-80. doi:10.1130/0016-7606(1964)75[63:LQSCAC]2.0.CO;2.

Mencher, E., Copeland, R.A., and Payson, H., JR., 1968. Surficial sediments of Boston Harbor, Massachusetts. *Journal of Sedimentary Petrology*, 38(1): 79-86.

Mitchell, J.K., 1993. Fundamentals of soil behavior. Hoboken, N.J., John Wiley & Sons.

Phipps, D., 1964. The geology of the unconsolidated sediments of Boston Harbor. Cambridge, Massachusetts Institute of Technology, 54 p.

Robinson, R.G., and Allam, M.M., 1998. Effect of clay mineralogy on coefficient of consolidation. *Clays and Clay Minerals*, 46(5): 596-600. doi:10.1346/CCMN.1998.0460514.

Santamarina, J.C., Klein, K.A., Wang, Y.H., and Prencke, E., 2002. Specific surface: determination and relevance. *Can. Geotech. J.*, 39: 233-241. doi:10.1139/T01-077.

Terzaghi, K., and Peck, R.B., 1967. Soil mechanics in engineering practice. New York, J. Wiley, 86 p.

Underwood, M.B., and Steurer, J.F., 2003. Composition and sources of clay from trench slope and shallow accretionary prism of Nankai Trough. *In* Mikada, H., Moore, G.F., Taira, A., Becker, K., Moore, J.C., and Klaus, A., eds., Proc. ODP, *Sci. Results*, Volume 190/196.

Appendix 1: Data Report: Permeability, compressibility, and microstructure of resedimented mudstones composed of Boston Blue Clay and silt

ABSTRACT

I conducted grain size analyses and uniaxial, constant-rate-of-strain (CRS) consolidation experiments on five sediment samples prepared in the laboratory using the method resedimentation to analyze compression and flow behavior. The five samples are sediment mixtures composed of varying proportions of Boston Blue Clay and silt-sized silica from US Silica. I performed all experiments in the GeoMechanics Laboratory at The University of Texas at Austin. The initial void ratio systematically decreases from 1.23 to 0.77 and the compression index decreases from 0.35 to 0.16 with clay-size fractions varying between 57% and 36%. Vertical intrinsic permeability decreases with increasing vertical effective stress and varies log-linearly with porosity. Slopes of this log-linear relationship vary between 7.61 and 6.94. At a given porosity, vertical permeability increases by one order of magnitude for clay contents ranging from 57% to 36%.

A1.1 INTRODUCTION

Mudstones compose nearly 70% of the volume of sedimentary basins (Dewhurst et al., 1998), yet they are among the least studied of sedimentary rocks. Their low permeability and high compressibility contribute to overpressure around the world (Broichhausen et al., 2005). Mudstone reservoirs contain large volumes of natural gas that is now being economically extracted (Zoback et al., 2010). In addition, they serve as hydrocarbon traps and are employed as barriers in CO_2 sequestration and waste

repositories. Despite their fundamental importance in geologic processes and as seals for anthropogenic-related storage, a systematic, process-based understanding of the interactions between porosity, compressibility, permeability, and pore size distribution in mudstones remains elusive (Dewhurst et al., 1999).

I used Boston Blue Clay (BBC) from the Boston area in Massachusetts, USA, which is a glacial clay that has been analyzed extensively in the geotechnical community (Sheahan, 1991; Santagata and Kang, 2007). It is an illitic glacio-marine clay (Kenney, 1964) composed of 57% clay-sized particles (<2μm by mass) with a wide grain size distribution. I used a homogenous batch of BBC to prepare homogeneous samples in the laboratory using a method called resedimentation. I then conducted grain size analyses and constant-rate-of-strain (CRS) consolidation tests in order to understand the compositional influence on deformation and flow behavior.

A1.2 Experimental Methods

A1.2.1 Sample Descriptions

Bulk Boston Blue Clay was air-dried, ground, and homogenized to a single batch. The specific gravity of Boston Blue Clay is 2780 kg/m^3. I added silt-sized silica (MIN U SIL 40) from US Silica to the baseline batch of BBC in the following proportions of mud to silica: 100:00, 84:16, 75:25, 68:32, and 50:50 (Table A1.1).

% BBC : % Silt[a]	*% Clay*[b]	*Resed #*[c]	*CRS #*[d]	*GS #*[e]
100 : 00	57	Resed 017	CRS 046	GS 094
84 : 16	52	Resed 018	CRS 047	GS 096
75 : 25	48	Resed 019	CRS 048	GS 098
68 : 32	44	Resed 020	CRS 050	GS 100
50 : 50	36	Resed 021	CRS 051	GS 102
Silt[a]	10			GS 103

Table A1.1: Summary table of various tests performed on Boston Blue Clay (BBC) – silt mixtures.

[a] Silt: silt-sized silica (US MIN U SIL 40 purchased from US Silica)
[b] % Clay: clay fraction by mass measured in grain size analysis (for test number see this table, column 5)
[c] Resed #: resedimentation test number
[d] CRS #: constant-rate-of-strain (CRS) consolidation test number
[e] GS #: grain size analysis test number

A1.2.2 Index Properties

The mineralogic composition of the pure Boston Blue Clay was measured by *Macaulay Scientific Consulting LTD* in Aberdeen, UK. Both whole rock and <2μm clay fraction analyses were performed by X-ray powder diffraction (XRPD).

I determined Atterberg Limits such as liquid limit (LL), plastic limit (PL) and plasticity index (PI) on the pure BBC in accordance to ASTM Standard D4318-05 (ASTM International, 2005). Atterberg Limits are used to characterize the fine-grained fraction of soils and, together with other soil properties, to correlate with engineering behavior such as compressibility, hydraulic conductivity, intrinsic permeability, and shear strength, for example. Liquid and plastic limit are water contents that separate different consistency states from each other. I performed the multipoint liquid limit method (ASTM International, 2005) using a hand-operated liquid limit device, also called Casagrande cup. I determined the plastic limit by the hand method (ASTM International, 2005). The plasticity index is the range of water content over which the soil behaves plastically, or numerically the difference between liquid limit and plastic limit.

I determined the particle size distributions of all five samples using the hydrometer method in general accordance with ASTM D422-63 guidelines (ASTM International, 2007) and Sawyer et al. (2008). The hydrometer method uses a suspension of sediment and water, which is thoroughly mixed, after which particles settle out. A hydrometer measures the density of the suspension at a known depth below the surface and time. From the hydrometer tests we obtain the particle diameter at a specific time and depth and the percentage of the original sample mass still left in suspension.

A1.2.3 Resedimentation

I prepared sediment samples in the laboratory using a method called resedimentation (Sheahan, 1991; Santagata and Kang, 2007) which was developed at the Massachusetts Institute of Technology and simulates natural sedimentation under controlled stress conditions. Homogeneity and no disturbance are key advantages of resedimented over intact samples. The dry, ground, and homogenized BBC is mixed with water at a water content of 100% and 16g/l sea salt to form a slurry. In case of the BBC – silica mixtures these values for water and salt content are used only per mud fraction. The silica fraction is just moistened with 33% water content and mixed in with the BBC. After homogenizing the slurry with a spatula for at least 20 minutes, the slurry is de-aired using a vacuum pump to eliminate any air bubbles. Then I poured the slurry into a consolidometer with an inside diameter of 6.9 cm. Below and on top of the slurry are a porous stone and filter paper allowing pore fluids to drain in both directions but preventing fines from being washed out. The initial height of all samples varied between 4.8 and 3.6 cm.

Then I incrementally loaded the slurry, doubling the mass on the slurry every time, to a vertical effective stress of 100 kPa (in this study). A linear position transducer (LPT), which at the time of measurement could not be mounted onto the system until the beginning of the fifth stress increment due to weight restrictions, monitors the vertical displacement throughout the resedimentation experiment. The last weight increment is left on the slurry till the sediment reaches secondary consolidation. After unloading the sample to an overconsolidation ratio (OCR), which is the maximum past effective stress divided by the current effective stress, of four, I carefully and slowly extruded the samples. The final height of all samples varied between 3.1 and 2.6 cm.

A1.2.4 Consolidation Testing

After resedimenting the five sediment mixtures composed of varying proportions of BBC and silt-sized silica, I conducted constant-rate-of-strain (CRS) consolidation tests according to American Society for Testing and Materials (ASTM) D4186-06 guidelines (ASTM International, 2006). The temperature in the UT laboratory is controlled to a constant temperature of 23.9°. The specimens were trimmed into a steel ring using a trimming jig, wire saw, and a sharp-edge spatula. Once the specimen is in the ring, a wire-saw, razor blade, and recess tool was used to smoothen the top and bottom of the specimen and to ensure consistent specimen dimensions. The initial height (H_0) and diameter are 2.35cm and 6.31cm, respectively. I flushed all lines with de-ionized water and applied a constant backpressure of 386 kPa for at least 12 hours to ensure full saturation.

The specimens, laterally confined in the steel ring, are consolidated at a constant rate of strain (i.e. uniaxial strain). The strain rate for all six specimens varies between 1.0%/hr and 3.3%/hr, increasing with increasing silica content (Table A1.4). These strain rates were not adjusted during the test, yet they ensured pore pressure ratios (ratio of excess pore pressure to total axial stress) to be smaller than 0.1. The top of the specimen is open to the cell pressure (u_c) whereas the bottom is undrained. During the consolidation test I continuously monitored specimen height (H), total axial stress (σ_v), and base pressure (u). Experiments were run to a maximum vertical effective stress of 2.4 MPa where stresses were held for 6 hours to allow excess pore pressure to dissipate. Specimens were then unloaded to an overconsolidation ratio (OCR) of four.

I computed axial strain (ε), base excess pore pressure (Δu), average vertical effective stress (σ'_v), hydraulic conductivity (K), intrinsic permeability (k), coefficient of

volume compressibility (m_v), and coefficient of consolidation (C_v) as follows in accordance with ASTM Standard D4186-06 (ASTM International, 2006):

$$\varepsilon = \Delta H / H_0, \tag{A1.1}$$

where displacements are measured with linear position transducers. For definitions of variables see nomenclature. In Figures A1.4 to A1.8 I report strain as percentage.

$$\Delta u = u - u_c \tag{A1.2}$$

$$\sigma_v^{'} = \left[\sigma_v - \frac{2}{3}\Delta u\right] - u_c \tag{A1.3}$$

$$K = \frac{\dot{\varepsilon} H H_0 \gamma_w}{2\Delta u} \tag{A1.4}$$

$$k = \frac{K\mu_w}{\gamma_w} \tag{A1.5}$$

$$m_v = \frac{\Delta\varepsilon}{\Delta\sigma_v^{'}} \tag{A1.6}$$

$$C_v = \frac{K}{m_v \gamma_w} \tag{A1.7}$$

I computed compression index (C_c), which is the slope of the virgin consolidation line, from the change in specimen void ratio (e) with vertical effective stress (σ'_v):

$$C_c = \frac{\Delta e}{\Delta \log(\sigma_v^{'})} \tag{A1.8}$$

Maximum preconsolidation stress (σ'_{pc}) of all specimens is 100 kPa equal to the maximum vertical effective stress the slurry was preloaded to during resedimentation.

A1.2.5 SEM Imaging

Scanning Electron Microscope images, both backscattered (BSE) and secondary (SE), were taken on a field-emission scanning electron microscope (SEM). The samples were prepared using an argon-ion beam milling technique (Loucks et al., 2009), which avoids mechanical polishing and instead produces surfaces with only minor topographic variations using accelerated argon ions. BSE and SE images were taken at three different magnifications (1,000 x, 14,000 x, and 60,000 x) after consolidation of sediment mixtures to a maximum vertical effective stress of 2.4 MPa. Images represent a vertical cross-section of the sample. One BSE image at a magnification of 14,000 of each sediment mixture is shown here (Figure A1.9).

A1.3 RESULTS

A1.3.1 Index Properties

The X-ray powder diffraction (XRPD) results show that the bulk sample contains quartz, plagioclase, feldspars, amphibole, minor dolomite, calcite, pyrite, and halite and clay minerals (Figure A1.1A). The clay fraction is dominated by illite and a random mixed-layer illite-smectite with lesser amounts of chlorite and kaolinite (Figure. A1.1B). The expandibility of the illite-smectite is around 5%.

Atterberg Limits results on the pure Boston Blue Clay show that the liquid limit (LL) is 46%, the plastic limit (PL) is 23% and thus the plasticity index (PI) is 23% (Figure A1.2).

I conducted particle size distribution curves on the five specimens after consolidation to 2.4 MPa (Figure A1.3). The clay-size fractions (<2μm) by mass are 57%, 52%, 48%, 44%, and 36% for mixtures with 100%, 84%, 75%, 68% and 50% BBC

and silica as the remainder. Thus, the specimens fall into the categories silty clay and clayey silt. Sand, silt, and clay percentages are given in Table A1.3.

A

Quartz	*Plagioclase*	*K-feldspar*	*Calcite*	*Dolomite*	*Pyrite*
21.3	20.5	8.2	0.5	0.8	0.0

Halite	*Amphibole*	*Muscovite*	*Illite*	*Smectite*	*Illite + Illite-Smectite*
0.2	3.8	13.8	N/A	N/A	7.3

Kaolinite	*Chlorite*	*Tri-mica*	*Hydrobiotite*	*Talc*	*Total*
2.9	6.2	9.2	5.4	0.0	100.1

B

Chlorite	*Kaolinite*	*Illite*	*Illite-Smectite*	*% Expandibility*
5	2	65	28	5

Table A1.2: Mineralogy of Boston Blue Clay (BBC) (Resed 017, CRS 026). A) Mineralogy of whole rock as weight percent determined using the reference intensity ratio (RIR) method (Hillier, 2000). B) Mineralogy of clay fraction smaller than 2 μm expressed as relative weight percent.

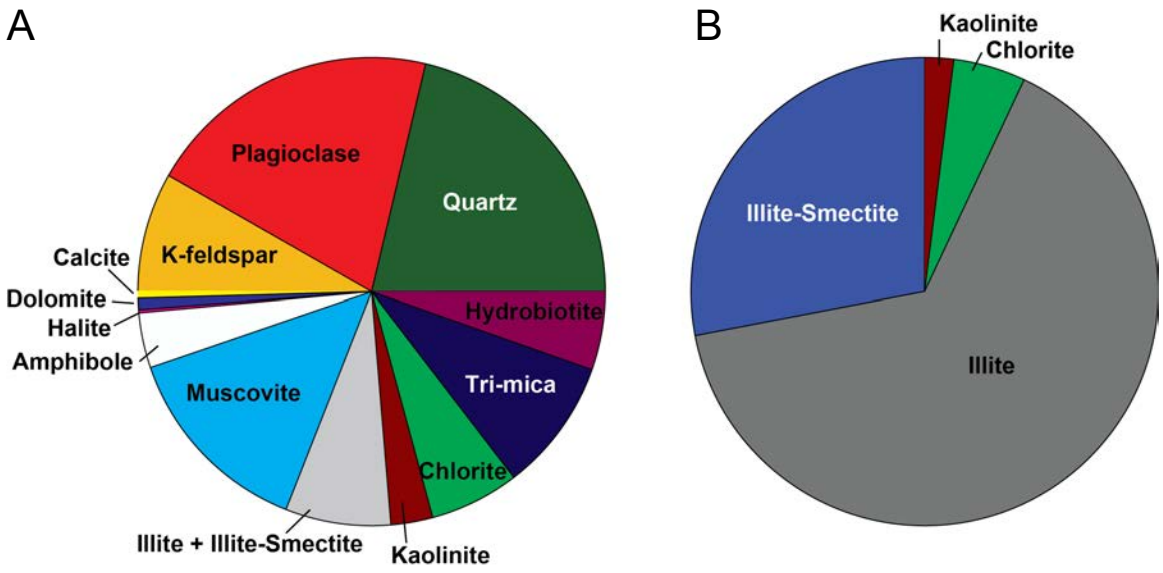

Figure A1.1: Mineralogy of Boston Blue Clay through X-ray powder diffraction (Table A1.2) measured by *Macaulay Scientific Consulting LTD*. (A) Whole rock analysis determined using the reference intensity ratio (RIR) method (Hillier, 2000). (B) Clay fraction <2μm expressed as relative weight percent.

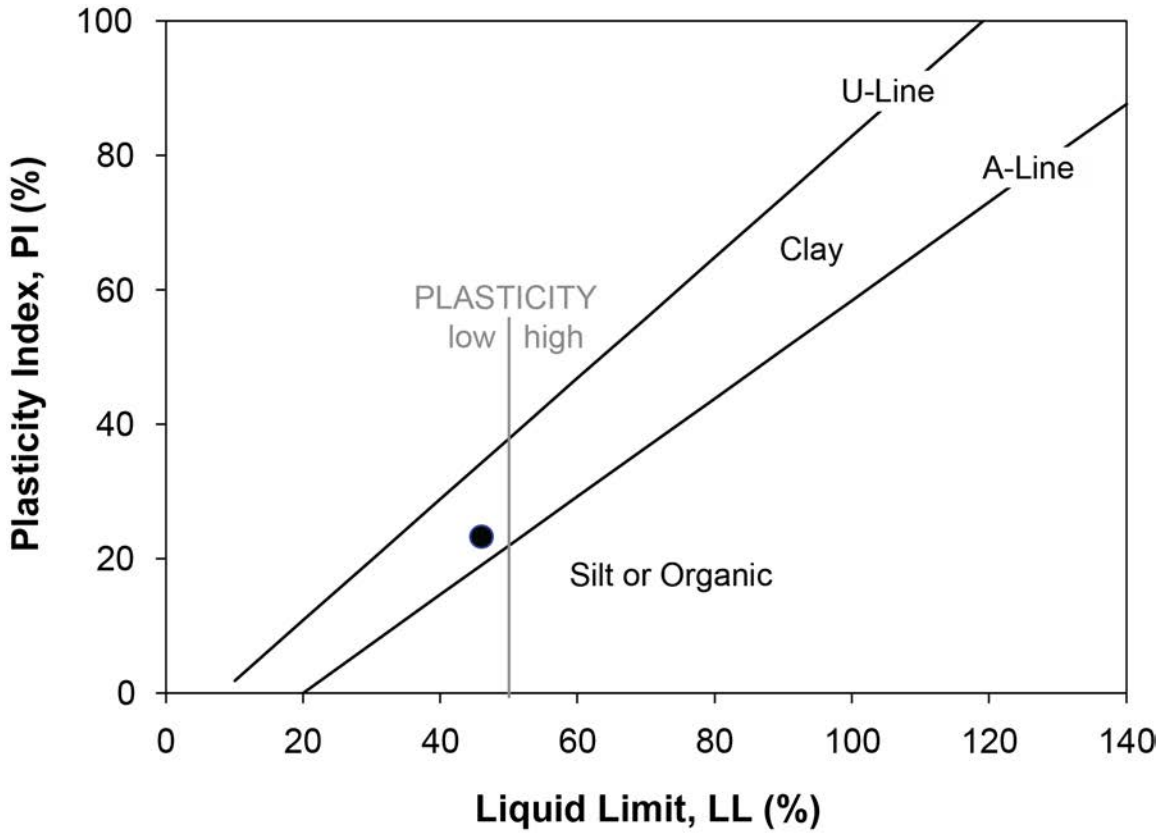

Figure A1.2: Atterberg Limits of Boston Blue Clay. LL = liquid limit, PI = plasticity index.

% BBC - % Silt[a]	*CRS #*[b]	*% Sand*[c]	*% Silt*[c]	*% Clay*[c]
100 : 00	CRS 46	0	43	57
84 : 16	CRS 47	0	48	52
75 : 25	CRS 48	0	52	48
68 : 32	CRS 50	0	56	44
50 : 50	CRS 51	0	64	36

Table A1.3: Particle size distributions. Boundary between sand and silt is defined at 62.5 μm and between silt and clay at 2 μm.

[a] Silt: silt-sized silica (US MIN U SIL 40 purchased from US Silica)
[b] CRS #: constant-rate-of-strain (CRS) consolidation test number
[c] %Sand, Silt, Clay: grain size analyses results (for test numbers see Table A1.1)

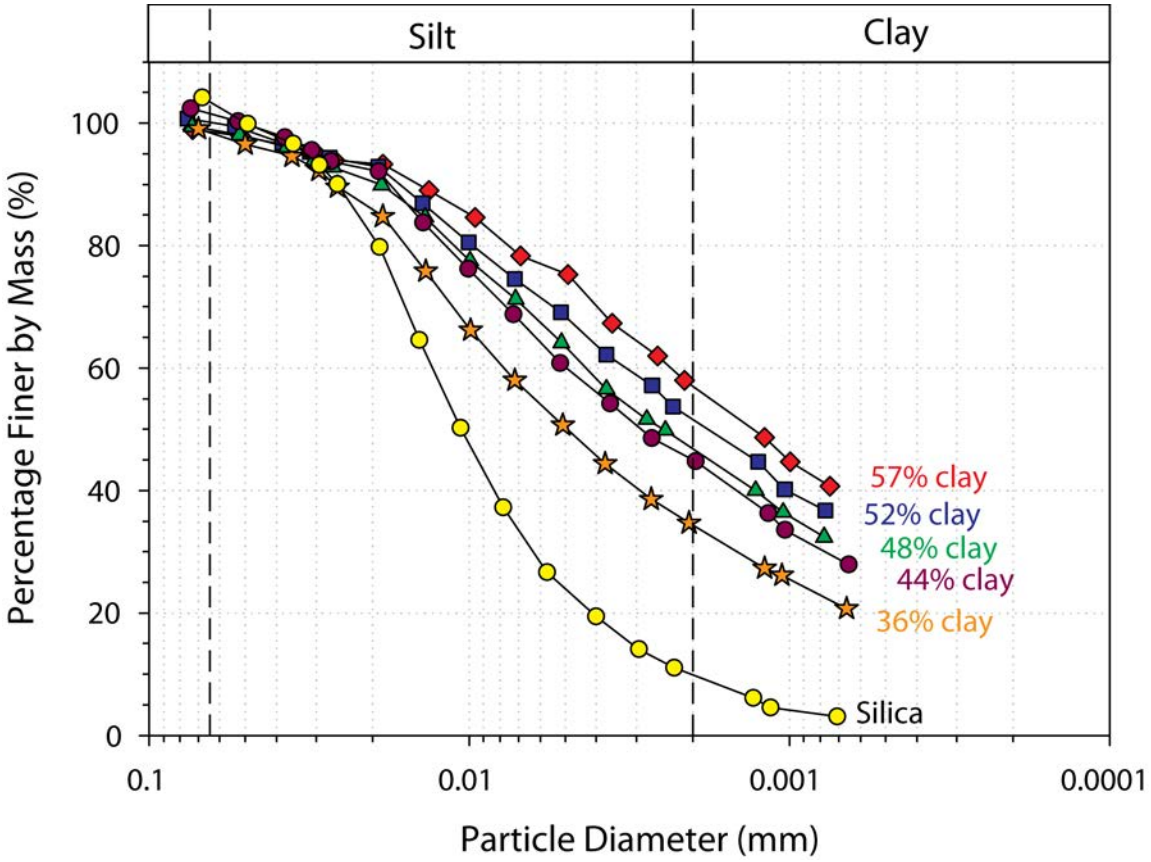

Figure A1.3: Particle size distribution plots on a semi-log scale (Table A1.1). All data points represent hydrometer readings. Sand/silt boundary is defined at 62.5 μm and silt/clay boundary is defined at 2 μm. Red diamonds = 57% clay, dark blue squares = 52% clay, green triangles = 48% clay, purple circles = 44% clay, orange stars = 36% clay, and yellow circles = silt-sized silica (10% clay).

A1.3.2 Consolidation Testing

Uniaxial constant-rate-of-strain consolidation tests on all six resedimented mixtures composed of Boston Blue Clay and silt-sized silica show a decrease in initial void ratio from 1.23 to 0.77 for samples with 100% to 50% BBC. The compression index (C_c) decreases from 0.35 to 0.16 for mixtures with 100% and 50% BBC. Vertical intrinsic permeability varies log-linearly with porosity and increases with decreasing clay fraction. At a given porosity of 40% the difference in permeability between 100% and 50% BBC mixtures is one order of magnitude. Coefficient of consolidation (C_v) decreases with increasing stress and varies between $2 * 10^{-7}$ m^2/s and $1 * 10^{-6} m^2/s$ for samples with 100% and 50% BBC mud.

Table A1.4 summarizes the details of each CRS test. Figures A1.4 to A1.8 show the consolidation curves in both ε-log(σ'_v) and e-log(σ'_v), normalized excess pore pressure ($\Delta u/\sigma_v$), hydraulic conductivity (K), intrinsic permeability (k), and coefficient of consolidation (C_v) for each CRS test.

CRS #[a]	*% BBC : Silt*[b]	σ'_{pc}	w_n	S_i	e_i	G_s	$d\varepsilon/dt$	C_c	C_e	γ	$\log(k_0)$
CRS 46	100 : 00	100	44.86	101.5	1.23	2.780	1.0	0.35	0.037	7.61	-20.31
CRS 47	84 : 16	100	40.50	102.0	1.10	2.759	1.4	0.29	0.028	7.19	-19.85
CRS 48	75 : 25	100	37.77	101.7	1.02	2.748	2.3	0.26	0.022	6.94	-19.55
CRS 50	68 : 32	100	36.55	100.4	1.00	2.738	2.5	0.24	0.020	7.14	-19.54
CRS 51	50 : 50	100	29.64	104.3	0.77	2.715	3.3	0.16	0.015	7.16	-19.11

Table A1.4: Consolidation properties. CRS #: Constant-rate-of-strain (CRS) consolidation test number. w_n: Water content measured on specimen. e_i: Initial void ratio calculated from water content measured on specimen and grain density. G_s: Grain density measured on bulk BBC and on silt-sized silica from US Silica, extrapolated for mixtures in between. $d\varepsilon/dt$: Strain rate in %/hr here. Strain rate was not adjusted during consolidation test. C_c: Determined between vertical effective stress of 400 kPa and 2400 kPa. C_e: Determined between vertical effective stress of 600 kPa and 2400 kPa.

[a] CRS #: constant-rate-of-strain (CRS) consolidation test number
[b] Silt: silt-sized silica (US MIN U SIL 40 purchased from US Silica)

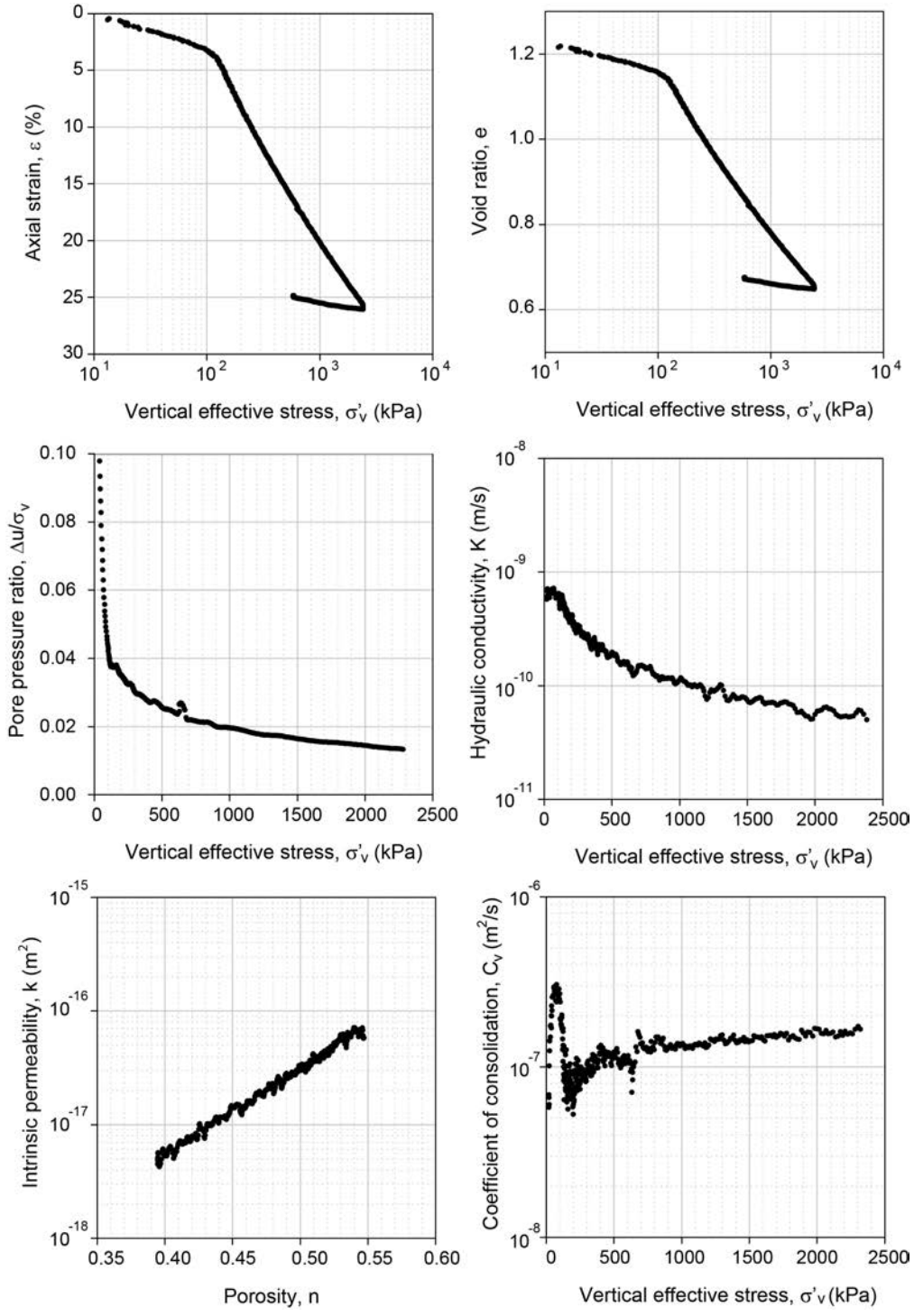

Figure A1.4: Experimental consolidation results for the sample with 57 % clay-sized particles (100% BBC mud and 00% silica, CRS046).

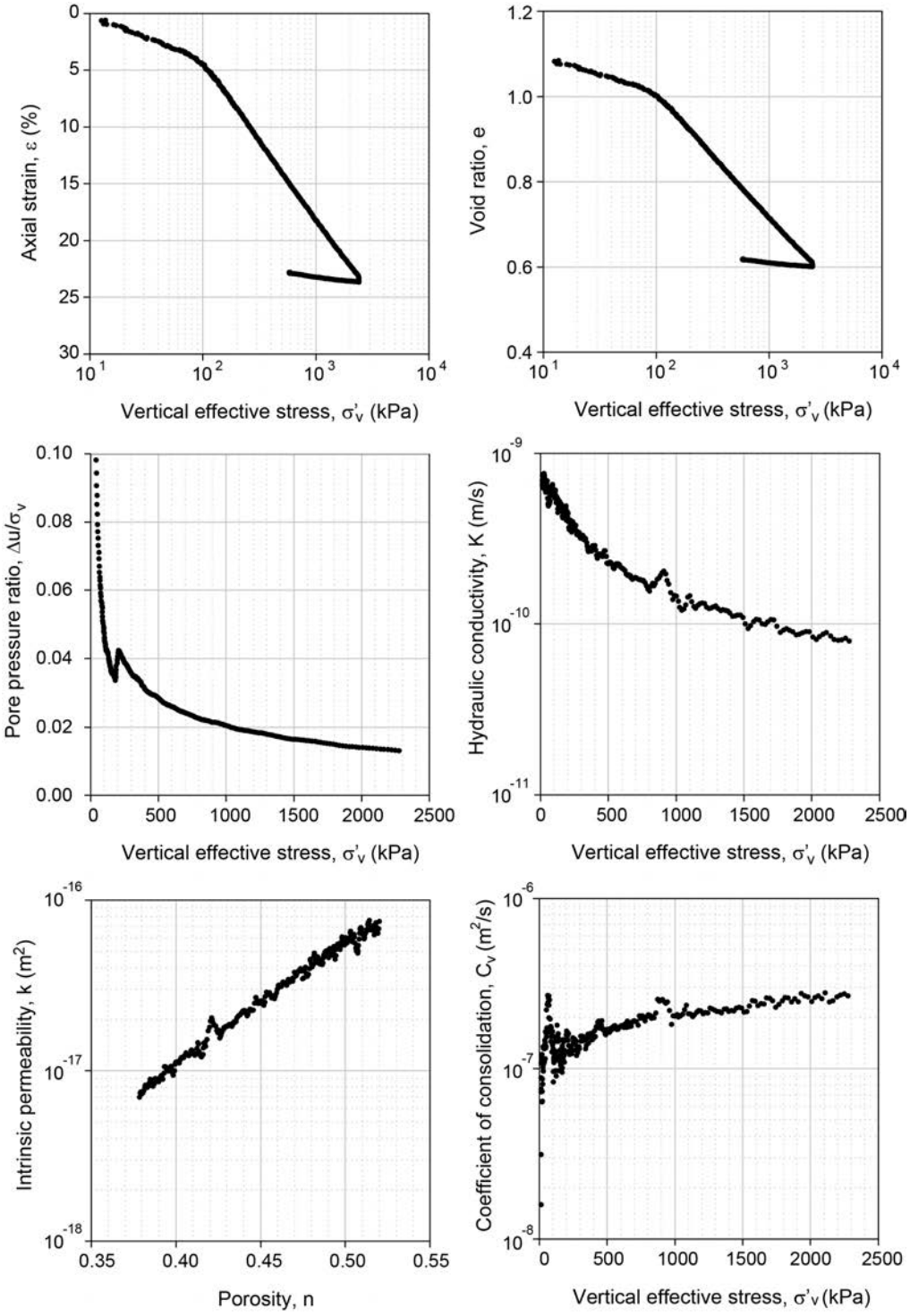

Figure A1.5: Experimental consolidation results for the sample with 52 % clay-sized particles (84% BBC and 16% silica, CRS047).

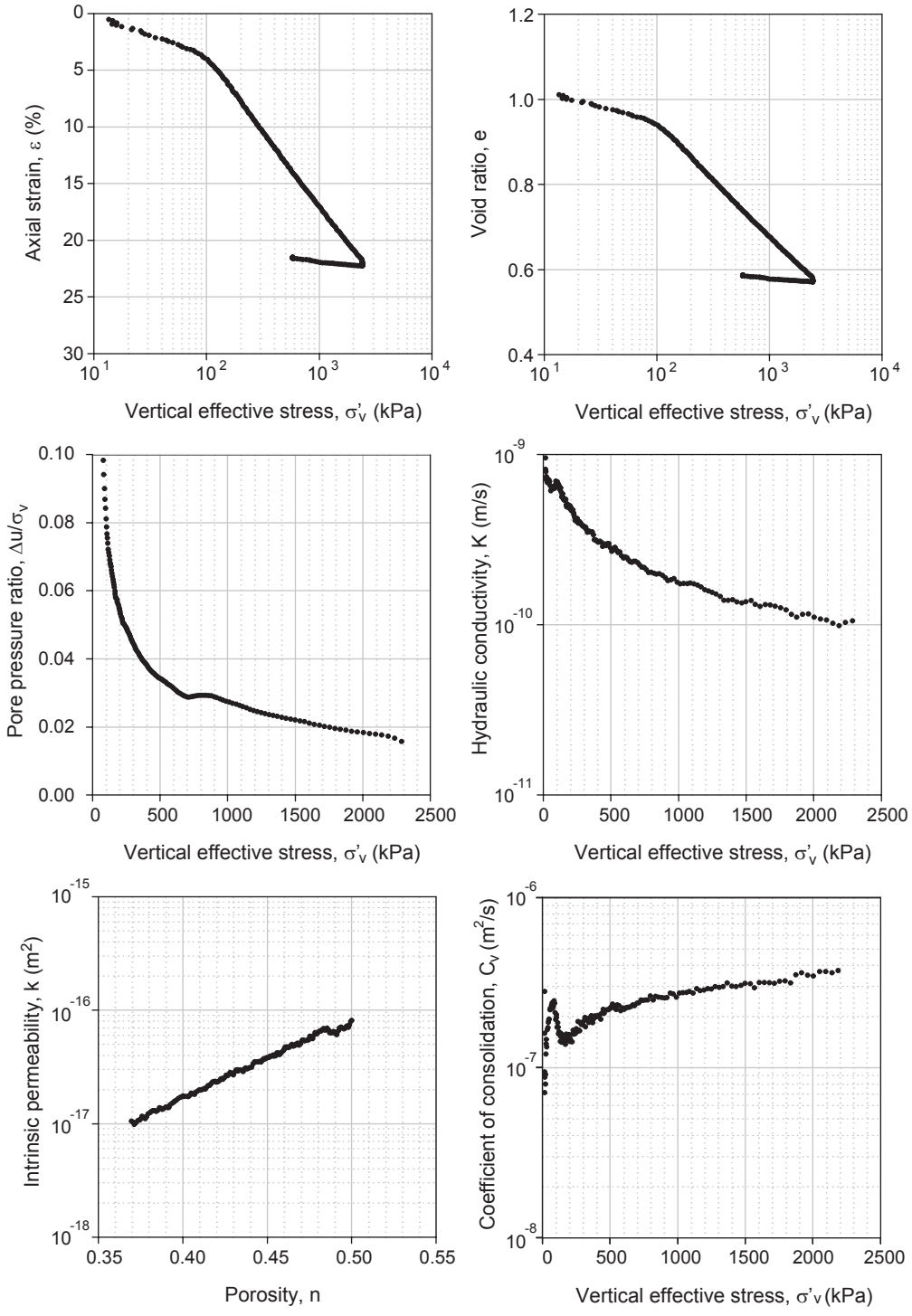

Figure A1.6: Experimental consolidation results for the sample with 48 % clay-sized particles (75% BBC and 25% silica, CRS048).

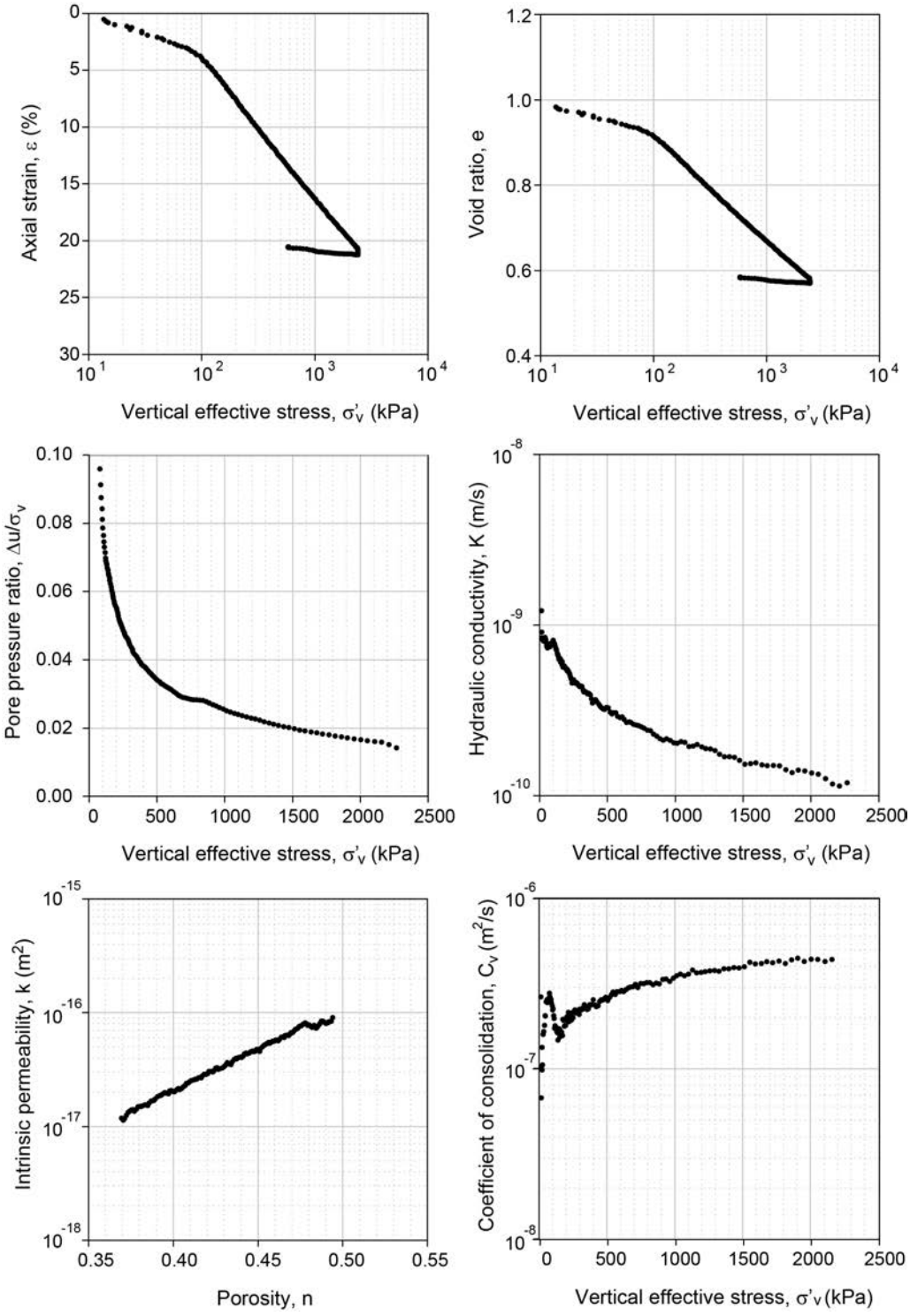

Figure A1.7: Experimental consolidation results for the sample with 44 % clay-sized particles (68% BBC and 32% silica, CRS050).

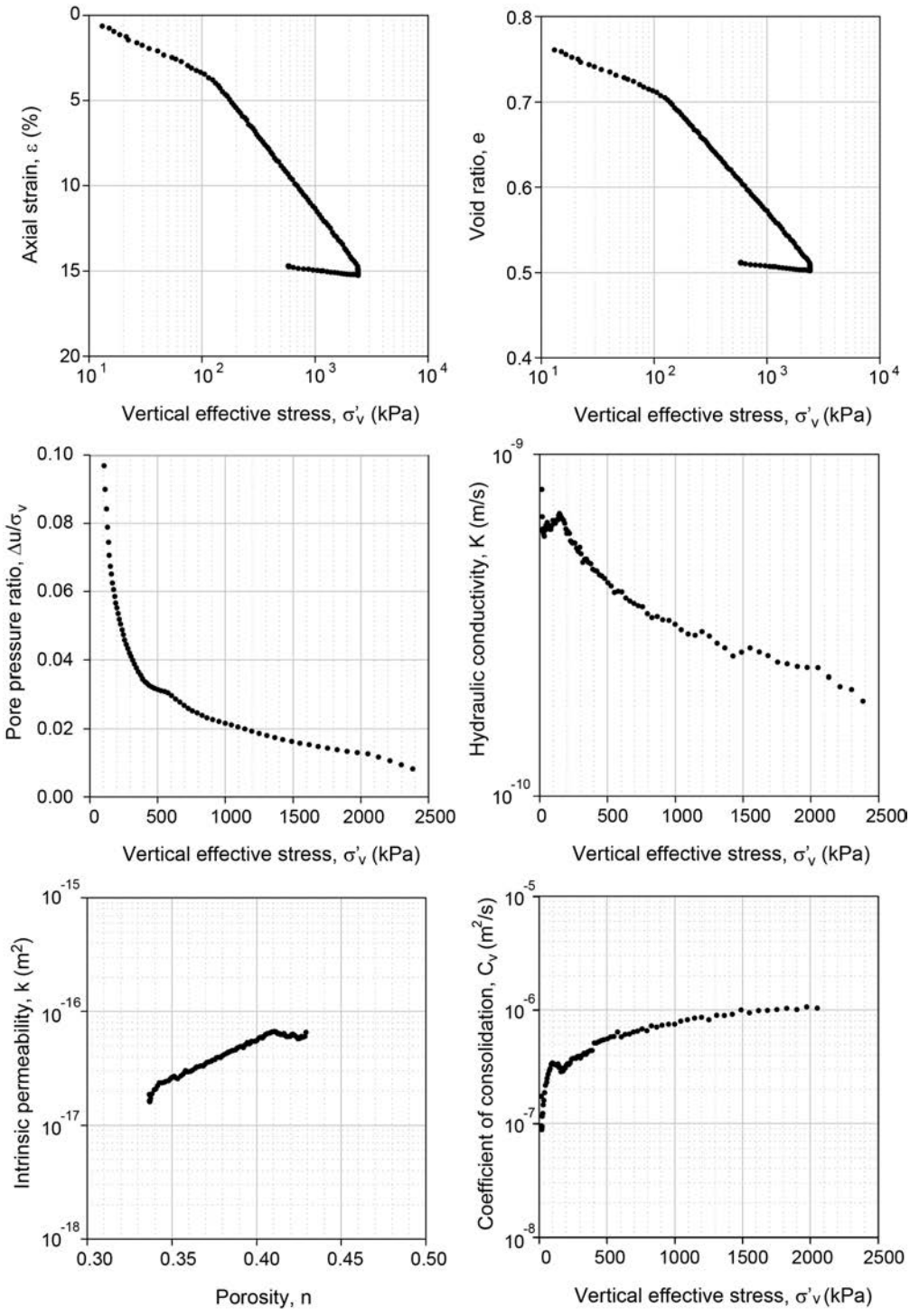

Figure A1.8: Experimental consolidation results for the sample with 36 % clay-sized particles (50% BBC and 50% silica, CRS051).

A1.3.3 SEM Imaging

Backscattered electron microscope (BSE) and secondary electron (SE) images show a strong decrease in clay particle alignment with decreasing clay fraction (Figure A1.9). Clay-rich samples show many small pores whereas silt-rich samples show several large pores as well as smaller ones more typical of clay-rich samples. Clay particles within these large pore spaces are randomly oriented.

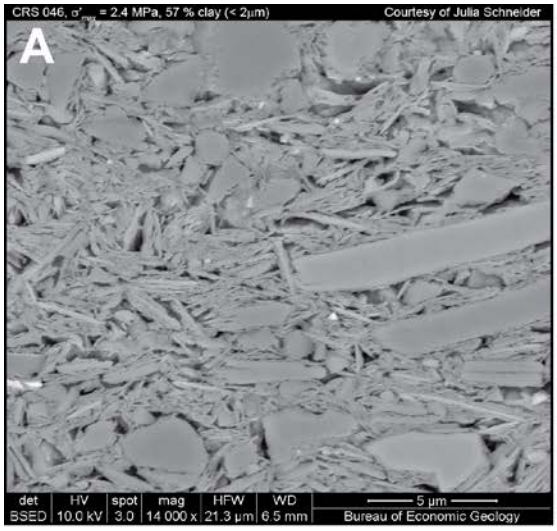
CRS 046, σ'vm = 2.4 MPa, 57 % clay (< 2μm)
Courtesy of Julia Schneider
A
det HV spot mag HFW WD
BSED 10.0 kV 3.0 14 000 x 21.3 μm 6.5 mm
5 μm
Bureau of Economic Geology

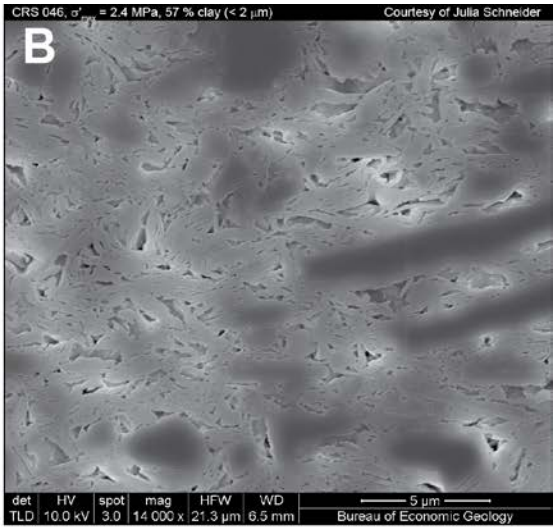
CRS 046, σ'vm = 2.4 MPa, 57 % clay (< 2 μm)
Courtesy of Julia Schneider
B
det HV spot mag HFW WD
TLD 10.0 kV 3.0 14 000 x 21.3 μm 6.5 mm
5 μm
Bureau of Economic Geology

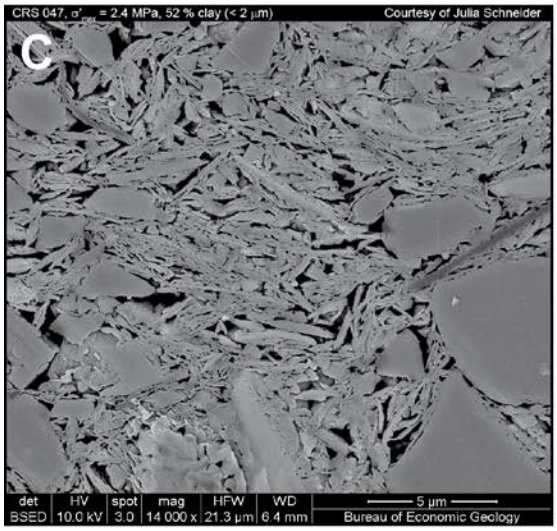
CRS 047, σ'vm = 2.4 MPa, 52 % clay (< 2 μm)
Courtesy of Julia Schneider
C
det HV spot mag HFW WD
BSED 10.0 kV 3.0 14 000 x 21.3 μm 6.4 mm
5 μm
Bureau of Economic Geology

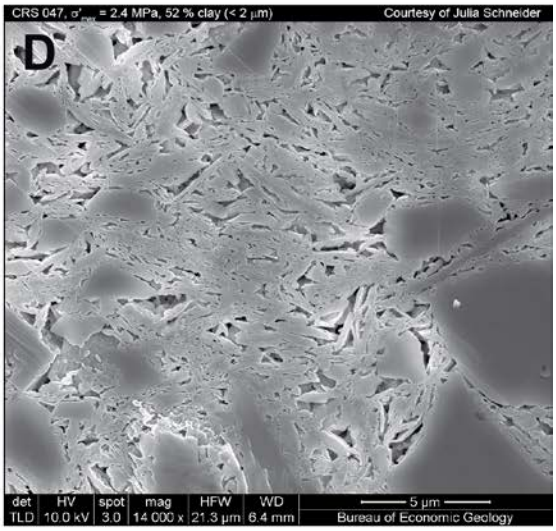
CRS 047, σ'vm = 2.4 MPa, 52 % clay (< 2 μm)
Courtesy of Julia Schneider
D
det HV spot mag HFW WD
TLD 10.0 kV 3.0 14 000 x 21.3 μm 6.4 mm
5 μm
Bureau of Economic Geology

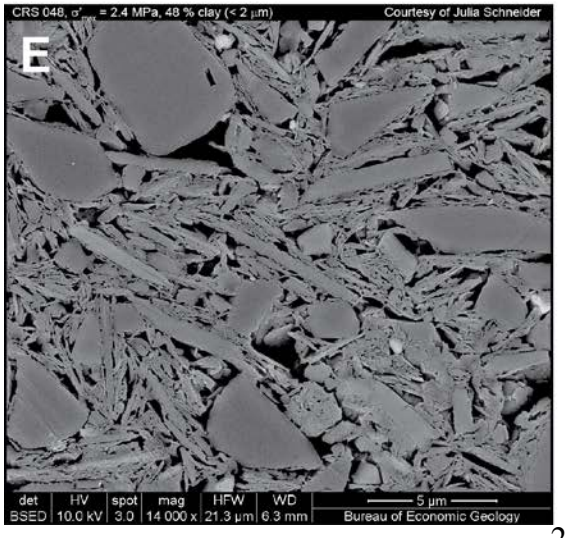
CRS 048, σ'vm = 2.4 MPa, 48 % clay (< 2 μm)
Courtesy of Julia Schneider
E
det HV spot mag HFW WD
BSED 10.0 kV 3.0 14 000 x 21.3 μm 6.3 mm
5 μm
Bureau of Economic Geology

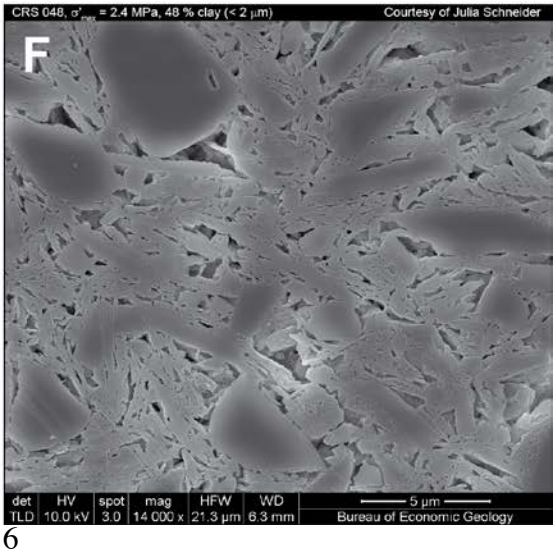
CRS 048, σ'vm = 2.4 MPa, 48 % clay (< 2 μm)
Courtesy of Julia Schneider
F
det HV spot mag HFW WD
TLD 10.0 kV 3.0 14 000 x 21.3 μm 6.3 mm
5 μm
Bureau of Economic Geology

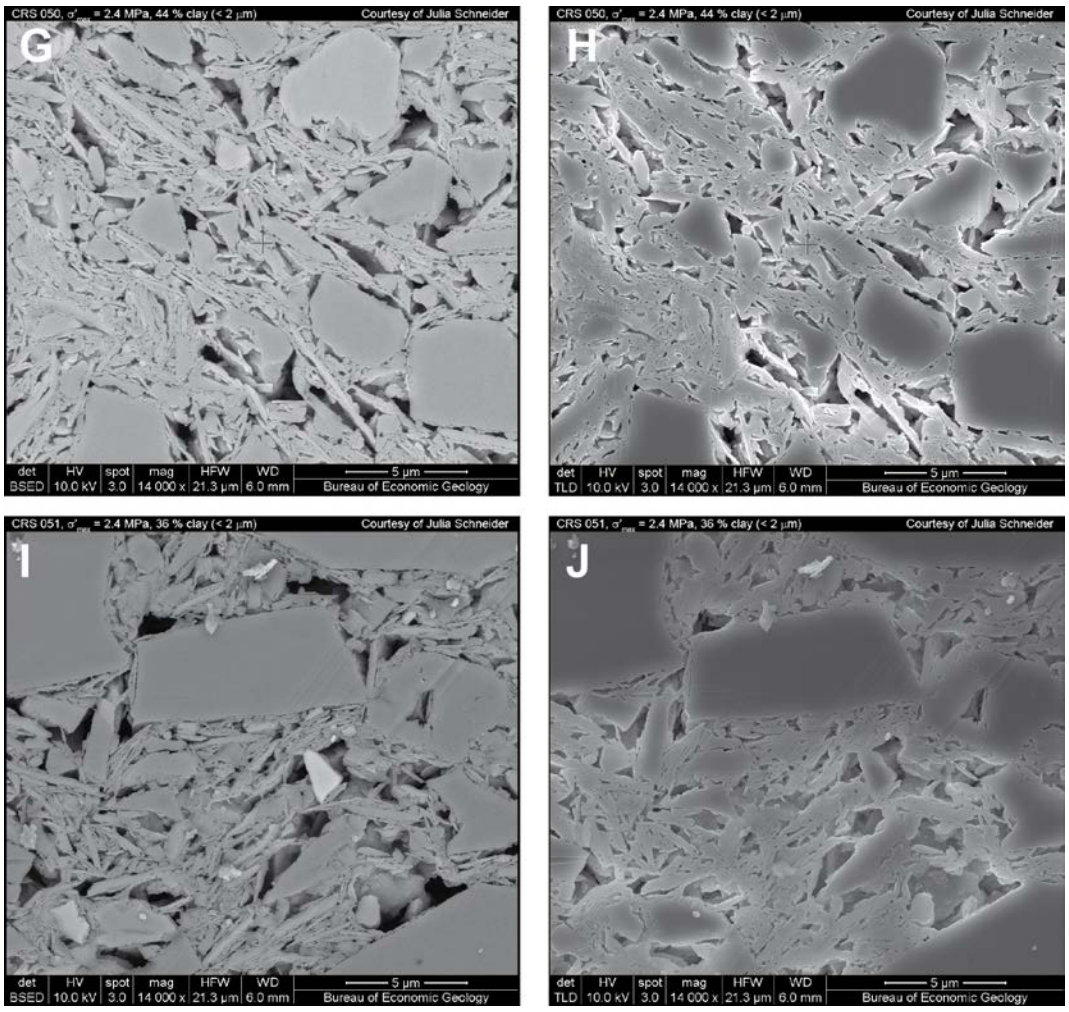

Figure A1.9: Scanning electron microscope images of Boston Blue Clay (BBC) –silt mixtures at maximum vertical effective stress of 2.4 MPa. Images represent vertical cross-section, i.e. load was applied from the top of the images. Left column are backscattered electron images. Right column are secondary electron images. Magnification of 14,000. A, B) 57% clay (SEM015_BSE_01_UT.tif and SEM015_TLSE_01_UT.tif). C, D) 52% clay (SEM016_BSE_05b_UT.tif and SEM016_TLSE_05b_UT.tif). E, F) 48% clay (SEM017_BSE_06_UT.tif and SEM017_TLSE_06_UT.tif). G, H) 44% clay (SEM018_BSE_04_UT.tif and SEM018_TLSE_04_UT.tif). I, J) 36% clay (SEM019_BSE_05b_UT.tif and SEM019_TLSE_05b_UT.tif).

NOMENCLATURE

Variable	*Definition*	*Dimensions*	*Unit*
C_c	Compression index	dimensionless	__
C_e	Expansion index	dimensionless	__
C_v	Coefficient of consolidation	L^2/T	m^2/s
$d\varepsilon/dt$	Strain rate	1/T	1/s
e	Void ratio	dimensionless	__
e_0	Reference void ratio at 1 MPa	dimensionless	__
e_i	Initial void ratio	dimensionless	__
G_s	Grain density	M/L3	kg/m^3
H	Specimen height	L	cm
H_0	Initial specimen height	L	cm
k	Vertical intrinsic permeability	L^2	m^2
k_0	Intercept of log-linear relationship between permeability and porosity	L^2	m^2
K	Hydraulic conductivity	L/T	m/s
LL	Liquid limit	dimensionless	__
m_v	Coefficient of volume compressibility	LT^2/M	1/kPa
OCR	Overconsolidation ratio	dimensionless	__
PI	Plasticity index	dimensionless	__
PL	Plastic limit	dimensionless	__
S_i	Initial saturation	dimensionless	__
u	Base pressure / pore pressure	M/T^2L	kPa
u_c	Backpressure / cell pressure	M/T^2L	kPa
w_n	Specimen water content	dimensionless	__
ΔH	Change in height / deformation	L	cm
Δu	Excess pore pressure	M/T^2L	kPa
ε	Strain	dimensionless	%
ϕ	Porosity	dimensionless	__
γ	Slope of log-linear relationship between permeability and porosity	dimensionless	__
γ_w	Unit weight of water	M/T^2L^2	Pa/m
μ_w	Dynamic viscosity of water	M/TL	Pa s
ρ_w	Density of water	M/L^3	kg/m^3
σ_v	Total axial stress	M/T^2L	kPa
σ'_{pc}	Preconsolidation stress	M/T^2L	kPa
σ_v'	Vertical effective stress	M/T^2L	kPa

ACKNOWLEDGEMENTS

Funding for this research was provided by the Consortium for Ocean Leadership through the Schlanger Ocean Drilling Fellowship received by J. Schneider. Robert M. Reed prepared the SEM images.

REFERENCES

ASTM International, 2005. Standard test methods for liquid limit, plastic limit, and plasticity index of soils (Standard D4318-05). *In* Annual Book of ASTM Standards (Vol. 04.08), ed., Soil and Rock (I): West Conshohocken, PA, American Society for Testing and Materials, p. 16.

ASTM International, 2006. Standard test method for one-dimensional consolidation properties of saturated cohesive soils using controlled-strain loading (Standard D4186-06). *In* Annual Book of ASTM Standards (Vol. 04.08), ed., Soil and Rock (I): West Conshohocken, PA, American Society for Testing and Materials, p. 15.

ASTM International, 2007. Standard test method for particle-size analysis of soils (Standard D422-63R07). *In* Annual Book of ASTM Standards (Vol. 04.08), ed., Soil and Rock (I): West Conshohocken, PA, American Society for Testing and Materials, p. 10-17.

Broichhausen, H., Littke, R., and Hantschel, T., 2005. Mudstone compaction and its influence on overpressure generation, elucidated by a 3D case study in the North Sea. *International Journal of Earth Sciences*, 94(5-6): 956-978. doi:10.1007/s00531-005-0014-1.

Dewhurst, D.N., Aplin, A.C., Sarda, J.P., and Yang, Y.L., 1998. Compaction-driven evolution of porosity and permeability in natural mudstones: An experimental study. *Journal of Geophysical Research*, 103(B1):651-661. doi:10.1019/97JB02540.

Dewhurst, D.N., Aplin, A.C., and Sarda, J.P., 1999. Influence of clay fraction on pore-scale properties and hydraulic conductivity of experimentally compacted mudstones. *Journal of Geophysical Research*, 104(B12):29261-29274. doi:10.1029/1999JB900276.

Hillier, S., 2000. Accurate quantitative analysis of clay and other minerals in sandstones by XRD: comparison of a Rietveld and a reference intensity ratio (RIR) method and the importance of sample preparation. *Clay Minerals*, 35(1): 291-302.

Kenney, T.C., 1964. Seal-level movements and the geologic histories of the post-glacial marine soils at Boston, Nicolet, Ottawa and Oslo. *Geotechnique*, 14(3): 203-230. doi:10.1680/geot.1964.14.3.302.

Loucks, R.G., Reed, R.M., Ruppel, S.C., and Jarvie, D.M., 2009. Morphology, genesis, and distribution of nanometer-scale pores in siliceous mudstones of the Mississippian Barnett Shale. *Journal of Sedimentary Research*, 79(12): 848-861. doi:10.2110/jsr.2009.092.

Santagata, M.C., and Kang, Y.I., 2007. Effects of geologic time on the initial stiffness of clays. *Engineering Geology*, 89: 98-111. doi: 10.1016/j.enggeo.2006.09.018.

Sawyer, D.E., Jacoby, R., Flemings, P.B., and Germaine, J.T., 2008. Data report: particle size analysis of sediments in the Ursa Basin, IODP Expedition 308 Sites U1324 and U1322, northern Gulf of Mexico. *In* Flemings, P.B., Behrmann, J.H., John, C.M., and the Expedition Scientists, eds., *Proc. IODP*, Volume 308: College Station, TX, p. 20. doi:10.2204/iodp.proc.308.205.2008.

Sheahan, T.C., 1991. An experimental study of the time-dependent undrained shear behavior of resedimented clay using automated stress path triaxial equipment [Ph.D. thesis]. Cambridge, Massachusetts Institute of Technology, 952 p.

Zoback, M.D., Kitasei, S., and Copithorne, B., 2010. Addressing the environmental risks from shale gas development, Worldwatch Institute, 19 p.

Appendix 2: Data Report: Permeability, compressibility, and microstructure of resedimented mudstones from the Shikoku Basin, seaward of the Nankai Trough, IODP Site C0011

ABSTRACT

I conducted grain size analyses and uniaxial, constant-rate-of-strain (CRS) consolidation experiments on six sediment samples prepared in the laboratory using the method resedimentation to analyze compression and flow behavior. The six samples are sediment mixtures composed of varying proportions of Nankai mud from Site C0011, collected during Integrated Ocean Drilling Program (IODP) Expedition 322, and silt-sized silica from US Silica. I performed all experiments in the GeoMechanics Laboratory at The University of Texas at Austin. The compression index systematically decreases with decreasing clay-size fraction. For clay-rich mixtures the compression index significantly decreases with vertical effective stress, whereas silt-rich mixtures show a constant compression index. Vertical intrinsic permeability decreases with increasing vertical effective stress and varies log-linearly with porosity. Slopes of this log-linear relationship vary for mixtures of 59% clay to 34% clay between 11.1 and 9.8. At a given porosity, vertical permeability increases by two orders of magnitude for clay contents ranging from 59% to 34%.

A2.1 INTRODUCTION

The Integrated Ocean Drilling Program (IODP) Expedition 322 sampled and logged the incoming sedimentary strata and uppermost igneous basement of the Shikoku Basin, seaward of the Nankai Trough (southwestern Japan) prior to their arrival and burial at the Nankai subduction front (Saito et al., 2009; Underwood et al., 2010). The

expedition is part of the Nankai Trough Seismogenic Zone Experiment (NanTroSEIZE) project and aimed at understanding the initial pre-subduction conditions because the down-dip evolution of those initial properties is what ultimately changes slip behavior along the plate interface from aseismic to seismic (Vrolijk, 1990; Hyndman et al., 1997; Moore and Saffer, 2001). Two sites were drilled during Expedition 322: Site C0011 on the northwest flank of the bathymetric high called Kashinosaki Knoll and Site C0012 near the crest of the seamount (Figure A2.1). Here I analyze samples from Site C0011.

During the early to middle Miocene the Shikoku Basin formed as part of the Philippine Sea plate (Okino et al., 1994; Kobayashi et al., 1995) which is currently moving toward the northwest beneath the Eurasian plate, roughly orthogonal to the axis of the Nankai Trough, at a rate of ~4 to 6 cm yr^{-1} (Seno et al., 1993; Miyazaki and Heki, 2001) (Figure A2.1). Deposits within the Shikoku Basin and the overlying Quaternary trench wedge are actively accreting at the deformation front (Tobin et al., 2009).

At Site C0011, measurement-while-drilling (MWD) and logging-while-drilling (LWD) data was collected at the end of Expedition 319 in Hole C0011A while a 536 m thick succession was cored in Hole C0011B during Expedition 322. Because coring started at 340 mbsf, Lithologic Unit I, which is upper Shikoku Basin facies consisting of hemipelagic mud with thin beds of volcanic ash, was not cored instead referred from logging data. The cored succession includes middle Shikoku Basin facies consisting of volcaniclastic and muddy turbidites as well as mass transport deposits and hemipelagic sediments, lower Shikoku Basin hemipelagic facies, lower Shikoku Basin turbidite facies, and volcaniclastic-rich facies. The age at the bottom of the cored succession is poorly constrained within the range of middle Miocene (~14.0 Ma). The igneous basement lies at ~1050 mbsf.

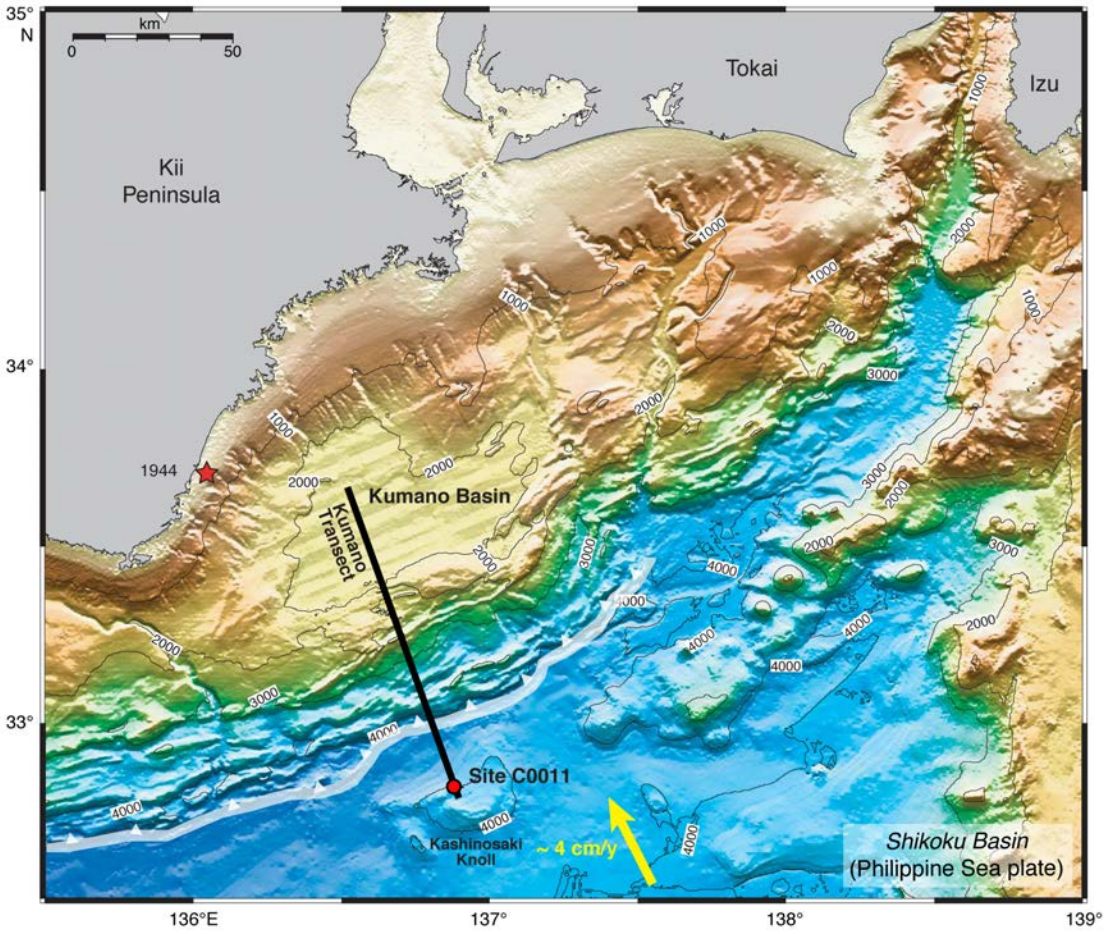

Figure A2.1: Bathymetry map with IODP Site C0011 drilled during IODP Expedition 322 (after Underwood et al., 2009). Black line indicates seismic line from Kumano Basin to Kashinosaki Knoll in the Shikoku Basin as shown in Figure 5.2. White transparent line indicates deformation front. Arrow shows convergence vector between Philippine Sea plate and Japanese Islands (Eurasian plate).

I used bulk mud mostly from the lower Shikoku Basin hemipelagic facies from depths between 586.8 and 774.69 mbsf at Hole C0011B to prepare homogenous and undisturbed samples in the laboratory using a method called resedimentation. I then conducted grain size analyses and constant-rate-of-strain (CRS) consolidation tests in order to understand the compositional influence on deformation and flow behavior.

A2.2 EXPERIMENTAL METHODS

A2.2.1 Sample Descriptions

Bulk material from cores 31R to 58R at Site C0011B, corresponding to depths of 586.8 mbsf to 774.69 mbsf, was collected and shipped to the UT laboratory. I then air-dried, ground, and homogenized the bulk material to a single batch. The average specific gravity over the sampled depth range is 2680 kg/m^3 based on moisture and density (MAD) measurements onboard the *JOIDES Resolution* during the IODP Expedition 322 (Underwood et al., 2009). I added silt-sized silica (MIN U SIL 40) from US Silica to the baseline batch of Nankai mud in the following proportions of mud to silica: 100:00, 88:12, 76:24, 64:36, 52:48, and 40:60 (Table A2.1).

% Nankai : % Silt[a]	*% Clay*[b]	*Resed #*[c]	*CRS #*[d]	*GS #*[e]
100 : 00	59	Resed 062 T	CRS 090	GS 147
88 : 12	54	Resed 051 B	CRS 091	GS 148
76 : 24	51	Resed 052 T	CRS 093	GS 149
64 : 36	43	Resed 054 T	CRS 094	GS 150
52 : 48	39	Resed 056 T	CRS 089	GS 146
40 : 60	34	Resed 059 T	CRS 088	GS 145
Silt[a]	10			GS 103

Table A2.1: Summary table of various tests performed on Nankai mudstone – silt mixtures.

[a] Silt: silt-sized silica (US MIN U SIL 40 purchased from US Silica)
[b] % Clay: clay fraction by mass measured in grain size analysis (for test number see this table, column 5)
[c] Resed #: resedimentation test number; 'T' and 'B' refer to top and bottom specimen out of the two specimens per resedimentation batch
[d] CRS #: constant-rate-of-strain (CRS) consolidation test number
[e] GS #: grain size analysis test number

A2.2.2 Index Properties

The mineralogic composition of the pure Nankai mud was measured by Macaulay Scientific Consulting LTD in Aberdeen, UK. Both whole rock and <2μm clay fraction analyses were performed by X-ray powder diffraction (XRPD).

I determined Atterberg Limits such as liquid limit (LL), plastic limit (PL) and plasticity index (PI) on the pure Nankai mud in accordance to ASTM Standard D4318-05 (ASTM International, 2005). Atterberg Limits are used to characterize the fine-grained fraction of soils and, together with other soil properties, to correlate with engineering behavior such as compressibility, hydraulic conductivity, intrinsic permeability, and shear strength, for example. Liquid and plastic limit are water contents that separate different consistency states from each other. I performed the multipoint liquid limit method (ASTM International, 2005) using a hand-operated liquid limit device, also called Casagrande cup. I determined the plastic limit by the hand method (ASTM International, 2005). The plasticity index is the range of water content over which the soil behaves plastically, or numerically the difference between liquid limit and plastic limit.

I determined the particle size distributions of all six samples using the hydrometer method in general accordance with ASTM D422-63 guidelines (ASTM International, 2007) and Sawyer et al. (2008). The hydrometer method uses a suspension of sediment and water, which is thoroughly mixed, after which particles settle out. A hydrometer measures the density of the suspension at a known depth below the surface and time. From the hydrometer tests we obtain the particle diameter at a specific time and depth and the percentage of the original sample mass still left in suspension.

A2.2.3 Resedimentation

I prepared sediment samples in the laboratory using a method called resedimentation (Sheahan, 1991; Santagata and Kang, 2007) which was developed at the Massachusetts Institute of Technology and simulates natural sedimentation under controlled stress conditions. Homogeneity and no disturbance are key advantages of resedimented over intact samples. The dry, ground, and homogenized Nankai mud is mixed with de-ionized water at a water content of 105% and 26g/l sea salt to form a slurry. In case of the Nankai mud – silica mixtures these values for water and salt content are used only per mud fraction. The silica fraction is just moistened with de-ionized water to water content of 33% and mixed in with the Nankai mud. After homogenizing the slurry with a spatula for at least 20 minutes, the slurry is de-aired using a vacuum pump to eliminate any air bubbles. Then I poured the slurry into a consolidometer with an inside diameter of 6.9 cm. Below and on top of the slurry are a porous stone and filter paper allowing pore fluids to drain in both directions but preventing fines from being washed out. The initial height of all samples varied between 11.5 and 13.6 cm.

Then I incrementally loaded the slurry, doubling the mass on the slurry every time, to a vertical effective stress of 100 kPa (in this study) (Table A2.3). A linear position transducer (LPT), which at the time of measurement could not be mounted onto the system until the beginning of the fifth stress increment due to weight restrictions, monitors the vertical displacement throughout the resedimentation experiment. The last weight increment is left on the slurry till the sediment reaches secondary consolidation. After unloading the sample to an overconsolidation ratio (OCR), which is the maximum past effective stress divided by the current effective stress, of four, I carefully and slowly extruded the samples. The final height of all samples varied between 8.2 and 9.2 cm. A small slice of material was cut off for determination of void ratio at the end of the

resedimentation experiment. The remaining sample yielded two specimens for consolidation testing of which one is only tested and shown here.

A2.2.4 Consolidation Testing

After resedimenting the six sediment mixtures composed of varying proportions of Nankai mud from Site C0011 and silt-sized silica, I conducted constant-rate-of-strain (CRS) consolidation tests according to American Society for Testing and Materials (ASTM) D4186-06 guidelines (ASTM International, 2006). The temperature in the UT laboratory is controlled to a constant temperature of 23.9°. The specimens were trimmed into a steel ring using a trimming jig, wire saw, and a sharp-edge spatula. Once the specimen is in the ring, a wire-saw, razor blade, and recess tool was used to smoothen the top and bottom of the specimen and to ensure consistent specimen dimensions. The initial height (H_0) and diameter are 1.73cm and 4.99cm, respectively. I flushed all lines with de-ionized water and applied a constant backpressure of 386 kPa for at least 12 hours to ensure full saturation. The interaction between de-ionized water in the chamber and salt water in the specimen most likely caused the low saturations (Table A2.5). Salt water should be used in the chamber in future experiments.

The specimens, laterally confined in the steel ring, are consolidated at a constant rate of strain (i.e. uniaxial strain). The strain rate for all six specimens varies between 0.2%/hr and 1.05%/hr, increasing with increasing silica content (Table A2.5). These strain rates were not adjusted during the test, yet they ensured pore pressure ratios (ratio of excess pore pressure to total axial stress) to be smaller than 0.1. The top of the specimen is open to the cell pressure (u_c) whereas the bottom is undrained. During the consolidation test I continuously monitored specimen height (H), total axial stress (σ_v),

and base pressure (u). Experiments were run to a maximum vertical effective stress of 20 MPa where stresses were held for 6 hours to allow excess pore pressure to dissipate. Specimens were then unloaded to an overconsolidation ratio (OCR) of four.

I computed axial strain (ε), base excess pore pressure (Δu), average vertical effective stress (σ'_v), hydraulic conductivity (K), intrinsic permeability (k), coefficient of volume compressibility (m_v), and coefficient of consolidation (C_v) as follows in accordance with ASTM Standard D4186-06 (ASTM International, 2006):

$$\varepsilon = \Delta H / H_0, \tag{A2.1}$$

where displacements are measured with linear position transducers. For definitions of variables see nomenclature. In Figures A2.6 to A2.11 I report strain as percentage.

$$\Delta u = u - u_c \tag{A2.2}$$

$$\sigma_v^{'} = \left[\sigma_v - \frac{2}{3}\Delta u\right] - u_c \tag{A2.3}$$

$$K = \frac{\dot{\varepsilon} H H_0 \gamma_w}{2\Delta u} \tag{A2.4}$$

$$k = \frac{K\mu_w}{\gamma_w} \tag{A2.5}$$

$$m_v = \frac{\Delta\varepsilon}{\Delta\sigma_v^{'}} \tag{A2.6}$$

$$C_v = \frac{K}{m_v \gamma_w} \tag{A2.7}$$

I computed compression index (C_c), which is the slope of the virgin consolidation line, from the change in specimen void ratio (e) with vertical effective stress (σ'_v):

$$C_c = \frac{\Delta e}{\Delta \log(\sigma_v')} \quad \text{(A2.8)}$$

Maximum preconsolidation stress (σ'_{pc}) of all specimens is 100 kPa equal to the maximum vertical effective stress the slurry was preloaded to during resedimentation.

A2.2.5 SEM Imaging

Scanning Electron Microscope images, both backscattered (BSE) and secondary (SE), were taken on a field-emission scanning electron microscope (SEM). The samples were prepared using an argon-ion beam milling technique (Loucks et al., 2009), which avoids mechanical polishing and instead produces surfaces with only minor topographic variations using accelerated argon ions. BSE and SE images were taken at three different magnifications (1,000 x, 14,000 x, and 60,000 x) after consolidation of sediment mixtures to a maximum vertical effective stress of 20 MPa. Images represent a vertical cross-section of the sample. One BSE image at a magnification of 14,000 of each sediment mixture is shown here (Figure A2.12).

A2.3 RESULTS

A2.3.1 Index Properties

The X-ray powder diffraction (XRPD) results show that the bulk sample contains quartz, feldspars, minor calcite, pyrite, and halite and clay minerals (Table A2.2, Figure A2.2A). The clay fraction is dominated by a random mixed-layer illite-smectite and illite with lesser amounts of chlorite and kaolinite (Figure. A2.2B). The expandibility of the illite-smectite is around 80%.

Atterberg Limits results on the pure Nankai mud show that the liquid limit (LL) is 68%, the plastic limit (PL) is 29% and thus the plasticity index (PI) is 39% (Figure A2.3).

I conducted particle size distribution curves on the six specimens after consolidation to 20 MPa (Figure A2.4). The clay-size fractions (<2μm) by mass are 59%, 54%, 51%, 43%, 39%, and 34% for mixtures with 100%, 88%, 76%, 64%, 52%, and 40% Nankai mud and silica as the remainder. Thus, the specimens fall into the categories silty clay and clayey silt. Sand, silt, and clay percentages are given in Table A2.3.

A

Quartz	*Plagioclase*	*K-feldspar*	*Calcite*	*Dolomite*	*Pyrite*
23.5	11.4	4.5	1.2	0.0	1.1

Halite	*Amphibole*	*Muscovite*	*Illite*	*Smectite*	*Illite + Illite-Smectite*
0.3	0.0	2.6	5.8	44.7	50.5

Kaolinite	*Chlorite*	*Tri-mica*	*Hydrobiotite*	*Talc*	*Total*
1.2	3.8	0.0	0.0	0.0	100.1

B

Chlorite	*Kaolinite*	*Illite*	*Illite-Smectite*	*% Expandibility*
3	1	11	85	80

Table A2.2: Mineralogy of Nankai mudstone (Resed 062, CRS 090). A) Mineralogy of whole rock as weight percent determined using the reference intensity ratio (RIR) method (Hillier, 2000). B) Mineralogy of clay fraction smaller than 2 μm expressed as relative weight percent.

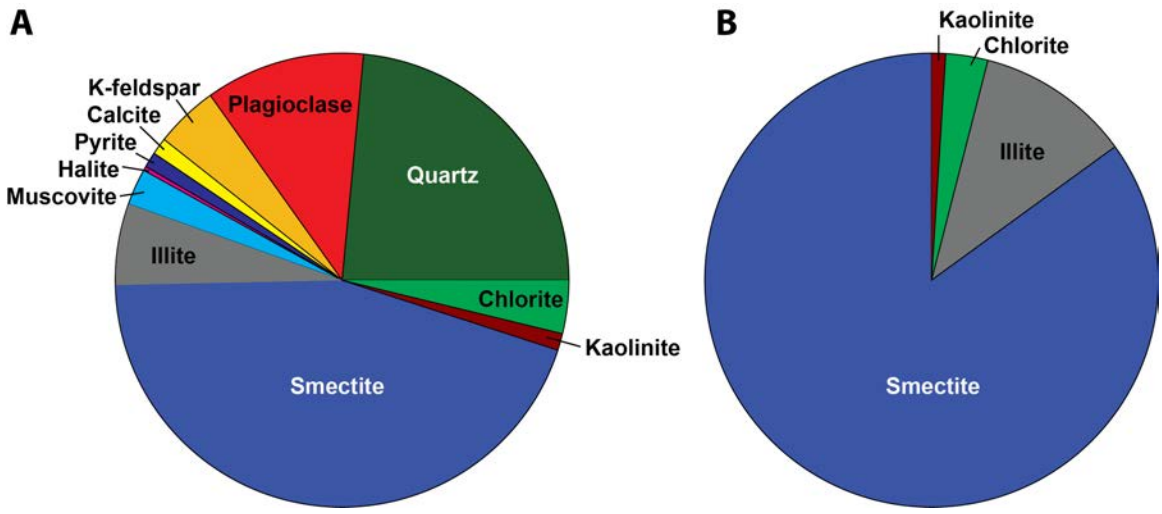

Figure A2.2: Mineralogy of Nankai mudstone measured through X-ray powder diffraction by *Macaulay Scientific Consulting LTD* (Table A2.2). A) Mineralogy of whole rock determined using the reference intensity ratio (RIR) method (Hillier, 2000). B) Mineralogy of clay fraction smaller than 2 μm expressed as relative weight percent.

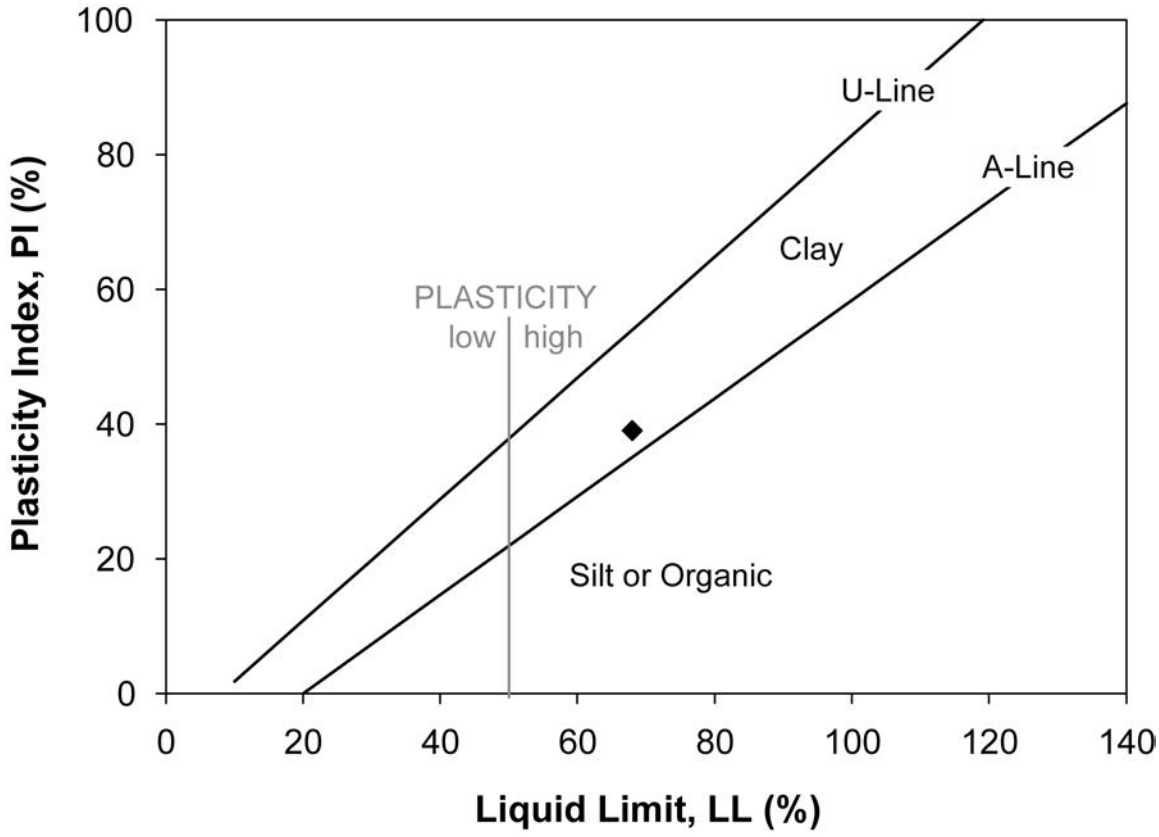

Figure A2.3: Atterberg Limits of Nankai mudstone. LL = liquid limit, PI = plasticity index.

% Nankai : % Silica [a]	*CRS #* [b]	*% Sand* [c]	*% Silt* [c]	**% Clay** [c]
100 : 00	CRS 90	0	41	59
88 : 12	CRS 91	0	46	54
76 : 24	CRS 93	0	49	51
64 : 36	CRS 94	0	57	43
52 : 48	CRS 89	0	61	39
40 : 60	CRS 88	0	66	34

Table A2.3: Particle size distributions of Nankai mudstone – silt mixtures. Boundary between sand and silt is defined at 62.5 μm and between silt and clay at 2 μm.

[a] Silt: silt-sized silica (US MIN U SIL 40 purchased from US Silica)
[b] CRS #: constant-rate-of-strain (CRS) consolidation test number
[c] %Sand, Silt, Clay: grain size analyses results (for test numbers see Table A2.1)

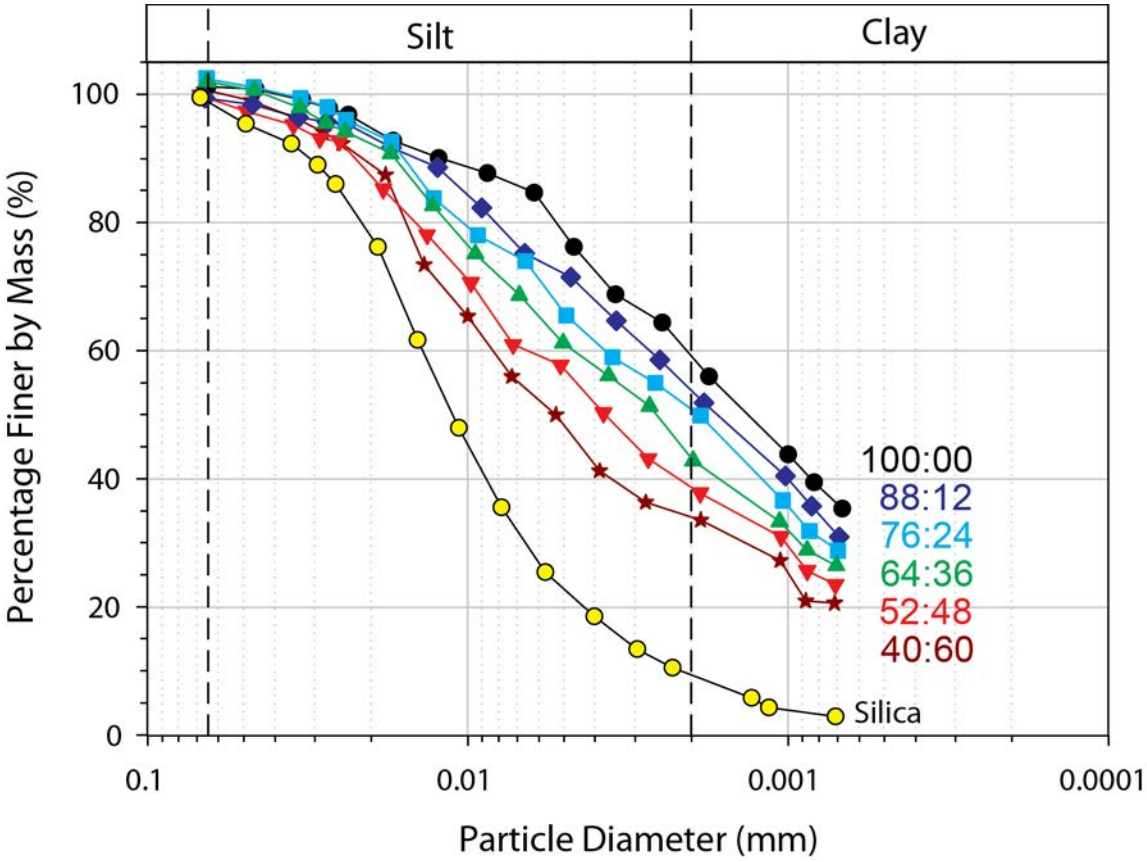

Figure A2.4: Particle size distribution plots on a semi-log scale (Table A2.3). All data points represent hydrometer readings. Sand/silt boundary is defined at 62.5 μm and silt/clay boundary is defined at 2 μm. Black circles = 59% clay, dark blue diamonds = 54% clay, light blue squares = 51% clay, green triangles pointing upward = 43% clay, red triangles pointing downward = 39% clay, brown stars = 34% clay, yellow circles = silt-sized silica (10% clay).

A2.3.2 Resedimentation

All six compression curves during resedimentation experiments are shown in Figure A2.5 (Table A2.4). Each data point represents the void ratio and vertical effective stress at the end of a stress increment. The first digitally measured void ratio (at 2.6 kPa) systematically decreases from 2.50 to 1.57 for specimens with 100% and 40% Nankai mud. The compression index (C_c) decreases from 0.63 to 0.37 for specimens with 100% and 40% Nankai mud showing that the samples become stiffer the more silica they contain.

% Nankai : % Silt[a]	*Resed #*[b]	*e*[c] *at 2.60 kPa*	*e at 5.22 kPa*	*e at 10.46 kPa*	*e at 20.95 kPa*	*e at 41.92 kPa*	*e at 68.15 kPa*	*e at 99.62 kPa*	*e at 24.88 kPa*
100 : 00	Resed 062 T	2.50	2.32	2.13	1.96	1.77	1.63	1.51	1.57
88 : 12	Resed 051 B	2.39	2.20	2.03	1.85	1.67	1.54	1.43	1.44
76 : 24	Resed 052 T	2.20	2.06	1.89	1.72	1.51	1.40	1.30	1.31
64 : 36	Resed 054 T	1.92	1.78	1.62	1.49	1.34	1.22	1.17	1.18
52 : 48	Resed 056 T	1.65	1.53	1.40	1.28	1.18	1.10	1.04	1.04
40 : 60	Resed 059 T	1.57	1.45	1.31	1.20	1.10	1.03	0.98	0.98

Table A2.4: Resedimentation results for Nankai mudstone – silt mixtures.

[a] Silt: silt-sized silica (US MIN U SIL 40 purchased from US Silica)
[b] Resed #: resedimentation test number; 'T' and 'B' refer to top and bottom specimen out of the two specimens per resedimentation batch
[c] e: void ratio at varying vertical effective stresses

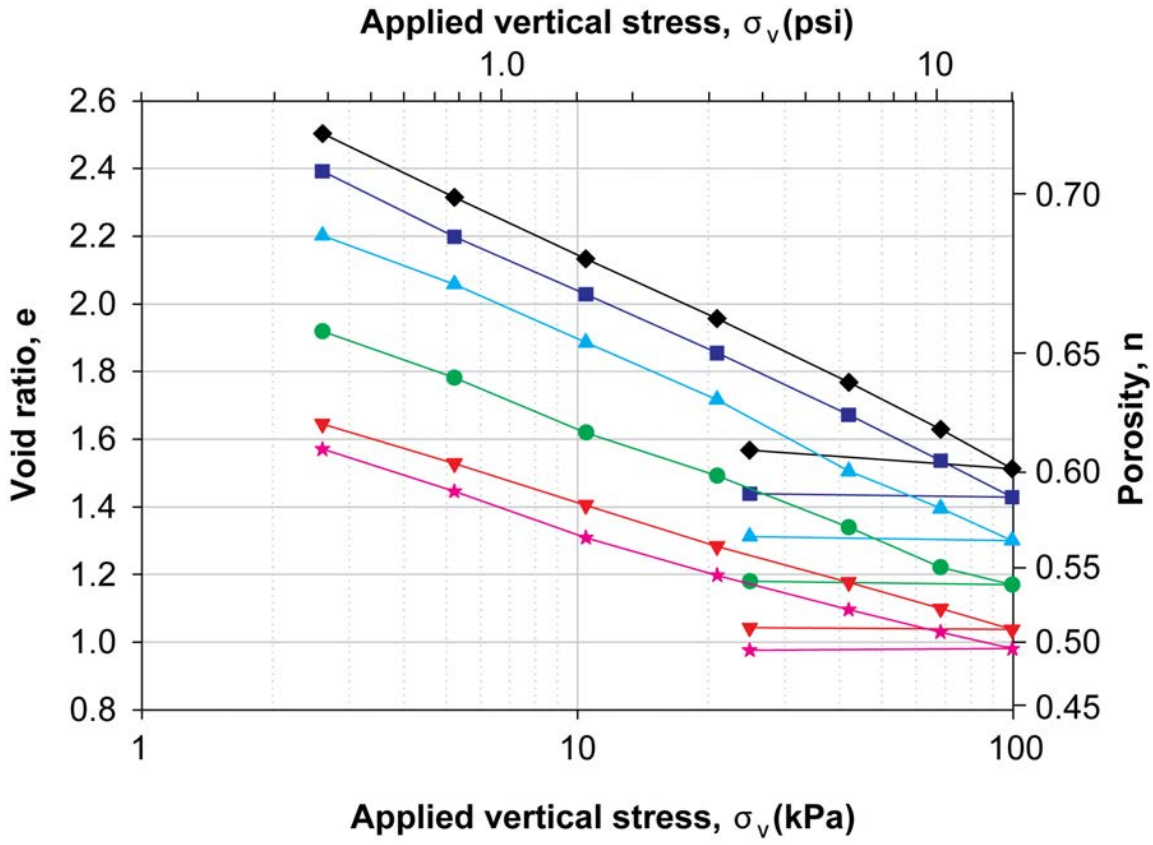

Figure A2.5: Compression curves during resedimentation (Table A2.4). Each data point represents the vertical effective stress and void ratio at the end of a stress increment. Black diamonds = 59% clay, dark blue squares = 54% clay, light blue triangles pointing upward = 51% clay, green circles = 43% clay, red triangles pointing downward = 39% clay, pink stars = 34% clay.

A2.3.3 Consolidation Testing

Uniaxial constant-rate-of-strain consolidation tests on all six resedimented mixtures composed of Nankai mud and silt-sized silica show a decrease in initial void ratio from 1.62 to 0.95 for samples with 100% to 40% Nankai mud. The compression index (C_c) changes significantly during consolidation. C_c decreases with increasing vertical effective stress, particularly for the clay-rich samples. Vertical intrinsic permeability varies log-linearly with porosity and increases with decreasing clay fraction. At a given porosity of 40% the difference in permeability between 100% and 40% Nankai mixtures is two orders of magnitude. Coefficient of consolidation (C_v) decreases with increasing stress and varies between $7 * 10^{-9}$ m^2/s and $3 * 10^{-7} m^2/s$ for samples with 100% and 40% Nankai mud.

Table A2.5 summarizes the details of each CRS test. Figures A2.6 to A2.11 show the consolidation curves in both ε-log(σ'_v) and e-log(σ'_v), normalized excess pore pressure ($\Delta u/\sigma_v$), hydraulic conductivity (K), intrinsic permeability (k), and coefficient of consolidation (C_v) for each CRS test.

CRS #[a]	*% Nankai : Silt*[b]	σ'_{pc}	w_n	S_i	e_i	G_s	$d\varepsilon/dt$	C_c	C_e	γ	k_0
CRS 90	100 : 00	100	56.64	93.1	1.63	2.680	0.2	0.36	0.056	11.1	-22.9
CRS 91	88 : 12	100	54.09	93.0	1.56	2.676	0.35	0.32	0.053	11.6	-22.8
CRS 93	76 : 24	100	47.97	93.8	1.37	2.673	0.5	0.31	0.040	11.2	-22.3
CRS 94	64 : 36	100	42.50	94.3	1.20	2.669	0.7	0.29	0.036	10.5	-21.5
CRS 89	52 : 48	100	38.06	96.15	1.06	2.666	0.9	0.27	0.030	9.9	-21.0
CRS 88	40 : 60	100	34.76	94.90	0.98	2.662	1.05	0.24	0.017	9.8	-20.5

Table A2.5: Consolidation properties. CRS #: Constant-rate-of-strain (CRS) consolidation test number. w_n: Water content measured on specimen. e_i: Initial void ratio calculated from water content measured on specimen and grain density. G_s: Grain density measured on bulk Nankai mudstone and on silt-sized silica from US Silica, extrapolated for mixtures in between. $d\varepsilon/dt$: Strain rate in %/hr here. Strain rate was not adjusted during consolidation test. C_c and C_e: Determined between vertical effective stress of 5000 kPa and 20000 kPa.

[a] CRS #: constant-rate-of-strain (CRS) consolidation test number
[b] Silt: silt-sized silica (US MIN U SIL 40 purchased from US Silica)

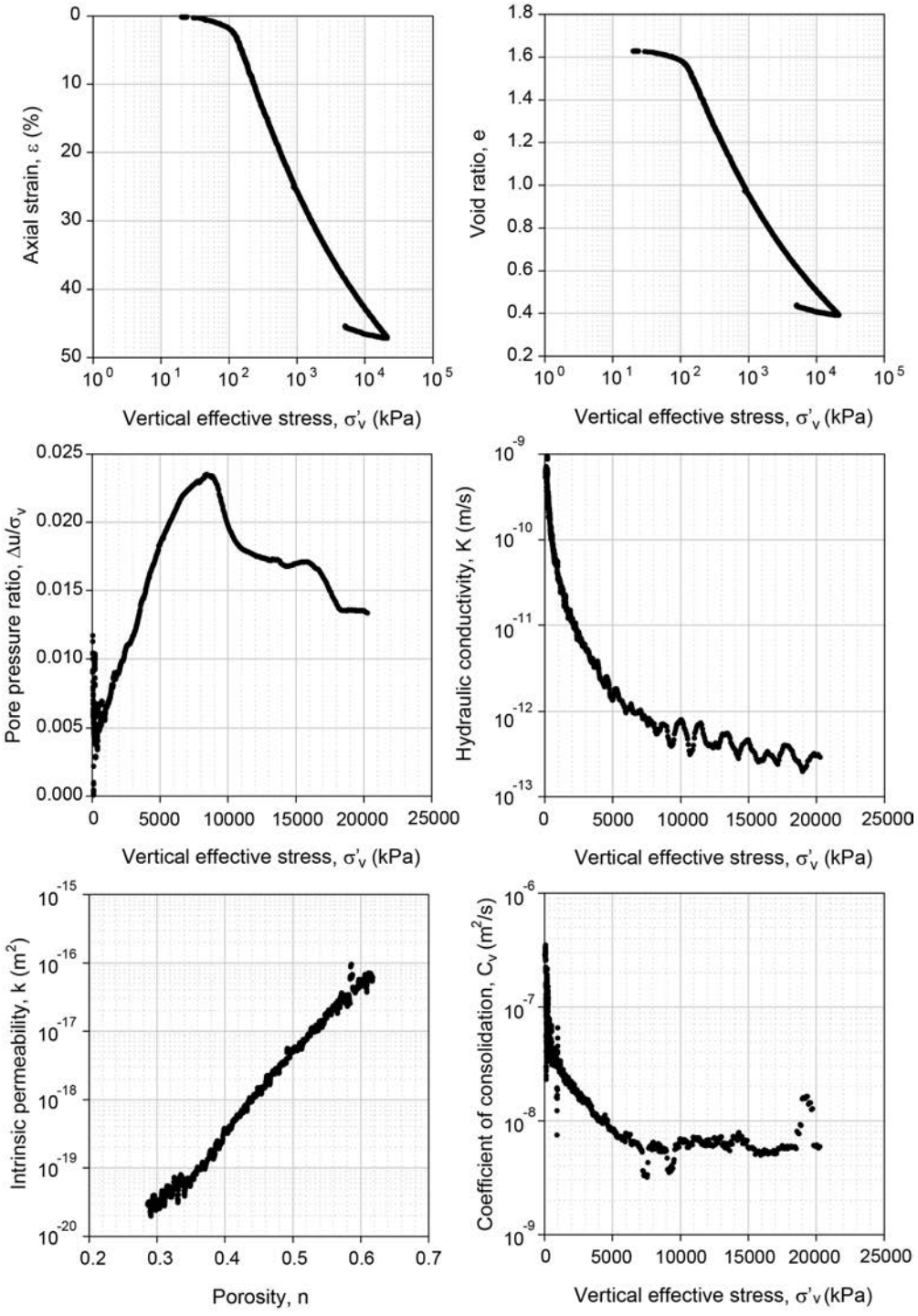

Figure A2.6: Experimental consolidation results for the sample with 59 % clay-sized particles (100% Nankai mudstone and 00% silica, CRS090).

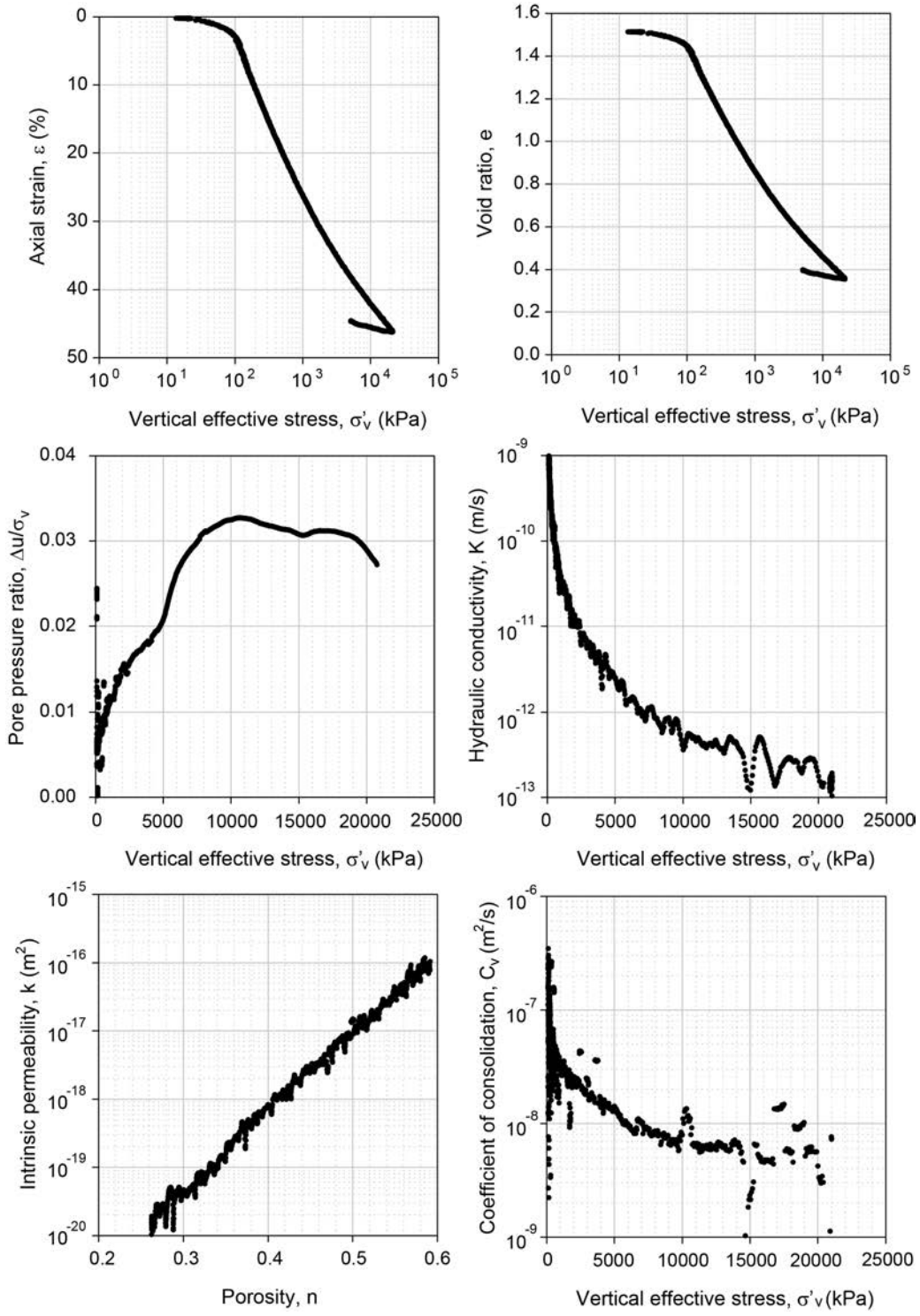

Figure A2.7: Experimental consolidation results for the sample with 54 % clay-sized particles (88% Nankai mudstone and 12% silica, CRS091).

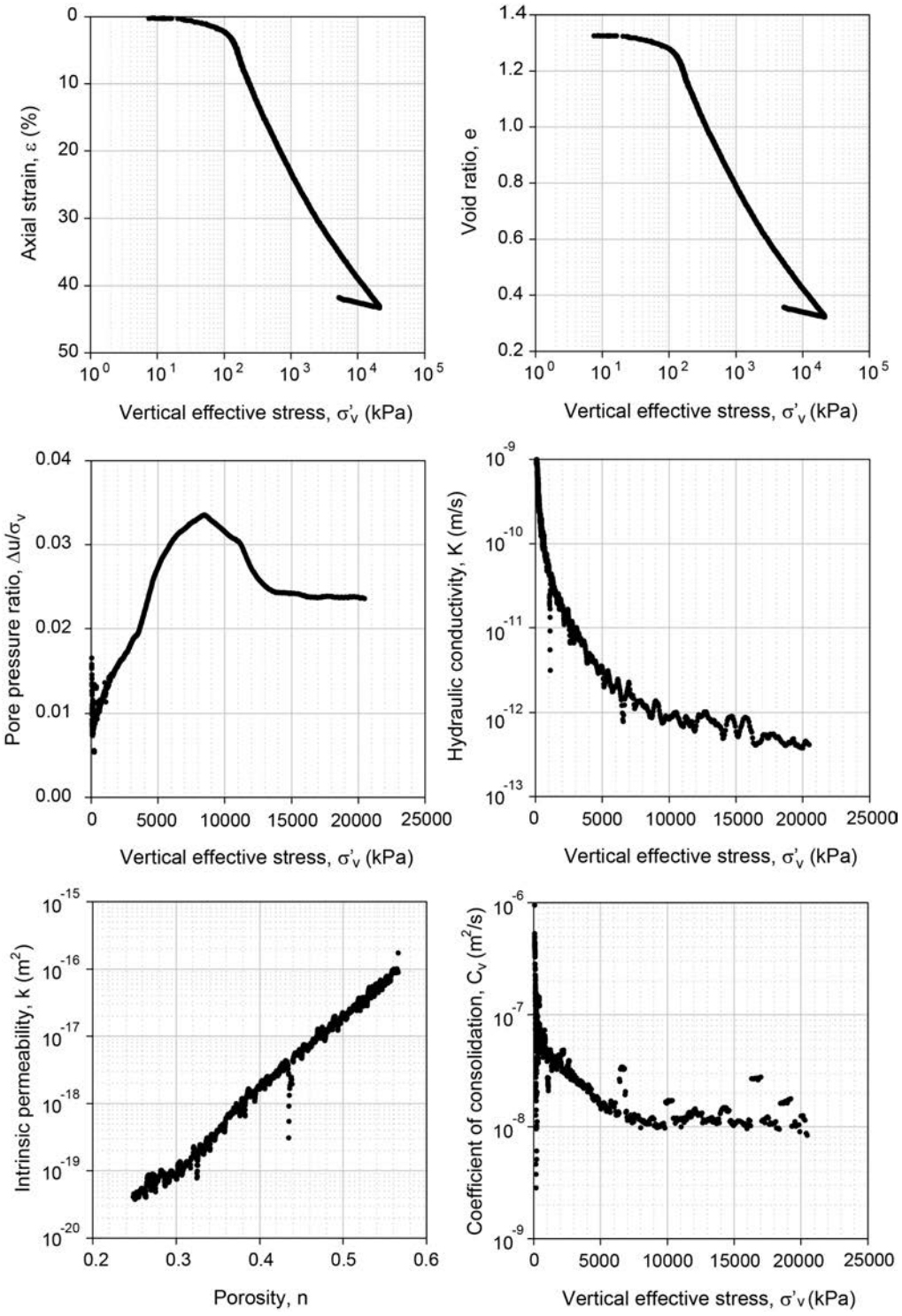

Figure A2.8: Experimental consolidation results for the sample with 51 % clay-sized particles (76% Nankai mudstone and 24% silica, CRS093).

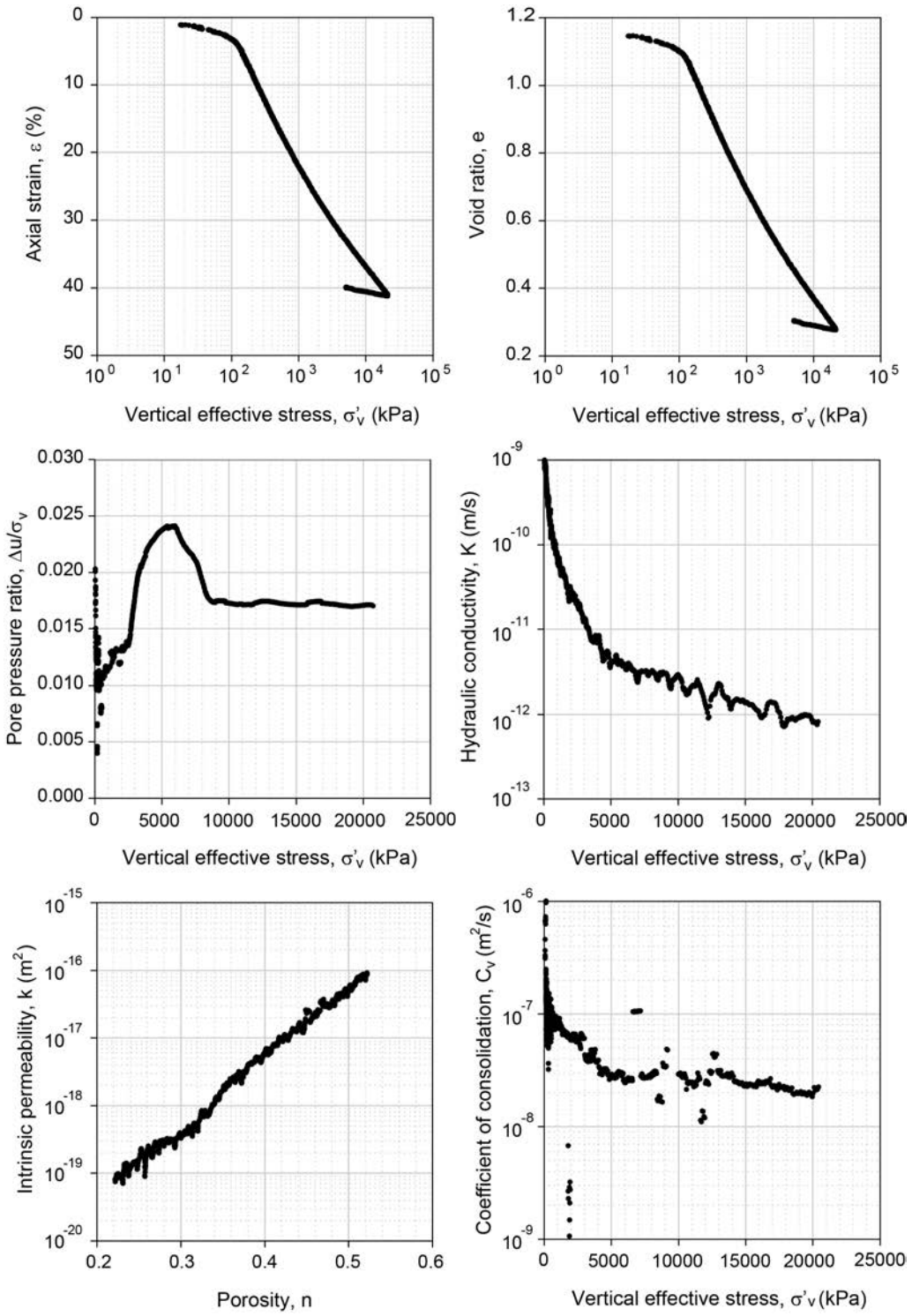

Figure A2.9: Experimental consolidation results for the sample with 43 % clay-sized particles (64% Nankai mudstone and 36% silica, CRS094).

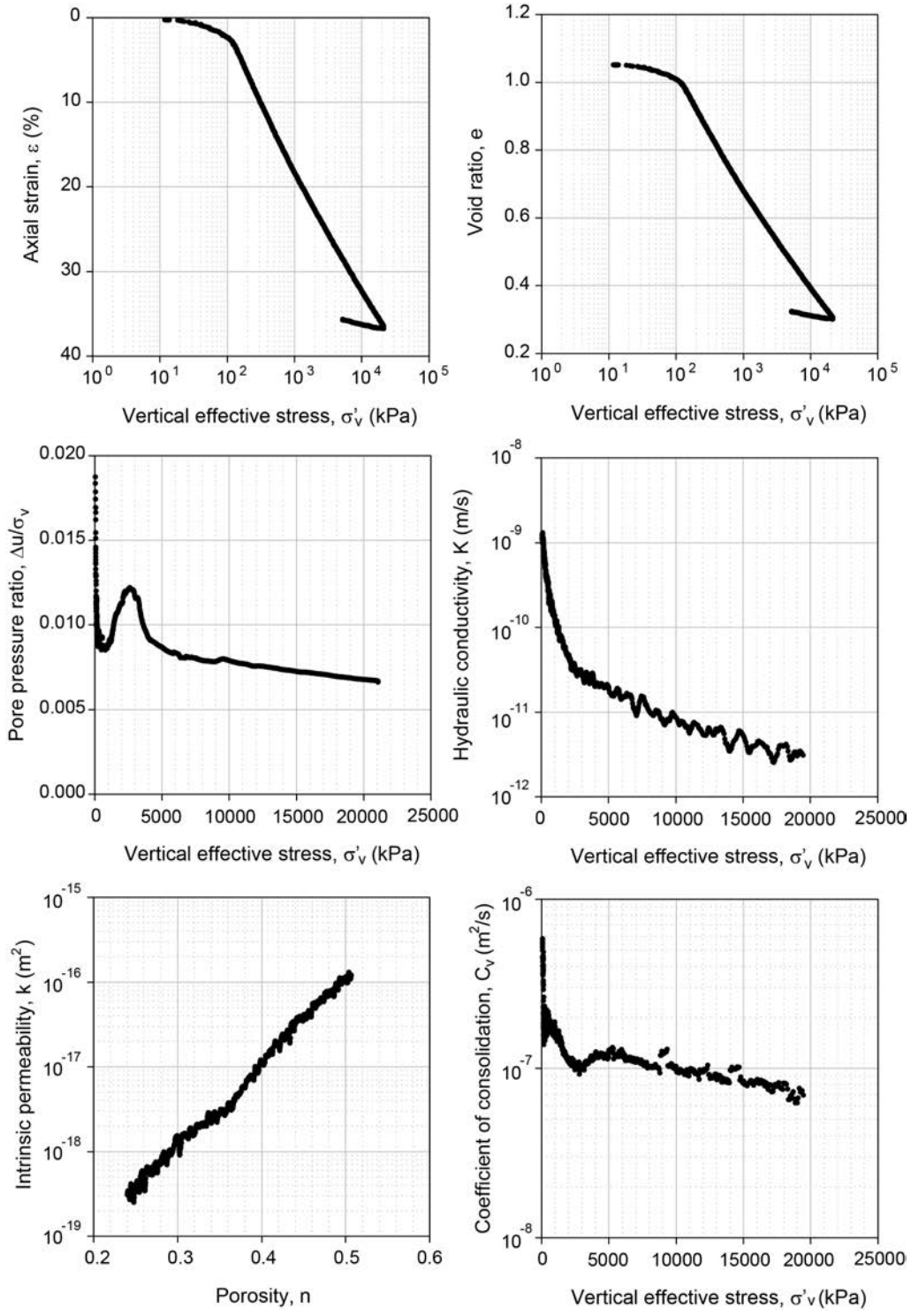

Figure A2.10: Experimental consolidation results for the sample with 39 % clay-sized particles (52% Nankai mudstone and 48% silica, CRS089).

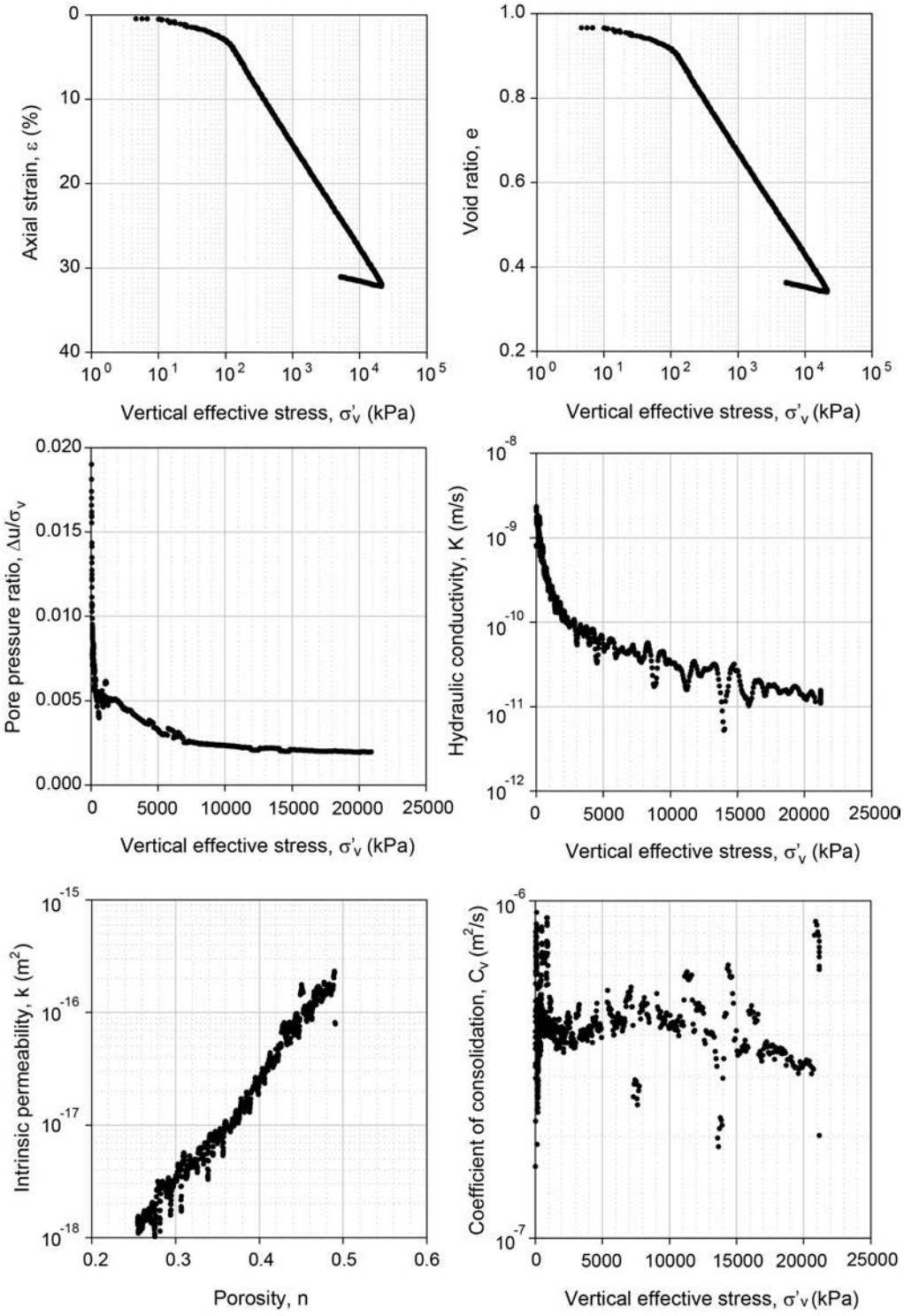

Figure A2.11: Experimental consolidation results for the sample with 34 % clay-sized particles (40% Nankai mudstone and 60% silica, CRS088).

A2.3.4 SEM Imaging

Backscattered electron microscope (BSE) images show a strong decrease in clay particle alignment with decreasing clay fraction (Figure A2.12). Pores in the pure Nankai mudstone are either elongated pores between similarly oriented clay sheets or triangular to crescent-shaped pores in folded clays, particular in between smectites (Figures A12.A, B). In coarser samples large jagged pores are preserved where silt grains touch each other and form silt bridges (Figures A12.I-L). A gradual increase in mean pore size with decreasing clay fraction occurs.

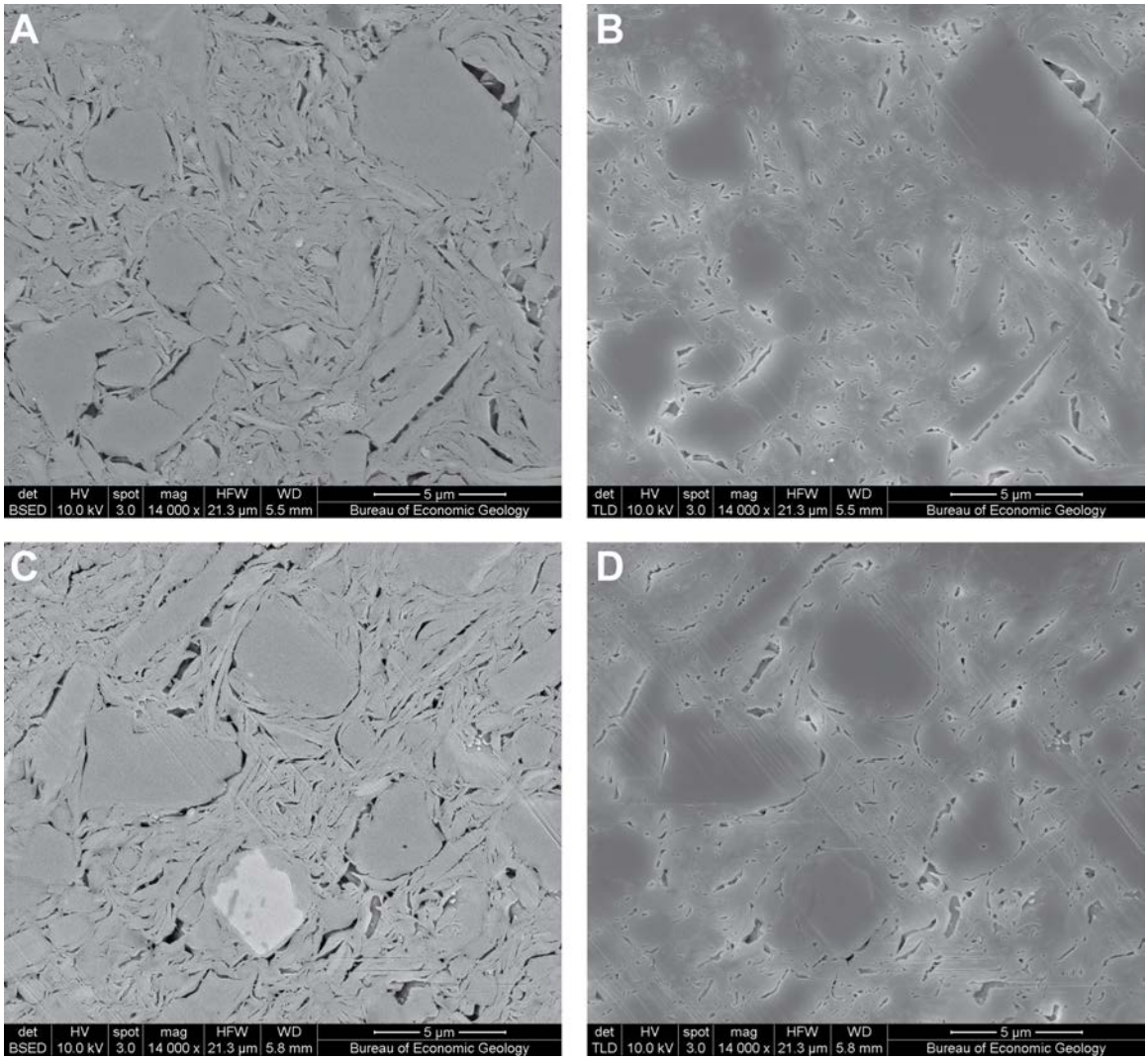

Figure A2.12: Scanning electron microscope images of Nankai –silt mixtures at maximum vertical effective stress of 20 MPa. Images represent vertical cross-section, i.e. load was applied from the top of the images. Left column are backscattered electron images. Right column are secondary electron images. A, B) Pure Nankai mudstone (59% clay) (SEM041_BSE_02b_UT.tif and SEM041_TLSE_02b_UT.tif). C, D) 54% clay (SEM042_BSE_02b_UT.tif and SEM042_TLSE_02b_UT.tif).

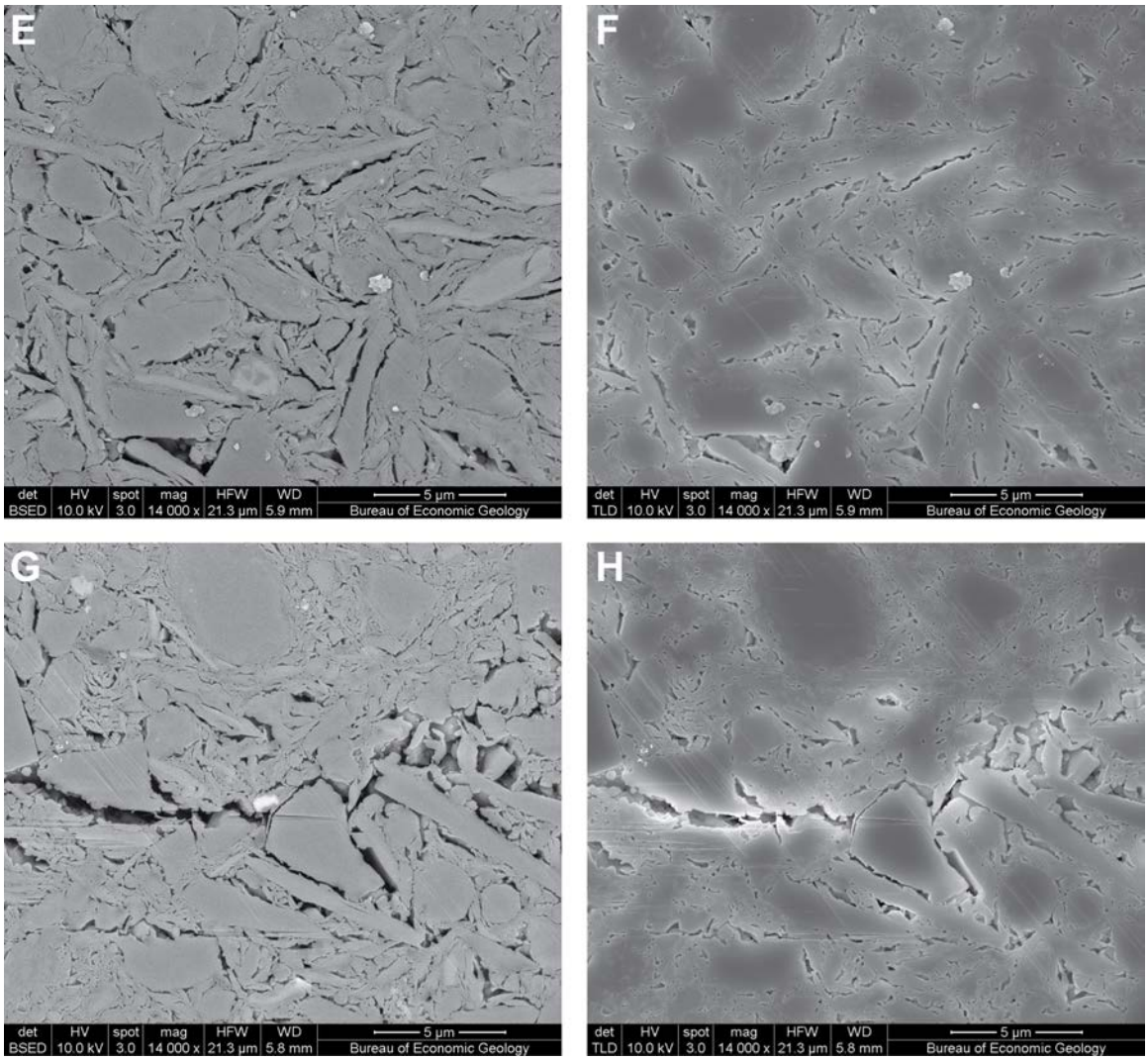

Figure A2.12: Continued. Scanning electron microscope images of Nankai –silt mixtures at maximum vertical effective stress of 20 MPa. Images represent vertical cross-section, i.e. load was applied from the top of the images. Left column are backscattered electron images. Right column are secondary electron images. E, F) 51% clay (SEM043_BSE_03b_UT.tif and SEM043_TLSE_03b_UT.tif). G, H) 43% clay (SEM044_BSE_03b_UT.tif and SEM044_TLSE_03b_UT.tif).

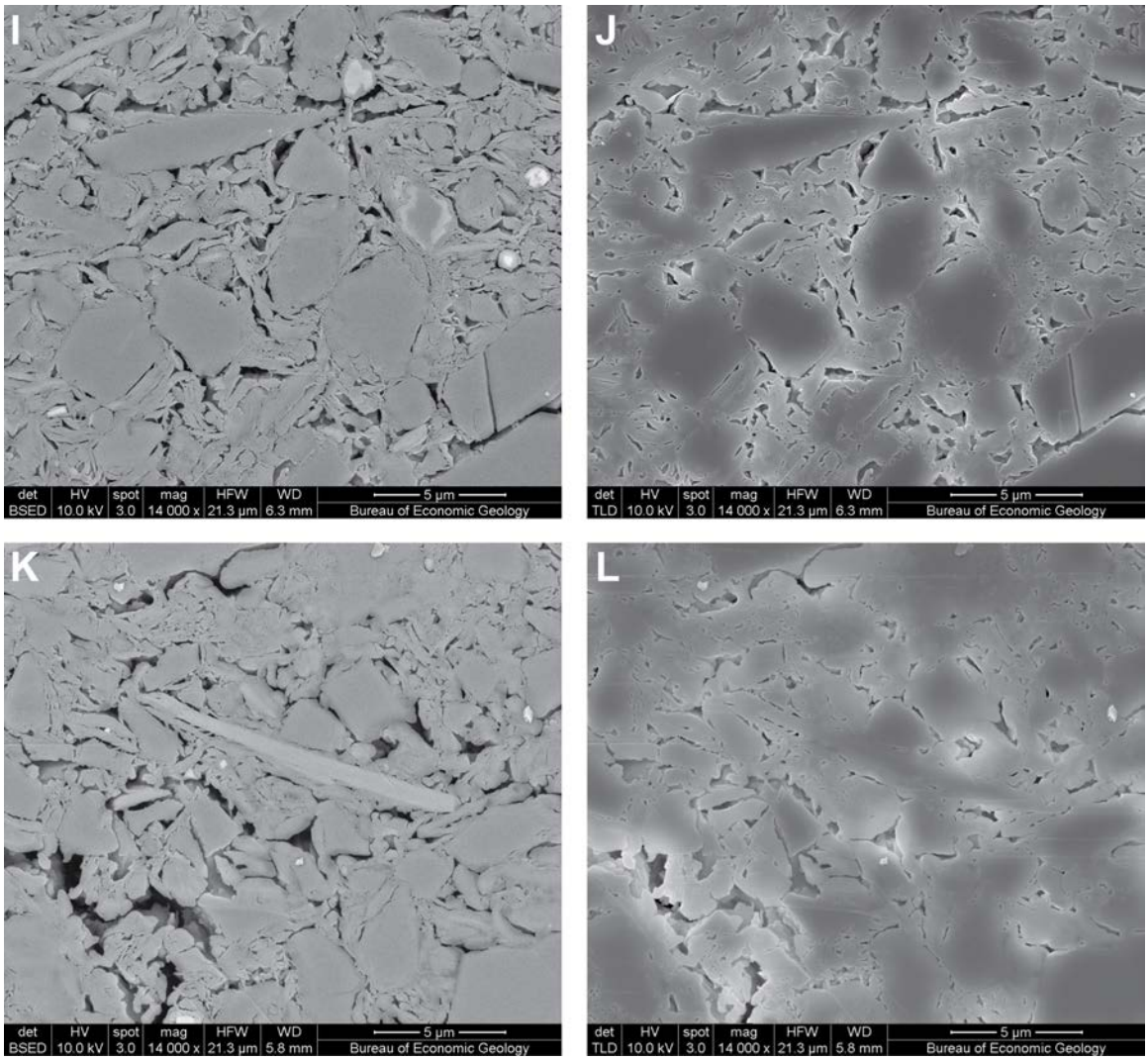

Figure A2.12: Continued. Scanning electron microscope images of Nankai –silt mixtures at maximum vertical effective stress of 20 MPa. Images represent vertical cross-section, i.e. load was applied from the top of the images. Left column are backscattered electron images. Right column are secondary electron images. I, J) 39% clay (SEM045_BSE_02b_UT.tif and SEM045_TLSE_02b_UT.tif). K, L) 34% clay (SEM046_BSE_01b_UT.tif and SEM046_TLSE_01b_UT.tif).

NOMENCLATURE

Variable	*Definition*	*Dimensions*	*Unit*
C_c	Compression index	dimensionless	__
C_e	Expansion index	dimensionless	__
C_v	Coefficient of consolidation	L^2/T	m^2/s
$d\varepsilon/dt$	Strain rate	1/T	1/s
e	Void ratio	dimensionless	__
e_0	Reference void ratio at 1 MPa	dimensionless	__
e_i	Initial void ratio	dimensionless	__
G_s	Grain density	M/L3	kg/m^3
H	Specimen height	L	cm
H_0	Initial specimen height	L	cm
k	Vertical intrinsic permeability	L^2	m^2
k_0	Intercept of log-linear relationship between permeability and porosity	L^2	m^2
K	Hydraulic conductivity	L/T	m/s
LL	Liquid limit	dimensionless	__
m_v	Coefficient of volume compressibility	LT^2/M	1/kPa
OCR	Overconsolidation ratio	dimensionless	__
PI	Plasticity index	dimensionless	__
PL	Plastic limit	dimensionless	__
S_i	Initial saturation	dimensionless	__
u	Base pressure / pore pressure	M/T^2L	kPa
u_c	Backpressure / cell pressure	M/T^2L	kPa
w_n	Specimen water content	dimensionless	__
ΔH	Change in height / deformation	L	cm
Δu	Excess pore pressure	M/T^2L	kPa
ε	Strain	dimensionless	%
ϕ	Porosity	dimensionless	__
γ	Slope of log-linear relationship between permeability and porosity	dimensionless	__
γ_w	Unit weight of water	M/T^2L^2	Pa/m
μ_w	Dynamic viscosity of water	M/TL	Pa s
ρ_w	Density of water	M/L^3	kg/m^3
σ_v	Total axial stress	M/T^2L	kPa
σ'_{pc}	Preconsolidation stress	M/T^2L	kPa
σ_v'	Vertical effective stress	M/T^2L	kPa

ACKNOWLEDGEMENTS

This research used samples and data provided by the Integrated Ocean Drilling Program (IODP). Funding for this research was provided by the Consortium for Ocean Leadership through the Schlanger Ocean Drilling Fellowship received by J. Schneider. Robert M. Reed prepared the SEM images.

REFERENCES

ASTM International, 2005, Standard test methods for liquid limit, plastic limit, and plasticity index of soils (Standard D4318-05), *in* Annual Book of ASTM Standards (Vol. 04.08), ed. Soil and Rock (I): West Conshohocken, PA, American Society for Testing and Materials, p. 16.

ASTM International, 2006. Standard test method for one-dimensional consolidation properties of saturated cohesive soils using controlled-strain loading (Standard D4186-06). *In* Annual Book of ASTM Standards (Vol. 04.08), ed., Soil and Rock (I): West Conshohocken, PA, American Society for Testing and Materials, p. 15.

ASTM International, 2007. Standard test method for particle-size analysis of soils (Standard D422-63R07). *In* Annual Book of ASTM Standards (Vol. 04.08), ed., Soil and Rock (I): West Conshohocken, PA, American Society for Testing and Materials, p. 10-17.

Hillier, S., 2000. Accurate quantitative analysis of clay and other minerals in sandstones by XRD: comparison of a Rietveld and a reference intensity ratio (RIR) method and the importance of sample preparation. *Clay Minerals*, 35(1): 291-302.

Hyndman, R.D., Yamano, M., and Oleskevich, D.A., 1997. The seismogenic zone of subduction thrust faults. *Island. Arc*, 6: 244-260.

Kobayashi, K., Kasuga, S., and Okino, K., 1995. Shikoku Basin and its margins. *In* Taylor, B., ed., Backarc Basins: Tectonics and Magmatism: New York, Plenum, p. 381-405.

Loucks, R.G., Reed, R.M., Ruppel, S.C., and Jarvie, D.M., 2009. Morphology, genesis, and distribution of nanometer-scale pores in siliceous mudstones of the Mississippian Barnett Shale. *Journal of Sedimentary Research*, 79(12): 848-861. doi:10.2110/jsr.2009.092.

Miyazaki, S., and Heki, K., 2001. Crustal velocity field of southwest Japan: subduction and arc-arc collision. *Journal of Geophysical Research*, 106(B3): 4305-4326. doi:10.1029/2000JB900312.

Moore, J.C., and Saffer, D., 2001. Updip limit of the seismogenic zone beneath the accretionary prism of southwest Japan: an effect of diagenetic to low-grade metamorphic processes and increasing effective stress. *Geology*, 29(2): 183-186. doi:10.1130/0091-7613(2001)029<0183:ULOTSZ>2.0.CO;2.

Okino, K., Shimakawa, Y., and Nagaoka, S., 1994. Evolution of the Shikoku Basin. *J. Geomagn. Geoelectr.*, 46: 463-479.

Saito, S., Underwood, M.B., and Kubo, Y., 2009. NanTroSEIZE Stage 2: subduction inputs. *IODP Sci. Prosp.*, 322. doi:10.2204/iodp.sp.322.2009.

Santagata, M.C., and Kang, Y.I., 2007. Effects of geologic time on the initial stiffness of clays. *Engineering Geology*, 89: 98-111. doi: 10.1016/j.enggeo.2006.09.018.

Sawyer, D.E., Jacoby, R., Flemings, P.B., and Germaine, J.T., 2008. Data report: particle size analysis of sediments in the Ursa Basin, IODP Expedition 308 Sites U1324 and U1322, northern Gulf of Mexico. *In* Flemings, P.B., Behrmann, J.H., John, C.M., and the Expedition Scientists, eds., *Proc. IODP*, Volume 308: College Station, TX, p. 20. doi:10.2204/iodp.proc.308.205.2008.

Seno, T., Stein, S., and Gripp, A.E., 1993. A model for the motion of the Philippine Sea Plate consistent with NUVEL-1 and geological data. *Journal of Geophysical Research*, 98(B10): 17941-17948. doi:10.1029/93JB00782.

Sheahan, T.C., 1991. An experimental study of the time-dependent undrained shear behavior of resedimented clay using automated stress path triaxial equipment [Ph.D. thesis]. Cambridge, Massachusetts Institute of Technology, 952 p.

Tobin, H.J., Kinoshita, M., Ashi, J., Lallemant, S., Kimura, G., Screaton, E., Thu, M.K., Masago, H., Curewitz, D., and the Expedition Scientists, 2009. NanTroSEIZE Stage 1 expeditions: introduction and synthesis of key results, *Proc. IODP*, Volume 314/315/316: Washington, DC, Integrated Ocean Drilling Program Management International, Inc. doi:10.2204/iodp.proc314315316.101.2009.

Underwood, M.B., Saito, S., Kubo, Y., and the Expedition Scientists, 2009. NanTroSEIZE Stage 2: subduction inputs. *IODP Prel. Rept.*, 322. doi:10.2204/iodp.pr.322.2009.

Underwood, M.B., Saito, S., Kubo, Y., and the Expedition Scientists, 2010. IODP Expedition 322 drills two sites to document inputs to the Nankai Trough subduction zone. *Scientific Drilling*, 10: 14-25. doi:10.2204/iodp.sd.10.02.2010.

Vrolijk, P., 1990. On the mechanical role of smectite in subduction zones. *Geology*, 18: 703-707.

Appendix 3: Matlab code for coupled permeability – compressibility model

code by Julia Schneider
The University of Texas at Austin, Jackson School of Geosciences
last updated: September 16, 2011

This code models the permeability and compressibility behavior of Nankai - Silt Mixtures using the geometric mean model after Schneider et al. (2011) (for permeability) and specific volume model after Long et al. (2011) (for compressibility). The model uses clay fraction based on grain size with a cutoff between clay-sized and silt-sized particles at 2 microns. The data are from constant-rate-of-strain (CRS) consolidation tests (CRS88, CRS89, CRS90, CRS91, CRS93, CRS94).

```
%-----------------------------------------------------------------------------------------------------

clear all
close all


%-----------------------------------------------------------------------------------------------------
% NOMENCLATURE
% All variables and constants defined in alphabetical order (without extensions which
% indicate the clay fraction)

% C []: exponent in Long et al.'s model
% Cc [1/kPa]: compression index (slope of virgin consolidation line)
% cfv [] : volumetric clay fraction with respect to total volume
% cfv_model []: volumetric clay fraction for varying btw. 0 – 1 (for contourplot)
% clayfraction []: measured volumetric clay fraction (for model)
% Cv [m2/s]: coefficient of consolidation (or diffusivity)
% Cv_X_pred [m2/s]: predicted coefficient of consolidation
% e []: void ratio
% e_model []: model void ratio varying btw. 0 – 1 (for contourplot)
% e0 [] : extrapolated void ratio to 1 kPa on linear-log relationship btw. void ratio and
% vertical effective stress
% gamma [m2]: slope of log-linear relationship btw. permeability and void ratio
% gamma_cl []: model parameter; slope of pure clay
% gamma_si []: model parameter; slope or pure silt
% gs : volumetric silt fraction with respect to solid volume
% k [m2] : vertical permeability
```

```
% k0 [m2] : intercept of log-linear relationship btw. permeability and void ratio
% k0_cl [m2]: model parameter; intercept of pure clay
% k0_si [m2]: model parameter; intercept of pure silt
% k_clay [m2]: clay permeability
% k_X_pred [m2]: predicted vertical permeability (for model)
% log_keff_model [m2]: modeled log of vertical permeability (for contourplot)
% Mv [1/kPa]: volume compressibility (for model)
% mv_model [1/lPa]: modeled coeff. of volume compressibility (for contourplot)
% mv_X_pred [1/kPa]: predicted coefficient of volume compressibility
% n_X_pred []: predicted porosity
% phi []: porosity
% phi_clay []: clay porosity
% sfv []: volumetric silt fraction with respect to total volume
% stress [MPa]: vertical effective stress (for model)
% stress_model [MPa]: vertical effective stress for model (for contourplot)
% stress_range [MPa]: range over which vertical effective stress defined
% VES [kPa]: vertical effective stress (data)
% v0 []: specific volume at 100 kPa; Long et al.'s model
% V_clay [cm3]: volume of clay
% V_silt [cm3] : volume of silt
% z [m]: depth in meters below seafloor


%-------------------------------------------------------------------------------------------------------
% LOAD DATA SETS
% Six samples with different mass ratios of Nankai Mud and silt-sized silica;
% Ratios by mass are: 100:00, 88:12, 76:24, 64:36, 52:48, and 40:60.
% Clay fractions (<2 microns) by mass are: 59%, 54%, 51%, 43%, 39%, and 34% as
% determined from hydrometer analyses.


% Load effective stress, void ratio, and permeability for each test.
data_59 = load('Nankai-Silt_Data_59.txt');
VES_59 = data_59(:,1);
e_59 = data_59(:,2);
k_59 = data_59(:,3);

data_54 = load('Nankai-Silt_Data_54.txt');
VES_54 = data_54(:,1);
e_54 = data_54(:,2);
k_54 = data_54(:,3);

data_51 = load('Nankai-Silt_Data_51.txt');
```

```
VES_51 = data_51(:,1);
e_51 = data_51(:,2);
k_51 = data_51(:,3);

data_43 = load('Nankai-Silt_Data_43.txt');
VES_43 = data_43(:,1);
e_43 = data_43(:,2);
k_43 = data_43(:,3);

data_39 = load('Nankai-Silt_Data_39.txt');
VES_39 = data_39(:,1);
e_39 = data_39(:,2);
k_39 = data_39(:,3);

data_34 = load('Nankai-Silt_Data_34.txt');
VES_34 = data_34(:,1);
e_34 = data_34(:,2);
k_34 = data_34(:,3);

%-----------------------------------------------------------------------------------------------------
% SET CONSTANTS
% Set clay fraction and silt fraction based on grain size with cutoff at 2 microns for each
% test.
% These clay fractions are volumetric clay fractions (converted from measured clay
% fraction by mass)

cfv_59 = 0.585;
cfv_54 = 0.535;
cfv_51 = 0.506;
cfv_43 = 0.426;
cfv_39 = 0.386;
cfv_34 = 0.337;

sfv_59 = 1 - cfv_59;
sfv_54 = 1 - cfv_54;
sfv_51 = 1 - cfv_51;
sfv_43 = 1 - cfv_43;
sfv_39 = 1 - cfv_39;
sfv_34 = 1 - cfv_34;

% Calculate porosities from void ratios
phi_59 = e_59./(1 + e_59);
phi_54 = e_54./(1 + e_54);
```

```
phi_51 = e_51./(1 + e_51);
phi_43 = e_43./(1 + e_43);
phi_39 = e_39./(1 + e_39);
phi_34 = e_34./(1 + e_34);

%-----------------------------------------------------------------------------------------------------
% MAKE PLOTS

% Figure 1: Compression Curves (void ratio vs. effective stress)
figure(1)
plot(VES_59,e_59,'.k','MarkerFaceColor','k','MarkerSize',5)
xlabel('vertical effective stress, s (kPa)')
ylabel('void ratio, e')
hold on
plot(VES_54,e_54,'db','MarkerFaceColor','b','MarkerSize',3)
hold on
plot(VES_51,e_51,'sc','MarkerFaceColor','c','MarkerSize',3)
hold on
plot(VES_43,e_43,'^g','MarkerFaceColor','g','MarkerSize',3)
hold on
plot(VES_39,e_39,'^r','MarkerFaceColor','r','MarkerSize',3)
hold on
plot(VES_34,e_34,'*m','MarkerFaceColor','m','MarkerSize',3)

set(gca,'Xscale','log','XGrid','on','YGrid','on','ylim',[0.2 1.8]);
legend('59% clay','54% clay','51% clay','43% clay','39% clay',...
        '34% clay','Location','NorthEast');


% Figure 2: Permeability vs. porosity
figure(2)
plot(phi_59(105:1194),k_59(105:1194),'.k','MarkerFaceColor','k','MarkerSize',5)
xlabel('porosity, phi')
ylabel('vertical permeability, k')
hold on
plot(phi_54(95:1170),k_54(95:1170),'db','MarkerFaceColor','b','MarkerSize',3)
hold on
plot(phi_51(26:1030),k_51(26:1030),'sc','MarkerFaceColor','c','MarkerSize',3)
hold on
plot(phi_43(49:975),k_43(49:975),'^g','MarkerFaceColor','g','MarkerSize',3)
hold on
plot(phi_39(45:895),k_39(45:895),'^r','MarkerFaceColor','r','MarkerSize',3)
hold on
```

```
plot(phi_34(3:836),k_34(3:836),'*m','MarkerFaceColor','m','MarkerSize',3)

set(gca,'Yscale','log','XGrid','on','YGrid','on','ylim',[1e-21 1e-15]);
legend('59% clay','54% clay','51% clay','43% clay','39% clay',...
        '34% clay','Location','SouthEast');


% LINEAR REGRESSIONS

hold on
k_59_log = log10(k_59);
p_59 = polyfit(phi_59(105:1194),k_59_log(105:1194),1);
        gamma_59 = p_59(1);
        k0_59 = p_59(2);
f_59_log = polyval(p_59,phi_59(105:1194));
f_59 = 10.^f_59_log;
plot(phi_59(105:1194),f_59,'-k','LineWidth',2);
R_59 = corr2(phi_59(105:1194),k_59_log(105:1194));

hold on
k_54_log = log10(k_54);
p_54 = polyfit(phi_54(95:1170),k_54_log(95:1170),1);
        gamma_54 = p_54(1);
        k0_54 = p_54(2);
f_54_log = polyval(p_54,phi_54(95:1170));
f_54 = 10.^f_54_log;
plot(phi_54(95:1170),f_54,'-k','LineWidth',2);
R_54 = corr2(phi_54(95:1170),k_54_log(95:1170));

hold on
k_51_log = log10(k_51);
p_51 = polyfit(phi_51(26:1030),k_51_log(26:1030),1);
        gamma_51 = p_51(1);
        k0_51 = p_51(2);
f_51_log = polyval(p_51,phi_51(26:1030));
f_51 = 10.^f_51_log;
plot(phi_51(26:1030),f_51,'-k','LineWidth',2);
R_51 = corr2(phi_51(26:1030),k_51_log(26:1030));

hold on
k_43_log = log10(k_43);
p_43 = polyfit(phi_43(49:975),k_43_log(49:975),1);
        gamma_43 = p_43(1);
```

```
        k0_43 = p_43(2);
f_43_log = polyval(p_43,phi_43(49:975));
f_43 = 10.^f_43_log;
plot(phi_43(49:975),f_43,'-k','LineWidth',2);
R_43 = corr2(phi_43(49:975),k_43_log(49:975));

hold on
k_39_log = log10(k_39);
p_39 = polyfit(phi_39(45:895),k_39_log(45:895),1);
        gamma_39 = p_39(1);
        k0_39 = p_39(2);
f_39_log = polyval(p_39,phi_39(45:895));
f_39 = 10.^f_39_log;
plot(phi_39(45:895),f_39,'-k','LineWidth',2);
R_39 = corr2(phi_39(45:895),k_39_log(45:895));

hold on
k_34_log = log10(k_34);
p_34 = polyfit(phi_34(3:836),k_34_log(3:836),1);
        gamma_34 = p_34(1);
        k0_34 = p_34(2);
f_34_log = polyval(p_34,phi_34(3:836));
f_34 = 10.^f_34_log;
plot(phi_34(3:836),f_34,'-k','LineWidth',2);
%R_34 = corr2(phi_34(3:836),k_34_log(3:836));

%-----------------------------------------------------------------------------------------------------
% GEOMETRIC MEAN PERMEABILITY MODEL
% Calculate model parameters

% Call subroutine (see bottom of the code)
Inversion_Nankai_2micron;
gamma_cl = gamma(1);
k0_cl = K0(1);
gamma_si = gamma(2);
k0_si = K0(2);

%-----------------------------------------------------------------------------------------------------
% VARIATION OF COMRPESSIBILITY WITH CLAY FRACTION

v0_59 = 1.9731;
v0_54 = 1.872;
v0_51 = 1.797;
```

```
v0_43 = 1.698;
v0_39 = 1.682;
v0_34 = 1.67;

C_59 = -0.119;
C_54 = -0.109;
C_51 = -0.102;
C_43 = -0.094;
C_39 = -0.083;
C_34 = -0.069;

v0 = [v0_59 v0_54 v0_51 v0_43 v0_39 v0_34];
C = [C_59 C_54 C_51 C_43 C_39 C_34];
cfv = [cfv_59 cfv_54 cfv_51 cfv_43 cfv_39 cfv_34];

% Figure 3: v0 vs. caly fraction
figure(3)
plot(cfv,v0,'dk','MarkerFaceColor','k','MarkerSize',5)
xlabel('volumetric clay fraction, cfv')
ylabel('v0')
set(gca,'XGrid','on','YGrid','on','Xlim',[0.3 0.6],'Ylim',[1.6 2.0]);

hold on
p = polyfit(cfv,v0,2);
        constA = p(1);
        constB = p(2);
        constC = p(3);
f = polyval(p,cfv);
plot(cfv,f,'-k','LineWidth',2);

% Figure 4: C vs. clay fraction
figure(4)
plot(cfv,C,'dk','MarkerFaceColor','k','MarkerSize',5)
xlabel('volumetric clay fraction, cfv')
ylabel('C')
set(gca,'XGrid','on','YGrid','on','Xlim',[0.3 0.6]);

hold on
p2 = polyfit(cfv,C,1);
        beta = p2(1);
        b = p2(2);
f2 = polyval(p2,cfv);
plot(cfv,f2,'-k','LineWidth',2);
```

```
%-----------------------------------------------------------------------------------------------------
% PREDICITON OF POROSITY AS A FUNCTION OF STRESS

% let vertical effective stress range from 0 to 20 MPa
stress=linspace(0.01, 20, 1000);

n_59_pred = zeros(1000);
n_54_pred = zeros(1000);
n_51_pred = zeros(1000);
n_43_pred = zeros(1000);
n_39_pred = zeros(1000);
n_34_pred = zeros(1000);

for k=1:1000
        n_59_pred(k)= (1-((constA*(cfv_59)^2+constB*cfv_59+constC)*...
                (stress(k))^(beta*cfv_59+b))^(-1));
        n_54_pred(k)= (1-((constA*(cfv_54)^2+constB*cfv_54+constC)*...
                (stress(k))^(beta*cfv_54+b))^(-1));
        n_51_pred(k)= (1-((constA*(cfv_51)^2+constB*cfv_51+constC)*...
                (stress(k))^(beta*cfv_51+b))^(-1));
        n_43_pred(k)= (1-((constA*(cfv_43)^2+constB*cfv_43+constC)*...
                (stress(k))^(beta*cfv_43+b))^(-1));
        n_39_pred(k)= (1-((constA*(cfv_39)^2+constB*cfv_39+constC)*...
                (stress(k))^(beta*cfv_39+b))^(-1));
        n_34_pred(k)= (1-((constA*(cfv_34)^2+constB*cfv_34+constC)*...
                (stress(k))^(beta*cfv_34+b))^(-1));
end

%-----------------------------------------------------------------------------------------------------
% COMPARISON OF POROSITY MODEL AND DATA

% Figure 5: Porosity vs. vertical effective stress
figure(5)
% plot data
plot(phi_59(105:1194),VES_59(105:1194)./1000,'.k','MarkerFaceColor','k','MarkerSize',5
        )
xlabel('porosity, n')
ylabel('vertical effective stress, sigma_v')
hold on
plot(phi_54(95:1170),VES_54(95:1170)./1000,'db','MarkerFaceColor','b','MarkerSize',3)
hold on
plot(phi_51(26:1030),VES_51(26:1030)./1000,'sc','MarkerFaceColor','c','MarkerSize',3)
```

```
hold on
plot(phi_43(45:975),VES_43(45:975)./1000,'^g','MarkerFaceColor','g','MarkerSize',3)
hold on

plot(phi_39(45:895),VES_39(45:895)./1000,'^r','MarkerFaceColor','r','MarkerSize',3)
hold on
plot(phi_34(3:836),VES_34(3:836)./1000,'*m','MarkerFaceColor','m','MarkerSize',3)

set(gca,'Yscale','linear','Xscale','linear','XGrid','on','YGrid','on',...
        'xlim',[0.2 0.6],'ylim',[0 20],'YDir','reverse',...
        'XAxisLocation','top');

legend('59% clay','54% clay','51% clay','43% clay','39% clay',...
        '34% clay','Location','SouthEast');


% plot model
hold on
plot(n_59_pred,stress,'-k','LineWidth',2)
hold on
plot(n_54_pred,stress,'-b','LineWidth',2)
hold on
plot(n_51_pred,stress,'-c','LineWidth',2)
hold on
plot(n_43_pred,stress,'-g','LineWidth',2)
hold on
plot(n_39_pred,stress,'-r','LineWidth',2)
hold on
plot(n_34_pred,stress,'-m','LineWidth',2)

%-----------------------------------------------------------------------------------------------------
% PREDICTION OF PERMEABILITY AS A FUNCTION OF STRESS USING
% DERIVED MODEL PARAMETERS

k_59_pred = zeros(1000);
k_54_pred = zeros(1000);
k_51_pred = zeros(1000);
k_43_pred = zeros(1000);
k_39_pred = zeros(1000);
k_34_pred = zeros(1000);

mv_59_pred = zeros(1000);
mv_54_pred = zeros(1000);
```

```
mv_51_pred = zeros(1000);
mv_43_pred = zeros(1000);
mv_39_pred = zeros(1000);
mv_34_pred = zeros(1000);

Cv_59_pred = zeros(1000);
Cv_54_pred = zeros(1000);
Cv_51_pred = zeros(1000);
Cv_43_pred = zeros(1000);
Cv_39_pred = zeros(1000);
Cv_34_pred = zeros(1000);

for k=1:1000
        k_59_pred(k)= 10.^(((1-((constA*(cfv_59)^2+constB*cfv_59+constC)*...
                (stress(k))^(beta*cfv_59+b))^(-1))).*(cfv_59*gamma_cl+...
                (1-cfv_59)*gamma_si)+cfv_59*k0_cl+(1-cfv_59)*k0_si);

        k_54_pred(k)= 10.^(((1-((constA*(cfv_54)^2+constB*cfv_54+constC)*...
                (stress(k))^(beta*cfv_54+b))^(-1))).*(cfv_54*gamma_cl+...
                (1-cfv_54)*gamma_si)+cfv_54*k0_cl+(1-cfv_54)*k0_si);

        k_51_pred(k)= 10.^(((1-((constA*(cfv_51)^2+constB*cfv_51+constC)*...
                (stress(k))^(beta*cfv_51+b))^(-1))).*(cfv_51*gamma_cl+...
                (1-cfv_51)*gamma_si)+cfv_51*k0_cl+(1-cfv_51)*k0_si);

        k_43_pred(k)= 10.^(((1-((constA*(cfv_43)^2+constB*cfv_43+constC)*...
                (stress(k))^(beta*cfv_43+b))^(-1))).*(cfv_43*gamma_cl+...
                (1-cfv_43)*gamma_si)+cfv_43*k0_cl+(1-cfv_43)*k0_si);

        k_39_pred(k)= 10.^(((1-((constA*(cfv_39)^2+constB*cfv_39+constC)*...
                (stress(k))^(beta*cfv_39+b))^(-1))).*(cfv_39*gamma_cl+...
                (1-cfv_39)*gamma_si)+cfv_39*k0_cl+(1-cfv_39)*k0_si);

        k_34_pred(k)= 10.^(((1-((constA*(cfv_34)^2+constB*cfv_34+constC)*...
                (stress(k))^(beta*cfv_34+b))^(-1))).*(cfv_34*gamma_cl+...
                (1-cfv_34)*gamma_si)+cfv_34*k0_cl+(1-cfv_34)*k0_si);

        mv_59_pred(k)= -(beta*cfv_59+b)./(stress(k).*1000);
        mv_54_pred(k)= -(beta*cfv_54+b)./(stress(k).*1000);
        mv_51_pred(k)= -(beta*cfv_51+b)./(stress(k).*1000);
        mv_43_pred(k)= -(beta*cfv_43+b)./(stress(k).*1000);
        mv_39_pred(k)= -(beta*cfv_39+b)./(stress(k).*1000);
        mv_34_pred(k)= -(beta*cfv_34+b)./(stress(k).*1000);
```

```
        Cv_59_pred(k) = k_59_pred(k)./((mv_59_pred(k)./1000).*0.001002);
        Cv_54_pred(k) = k_54_pred(k)./((mv_54_pred(k)./1000).*0.001002);
        Cv_51_pred(k) = k_51_pred(k)./((mv_51_pred(k)./1000).*0.001002);
        Cv_43_pred(k) = k_43_pred(k)./((mv_43_pred(k)./1000).*0.001002);
        Cv_39_pred(k) = k_39_pred(k)./((mv_39_pred(k)./1000).*0.001002);
        Cv_34_pred(k) = k_34_pred(k)./((mv_34_pred(k)./1000).*0.001002);

end

%-----------------------------------------------------------------------------------------------------
% COMPARISON OF PERMEABILITY MODEL AND DATA

% Figure 6: Vertical permeability vs. vertical effective stress
figure(6)
% plot data
plot(k_59(105:1194),VES_59(105:1194)./1000,'.k','MarkerFaceColor','k','MarkerSize',5)
xlabel('vertical permeability, k')
ylabel('vertical effective stress, sigma_v')
hold on
plot(k_54(95:1170),VES_54(95:1170)./1000,'db','MarkerFaceColor','b','MarkerSize',3)
hold on
plot(k_51(26:1030),VES_51(26:1030)./1000,'sc','MarkerFaceColor','c','MarkerSize',3)
hold on

plot(k_43(49:975),VES_43(49:975)./1000,'^g','MarkerFaceColor','g','MarkerSize',3)
hold on
plot(k_39(45:895),VES_39(45:895)./1000,'^r','MarkerFaceColor','r','MarkerSize',3)
hold on
plot(k_34(3:836),VES_34(3:836)./1000,'*m','MarkerFaceColor','m','MarkerSize',3)

set(gca,'Yscale','linear','Xscale','log','XGrid','on','YGrid','on',...
        'xlim',[1e-21 1e-15],'ylim',[0 20],'YDir','reverse',...
        'XAxisLocation','top');
legend('59% clay','54% clay','51% clay','43% clay','39% clay',...
        '34% clay','Location','SouthEast');

% plot model
hold on
plot(k_59_pred,stress,'-k','LineWidth',2)
hold on
plot(k_54_pred,stress,'-b','LineWidth',2)
hold on
```

```
plot(k_51_pred,stress,'-c','LineWidth',2)
hold on
plot(k_43_pred,stress,'-g','LineWidth',2)
hold on
plot(k_39_pred,stress,'-r','LineWidth',2)
hold on
plot(k_34_pred,stress,'-m','LineWidth',2)

% Figure 7: Subplots: Porosity, vertical permeability, coefficient of compressibility,
% and coefficient of consolidation vs. vertical effective stress
figure(7)
subplot(1,4,1);
plot(n_59_pred,stress,'-k','LineWidth',2)
xlabel('porosity, n')
ylabel('vertical effective stress, sigma_v')
hold on
plot(n_54_pred,stress,'-b','LineWidth',2)
hold on
plot(n_51_pred,stress,'-c','LineWidth',2)
hold on
plot(n_43_pred,stress,'-g','LineWidth',2)
hold on
plot(n_39_pred,stress,'-r','LineWidth',2)
hold on
plot(n_34_pred,stress,'-m','LineWidth',2)

set(gca,'Yscale','linear','Xscale','linear','XGrid','on','XMinorGrid','on',...
        'YGrid','on',...
        'xlim',[0.2 0.6],'ylim',[0 20],'YDir','reverse',...
        'XAxisLocation','top');
legend('59% clay','54% clay','51% clay','43% clay','39% clay',...
        '34% clay','Location','SouthEast');

subplot(1,4,2);
plot(k_59_pred,stress,'-k','LineWidth',2)
xlabel('vertical permeability, k')
ylabel('vertical effective stress, sigma_v')
hold on
plot(k_54_pred,stress,'-b','LineWidth',2)
hold on
plot(k_51_pred,stress,'-c','LineWidth',2)
hold on
plot(k_43_pred,stress,'-g','LineWidth',2)
```

```
hold on
plot(k_39_pred,stress,'-r','LineWidth',2)
hold on
plot(k_34_pred,stress,'-m','LineWidth',2)
set(gca,'Yscale','linear','Xscale','log','XGrid','on','XMinorGrid','on',...
        'YGrid','on',..
        'xlim',[1e-20 1e-15],'ylim',[0 20],'YDir','reverse',...
        'XAxisLocation','top');
legend('59% clay','54% clay','51% clay','43% clay','39% clay',...
        '34% clay','Location','SouthEast');

subplot(1,4,3);
plot(mv_59_pred,stress,'-k','LineWidth',2)
xlabel('volumetric compressibility, mv')
ylabel('vertical effective stress, sigma_v')
hold on
plot(mv_54_pred,stress,'-b','LineWidth',2)
hold on
plot(mv_51_pred,stress,'-c','LineWidth',2)
hold on
plot(mv_43_pred,stress,'-g','LineWidth',2)
hold on
plot(mv_39_pred,stress,'-r','LineWidth',2)
hold on
plot(mv_34_pred,stress,'-m','LineWidth',2)

set(gca,'Yscale','linear','Xscale','log','XGrid','on','XMinorGrid','on',...
        'YGrid','on',...
        'xlim',[1e-6 1e-2],'ylim',[0 20],'YDir','reverse',...
        'XAxisLocation','top');
legend('59% clay','54% clay','51% clay','43% clay','39% clay',...
        '34% clay','Location','SouthEast');

subplot(1,4,4);
plot(Cv_59_pred,stress,'-k','LineWidth',2)
xlabel('coefficient of consolidation, Cv')
ylabel('vertical effective stress, sigma_v')
hold on
plot(Cv_54_pred,stress,'-b','LineWidth',2)
hold on
plot(Cv_51_pred,stress,'-c','LineWidth',2)
hold on
plot(Cv_43_pred,stress,'-g','LineWidth',2
```

```
hold on
plot(Cv_39_pred,stress,'-r','LineWidth',2)
hold on
plot(Cv_34_pred,stress,'-m','LineWidth',2)

set(gca,'Yscale','linear','Xscale','log','XGrid','on','XMinorGrid','on',...
        'YGrid','on',...
        'xlim',[1e-9 1e-6],'ylim',[0 20],'YDir','reverse',..
        'XAxisLocation','top');
legend('59% clay','54% clay','51% clay','43% clay','39% clay',...
        '34% clay','Location','SouthEast');

% ------------------------------------------------------------------------------------------------
% CONTOURPLOTS SHOWING BEHAVIOR OF PERMEABILITY AND Mv AS A
% FUNCTION OF STRESS AND CLAY CONTENT

% define clay fraction at 2 microns
clayfraction_59 = [0.59 0.59];
clayfraction_54 = [0.54 0.54];
clayfraction_51 = [0.51 0.51];
clayfraction_43 = [0.43 0.43];
clayfraction_39 = [0.39 0.39];
clayfraction_34 = [0.34 0.34];

% define stress range
stress_range = [0.130 20];
cfv_model = rand(1000,1);
stress_model = [0.02:0.02:20];
e_model = ones(1000,1);
log_keff_model = zeros(1000,1);
mv_model = zeros(1000,1);

for i=1:1000
        e_model(i)=((constA*cfv_model(i).^2+constB*cfv_model(i)+constC).*...
                stress_model(i).^(beta*cfv_model(i)+b))-1.;

        log_keff_model(i) = cfv_model(i).*k0_cl+(1-cfv_model(i)).*k0_si+...
                (e_model(i)./(1.+e_model(i))).*((cfv_model(i).*gamma_cl)+…
                ((1-cfv_model(i)).*gamma_si));

        mv_model(i) = -(beta*cfv_model(i)+b)./(stress_model(i).*1000);
end
```

```
% Calculate start and end point of permeabilities
log_k_59s= (((1-((constA*(clayfraction_59(1))^2+constB*clayfraction_59(1)+...
        constC)*(stress_range(1))^(beta*clayfraction_59(1)+b))^(-1))).*...
        (clayfraction_59(1)*gamma_cl+(1-clayfraction_59(1))*gamma_si)+...
        clayfraction_59(1)*k0_cl+(1-clayfraction_59(1))*k0_si);

log_k_59e= (((1-((constA*(clayfraction_59(1))^2+constB*clayfraction_59(1)+...
        constC)*(stress_range(2))^(beta*clayfraction_59(1)+b))^(-1))).*...
        (clayfraction_59(1)*gamma_cl+(1-clayfraction_59(1))*gamma_si)+...
        clayfraction_59(1)*k0_cl+(1-clayfraction_59(1))*k0_si);

log_k_59 = [log_k_59s log_k_59e];

log_k_54s= (((1-((constA*(clayfraction_54(1))^2+constB*clayfraction_54(1)+...
        constC)*(stress_range(1))^(beta*clayfraction_54(1)+b))^(-1))).*...
        (clayfraction_54(1)*gamma_cl+(1-clayfraction_54(1))*gamma_si)+...
        clayfraction_54(1)*k0_cl+(1-clayfraction_54(1))*k0_si);

log_k_54e= (((1-((constA*(clayfraction_54(1))^2+constB*clayfraction_54(1)+...
        constC)*(stress_range(2))^(beta*clayfraction_54(1)+b))^(-1))).*...
        (clayfraction_54(1)*gamma_cl+(1-clayfraction_54(1))*gamma_si)+...
        clayfraction_54(1)*k0_cl+(1-clayfraction_54(1))*k0_si);

log_k_54 = [log_k_54s log_k_54e];

log_k_51s= (((1-((constA*(clayfraction_51(1))^2+constB*clayfraction_51(1)+...
        constC)*(stress_range(1))^(beta*clayfraction_51(1)+b))^(-1))).*...
        (clayfraction_51(1)*gamma_cl+(1-clayfraction_51(1))*gamma_si)+...
        clayfraction_51(1)*k0_cl+(1-clayfraction_51(1))*k0_si);

log_k_51e= (((1-((constA*(clayfraction_51(1))^2+constB*clayfraction_51(1)+...
        constC)*(stress_range(2))^(beta*clayfraction_51(1)+b))^(-1))).*...
        (clayfraction_51(1)*gamma_cl+(1-clayfraction_51(1))*gamma_si)+...
        clayfraction_51(1)*k0_cl+(1-clayfraction_51(1))*k0_si);

log_k_51 = [log_k_51s log_k_51e];

log_k_43s= (((1-((constA*(clayfraction_43(1))^2+constB*clayfraction_43(1)+…
        constC)*(stress_range(1))^(beta*clayfraction_43(1)+b))^(-1))).*...
        (clayfraction_43(1)*gamma_cl+(1-clayfraction_43(1))*gamma_si)+...
        clayfraction_43(1)*k0_cl+(1-clayfraction_43(1))*k0_si);

log_k_43e= (((1-((constA*(clayfraction_43(1))^2+constB*clayfraction_43(1)+...
```

```
        constC)*(stress_range(2))^(beta*clayfraction_43(1)+b))^(-1))).*...
        (clayfraction_43(1)*gamma_cl+(1-clayfraction_43(1))*gamma_si)+...
        clayfraction_43(1)*k0_cl+(1-clayfraction_43(1))*k0_si);

log_k_43 = [log_k_43s log_k_43e];

log_k_39s= (((1-((constA*(clayfraction_39(1))^2+constB*clayfraction_39(1)+...
        constC)*(stress_range(1))^(beta*clayfraction_39(1)+b))^(-1))).*...
        (clayfraction_39(1)*gamma_cl+(1-clayfraction_39(1))*gamma_si)+...
        clayfraction_39(1)*k0_cl+(1-clayfraction_39(1))*k0_si);

log_k_39e= (((1-((constA*(clayfraction_39(1))^2+constB*clayfraction_39(1)+...
        constC)*(stress_range(2))^(beta*clayfraction_39(1)+b))^(-1))).*...
        (clayfraction_39(1)*gamma_cl+(1-clayfraction_39(1))*gamma_si)+...
        clayfraction_39(1)*k0_cl+(1-clayfraction_39(1))*k0_si);

log_k_39 = [log_k_39s log_k_39e];

log_k_34s= (((1-((constA*(clayfraction_34(1))^2+constB*clayfraction_34(1)+...
        constC)*(stress_range(1))^(beta*clayfraction_34(1)+b))^(-1))).*...
        (clayfraction_34(1)*gamma_cl+(1-clayfraction_34(1))*gamma_si)+...
        clayfraction_34(1)*k0_cl+(1-clayfraction_34(1))*k0_si);

log_k_34e= (((1-((constA*(clayfraction_34(1))^2+constB*clayfraction_34(1)+...
        constC)*(stress_range(2))^(beta*clayfraction_34(1)+b))^(-1))).*...
        (clayfraction_34(1)*gamma_cl+(1-clayfraction_34(1))*gamma_si)+...
        clayfraction_34(1)*k0_cl+(1-clayfraction_34(1))*k0_si);

log_k_34 = [log_k_34s log_k_34e];

ti = 0:.001:1;
ui = 0.02:0.02:20;
[XI,YI] = meshgrid(ti,ui);
ZI = griddata(cfv_model,stress_model,log_keff_model,XI,YI);

% Figure 8: Contourplot of permeability as function of stress and clay fraction
figure(8)
contourf(XI,YI,ZI,10);
colormap Jet
[C,h]=contourf(XI,YI,ZI);
clabel(C,h,'BackgroundColor','white');
axis square
xlabel('clay fraction of solid volume')
```

```
ylabel('vertical effective stress')
xlim([0 1])
ylim([0 20])
set(gca,'Yscale','linear','Xscale','linear','YDir','reverse',...
'XAxisLocation','top');

hold on
grid on
plot(clayfraction_59,stress_range,'-k','LineWidth',2);
hold on
plot(clayfraction_54,stress_range,'-b','LineWidth',2);
hold on
plot(clayfraction_51,stress_range,'-c','LineWidth',2);
hold on

plot(clayfraction_43,stress_range,'-g','LineWidth',2);
hold on
plot(clayfraction_39,stress_range,'-r','LineWidth',2);
hold on
plot(clayfraction_34,stress_range,'-m','LineWidth',2);
hold on

%-----------------------------------------------------------------------------------------------------------
tj = 0:0.1:1;
uj = 0:2:20;
[X2,Y2] = meshgrid(tj,uj);
Z2 = griddata(cfv_model,stress_model,mv_model,X2,Y2);

% Figure 9: contourplot of mv as a function of stress and clay fraction
figure(9)
contourf(X2,Y2,Z2,10);
colormap Jet
[D,g]=contourf(X2,Y2,Z2);
clabel(D,g,'BackgroundColor','white');
%caxis([cmin 0]);
axis square
xlabel('clay fraction of solid volume')
ylabel('vertical effective stress')
xlim([0 1])
ylim([0 20])
set(gca,'Yscale','linear','Xscale','linear','YDir','reverse',...
'XAxisLocation','top');
hold on
```

```
grid on

%-----------------------------------------------------------------------------------------------------
% SUBROUTINE

% all experiments considered; cut-off at 2 microns
interceptMatrix=[0.585 (1-0.585)
        0.535 (1-0.535)
        0.506 (1-0.506)
        0.426 (1-0.426)
        0.386 (1-0.386)
        0.337 (1-0.337)
        ];
interceptBVec=-[22.92 22.84 22.30 21.47 20.95 20.47];
K0=pinv(interceptMatrix)*interceptBVec';
slopeMatrix=interceptMatrix;
slopeBVec=[11.12 11.62 11.17 10.45 9.99 9.76];
gamma=pinv(slopeMatrix)*slopeBVec';
```

Appendix 4: Resedimentation procedure (UT GeoMechanics Lab)

A4.1 PREPARING CONSOLIDOMETER SETUP

1. All resedimentation setup parts are shown in Figure A4.1.
2. Gather two porous stones with filter paper.
3. Place porous stones and filter paper in a beaker filled with de-ionized water into the ultrasonic bath for about 15 minutes to clean and saturate.
4. Gather small tubing and small bucket with de-ionized water to place behind the apparatus (outflow reservoir) (Figure A4.2B). One end of the tubing fits in the white cone tip at the side of the consolidometer base (Figure A4.2A). The other end has a weight attached to it and drains into the bucket (Figure A4.2B).
5. Saturate the drainage line completely with a syringe till water comes up the hole inside the base of the consolidometer. Note that the water level in the bucket drives the pressure gradient. Adjust its elevation so that there is no flow between bucket and base of consolidometer.
6. Grease the O-ring with vacuum grease.
7. Grease the inside of the cylinder with thinner silicone oil.

Figure A4.1: Individual parts of resedimentation setup. (1) porous stone (not shown here) and filter paper (2) consolidometer base (3) cylinder (4) silicone oil (5) acrylic spacer (6) bracket with center hole (7) aluminum rod (8) LPT bracket (9) linear positioning transducer (LPT) (10) steel pipe (11) hangars.

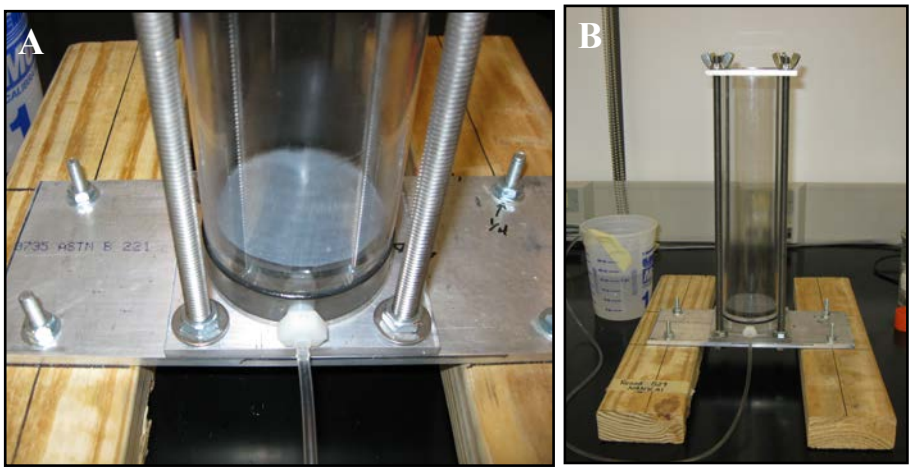

Figure A4.2: Initial setup of consolidometer. A) Porous stone with filter paper in consolidometer base. B) Bucket filled with water is connected to base of consolidometer via small tube to drain soil.

A4.2 SLURRY PREPARATION

A4.2.1 Decisions to be made before preparing slurry

- Decide whether one of two specimens are desired. The necessary amount of dry material varies accordingly. Mineralogy and composition affect compressibility, thus affect the amount of necessary material. Consider that material is also being lost during the process. The key point is to have enough material so that the specimen at the end of the resedimentation test is taller than the height of the CRS specimen ring (2.36 cm).
    - *For BBC – silt mixtures, one specimen was prepared out of one resedimentation test. The initial dry mass was between 220 and 250g.*
    - *For Nankai – silt mixtures, two specimens were prepared out of one resedimentation test. The initial dry mass was 500g.*
- Decide what water content the slurry should be prepared at. Rule of thumb: water content is equal to twice the liquid limit (→ see Atterberg Limits, ASTM Standard D4318-05). The slurry needs to be liquid enough to be poured into the consolidometer, but thick enough so that particles do not settle out. A test tube experiment is recommended to determine whether particle segregation is an issue at chosen water content.
    - *BBC forms a stable slurry at a water content of 100%.*
    - *Nankai mud forms a stable slurry at a water content of 105%.*
    - *In the case of mixtures with silt, additional water needs to be added because the silt attracts water. An additional water content of 33% per silt fraction is added.*
- If applicable, decide which salinity the slurry should be prepared at from *in-situ* salinity information and water content the slurry is prepared at. Because the

chosen water content for resedimentation is higher than the *in-situ* water content, the natural salt concentration will be diluted. Thus, salt has to be added to represent *in-situ* salinity.

- *For BBC add 16 g/l of sodium chloride.*
- *For Nankai mud add 26 g/l of seasalt.*
- *In the case of mixtures with silt, calculate the amount of salt to be added only based on clay fraction (BBC or Nankai mud).*

A4.2.2 Preparing slurry

1. Gather at least 250 grams (or more for two specimens) of air-dried, ground, and homogenized material and place it into mixing bowl with flat bottom.
2. Weigh out de-ionized water at chosen water content.
    a. *In case of mixtures with silt, weigh water for clay and water for silt (water content of 33%) out separately. For BBC use water content of 100%, for Nankai mud use water content of 105%.*
3. Weigh out amount of salt at chosen salinity.
    a. *For BBC use sodium chloride, for Nankai mud use seasalt.*
4. Add salt to de-ionized water and mix well.
    a. *In case of mixtures with silt, add salt to de-ionized water that is reserved for clay fraction.*
5. Add water-salt solution to air-dried sample.
    a. *In case of mixtures with silt, add water fraction for silt (water content of 33%) to silt and mix well so that all silt grains are moist. Then add moistened silt and water-salt solution to air-dried clay fraction.*
6. Mix all components well with rubber spatula for at least 20 minutes or until the slurry is homogeneous and no clumps are visible anymore. The larger the sample, the longer this process takes.
7. Cover the slurry with plastic wrap. Make sure the plastic wrap fits tightly around the bowl so that no evaporation occurs and the moisture content is kept constant.
8. Let the slurry sit and equilibrate over night (at least 16 hrs).

A4.2.3 De-airing process

1. Use a glas flask to apply vacuum to slurry (Figure A4.3). For only one sample a 1L flask is desirable, for two specimens a 2L flask.
2. Attach the vacuum pump to the small flask with orange colored crystals (desiccant) with a ¼ " latex vacuum tubing covering the small glass opening on the side of the flask (Figure A4.3). A filter is placed between pump and flask that contains desiccant to collect escaped oil (Figure A4.3). *Note*: If desiccant turns pink it has collected too much moisture and needs to be dried in the oven.

3. Place a black rubber stopper that has a small metal pipe through the whole in the middle of the stopper into the large opening on top of the flask with the desiccant (Figure A4.3). Use vacuum tubing to connect the metal pipe to the side opening of the flask, which will later contain the slurry (Figure A4.3).
4. Place another black rubber stopper with small metal pipe into top opening of the flask that will contain slurry (Figure A4.3). Attach vacuum tubing to the metal pipe and leave the other end free in the mixing bowl.
5. Turn on the vacuum and use the free tubing end to suck up as much of the slurry as possible into the large glas flask. Use a spatula to scrape slurry together in the bowl.
6. After sucking the slurry into the glas flask, seal off the free end of the tubing by tightening a pinch clamp around the tubing.
7. Let the vacuum pump run until all air bubbles disappear. Agitate the flask once in a while to allow air bubbles to move to the surface. The de-airing process can take a couple of hours, especially for large amounts of material.

Figure A4.3: Vacuum setup to de-air the slurry.

A4.3 ASSEMBLING CONSOLIDOMETER SETUP

1. Just before the slurry is ready to be poured into the consolidometer, place one saturated stone into the consolidometer base (Figure A4.2A). Put one filter paper on top of the stone.
2. Place the O-ring around the base of the consolidometer (Figure A4.2A).
3. Place cylinder tightly over base.
4. Place the square metal plate on top of the cylinder with the grooves fitting tightly over the sidewall of the cylinder. Tighten the metal plate down with four screws (Figure A4.2B). Only when metal plate is tightened down and therefore pressure is applied, the O-ring seals.

5. Gather a small funnel and tubing that fits over the funnel (2 ft long). The tubing must be long enough to reach the bottom of the cylinder, but not too long that it is difficult to deal with.
6. Attach one end of the tubing to the funnel.
7. Lower this assembly into the consolidometer.
8. Pour the slurry through the funnel and tubing into the consolidometer. While pouring, hold the bottom end of the tubing stable and do not touch the inside wall of the consolidometer. As the slurry gets poured through the funnel into the consolidometer, slightly lift the funnel-tubing assembly up but keep the bottom of the tubing always in the soil. This ensures that no additional air gets incorporated. Two people may be useful for this step. One to hold and lift the assembly and one to work the material through the funnel.
9. Lower the acrylic cap with a saturated porous stone and filter paper down to the slurry using two metal rods with hooks at the end. Let the cap rest on top of the slurry. The filter paper should be placed at the bottom of the porous stone, i.e. between slurry and stone to prevent small particles from being washed out. Make sure the stone fits tightly into the acrylic cap before lowering the stone down.
10. Add some de-ionized water on top of the stone and make sure to keep it saturated with de-ionized water.
11. Place plastic wrap over the consolidometer to prevent evaporation and contamination.

A4.4 LOADING AND UNLOADING

1. Determine when secondary consolidation occurs. Each soil needs a specific time till end of primary consolidation, which is when deformation does not change significantly anymore with time.
    a. *For BBC, add a weight in 24 hrs increments until digital data is acquired which allows better judgment. For Nankai mud, add a weight in 48 hrs increments until digital data is acquired.*
    b. *Once digital data acquired, plot axial strain vs. square root of time following square-root-of-time theory by Taylor (1948). The time where the maximum curvature is and after which deformation is negligible with time is the end of primary consolidation (start of secondary consolidation). For details see Taylor (1948).*
2. Increment 1
    a. Add Acrylic Spacer weighing approximately 60g.
    b. Make sure the weights are still sitting on top of the slurry. Under initial weights slurry and stone can easily separate.
3. Increment 2
    a. Add PVC tube weighing approximately 120g.

4. Increment 3
    a. Add UHMW rod weighing approximately 250g.
5. Increment 4
    a. Remove 250g UHMV rod and add 120g PVC pipe.
    b. Grease the bottom of the 14" aluminum rod.
    c. Pull the non-greased end of the aluminum rod through the bracket with the center whole and lower it into the consolidometer on top of the acrylic spacer.
    d. Attach the bracket with center whole, through which aluminum rod sticks out, to the metal plate on top of the consolidometer and tighten with screws (Figure A4.2B).
    e. Attach LPT bracket to the aluminum rod.
    f. Plug linear positioning transducer (LPT) into network module and place it in the LPT bracket. Tighten with screws.
        i. Make sure the cord is facing toward you.
        ii. Make sure to give the core of the transducer enough room for movement. Also make sure that the steel pipe, which will be added later, can still fit over the aluminum rod above the LPT.
    g. Replace 120g PVC pipe on top.
    h. Set up file on Test Net GP-data acquisition.
        i. Check calibration number (see tag on transducer) and network module the transducer is plugged in to.
        ii. "Test" Transducer.
        iii. Take Zero.
        iv. Go to "Task".
        v. Click on "Add".
        vi. Name file with resedimentation experiment number, your initials, and increment (i.e. Resed024_JSinc4).
        vii. Click "save".
        viii. Select the appropriate sensor group the transducer is plugged in to.
        ix. Choose "resedimentation schedule". This assumes the resedimentation schedule has been setup yet. Choose a schedule with frequent readings at the beginning and less and less readings with increasing time (due to the log-linear relationship between strain and time).
        x. Click "OK".
6. Increment 5
    a. Begin new data Acquisition file.
        i. Once the new file has begun, remove the increment 4 file.
    b. Remove 120g PVC pipe.
    c. Add steel pipe on top of aluminum rod and screw on. Do not add the weight hangers yet.
7. Increment 6

    a. Begin new data Acquisition file.
        i. Once the new one has begun, remove the increment 5 file.
    b. Add weight hangars to each end of the steel pipe. Large coupler nut goes on top of the pipe and a small one below (Figure A4.1). Add one 500g weight to each weight hangar.
8. Increment 7
    a. Begin new data Acquisition file.
        i. Once the new one has begun, remove the increment 6 file.
    b. Add one 2kg weight to each weight hangar.
9. Increment 8
    a. Begin new data Acquisition file.
        i. Once the new one has begun, remove the increment 7 file.
    b. Remove the 2kg weight from each weight hangar.
    c. Add one 5kg weight and one 1kg weight to each side.
10. Increment 9
    a. Begin new data Acquisition file.
        i. Once the new one has begun, remove the increment 8 file.
    b. Remove the 5kg weight.
    c. Add 10kg weight to each side.
11. Increment 10
    a. Begin new data Acquisition file.
        i. Once the new one has begun, remove the increment 9 file.
    b. Remove the 1kg weight from each side.
    c. Add one 5kg weight and one 2kg weight to each side to each side.
    d. Leave sample under maximum load for at least five times the end of primary consolidation.
12. Unload (Figure A4.4)
    a. Begin new data Acquisition file.
        i. Once the new one has begun, remove the increment 10 file.
        ii. Instead of Resedimentation schedule, choose “ten min” reading schedule.
    b. Remove all weights from hangars.
    c. Add one 2kg weight and one 1kg weight to each side.
13. Extrude sample with jig particularly designed for this purpose.
14. Take a subsample (thin slice) for porosity measurement. Get wet mass and put in oven at 105 degrees Celsius for at least 24 hrs. Then determine dry mass and calculate porosity.
15. Use immediately remaining sample or store in refrigerated room. In case of storing, wrap sample in plastic wrap. Place plastic disk underneath and on top of sample. Put in plastic container with lid. Add moistened paper towel into the container. Keep in refrigerated room until use.
16. Take assembly apart and clean individual pieces.

Figure A4.4: Resedimentation setup at unload.

Appendix 5: Uniaxial constant-rate-of-strain (CRS) consolidation procedure (UT GeoMechanics Lab)

I perform uniaxial constant-rate-of-strain (CRS) consolidation tests in accordance to ASTM Standard D4186-06 (ASTM International, 2006) and the UT Geomechanics Lab procedure. For the BBC – silt mixtures, I used the 2,000 lbs load cell and large specimen ring (50mm) in order to load the samples to 2.5 MPa. For the Nankai – silt mixtures, I used the 10,000 lbs load cell and small specimen ring (2.5") in order to load the samples to 20 MPa. I have only done a one modification to the standard procedure which is explained below.

A5.1 Difference from standard CRS test in UT Geomechanics Lab

1. In case of the Nankai – silt mixtures, I added a second porous stone into the specimen ring in order to preserve the correct aspect ratio of specimen height to diameter. The available specimen rings in the UT Geomechanics Lab all have the same height, independent of their diameter. So the specimen needs to be shortened which is achieved by adding a second porous stone.
    - Follow standard procedure to trim the specimen into the specimen ring.
    - Put the specimen ring on its top end.
    - Use a wire-saw to carefully cut off excess soil from the base of the specimen ring.
    - Smoothen the bottom of the specimen with a razor blade. Do not leave any streaks or holes.

- Place a saturated but not dripping porous stone onto the bottom of the specimen, align the stone well within the inner diameter of the specimen ring.
- Place the recess tool on top of the porous stone and carefully flip the entire assembly upside down so that the recess tool is at the bottom (sitting on the table).
- Make sure recess tool, porous stone, and specimen ring are aligned. Then carefully and slowly push the specimen ring down onto the recess tool. The stone will then be inside the specimen ring.
- Cut excess soil off the top of the specimen with a wire-saw.
- Smoothen the top of the specimen out with a razor blade.
- Place a moistened but not dripping filter paper (get the mass first as in the standard procedure) onto the top of the specimen.
- Lift the specimen ring up, flip it over and align the top of the ring with the recess tool. Push the ring down onto the recess tool. Now the first porous stone is being pushed to the bottom end of the specimen ring and a gap/recess is created at the top of the specimen, where the second porous stone goes (get mass first as outlined in standard procedure).
- From here on the procedure is the same.

REFERENCES

ASTM International, 2006. Standard test method for one-dimensional consolidation properties of saturated cohesive soils using controlled-strain loading (Standard D4186-06). *In* Annual book of ASTM standards volume 04.08: West Conshohocken, Pennsylvania, American Society for Testing and Materials, p. 15, doi:10.1520/D4186-06.

Appendix 6: Alternative permeability models (GSA Data Repository for Chapter 4)

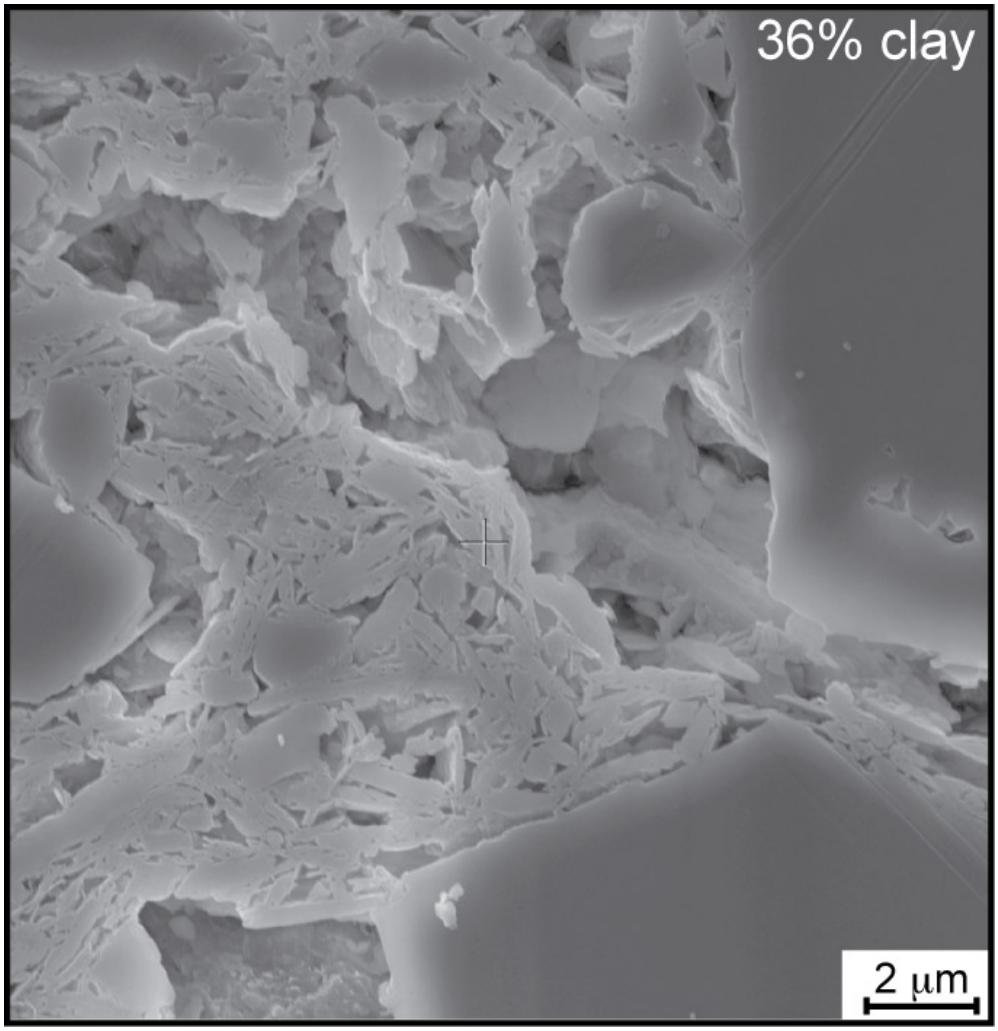

Figure A6.1: Secondary electron microscope image of BBC and silt mixture with 36% clay at a magnification of 14,000 (SEM0019 CRS051-03-tlse.tif). Image was taken after consolidation to a maximum effective vertical stress of 2.4 MPa. It represents a vertical cross section of the sample.

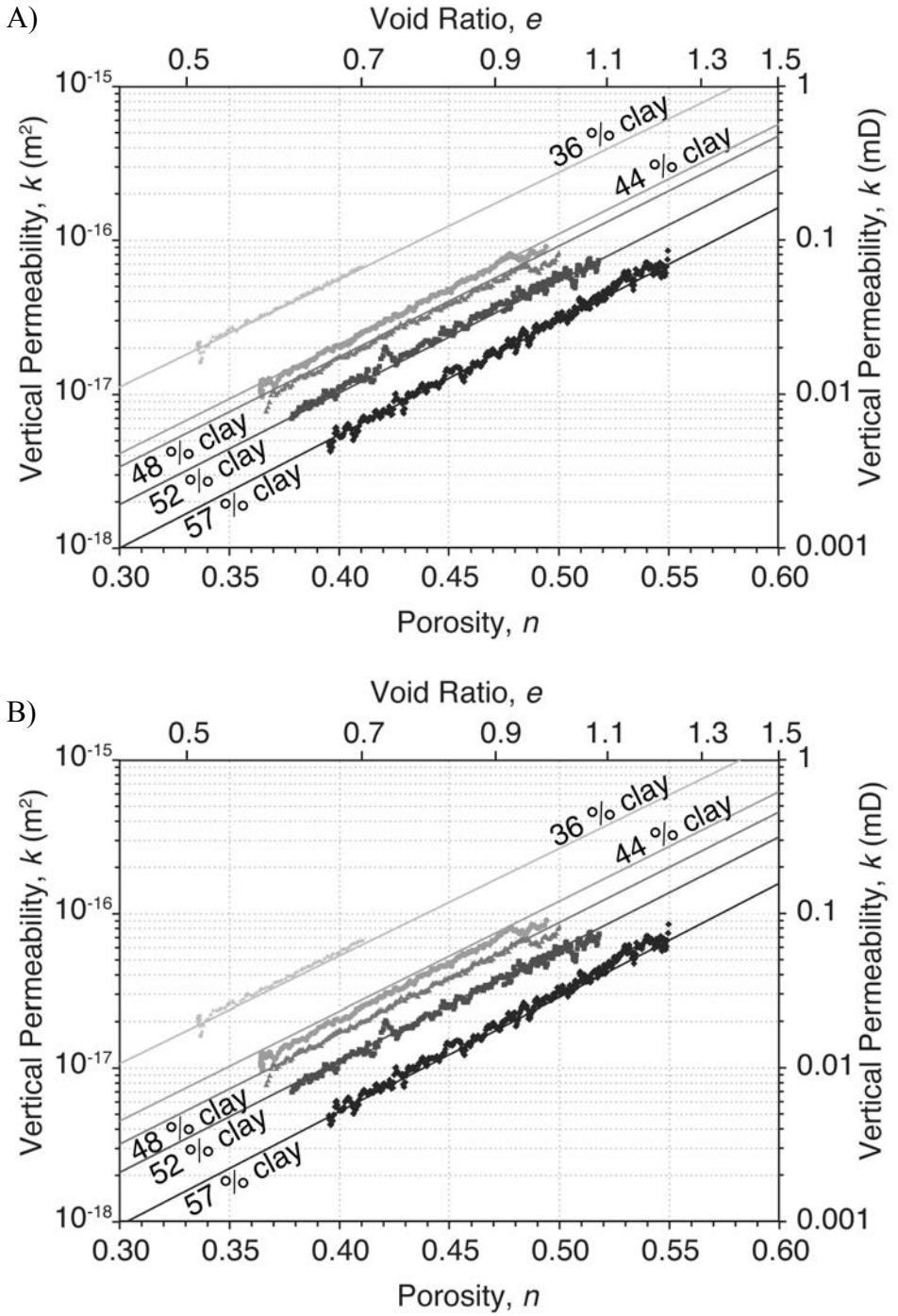

Figure A6.2: Vertical permeabilities of BBC–silt mixtures derived from uniaxial constant-rate-of-strain consolidation tests (for test numbers see Table 4.1) along with predicted permeabilities (solid lines) using our geometric mean

model based on A) grain size with a cutoff between clay and silt at 4μm and B) mineralogy.

γ_{cl}	$log(k_0^{cl})$	γ_{si}	$log(k_0^{si})$
Grain size cut-off at 4 μm			
7.92	-21.72	6.25	-16.91
Mineralogy			
8.54	-23.40	6.59	-17.96

Table A6.1: Alternative permeability model parameters.

Bibliography

Abeele, W.V., 1986. The influence if bentonite on the permeability of sandy silts. *Nuclear and Chemical Waste Management*, 6(1): 81-88, doi:10.1016/0191-815X(86)90091-4.

Alt, J.C., and Teagle, D.A.H., 1999. The uptake of carbon during alteration of ocean crust. *Geochim. Cosmochim. Acta*, 63(10): 1,527-1,535.

Alt, J.C., 2004. Alteration of the upper oceanic crust: mineralogy, chemistry, and processes. *In* Davis, E.E., and Elderfield, H., eds., Hydrogeology of the Oceanic Lithosphere: Cambridge, Cambridge University Press, p. 706.

Anderson, R.N., and Hobart, M.A., 1976. The relation between heat flow, sediment thickness, and age in the Eastern Pacific. *J. Geophs. Res.*, 81: 2,968-2,989.

Aplin, A.C., Yang, Y.L., and Hansen, S., 1995. Assessment of beta, the compression coefficient of mudstones and its relationship with detailed lithology. *Marine and Petroleum Geology*, 12(8): 955-963, doi:10.1016/0264-8172(95)98858-3.

ASTM International, 2005, Standard Test Methods for Liquid Limit, Plastic Limit, and Plasticity Index of Soils (Standard D4318-05), *in* Annual Book of ASTM Standards (Vol. 04.08), ed., Soil and Rock (I): West Conshohocken, PA, American Society for Testing and Materials, p. 16, doi:10.1520/D4318-05.

ASTM International, 2006. Standard test method for one-dimensional consolidation properties of saturated cohesive soils using controlled-strain loading (Standard D4186-06). *In* Annual Book of ASTM Standards (Vol. 04.08), ed., Soil and Rock (I): West Conshohocken, PA, American Society for Testing and Materials, p. 15, doi:10.1520/D4186-06.

ASTM International, 2007. Standard test method for particle-size analysis of soils (Standard D422-63R07). *In* Annual Book of ASTM Standards (Vol. 04.08), ed., Soil and Rock (I): West Conshohocken, PA, American Society for Testing and Materials, p. 10-17, doi:10.1520/D0422-07.

Athy, L.F., 1930. Density, porosity, and compaction of sedimentary rocks. *Am. Assoc. Pet. Geol. Bull.*, 14: 1-22.

Badalini, G., Kneller, B., and Winker, C.D., 2000, Architecture and Processes in the Late Pleistocene Brazos-Trinity Turbidite System, Gulf of Mexico Continental Slope, GCSSEPM Foundation 20th Annual Research Conference, Deep-Water Reservoirs of the World.

Bandini, P., and Sathiskumar, S., 2009. Effects of Silt Content and Void Ratio on the Saturated Hydraulic Conductivity and Compressibility of Sand-Silt Mixtures. *Journal of Geotechnical and Geoenvironmental Engineering*, 135(12): 1976-1980, doi:10.1061/(ASCE)GT.1943-5606.0000177.

Beaubouef, R.T., and Friedmann, S.J., 2000, High Resolution Seismic/Sequence Stratigraphic Framework for the Evolution of Pleistocene Intra Slope Basins, Western Gulf of Mexico: Depositional Models and Reservoir Analogs, GCSSEPM Foundation 20th Annual Research Conference, Deep-Water Reservoirs of the World.

Becker, D.E., Crooks, J.H.A., Been, K., and Jefferies, M.G., 1987. Work as a Criterion for Determining Insitu and Yield Stresses in Clays. *Canadian Geotechnical Journal*, 24(4): 549-564.

Bekins, B.A., McCaffrey, A.M., and Dreiss, S.J., 1995. Episodic and constant flow models for the origin of low-chloride waters in a modern accretionary complex. *Water Resources Research*, 31(12): 3205-3215.

Bickle, M., and Elderfield, H., 2004. Hydrothermal fluxes in a global context. *In* Davis, E.E., and Elderfield, H., eds., Hydrogeology of the Oceanic Lithosphere: Cambridge, Cambridge University Press, p. 706.

Binh, N.T.T., Tokunaga, T., Nakamura, T., Kozumi, K., Nakajima, M., Kubota, M., Kameya, H., and Taniue, M., 2009. Physical properties of the shallow sediments in late Pleistocene formations, Ursa Basin, Gulf of Mexico, and their implications for generation and preservation of shallow overpressures. *Marine and Petroleum Geology*, 26(4): 474-486, doi:10.1016/j.marpetgeo.2009.01.018.

Biscaye, P.E., 1965. Mineralogy and sedimentation of recent deep-sea clays in the Atlantic Ocean and adjacent seas and oceans. *Geol. Soc. Am. Bull.*, 76(7): 803-832, doi:10.1130/0016-7606(1965)76[803:MASORD]2.0.CO;2.

Broichhausen, H., Littke, R., and Hantschel, T., 2005. Mudstone compaction and its influence on overpressure generation, elucidated by a 3D case study in the North Sea. *International Journal of Earth Sciences*, 94(5-6): 956-978, doi:10.1007/s00531-005-0014-1.

Burland, J.B., 1990. On the compressibility and shear strength of natural clays. *Geotechnique*, 40(3): 329-378.

Burmister, D.M., 1942. Laboratory investigations of soils at Flushing Meadow Park. *Transactions of the American Society of Civil Engineers*, 107: 187.

Burmister, D.M., 1951. The application of controlled test methods in consolidation testing. *Symposium on Consolidation Testing of Soils, American Society for Testing and Materials*, Special Technical Publication 126: 83.

Butterfield, R., 1980. A natural compression law for soils (an advance on e-logp'). *Geotechnique*, 29: 469-480.

Casagrande, A., 1936. The determination of the pre-consolidation load and its practical significance. *In* Casagrande, A., Rutledge, P.C., and Watson, J.D., eds., Proc. 1st International Conf. Soil Mech. Foun. Eng., Am. Soc. Civ. Eng., p. 60-64.

Chandler, R.J., 2000. Clay Sediments in Depositional Basins: the Geotechnical Cycle. *Quaterly Journal of Engineering Geology and Hydrogeology*, 33: 7-39.

Chapuis, R.P., and Aubertin, M., 2003. On the use of the Kozeny-Carman equation to predict the hydraulic conductivity of soils. *Canadian Geotechnical Journal*, 40: 616-628, doi:10.1139/T03-013.

Clennell, M.B., Dewhurst, D.N., Brown, K.M., and Westbrook, G.K., 1999. Permeability anisotropy of consolidated clays. *In* Aplin, A.C., Fleet, A.J., and Macquaker, J.H.S., eds., Muds and Mudstones: Physical and Fluid Flow Properties, Volume 158: London, The Geological Society of London, p. 79-96.

Craig, R.F., 1974. Soil Mechanics. New York, Van Nostrand Reinhold, 275 p.

Davis, E.E., and Fisher, A.T., 1994. On the nature and consequences of hydrothermal circulation in the Middle Valley sedimented rift: Inferences from geophysical and geochemical observations, Leg 139. *In* Motte, M.J., Davis, E.E., Fisher, A.T., and Slack, J.F., eds., Proceedings of the Ocean Drilling Program, Scientific Results, Volume 139: College Station, TX, Ocean Drilling Program, p. 695-717.

Davis, E.E., and Becker, K., 2004. Observations of temperature and pressure: constraints on ocean crustal hydrologic state, properties, and flow. *In* Davis, E.E., and Elderfield, H., eds., Hydrogeology of the Oceanic Lithosphere: Cambridge, Cambridge University Press, p. 706.

Day-Stirrat, R.J., Flemings, P.B., Strong, H.E., Schneider, J., Sawyers, D.E., Schleicher, A.M., and Germaine, J.T., 2009, The fabric of mass transport deposits in the Ursa Basin, Gulf of Mexico, American Geophysical Union Fall Meeting, Volume 90(52): San Francisco, *Eos Trans. AGU*, Abstract T53C-1607.

Day-Stirrat, R.J., Schleicher, A.M., Schneider, J., Flemings, P.B., Germaine, J.T., and van der Pluijm, B.A., 2011, Preferred orientation of phyllosilicates: Effects of composition and stress on resedimented mudstone fabric: Journal of Structural Geology, v. 33, no. 9, p. 1347-1358, doi:10.1016/j.jsg.2011.06.007.

Dewhurst, D.N., Brown, K.M., Clennell, M.B., and Westbrook, G.K., 1996. A comparison of the fabric and permeability anisotropy of consolidated and sheared silty clay. *Engineering Geology*, 42(4): 253-267, doi:10.1016/0013-7952(95)00089-5.

Dewhurst, D.N., Aplin, A.C., Sarda, J.P., and Yang, Y.L., 1998. Compaction-driven evolution of porosity and permeability in natural mudstones: An experimental study. *Journal of Geophysical Research*, 103(B1): 651-661, doi:10.1019/97JB02540.

Dewhurst, D.N., Aplin, A.C., and Sarda, J.P., 1999. Influence of clay fraction on pore-scale properties and hydraulic conductivity of experimentally compacted mudstones. *Journal of Geophysical Research*, 104(B12): 29261-29274, doi:10.1029/1999JB900276.

Dugan, B., and Flemings, P.B., 2000. Overpressure and Fluid Flow in the New Jersey Continental Slope: Implications for Slope Failure and Cold Seeps. *Science*, 289(5477): 288-291.

Dugan, B., Flemings, P.B., Olgaard, D.L., and Gooch, M.J., 2003. Consolidation, effective stress, and fluid pressure of sediments from ODP Site 1073, US mid-Atlantic continental slope. *Earth and Planetary Science Letters*, 215: 13-26, doi:10.1016/S0012-821X(03)00425-4.

Dugan, B., 2008. Fluid flow in the Keathley Canyon 151 Mini-Basin, northern Gulf of Mexico. *Marine and Petroleum Geology*, 25(9): 919-923, doi:10.1016/j.marpetgeo.2007.12.005.

Dugan, B., and Germaine, J., 2008. Near-seafloor overpressure in the deepwater Mississippi Canyon, northern Gulf of Mexico. *Geophysical Research Letters*, 35(L02304), doi:10.1029/2007GL032275.

Farrar, D.M., and Coleman, J.D., 1967. The correlation of surface area with other properties of nineteen British clays. *Journal of Soil Science*, 18(1): 118-124.

Fertl, W.H., and Chilingarian, G.V., 1987. Abnormal formation pressures and their detection by pulsed neutron capture logs. *Journal of Petroleum Science and Engineering*, 1: 23-38.

Fisher, A.T., 2004. Rates of flow and patterns of fluid circulation. *In* Davis, E.E., and Elderfield, H., eds., Hydrogeology of the Oceanic Lithosphere: Cambridge, Cambridge University Press, p. 706.

Fjaer, E., Holt, R.M., Horsrud, P., Raaen, A.M., and Risnes, R., 2008. Petroleum related rock mechanics. Amsterdam, Netherlands, Elsevier.

Flemings, P.B., Stump, B.B., Finkbeiner, T., and Zoback, M., 2002. Flow focusing in overpressured sandstones: Theory, observations, and applications. *American Journal of Science*, 302(10): 827-855, doi:10.2475/ajs.302.10.827.

Flemings, P.B., and Lupa, J.A., 2004. Pressure prediction in the Bullwinkle Basin through petrophysics and flow modeling (Green Canyon 65, Gulf of Mexico). *Marine and Petroleum Geology*, 21: 1311-1322, doi:10.1016/j.marpetgeo.2004.09.005.

Flemings, P.B., Behrmann, J.H., John, C.M., and Expedition 308 Scientists, 2006a. Gulf of Mexico Hydrogeology, *Proc. IODP*, Volume 308: College Station, TX (Integrated Ocean Drilling Program Management International, Inc.), doi:10.2204/iodp.proc.308.2006.

Flemings, P.B., Germaine, J., Long, H., Dugan, B., Sawyer, D., Behrmann, J.H., John, C., and IODP Expedition Shipboard Scientific Party, 2006b, Measuring Temperature and Pressure with the Temperature Two Pressure (T2P) Probe in the Ursa Basin, Gulf of Mexico: Development of a New Pressure and Temperature Probe for the

IODP, Offshore Technology Conference, Volume OTC 17957: Houston, Texas, USA, p. 5.

Flemings, P.B., Long, H., Dugan, B., Germaine, J.T., John, C., Behrmann, J.H., Sawyer, D.E., and IODP Expedition 308 Scientists, 2008. Pore pressure penetrometers document high overpressure near the seafloor where multiple submarine landslides have occurred on the continental slope, offshore Louisiana, Gulf of Mexico. *Earth and Planetary Science Letters*, 269: 309-325, doi:10.1016/j.epsl.2007.12.005.

Garcia-Bengochea, I., Lovell, C.W., and Altchaeffl, A.G., 1979. Pore distribution and permeability of silty clays. *J. Geotech. Eng. Div., ASCE*, 105: 839-856.

Garg, S.K., Pritchett, J.W., Katoh, A., Baba, K., and Fujii, T., 2008. A mathematical model for the formation and dissociation of methane hydrates in the marine environment. *Journal of Geophysical Research-Solid Earth*, 113(B01201), doi:10.1029/2006JB004768.

Gerke, H.H., and Van Genuchten, M.T., 1993. A dual-porosity model for simulating the preferential movement of water and solutes in structured porous media. *Water Resources Research*, 29(2): 305-319.

Giambalvo, E.R., Fisher, A.T., Martin, J.T., Darty, L., and Lowell, R.P., 2000. Origin of elevated sediment permeability in a hydrothermal seepage zone, eastern flank of the Juan de Fuca Ridge, and implications for transport of fluid and heat. *J. Geophs. Res.*, 105(B1): 913-928.

Gibson, R.E., 1958. The progress of consolidation in a clay layer increasing in thickness with time. *Geotechnique*, 8: 171-182.

Gordon, D.S., and Flemings, P.B., 1998. Generation of overpressure and compaction-driven fluid flow in a Plio-Pleistocene growth-faulted basin, Eugene Island 330, offshore Louisiana. *Basin Research*, 10(2): 177-196, doi:10.1046/j.1365-2117.1998.00052.

Gorsline, D.S., 1984. A review of fine-grained sediment origins, characteristics, transport, and deposition. *In* Stow, D.A.V., and Piper, D.J.W., eds., Fine-grained sediments, Volume 15, Geol. Soc. Spec. Publ., p. 17-34.

Grevemeyer, I., and Bartetzko, A., 2004. Hydrothermal aging of oceanic crust: inferences from seismic refraction and borehole studies. *In* Davis, E.E., and Elderfield, H., eds., Hydrogeology of the Oceanic Lithosphere: Cambridge, Cambridge University Press, p. 706.

Harris, R.N., and Chapman, D.S., 2004. Deep-seated oceanic heat flow, heat deficits, and hydrothermal circulation. *In* Davis, E.E., and Elderfield, H., eds., Hydrogeology of the Oceanic Lithosphere: Cambridge, Cambridge University Press, p. 706.

Harrison, W.J., and Summa, L.L., 1991. Paleohydrology of the Gulf of Mexico Basin. *American Journal of Science*, 291(2): 109-176.

Hart, B.S., Flemings, P.B., and Deshpande, A., 1995. Porosity and Pressure - Role of Compaction Disequilibrium in the Development of Geopressures in a Gulf-Coast Pleistocene Basin. *Geology*, 23(1): 45-48.

Hawkins, A.B. and Pinches, G.M., 1992, Engineering description of mudrocks: Quaterly Journal of Engineering Geology, v. 25, p. 17-30.

Heath, J.E., Dewers, T.A., McPherson, B.J.O.L., Petrusak, R., Chidsey, T.C., Rinehart, A.J., and Mozley, P.S., 2011. Pore networks in continental and marine mudstones: characteristics and controls on sealing behavior. *Geosphere, Advances in 3D imaging and and analysis of geomaterials themed issue*, 7(2): 429-454, doi:10.1130/GES00619.1.

Hermanrud, C., 1993. Basin modeling techniques - An overview. *In* Doré, A.G., ed., Basin Modelling: Advances and Applications, Norwegian Petroleum Society Spec. Publ. 3: New York, Elsevier, p. 1-34.

Hillier, S., 2000. Accurate quantitative analysis of clay and other minerals in sandstones by XRD: comparison of a Rietveld and a reference intensity ratio (RIR) method and the importance of sample preparation. *Clay Minerals*, 35(1): 291-302.

Hyndman, R.D., Yamano, M., and Oleskevich, D.A., 1997. The seismogenic zone of subduction thrust faults. *Island. Arc*, 6: 244-260.

Jacobson, R.S., 1992. Impact of crustal evolution of changes of the seismic properties of the uppermost ocean crust. *Rev. Geophys.*, 30: 23-42.

Jamiolkowski, M., 1985, New developments in field and laboratory testing of soils, 11th Int. Conf. on Soil Mechanis and Foundation Engineering, Volume 1: San Francisco, p. 57-153.

Janbu, N., Tokheim, O., and Senneset, K., 1981, Consolidation test with continuous loading, 10th International Conference on Soil Mechanics and Foundation Engineering, Volume 1: Stockholm, p. 645-654.

Karig, D.E., and Hou, G., 1992. High-stress consolidation experiments and their geologic implications. *Journal of Geophysical Research*, 97(B1): 289-300, doi:10.1029/91JB02247.

Kaye, C.A., and Barghoorn, E.S., 1964. Late Quaternary sea-level change and crustal rise at Boston Harbor, Massachusetts, with notes on the autocompaction of peat. *Geological Soc. America Bulletin*, 75(2): 63-80, doi:10.1130/0016-7606(1964)75[63:LQSCAC]2.0.CO;2.

Kennett, J.P., and Huddleston, P., 1972. Late Pleistocene paleoclimatology, foraminiferal biostratigraphy, and tephrochronology: Western Gulf of Mexico. *Quaternary Research*, 2: 38-69.

Kenney, T.C., 1964. Sea-level movements and the geologic histories of the post-glacial marine soils at Boston, Nicolet, Ottawa and Oslo. *Geotechnique*, 14(3): 203-230, doi:10.1680/geot.1964.14.3.302.

Kobayashi, K., Kasuga, S., and Okino, K., 1995. Shikoku Basin and its margins. *In* Taylor, B., ed., Backarc Basins: Tectonics and Magmatism: New York, Plenum, p. 381-405.

Koltermann, C.E., and Gorelick, S.M., 1995. Fractional packing model for hydraulic conductivity derived from sediment mixtures. *Water Resources Research*, 31(12): 3283-3297, doi:10.1029/95WR02020.

Lambe, T.W., and Whitman, R.V., 1979. Soil Mechanics: SI Version. New York, Wiley, 553 p.

Leonards, G.H., 1962. Engineering Properties of Soils. New York, McGraw-Hill.

Long, H., Flemings, P.B., and Germaine, J.T., 2007. Interpreting in situ pressure and hydraulic properties with borehole penetrometers in ocean drilling: DVTPP and Piezoprobe deployments at southern Hydrate Ridge, offshore Oregon. *Journal of Geophysical Research*, 112(B4), doi:10.1029/2005JB004165.

Long, H., Flemings, P.B., Germaine, J.T., Saffer, D.M., and Dugan, B., 2008. Data report: consolidation characteristics of sediments from IODP Expedition 308, Ursa Basin, Gulf of Mexico. *In* Flemings, P.B., Behrmann, J.H., and John, C.M., eds., Proc. IODP, Volume 308: College Station, TX, *Proc. IODP, Sci. Results*, p. 47, doi:10.2204/iodp.proc.308.204.2008.

Long, H., Flemings, P.B., Germaine, J.T., and Saffer, D.M., 2011. Consolidation and overpressure near the seafloor in the Ursa Basin, Deepwater Gulf of Mexico. *Earth and Planetary Sceince Letters*, 305: 11-20, doi:10.1016/j.epsl.2011.02.007.

Loucks, R.G., Reed, R.M., Ruppel, S.C., and Jarvie, D.M., 2009. Morphology, genesis, and distribution of nanometer-scale pores in siliceous mudstones of the Mississippian Barnett Shale. *Journal of Sedimentary Research*, 79(12): 848-861, doi:10.2110/jsr.2009.092.

Mallarino, G., Beaubouef, R.T., Droxler, A.W., Abreu, V., and Labeyrie, L., 2006. Sea level influence on the nature and timing of a minibasin sedimentary fill (northwestern slope of the Gulf of Mexico). *AAPG Bulletin*, 90(7): 1089-1119, doi:10.1306/02210605058.

Mencher, E., Copeland, R.A., and Payson, H., JR., 1968. Surficial sediments of Boston Harbor, Massachusetts. *Journal of Sedimentary Petrology*, 38(1): 79-86.

Mesri, G., and Olson, R.E., 1971. Mechanisms controlling the permeability of clays. *Clays and Clay Minerals*, 19: 151-158.

Mitchell, J.K., 1993. Fundamentals of soil behavior. Hoboken, N.J., John Wiley & Sons.

Miyazaki, S., and Heki, K., 2001. Crustal velocity field of southwest Japan: subduction and arc-arc collision. *Journal of Geophysical Research*, 106(B3): 4305-4326, doi:10.1029/2000JB900312.

Mondol, N.H., Bjørlykke, K., Jahren, J., and Høeg, K., 2007. Experimental mechanical compaction of clay mineral aggregates - Changes in physical properties of mudstones during burial. *Marine and Petroleum Geology*, 24: 289-311, doi:10.1016/j.marpetgeo.2007.03.006.

Mondol, N.H., Bjørlykke, K., and Jahren, J., 2008a. Experimental compaction of clays: relationship between permeability and petrophysical properties in mudstones. *Petroleum Geoscience*, 14: 319-337, doi:10.1144/1354-079308-773.

Mondol, N.H., Fawad, M., Jahren, J., and Bjørlykke, K., 2008b. Synthetic mudstone compaction trends and their use in pore pressure prediction. *First Break*, 26: 43-51, doi:10.3997/1365-2397.2008018.

Mondol, N.H., 2009, Porosity and permeability development in mechanically compacted silt-kaolinite mixtures, SEG Houston 2009 International Exposition and Annual Meeting: Houston, Society of Economic Geologists.

Mondol, N.H., Jahren, J., Berre, T., Grande, L., and Bjørlykke, K., 2010, Permeability anisotropy in mudstones - an experimental study, Search and Discover Article #40649, AAPG Annual Convention and Exhibition: New Orleans, Louisiana, American Association of Petroleum Geologists.

Moore, G.F., Park, J.-O., Bangs, N.L., Gulick, S.P., Tobin, H.J., Nakamura, Y., Sato, S., Tsuji, T., Yoro, T., Tanaka, H., Uraki, S., Kido, Y., Sanada, Y., Kuramoto, S., and Taira, A., 2009. Structural and seismic stratigraphic frameworkof the NanTroSEIZE Stage 1 transect. *In* Kinoshita, M., Tobin, H., Ashi, J., Kimura, G., Lallemand, S.E., Screaton, E., Curewitz, D., Masago, H., Moe, K.T., and the Expedition Scientists, eds., *Proc. IODP 314/315/316*: Washington, DC, Integrated Ocean Drilling Program Management International, Inc., doi:10.2204/iodp.proc.314315316.102.2009.

Moore, J.C., and Saffer, D., 2001. Updip limit of the seismogenic zone beneath the accretionary prism of southwest Japan: an effect of diagenetic to low-grade metamorphic processes and increasing effective stress. *Geology*, 29(2): 183-186, doi:10.1130/0091-7613(2001)029<0183:ULOTSZ>2.0.CO;2.

Mottl, M.J., and Wheat, C.G., 1994. Hydrothermal circulation through mid-ocean ridge flanks: fluxes of heat and magnesium. *Geochim. Cosmochim. Acta*, 58: 2,225-2,237.

Mueth, D.M., Jaeger, H.M., and Nagel, S.R., 1998. Force distribution in a granular medium. *Physical Review E*, 57: 3164-3169, doi:10.1103/PhysRevE.57.3164.

O'Brien, N.R., 1971. Fabric of kaolinite and illite floccules. *Clays and Clay Minerals*, 19: 353-359.

O'Hayer, W.W., 2009. Laurentide Ice Sheet Meltwater Influences and Millennial Scale Climate Oscillations on the Northwestern Slope of the Gulf of Mexico During Marine Isotope Stage 6 and Termination II [MS thesis]. Houston, Texas, Rice University, NNN p.

Okino, K., Shimakawa, Y., and Nagaoka, S., 1994. Evolution of the Shikoku Basin. *J. Geomagn. Geoelectr.*, 46: 463-479.

Orange, D.L., Saffer, D.M., Jeanjean, P., Al-Khafaji, Z., Humphrey, G., and Riley, G., 2003. Measurements and modeling of the shallow pore pressure regime at the Sigsbee Escarpment: Successful prediction of overpressure and ground-truthing with borehole measurements. *Leading Edge*, 22: 906-913.

Ostermeier, R.M., Pelletier, J.H., Winker, C.D., Nicholson, J.W., Rambow, F.H., and Cowan, K.M., 2000. Dealing with shallow-water flow in the deepwater Gulf of Mexico. *paper presented at Offshore Technology Conference 2000*, Soc. of Petrol. Eng., Houston, TX.

Ostermeier, R.M., Pelletier, J.H., Winker, C.D., and Nicholson, J.W., 2001. Trends in shallow sediment pore pressures: Deepwater Gulf of Mexico. *paper presented at 2001 SPE/IADC Drilling Conference*, Soc. of Petrol. Eng., Amsterdam.

Park, J.-O., Tsuru, T., No, T., Takizawa, K., Sato, S., and Kaneda, Y., 2008. High-resolution 3D seismic reflection survey and prestack depth imaging in the Nankai Trough off southeast Kii Peninsula. *Butsuri Tansa*, 61: 231-241 (in Japanese with English abstract).

Phipps, D., 1964. The geology of the unconsolidated sediments of Boston Harbor. Cambridge, Massachusetts Institute of Technology, 54 p.

Pittman, E.D., 1992. Relationship of porosity and permeability to various parameters derived from mercury injection-capillary pressure curves for sandstone. *AAPG Bulletin*, 76: 191-198.

Prior, D.B., and Suhayda, J.N., 1979. Application of infinite slope analysis to subaqueous sediment instability, Mississippi delta. *Engineering Geology*, 14(1): 1-10.

Prior, D.B., and Coleman, J.M., 1982. Active slides and flows in underconsolidated marine sediments on the slope of the Mississippi delta. *In* Saxov, S., and Nieuwenhuis, J.K., eds., Marine slides and other mass movements: New York, NY: Plenum Press, p. 21-49.

Renard, P., and LeLoc'h, G., 1996. A new upscaling technique for permeability of porous media: the simplified renormalization. *Comptes Rendus de l'Ac. des Sc. Serie II Fascicule*, 323(10): 859-864.

Revil, A., and Cathles, L.M., 1999. Permeability of shaly sands. *Water Resources Research*, 35(3): 651-662, doi:10.1029/98WR02700.

Revil, A., Grauls, D., and Brévart, O., 2002. Mechanical compaction of sand/clay mixtures. *Journal of Geophysical Research*, 107(B11): 2293, doi:10.1029/2001JB000318.

Robinson, R.G., and Allam, M.M., 1998. Effect of clay mineralogy on coefficient of consolidation. *Clays and Clay Minerals*, 46(5): 596-600, doi:10.1346/CCMN.1998.0460514.

Rubey, W.W., and Hubbert, M.K., 1959. Overthrust belt in geosynclinal area of western Wyoming in light of fluid-pressure hypothesis, 2: Role of fluid pressure in mechanics of overthrust faulting. *GSA Bulletin*, 70(2): 167-205.

Ruppel, C., Dickens, G.R., Castellini, D.G., Gilhooly, W., and Lizarralde, D., 2005. Heat and salt inhibition of gas hydrate formation in the northern Gulf of Mexico. *Geophys. Res. Lett.*, 32(L04605), doi:10.1029/2004GL021909.

Saffer, D.M., and Bekins, B.A., 1998. Episodic fluid flow in the Nankai accretionary complex: Timescale, geochemistry, flow rates, and fluid budget. *Journal of Geophysical Research*, 103(B12): 30351-30370.

Saffer, D.M., Silver, E.A., Fisher, A.T., Tobin, H., and Moran, K., 2000. Inferred pore pressures at the Costa Rica subduction zone: implications for dewatering processes. *Earth and Planetary Science Letters*, 177(3-4): 193-207, doi:10.1016/S0012-821X(00)00048-0.

Saffer, D.M., and Bekins, B.A., 2002. Hydrologic controls on the morphology and mechanics of accretionary wedges. *Geology*, 30(3): 271-274.

Saffer, D.M., 2003. Pore pressure development and progressive dewatering in underthrust sediments at the Costa Rican subduction margin: Comparison with northern Barbados and Nankai. *Journal of Geophysical Research*, 108(B5): 2261, doi:10.1029/2002JB001787.

Saffer, D.M., and Bekins, B.A., 2006. An evaluation of factors influencing pore pressure in accretionary complexes: Implications for taper angle and wedge mechanics. *Journal of Geophysical Research*, 111(B04101), doi:10.1029/2005JB003990.

Saito, S., Underwood, M.B., and Kubo, Y., 2009. NanTroSEIZE Stage 2: subduction inputs. *IODP Sci. Prosp.*, 322, doi:10.2204/iodp.sp.322.2009.

Santagata, M.C., and Germaine, J.T., 2002. Sampling disturbance effects in normally consolidated clays. *J. Geotech. Geoenviron. Eng.*, 128(12): 997-1006, doi:10.1061/(ASCE)1090-0241(2002)128:12(997).

Santagata, M.C., and Kang, Y.I., 2007. Effects of geologic time on the initial stiffness of clays. *Engineering Geology*, 89: 98-111, doi: 10.1016/j.enggeo.2006.09.018.

Santamarina, J.C., Klein, K.A., Wang, Y.H., and Prencke, E., 2002. Specific surface: determination and relevance. *Can. Geotech. J.*, 39: 233-241, doi:10.1139/T01-077.

Satterfield, W.M., and Behrens, E.W., 1990. A Late Quaternary Canyon Channel System, Northwest Gulf of Mexico Continental-Slope. *Marine Geology*, 92(1-2): 51-67, doi:10.1016/0025-3227(90)90026-G.

Sawyer, D.E., Flemings, P.B., Shipp, R.C., and Winker, C.D., 2007. Seismic geomorphology, lithology, and evolution of the late Pleistocene Mars-Ursa turbidite region, Mississippi Canyon area, northern Gulf of Mexico. *AAPG Bulletin*, 91(2): 215-234, doi:10.1306/08290605190.

Sawyer, D.E., Jacoby, R., Flemings, P.B., and Germaine, J.T., 2008. Data report: particle size analysis of sediments in the Ursa Basin, IODP Expedition 308 Sites U1324 and U1322, northern Gulf of Mexico. *In* Flemings, P.B., Behrmann, J.H., John, C.M., and the Expedition 308 Scientists, eds., *Proc. IODP*, Volume 308: College Station, TX, p. 20, doi:10.2204/iodp.proc.308.205.2008.

Sawyer, D.E., Flemings, P.B., Dugan, B., and Germaine, J.T., 2009. Retrogressive Failures Recorded in Mass Transport Deposits in the Ursa Basin, Northern Gulf of Mexico. *J. Geophs. Res.*, 114(B10102), doi: 10.1029/2008JB006159.

Scheidegger, 1974. The Physics of Flow Through Porous Media. Toronto, University of Toronto Press.

Schmertmann, J.M., 1955. The undisturbed consolidation of clay. *Transactions of the American Society of Civil Engineers*, 120: 1201.

Schneider, F., Burrus, J., and Wolf, S., 1993. Modelling overpressures by effective-stress/porosity relationships in low-permeability rocks: Empirical artifice of physical reality? *In* Doré, A.G., ed., Basin Modelling: Advances and Applications, Norw. Pet. Soc. Spec. Publ. 3: New York, Elsevier, p. 333-341.

Schneider, J., Flemings, P.B., Dugan, B., Long, H., and Germaine, J.T., 2009. Overpressure and consolidation near the seafloor of Brazos-Trinity Basin IV, Northwest Deepwater Gulf of Mexico. *J. Geophys. Res.*, 114(B05102): 13, doi:10.1029/2008JB005922.

Schneider, J., Flemings, P.B., Day-Stirrat, R.J., and Germaine, J.T., 2011. Insights into pore-scale controls on mudstone permeability through resedimentation experiments. *Geology*, 39(11): 1011-1014, doi:10.1130/G32475.1.

Sclater, J.G., Crowe, J., and Anderson, R.N., 1976. On the reliability of oceanic heat flow averages. *J. Geophs. Res.*, 81: 2,997-3,006.

Screaton, E., Saffer, D.M., Henry, P., and Hunze, S., 2002. Porosity loss within the underthrust sediments of the Nankai accretionary complex: Implications for overpressures. *Geology*, 30(1): 19-22, doi:10.1130/0091-7613(2002)030<0019:PLWTUS>2.0.CO;2.

Screaton, E., and Saffer, D.M., 2005. Fluid expulsion and overpressure development during initial subduction at the Costa Rica convergent margin. *Earth and Planetary Science Letters*, 233(3-4): 361-374, doi:10.1016/j.epsl.2005.02.017.

Seno, T., Stein, S., and Gripp, A.E., 1993. A model for the motion of the Philippine Sea Plate consistent with NUVEL-1 and geological data. *Journal of Geophysical Research*, 98(B10): 17941-17948, doi:10.1029/93JB00782.

Shafiee, A., 2008. Permeability of compacted granule - clay mixtures. *Engineering Geology*, 97: 199-208, doi:10.1016/j.enggeo.2008.01.002.

Sharp, J.M., and Domenico, A., 1976. Energy transport in thick sequences of compacting sediment. *Geol. Soc. Am. Bull.*, 87: 390-400.

Sheahan, T.C., 1991. An experimental study of the time-dependent undrained shear behavior of resedimented clay using automated stress path triaxial equipment [Ph.D. thesis]. Cambridge, Massachusetts Institute of Technology, 952 p.

Shipboard Scientific Party, 2002. Site 1173, Leg 196 summary: Deformation and fluid flow processes in the Nankai Trough accretionary prism: Logging while drilling and Advanced CORKs, *Proc. Ocean Drill. Program Initial Rep.*, 196, Volume 196, p. 1-29, doi:10.2973/odp.proc.ir.196.101.2002.

Skempton, A.W., 1970. The consolidation of clays by gravitational compaction. *J. Geol. Soc. London*, 125: 373-411.

Smith, J.E., 1971. The dynamics of shale compaction and evolution of pore fluid pressure. *Math. Geol.*, 3: 239-263.

Spinelli, G.A., Giambalvo, E.R., and Fisher, A.T., 2004. Sediment permeability, distribution, and influence on fluxes in oceanic basement. *In* Davis, E.E., and Elderfield, H., eds., Hydrogeology of the Oceanic Lithosphere: Cambridge, Cambridge University Press, p. 706.

Stein, C.A., and Stein, S., 1994. Comparison of plate and asthenospheric flow models for the thermal evolution of oceanic lithosphere. *Geophys. Res. Lett.*, 99: 3,081-3,095.

Tan, B., Germaine, J.T., and Flemings, P.B., 2006. Data Report: Consolidation and strength characteristics of sediments from ODP Site 1244, Hydrate Ridge, Cascadia continental margin. *In* Trehu, A.M., Bohrmann, G., Torres, M.E., and Colwell, F.S., eds., Proc. ODP, Sci. Results, Volume 204: College Station, TX.

Tavenas, F., Jean, P., Leblond, P., and Leroueil, S., 1983. The permeability of natural soft clays. Part 2: Permeability characteristics. *Canadian Geotechnical Journal*, 20: 645-660.

Tegnander, C., and Gimse, T., 1998. Flow Simulations To Evaluate Upscaling of Permeability. *Math. Geol.*, 30(6): 717-731.

Terzaghi, K., 1925. Erdbaumechanik auf bodenphysikalischer Grundlage. Leipzig, 399 p.

Terzaghi, K., 1943. Theoretical Soil Mechanics. London, Chapman and Hall, 510 p.

Terzaghi, K., and Peck, R.B., 1948. Soil mechanics in engineering practice. New York, Wiley.

Tobin, H.J., Kinoshita, M., Ashi, J., Lallemant, S., Kimura, G., Screaton, E., Thu, M.K., Masago, H., Curewitz, D., and Expedition 314/315/316 Scientists, 2009. NanTroSEIZE Stage 1 expeditions: introduction and synthesis of key results, *Proc. IODP*, Volume 314/315/316: Washington, DC, Integrated Ocean Drilling Program Management International, Inc., doi:10.2204/iodp.proc314315316.101.2009.

Underwood, M.B., and Steurer, J.F., 2003. Composition and sources of clay from trench slope and shallow accretionary prism of Nankai Trough. *In* Mikada, H., Moore, G.F., Taira, A., Becker, K., Moore, J.C., and Klaus, A., eds., *Proc. ODP, Sci. Results*, Volume 190/196.

Underwood, M.B., Saito, S., Kubo, Y., and the Expedition Scientists, 2009. NanTroSEIZE Stage 2: subduction inputs. *IODP Prel. Rept.*, 322, doi:10.2204/iodp.pr.322.2009.

Underwood, M.B., Saito, S., Kubo, Y., and IODP Expedition 322 Scientists, 2010. IODP Expedition 322 drills two sites to document inputs to the Nankai Trough subduction zone. *Scientific Drilling*, 10: 14-25, doi:10.2204/iodp.sd.10.02.2010.

Vasseur, G., Djeran-Maigre, I., Grunberger, D., Rousset, G., Tessier, D., and Velde, B., 1995. Evolution of structural and physical parameters of clays during experimental compaction. *Marine and Petroleum Geology*, 12(8): 941-954.

Vrolijk, P., 1990. On the mechanical role of smectite in subduction zones. *Geology*, 18: 703-707.

Wagg, T.B., and Konrad, J.-M., 1990, Index properties of clay-silt mixtures, 43rd Canadian Geotechnical Conference, Volume 2: Québec City, Canada, p. 705-710.

Wheat, C.G., and Mottl, M.J., 2004. Geochemical fluxes through mid-ocean ridge flanks. *In* Davis, E.E., and Elderfield, H., eds., Hydrogeology of the Oceanic Lithosphere: Cambridge, Cambridge University Press, p. 706.

Winker, C.D., 1996, High-resolution seismic stratigraphy of a Late Pleistocene submarine fan ponded by salt-withdrawal mini-basins on the Gulf of Mexico continental slope, Proceedings from 1996 Offshore Technology Conference: Houston, Texas, p. 619-628, Paper OTC 8024, May 6-9, 1996.

Wood, D.M., 1990. Soil Behaviour and Critical State Soil Mechanics. Cambridge, U.K., Cambridge Univ. Press, 462 p.

Xu, W., and Ruppel, C., 1999. Predicting the occurrence, distribution, and evolution of methane gas hydrate in porous marine sediments. *J. Geophs. Res.*, 104(B3): 5081-5095.

Yang, Y., and Aplin, A.C., 2010. A permeability-porosity relationship for mudstones. *Marine and Petroleum Geology*, 27: 1692-1697, doi:10.1016/j.marpetgeo.2009.07.001.

Yang, Y.L., and Aplin, A.C., 1998. Influence of lithology and compaction on the pore size distribution and modelled permeability of some mudstones from the Norwegian margin. *Marine and Petroleum Geology*, 15(2): 163-175, doi:10.1016/S0375-6742(03)00035-9.

Yang, Y.L., and Aplin, A.C., 2004. Definition and practical application of mudstone porosity-effective stress relationships. *Petroleum Geoscience*, 10(2): 153-162.

Yang, Y.L., and Aplin, A.C., 2007. Permeability and petrophysical properties of 30 natural mudstones. *Journal of Geophysical Research*, 112(B03206), doi:10.1029/2005JB004243.

Zoback, M.D., Kitasei, S., and Copithorne, B., 2010. Addressing the environmental risks from shale gas development, Worldwatch Institute, 19 p.

Vita

Julia Schneider grew up in Delmenhorst, Germany, where one of her favorite memories is going on long bike rides with her Opa. In 2001, she entered The University of Bremen, Germany, where she completed bachelors and Diplom degrees in Geosciences in October 2004 and August 2006, respectively. Julia became fascinated with marine geology and geophysics and had the opportunity to participate in three research expeditions. She met her PhD advisor, Dr. Peter Flemings, on one of these expeditions, and a year later in August, 2006, she started her PhD with him at The Pennsylvania State University. In 2007, both transferred to the Graduate School at The University of Texas at Austin. Julia's goal is to pursue a career in academic research.

This dissertation was typed by Julia Schneider.